



HAL
open science

Fabrication and characterization of flexible strain sensors based on assembly of 1D nanostructures with cross-linked gold nanoparticles

Aarushee Rangra

► **To cite this version:**

Aarushee Rangra. Fabrication and characterization of flexible strain sensors based on assembly of 1D nanostructures with cross-linked gold nanoparticles. Micro and nanotechnologies/Microelectronics. INSA, 2021. English. NNT : 2021ISAT0030 . tel-03738141v1

HAL Id: tel-03738141

<https://laas.hal.science/tel-03738141v1>

Submitted on 14 Feb 2022 (v1), last revised 25 Jul 2022 (v2)

HAL is a multi-disciplinary open access archive for the deposit and dissemination of scientific research documents, whether they are published or not. The documents may come from teaching and research institutions in France or abroad, or from public or private research centers.

L'archive ouverte pluridisciplinaire **HAL**, est destinée au dépôt et à la diffusion de documents scientifiques de niveau recherche, publiés ou non, émanant des établissements d'enseignement et de recherche français ou étrangers, des laboratoires publics ou privés.



THÈSE

En vue de l'obtention du
DOCTORAT DE L'UNIVERSITÉ DE TOULOUSE
Délivré par l'Institut National des Sciences Appliquées de
Toulouse

Présentée et soutenue par
Aarushee RANGRA

Le 25 novembre 2021

**Fabrication et caractérisation de capteurs de déformation
flexibles à base d'assemblage de nanoparticules d'or greffées
sur des nanostructures 1D**

Ecole doctorale : **GEETS - Génie Electrique Electronique, Télécommunications et
Santé : du système au nanosystème**

Spécialité : **MicroNano Systèmes**

Unité de recherche :
LAAS - Laboratoire d'Analyse et d'Architecture des Systèmes

Thèse dirigée par
Christian BERGAUD

Jury

M. Lionel BUCHAILLOT, Rapporteur
M. Lionel ROUSSEAU, Rapporteur
Mme Reiko ODA, Examinatrice
Mme Marie-Hélène DELVILLE, Examinatrice
M. Fabrice SEVERAC, Examineur
M. Frédéric MORANCHO, Examineur
M. Christian BERGAUD, Directeur de thèse

To Kamaljit & Bittu

Acknowledgements

This work has been achieved thanks to the collaboration of many people and different institutions mention as follows: Institut de Chimie de la Matière Condensée de Bordeaux (ICMCB), Institute of Chemistry & Biology of Membranes & Nano-objects (CBMN), Nanomade and the Laboratory of Analysis and Architecture of Systems (LAAS). I am deeply grateful with all the members of the jury: Frédéric MORANCHO (President), Reiko ODA, Marie-Hélène DELVILLE, Fabrice SEVERAC, Lionel BUCHAILLOT, Lionel ROUSSEAU, Christian BERGAUD (Supervisor) for agreeing to read the manuscript and to participate in the defense process of this thesis.

I would like to thank my supervisor Christian BERGAUD for sharing with me his expertise and scientific knowledge through discussions and ideas to enrich this work all along my thesis. I have benefited greatly from his thorough editing. I am extremely grateful that he took me on as an internship student and continued to have faith in me over the years of my PhD.

I want to thank the engineer Fabrice MATHIEU at LAAS who helped in improving the characterization set-up. His expertise made him an essential part of this thesis and results harvested from it. I would thank Fabrice SEVERAC and Estelle MAZALEYRAT at Nanomade for helping to test sensors at their company. I thank them for their time and valuable insights to experimental results. I warmly thank various participants of this project Christina VILLENEUVE-FAURE, Emmanuel FLAHAUT, Richard MONFLIER, Nicolas MAURAN & Elodie VIEU for following this project very closely and always giving time for discussions. It was an honor for me to share with them not only their scientific knowledge, but also their extraordinary human qualities which helped me a lot to lead this project with confidence. I want to thank all the members from the clean room in LAAS, especially my responsible Adrian LABORDE for all his guidance on the microfabrication process. I also thank Daisuke SAYA for walking me through each step of fabrication in the beginning of my thesis.

If I enjoyed these three years of thesis, it was in big part due to the atmosphere in LAAS, for this reason I want to thank all my colleagues and friends from research teams MEMS, ELIA & MILE. Gratitude to people I had endless hours of soulful talking with. Thanks to my numerous office mates, the neighbors in next offices and lunch

team for sharing a little part of their everyday life. I want to thank all my Hindi-speaking friends who made me feel closer to my home and made me miss it a little less all along these years. To Brazilian, Mexican, Spanish, Italian, Turkish, French, Czechia, Serbian, Portuguese, basically everyone at LAAS who didn't help in learning French, I thank you! I want to thank members of many artistic community I have been a part of. They made this journey more colorful and theatrical. Thanks to the LAAS choral team members. As well to Julien Marocco and Matthieu Joly, the music gurus.

I would also thank the Joly family for their overwhelming generosity. Also not forgetting to mention my Jojo and little Sophie who has been the rare blessing of year 2020. I thank Dolores who has been my constant since I joined LAAS. And thanking back people who mentioned me in their thesis manuscript.

Finally, I would thank my support system, my brother. He gave me the courage, motivation and strength to take up this PhD project at the first place. He has made my stay at France painless. I thank my father, his understanding not only emotional but also scientific which inspired me. He introduced me to MEMS community at the first place and made sure I had every skill set required to achieving my goals. And I dedicate all my tiny victories to my mommy who taught me how to live & love.

Lastly, I would express my gratitude towards Almighty and my younger self.

This thesis is partially dedicated to the research and engineering community, the reference list of this manuscript is a testimony to their groundwork upon which this work is built.

I do not thank you, who has opened this manuscript only to read acknowledgements.

Table of Contents

ACKNOWLEDGEMENTS.....	IV
TABLE OF CONTENTS	VI
ABBREVIATIONS.....	VIII
TABLE OF FIGURES	IX
GENERAL INTRODUCTION	17
BIBLIOGRAPHY	20
1. CHAPTER 1: FLEXIBLE STRAIN SENSORS: STATE-OF-THE-ART	21
INTRODUCTION	23
1.1 STRAIN SENSING DEVICES.....	26
1.1.1 Stretchable devices.....	28
1.1.2 Flexible devices.....	31
1.1.3 Conclusion	32
1.2 FLEXIBLE STRAIN SENSOR	34
1.2.1 Transduction mechanism	34
1.2.2 Responsive Mechanism	38
1.2.3 Sensing Materials	41
1.3 NANOMATERIAL ASSEMBLY FOR NANOPARTICLES AND NANOWIRES.....	45
1.3.1 Chemically Driven	46
1.3.2 Flow fields.....	47
1.3.3 Shear force	47
1.3.4 Electric and Magnetic field.....	47
1.4 CHARACTERIZATION PLATFORM	48
1.4.1 Performance parameters	48
1.4.2 Sensitivity	48
1.4.3 Non-Linearity.....	54
1.4.4 Hysteresis	55
1.4.5 Reproducibility and Dynamic Durability	56
1.4.6 Characterization Set-up.....	57
1.5 CONCLUSION	62
BIBLIOGRAPHY	63
2. CHAPTER 2: FABRICATION OF FLEXIBLE STRAIN SENSORS	83
INTRODUCTION	85
2.1 TECHNIQUES FOR NANOPARTICLES DEPOSITION.....	86
2.1.1 Drop cast method.....	88
2.1.2 Inkjet Printing	90
2.1.3 Spin Coating	93
2.1.4 Vacuum filtration	94
2.2 TECHNIQUES TO ALIGNING 1D NANOSTRUCTURES	96
2.2.1 Contact printing.....	97
2.2.2 Convective flow/Dip coating	99
2.2.3 Langmuir Blodgett.....	100
2.2.4 Magnetic Field Induction.....	102
2.2.5 Nanoimprint lithography.....	105
2.2.6 Spray alignment	106
2.2.7 Electric field induced alignment	108
Conclusion	110
2.3 DIELECTROPHORESIS	111
2.3.1 Dielectrophoresis Force	112

2.3.2	<i>Clausius-Mossotti factor $K(\omega)$</i>	113
2.3.3	<i>Electrode configurations</i>	115
2.3.4	<i>Operating modes</i>	116
2.3.5	<i>External Impact factor of Dielectrophoresis</i>	117
2.3.6	<i>Synthesis of 1D nanohelices with grafted nanoparticles</i>	121
2.4	DEVICE FABRICATION	125
2.4.1	<i>Fabrication process for the interdigitated electrodes</i>	126
2.4.2	<i>Fabrication process for the ‘active area’</i>	134
2.5	DISCUSSION.....	138
2.5.1	<i>Dielectrophoresis comparison with Drop-Casting</i>	138
2.5.2	<i>Helical nanostructures</i>	140
2.6	DIELECTROPHORESIS BOUNDARY CONDITIONS.....	141
2.6.2	<i>Dielectrophoresis Challenges</i>	144
2.7	CONCLUSION	146
	BIBLIOGRAPHY	148
3.	CHAPTER 3: MECHANICAL CHARACTERIZATION	157
	INTRODUCTION	159
3.1.	MEASUREMENT PROTOCOLS	159
3.1.1.	<i>Flexural Test Setup</i>	159
3.1.2.	<i>Sample Preparation</i>	161
3.2.	CALIBRATION PROTOCOL.....	162
3.2.1.	<i>Strain Calculation</i>	166
3.2.2.	<i>Electrical connection and encapsulation layer</i>	168
3.3.	PERFORMANCE CHARACTERISTICS	170
3.3.1.	<i>Sensitivity</i>	171
3.3.2.	<i>Linearity</i>	181
3.3.3.	<i>Durability and Stability</i>	183
3.3.4.	<i>Hysteresis</i>	185
3.3.5.	<i>Response Time</i>	187
3.3.6.	<i>Vibration test</i>	189
3.4.	CONCLUSION	192
	BIBLIOGRAPHY	193
4.	CHAPTER 4: TEMPERATURE & HUMIDITY TESTS, PRELIMINARY RESULTS FOR WEARABLE STRAIN SENSORS	197
	INTRODUCTION	199
4.1	TEMPERATURE & HUMIDITY RESPONSE	199
4.1.1	<i>Temperature Tests</i>	201
4.1.2	<i>Humidity Tests</i>	205
4.2	BIOLOGICAL SIGNAL MEASUREMENTS.....	210
4.2.1	<i>Cardiac Pulse Measurement</i>	210
4.2.2	<i>Hand movements</i>	215
4.3	CONCLUSION	224
	BIBLIOGRAPHY	225
	GENERAL CONCLUSIONS & FUTURE DIRECTIONS.....	231
	APPENDIX.....	234
	BIBLIOGRAPHY	236

Abbreviations

1D	: One-Dimension
DEP	: Dielectrophoresis
CVD	: Chemical Vapor Deposition
PET	: Polyethylene terephthalate
SHM	: Structural health monitoring
CNT	: Carbon nanotube
NP	: Nanoparticle
GF	: Gauge Factor
CNT	: Carbon Nanotube
IDE	: Interdigitate Electrode
NP	: Nanoparticle
PI	: Polyimide
SiP	: Silicon wafer
PDMS	: Polydimethylsiloxane
PR	: Photoresist
DEP	: Dielectrophoresis
AuNP	: Gold Nanoparticle
NS	: Nanostructure
HNS	: Helical Nanostructure
R0	: Baseline Resistance of the sensor

Table of Figures

Figure 1.1: Flexible and stretchable strain sensors application.....	23
Figure 1.2: The illustration of top-down and bottom-up fabrication. In top down fabrication [20], materials with micron and centimeter dimensions, are cut into nanostructures via photolithography, including nanoimprint lithography, electron beam lithography, helium ion beam lithography [21], and chemical oxidation. The bottom-up approach fabricates large-scale nanomaterials from the nanoscale to micron and even centimeter size. It mainly involves of in situ growth [22], chemical vapor deposition (CVD) [23], and self-assembly.	25
Figure 1.3: (a) Illustration shows classical, transparent, and stretchable regimes, Flexible electronics is subset of the stretchable electronics, and textile electronics is subset of the flexible electronics [27]. (b) Classification based on substrates type: Solid substrates, flexible substrates, and stretchable substrates [28].....	27
Figure 1.4: Examples of flexible electronics on bendable substrate (a) Photograph of flexible integrated sensing array for the purpose of perspiration analysis. Sensor fabricated on mechanically flexible polyethylene terephthalate (PET) [29]. (b) Schematics of multiplexed fingerprint sensor with multifunctional detection of finger pressure and skin temperature using AgNF–AgNW hybrid [30]. (c) Image flexible temperature sensor based on reduced graphene oxide and its possible application for robot skin [31]. (d) 3D schematics (top) and photograph (bottom) of a flexible hydrophilic polytetrafluoroethylene (H-PTEF) humidity sensor. To enhance mechanical stability of sensors, polyethylene terephthalate film (70 μm) is laminated beneath the thin H-PTEF film [32].....	28
Figure 1.5: Structural stretchability examples: (a) Schematic illustration of wavy structures with two different bonding strategies on the elastomeric PDMS substrate, that are fully and selectively bonded onto the substrate [33]. (b) Atomic force micrographs of the 1D and 2D wavy ribbons fully bonded onto PDMS substrate [34]. (c) Response of 3D buckled nanoribbons to stretching and compressing (top). SEM image of a sample formed (below) [35]. (d) Design optimization of the 2 nd order serpentine interconnects in an island–bridge structure [36]. (e) structure of stretchable battery, stretchable current collectors with an island-bridge structure [37].	29
Figure 1.6: Various stretchable structure configuration on scale of increasing stretchability with respect to the scale of structure size [47][48].....	31
Figure 1.7: (a) Diagram of a bent strain device (b) Compression and tension zone created during the bending.....	31
Figure 1.8: (a) Stress vs strain graph (b) Web chart summarizing various properties of stretchable and flexible strain sensor. In the four level of each property, higher/more marking corresponds to higher point. Example: The ease of fabrication scores 1point for stretchable strain sensor representing very low flexibility in fabrication.	34
Figure 1.9: Schematics illustrating the different modalities of electromechanical sensors. (a) Piezoresistivity, (b) capacitance, (c) piezoelectricity. [51]	35
Figure 1.10: Capacitive sensing with (a) parallel plate configuration (b) interdigitated configuration [52]	36
Figure 1.11: (a) Series of optical images of the CNT films/PDMS composites stretched from 0% to 60%. (b) Simulation using Chinese paper cuttings show the change of crack morphology from unstrained to strained states. (c) Average gap width versus strain loading (d) the resistance model of a sensing unit [61].....	39
Figure 1.12 : Characteristics of the nanoparticles	42

Figure 1.13 : Illustration of size distribution of nanoparticle – 0D, 1D, 2D, 3D. (a) TEM images of gold nanoparticle samples [87]. (b) Diagram of strain sensing measurement where inter-particle distance increased as the sensor is bending [88]. (c) SEM image of higher density aligned 1D AgNWs [89]. (d) Stretchable electric nanomaterial consisting of aligned single-walled carbon nanotube (SWCNT) thin films for the application of human motion detection[62]. (e) AFM image shows two-dimensional structure of lead iodide nanosheet. (f) Diagram showing the electricity generation process of a 2D piezoelectric device [90]. (g) Cross-sectional SEM images of flexible resistive pressure sensor based on a CNT network-coated thin porous PDMS sponge at compressions of 0% and 80%, showing the formation of overlapped CNT layers upon compression [91]. (h) Schematic showing application mechanical pressure to 3D porous device [92].	43
Figure 1.14 : Nanomaterial alignment on different dimensions [104].	46
Figure 1.15: Gauge factor is the ratio of resistance variation to the length deformation	49
Figure 1.16: (a) Basic tensile electromechanical response of CNT/TPU sensor. Relative resistance changes of strain sensor with high sensitivity and linear response in three strain ranges [163]. (b) Relative resistance change of CNT-CB/PDMS strain sensor as a function of applied tensile strain shows a non-linear response [168]. (c) Measured sensor response under one cycle strain for 100% strain amplitude. As seen capacitive type exhibited linear sensor response ($R^2 = 0.9995$), while the resistive type exhibited nonlinearity and variable gauge factor. Sensors consist of a carbon black-filled elastomer composite [81].	55
Figure 1.17 : (a-b) Long-term relative variation in resistance of the MWCNT/PDMS strain sensor when subjected to the 1000 cycles of stretching/releasing (from 0–10% strain) [174]. (c) Hysteresis loops of a $Ti_3C_2Tx-AgNW-poly$ (dopamine)/ Ni^{2+} strain sensor subjected to 5000 stretching and releasing cycles [175].	56
Figure 1.18 : Overview of strain measuring system	58
Figure 1.19 : Schematics of stretching	59
Figure 1.20 : Schematic set-up used for the tensile testing. In red is the zoom image of sensor closer to the clamp.	60
Figure 1.21 : (a) Cantilever beam or two-point bending (b) Three-point-bending (c) Four-point bending.	60
Figure 1.22 : Illustration of deformation by the 3-point bending load	61
Figure 2.1 : Material overview for flexible and stretchable strain sensors.	86
Figure 2.2 : Advantages and limitations of geometrically different nanomaterials [17].	87
Figure 2.3: Schematic diagram of drop cast method. Step 1: A drop is poured onto a substrate; Step 2: the solution spreads spontaneously on the substrate and dries naturally or by using elevated temperature; Step 3: Resultant thin film. SEM image shows gold nanoparticle assemblies formed. reprinted from Ref.[24]. The scale bar is 100 nm.	89
Figure 2.4: Schematic illustration of drop casting: ((a) - top line) vs the sweeping ((e) bottom line) techniques, (b) Microscopic image of AuNP after five-drop cast cycles. Corresponding SEM images of nano gap at (c) 130 nm and (d) 500 nm (f) Microscopic image of AuNP drop casted, followed by sweeping procedures. Corresponding SEM images of nano gap at (g) 130 nm (h) 500 nm, (i) Calculated AuNP ratio is nano gap by two techniques [27].	90
Figure 2.5: (a) Inkjet printing working principle (b) Processing steps for silver nanoparticle colloidal solutions (TEM image of nanoparticles on the carbon/copper grid). (c) SEM images: dried for 15 min. at 80 °C [32].	92
Figure 2.6 : (a) Coffee ring effect appears to be darker as the size of the drop increases. Smallest drop ($R = 1.5 \mu m$), medium sized drop ($R = 5 \mu m$), largest drop size ($R = 25 \mu m$). The critical diameter D_c for the transition between ring formation and no ring formation. [34] (b) Jet of ink emerging from a drop on-demand nozzle, along with unwanted secondary droplets called satellite drops. [35]	93

Figure 2.7: Schematic diagram of spin coating.....	94
Figure 2.8 : (a-c) Schematic representation of the vacuum filtration procedure, (b) SEM image shows surface morphology of tin nanoparticle (having particle size ~50 nm) composite film prepared by vacuum filtration method [39].	95
Figure 2.9: (a) Schematic of the process flow for Contact Printing. (b) SEM image of a wafer-scale nanowire printing. Large area and highly uniform parallel arrays of aligned NWs were assembled on a 4 in. Si/SiO ₂ wafer by contact printing. [45].....	97
Figure 2.10 : Sequential stages of dip-coating techniques: (1) Substrate is dipped in the sol precursor, (2) Substrate is withdrawn at a constant speed, (3) To yield the gelation layer, and solvent is let to dry. (a, b) SEM image of silver nanowire monofilm generated from one dip coating at water-bath temperature of room temperature (a) and 90°C (b). (c-d) SEM image of ordered multilayer silver nanowire of two(c) and three (d) orthogonal dip coating at water bath of 80°C [33]......	99
Figure 2.11: Schematic diagram of Langmuir–Blodgett technique	101
Figure 2.12 : (a) Photographs of Langmuir–Blodgett nanowire assembly process at different compression stages. SEM images (b, c) of a parallel nanowire array, and (c) crossed nanowire array. (d) SEM image at different magnifications for crossed nanowire array. [32]	102
Figure 2.13: Schematic diagram of Magnetic induced	103
Figure 2.14: Fabrication of aligned network of nanowires: (a) Magnet is placed under the substrate and the inhomogeneous magnetic field directs nanowires towards the substrate. The tangential component of the magnetic field aligns nanowires (b) the second layer is deposited when the magnet is rotated 90° degrees; (c-d) Show the corresponding SEM images. [48]	104
Figure 2.15: (a-d) Schematic diagram of nanoimprint lithography. (e, f) SEM images showing the resist structures after the imprint, sub-micrometer features of top and side surfaces of CNT [51].	105
Figure 2.16 : (a) Schematically depiction of a spray jet in which the central axis of the spray cone is parallel to the surface normal. As a consequence, there is almost no macroscopically directed shear flow induced when spraying at a 90° angle against the receiving surface, especially when using small droplet speeds and when spraying from large distances. (b) The angle between the center of the spray jet and the surface is typically less than 20° (red lines), this technique is called Grazing incidence spraying. Spraying at this geometry produces a liquid flow on the surface in the spraying direction (away from the nozzle). [53] (d) surface coverage measured on SEM pictures as a function of the spraying time (d-f) SEM pictures of AgNW monolayers deposited for 10 s , 50 s and 800 s. [54]	107
Figure 2.17: Schematic diagram of Electric field induction	108
Figure 2.18 : (a) Schematic illustration of test pattern that comprised (a) two electrodes, (b) four electrodes, (c) six electrodes, (d-f) corresponding dark-field microscope graphs showing alignment of nanofibers. [56]	109
Figure 2.19 : Diagram of a positive dielectrophoresis (a) In uniform electric field, particle is symmetrically polarized resulting in zero amplitude net DEP force (b) In non-uniform electric field, particle is asymmetrically polarized, resulting in motion of the particle to an area with maximum electric field amplitude. [58]	112
Figure 2.20 : Schematic representation of DEP alignment of 1D nanostructure.....	113
Figure 2.21 : Variation in Real part of Clausius-Mossotti factor, Re [K(ω)] with frequency when: (a) $\epsilon_m < \epsilon_p$ and $\sigma_m \gg \sigma_p$ (b) $\epsilon_m > \epsilon_p$ and $\sigma_m \ll \sigma_p$	114
Figure 2.22: Examples for 2D electrode: (a) parallel or interdigitated, (b) crenellated, (c) oblique, (d) quadrupole, (e) curved, and (f) matrix	116
Figure 2.23: Examples for 3D electrode: (a) extruded, (b) insulator-based or electrodeless and (c) contactless	116

Figure 2.24 : Scanning electron micrographs of structures fabricated at two different voltage (a, b) using solutions 0.2 mg/ml of CNFs in water. The gap between the electrodes is 3 μm	118
Figure 2.25 : Scanning electron micrographs of structures fabricated at two different frequency 10 kHz and 1000 kHz (c, d) Using solution of 0.01 mg/ml of gold nanoparticle grafter over inorganic silica nano helices. The gap between the electrodes is 3 μm	119
Figure 2.26 : SEM images of aligned nanofibers with the 3 μm -wide castellated electrode, solutions have two different concentrations: (a) 0.02 mg/ml, (b) 0.002 mg/ml. DEP boundary conditions: 5 V_{p-p} , 1 kHz, 6 s.	119
Figure 2.27 : (a) Influence on the nanowire orientation as a function of direction of electric field gradient. (b) Clausius-Mossotti factor according to the long and short axis as a function of frequency, for InAs wires suspended in deionized water.	121
Figure 2.28 : Reaction scheme of the manufacturing process of silica nanohelices.	122
Figure 2.29 : (a) Schematic of gold nanoparticles functionalized with different ratios of mercaptopropionic acid (MPA) and SH-PEG-COOH (PEG).....	124
Figure 2.30 : (a) Reaction scheme for the fabrication of nano-helices @Au-NPs. (b) TEM image of a nano-helices @Au-NPs.....	125
Figure 2.31 : Diagram of flexible strain sensor labeled with the techniques of fabrication and material used in this study.....	126
Figure 2.32 : (a) 10-alignment site design with three different castellated shapes, (b) 720-alignment site design to use for strain sensing purposes	127
Figure 2.33 : Step-by-step fabrication process for interdigitated electrodes on polyimide: (a) Top view, (b) Cross-sectional view; In the cross-sectional view: (I) 4" p-type silicon wafer, (II) PDMS layer spin-coated on the silicon wafer, (III) Polyimide (PI) lamination, (IV) Deposition of a negative photoresist (PR) layer (nLOF) and transfer of the mask pattern onto the PR layer, (V) Development for 30 seconds (VI) Sputtering of a bilayer of Ti/Au (50 nm/20 nm), (VII) Lift-off and (VIII) Delamination and cutting of the PI layer.	128
Figure 2.34: (a) Labeled image Spin coater for PDMS deposition (b) Manual laminator model ML 360 is designed to provide reliable lamination	130
Figure 2.35 : (a) PI substrate with IDE (b) Dimensions of individual chip (c) IDE over (1) Silicon Dioxide substrate (2) Glass Substrate (3) polyimide substrate.	132
Figure 2.36: (a) Interdigitated part is lost during lift-off because of over-development (b) structures after process optimization (c) Magnified SEM image of well-resolved interdigitated part.	133
Figure 2.37 : Output of a 4-inch wafer with proper 3 μm gap separation between IDE is never 100%.....	134
Figure 2.38 : Image showing the placement of connecting probe on IDE	134
Figure 2.39 : (a) Schematic of Dielectrophoresis: Step 1. Droplet of solution placed over IDE, Step.2 10 V_{p-p} applied between the IDE, Step.3 Sample is cleaned off the excess solution, Step 4. SEM picture of aligned gold helices across the electrode gap, Sample (Sensor chip) is now ready for electrical and mechanical characterization (b) Impedance analyzing system.	136
Figure 2.40 : Multiple dielectrophoresis is performed to tune the resistance within the appropriate range for the strain sensor.....	137
Figure 2.41 : SEM image show the deposition of Gold Helices between 3 μm gaps (1) Initial state of DEP showing dispersed Gold Helices around the electrode (2) In later state of DEP, earlier scattered particles are now well aligned and forming a bridge between the electrode.	138
Figure 2.42 : Dielectrophoresis vs Drop-Cast; (a-c) Results of DEP deposition; (d-f) Results of Drop-Cast.....	139

Figure 2.43 : SEM image of various nanoparticles deposition using DEP at same boundary condition. (a) Dense deposition of helical nanostructure made with only PEG ligand attached to AuNP, (b) Clustered deposition of helical nanostructure made with only MPA ligand attached to AuNP.....	140
Figure 2.44: (a) Schematic diagram and SEM image of IDE with 10 castellation (b) Deposition morphology at three frequency regimes: (1) Aggregated and scattered deposition observed at lower frequencies (2) Uniform deposition at frequency range 10 -100 kHz (3) Very low and almost no deposition observed at higher frequencies	142
Figure 2.45: Resulting device resistance vs input DEP frequency relation is almost linear.	143
Figure 2.46 : SEM images of deposition made at: (a) 10 kHz frequency (b) 50 kHz frequency (c) 300 kHz frequency.....	143
Figure 2.47 : Scanning electron microscope image of DEP process at (a) t seconds and (b) t + Δt seconds, density increased because of longer time during which the DEP force is applied	144
Figure 2.48 : SEM image of (a) Uniform DEP deposition (b) Incomplete DEP process hindered in presence of aggregate.....	145
Figure 3.1: Three point bending setup: HNS sensors are place over two supporting points by use of an additional base-substrate under HNS Kapton sensors. Electrical connections are made via alligator clips to the Sourcemeter and output data is observed and recorded through LabVIEW software.....	160
Figure 3.2 : (a) Strain sensor placed facing downwards on a three-point bending machine. (b) Graph shows input parameter i.e., speed of the probe and dwell time for three-point bending.	161
Figure 3.3: Sample preparation: 4inch wafer sized Kapton film, with many individual IDE is first cut. One fabricated IDE sample is 18 mm long and 8 mm wide, with an active area of interdigitated electrode of 16 mm ² . Single IDE is glued to glass or PVC base-substrate and later placed over two supporting points on three-point bending setup.....	162
Figure 3.4 : LabVIEW software interface showing eight complete loading and unloading cycles.	163
Figure 3.5: Inconsistency in applied uniform (a) Force (N) and the resulting (b) Deformation (mm).	164
Figure 3.6 : (a) Force, length vs number of points recorded. (b) Image showing the three-point bending set-up, force probe moves in downward direction to approach the sensor sample.	166
Figure 3.7: (a) Schematic explanation of proportionality factor 'm' between applied force and generated strain. (b)Value of slope m for different support substrate. (c) Strain and Force relation for three different substrates established using commercial sensor.	167
Figure 3.8: Possible ways to connect sensor to Keithley 2450 Source Meter by (a) crocodile clamps and (b) soldering wires on commercial sensors where adding clamps is not possible. (c) Comparison between two different means for the electrical connection of the sensor....	169
Figure 3.9: Calibration Figure: Relative resistance variation as a function of induced strain ϵ (%) for bare strain sensor (red) and same sensor after encapsulation (blue), where the points and lines show the experimental and linear data fit respectively.	170
Figure 3.10: The features of HNS-based strain sensors that need to be evaluated.....	171
Figure 3.11: Gauge factors for various materials used for strain sensors.....	172
Figure 3.12: (a) Graph showing the significance of deposition via DEP, Resistance, and Gauge Factor. (b) Schematic illustration of the conductive mechanism. (c) SEM image of HNS between two gold electrodes separated by a 3 μm gap (bottom).....	173
Figure 3.13: Schematic of Multiple depositions.	174

Figure 3.14: Influence of the nanoparticle density on the strain sensitivity. (a) relative resistance change as a function of strain of nanoparticle films of various platinum nanoparticle densities (b) the gauge factor as a function of surface coverage [13].	175
Figure 3.15: (a) Set of sensors at different resistance value and their resistance variation response to strain. (b) Change in Gauge Factor value obtained from sensors at different resistances (k Ω).	175
Figure 3.16: Resistance cycles of Sensor (1) with initial resistance of 70 k Ω , i.e., smaller amount of HNS present between the electrode. The calculated gauge factor of 115. Blue line represents the resistance variation and red represents the strain variation.	176
Figure 3.17: Resistance cycles of Sensor (2) with initial resistance of 2.5 k Ω and calculated gauge factor of 119. Device with optimized amount of deposition show no drift during the cycling response. Blue line represents the resistance variation and red represents the strain variation.	177
Figure 3.18: Resistance cycles of Sensor (3) with initial resistance of 58 Ω . The extremely dense deposition is the reason device is not able to detect small strain values accurately. Substrate straining is not enough to induce modification to the inter-particle distances. Blue line represents the resistance variation and red represents the strain variation.	178
Figure 3.19: The significant relation between deposition via DEP, device resistance and Gauge Factor.	178
Figure 3.20: Two sensors with resistance \sim 70 k Ω and \sim 400 k Ω having a similar gauge factor 40.	179
Figure 3.21: Comparison of HNS sensors (red) to commercial sensors (black) and strain sensors fabricated by Nanomade (blue). Two curves on HNS sensor and Nanomade sensor represents two trials to measure the resistance variation over similar sensor.	180
Figure 3.22: Resistance response of the strain sensor to the cycle of bending/releasing with low strain variation (0.01 - 0.05%).	181
Figure 3.23: Relative variation of the resistance $\Delta R/R_0$ as a function of the applied strain for HNS based strain sensors, (a) Glass as base-substrate, the sensor shows linear response at low strain. (b) PVC as base-substrate, the sensor shows non-linear trend seen at higher strain [19].	182
Figure 3.24: Durability of HNS under 2200 cycles with low tensile deformation. $\Delta R/R_0$ as a function of multiple bending and releasing cycles with 0.06% strain. $\Delta R/R_0$ refers to the relative resistance variation under bending and release, R_0 is the resistance in the relaxed state. Resistance variation shifts by 3% in the second half of the bending cycle; however, the ratio remains the same.	184
Figure 3.25: (a) Equipment to test measurement for mechanical aging: Key Life Test Machine (ZL – 2806). (b) Relative resistance variation as a function of applied force after different pulsing strain cycles of 0.03%. Init refers to measurement before subjecting to cycling test. ΔR refers to the resistance differences under bending and release (Picture and figure from Nanomade).	185
Figure 3.26: Resistive change at 10 bending cycles for HNS based strain sensor.	186
Figure 3.27: Comparison of hysteresis between HNS sensor (blue) and Nanomade (red) fabricated sensor that clearly show the advantage of using HNS to reduce or even suppress the hysteresis (Figure from Nanomade).	187
Figure 3.28 : Response (16.1 ms) and recovery time (23.5 ms) test for AuNPs–TEG network based strain sensor [29].	188
Figure 3.29: (a) Illustration of 'Response time' setup. (b) Response time measurement when a pressure is suddenly applied and then removed.	189
Figure 3.30: Illustration of the vibration test setup	189

Figure 3.31: (a) Current response to vibration signal (b) Magnification of the signals in the red square in (b)	190
Figure 3.32: (a) Electrical response to vibration signal. (b) Magnification of the damping signals in the red square in (a) [29].	191
Figure 4.1: (a) Image of the fabricated polyimide network (10 × 10 array, scale bar: 5 mm). (b) SEM image of the polyimide network. (c) Schematic layout of an integrated sensor array with eight functions[13]. (d) Multifunctional Electronic Tattoos based on Silk and Graphene. (e) Temperature sensor performance of the corresponding tattoo-based sensor. (f) Real-time relative humidity sensing at several specific relative values [14].	200
Figure 4.2: (a) Climatic chamber. (b) Sensor connection inside climatic chamber via PCB. (c) Three-point bending set-up.	202
Figure 4.3: Resistance variations of encapsulated (green curve) and non-encapsulated sensors (blue curve) at elevated temperature from room temperature to 85°C (Figure from Nanomade).	203
Figure 4.4: Resistance variations of encapsulated (green curve) and non-encapsulated sensors (blue curve) at low temperature (Figure from Nanomade).	204
Figure 4.5: Stability over high temperature and low temperature cycles – Resistance variation as function of strain. Graph presents two HNS sensor samples encapsulated N8 (black) and non-encapsulated N10 (green). ‘Inti’ refers to measurement before temperature cycle. HT refers to High Temperature, LT refers to Low Temperature (Figure from Nanomade).	205
Figure 4.6: (a) Resistance variations of encapsulated (blue) and non-encapsulated sensors (pink) during the humidity cycle (red). The temperature is constant and equal to 35°C throughout the whole cycle. (b) Resistance variations with (blue) and w/o encapsulate (pink), zoomed on the beginning of the humidity cycle (Figures from Nanomade).	206
Figure 4.7: Resistance vs Relative humidity of AuNPs TEG and HEG based humidity sensors.	207
Figure 4.8: The relative resistance and capacitance changes with respect to relative humidity (RH%) [17].	208
Figure 4.9: Illustration of sensing mechanism (a) the first and (b) the second physisorbed layer of the H ₂ O molecules. (c) Resistance of Graphene Quantum Dots(GQD) /AgNPs as a function of RH, the inset shows a humidity response of GQD/AgNPs sensor in comparison to a commercial humidity sensor [19].	209
Figure 4.10: (a) Photographs of Graphene/Silver nanowire nanocomposite strain sensor attached onto the wrist, with an adhesive tape. (b) Real-time monitoring of radial artery pulse [24]. (c) Current variation of the Thermoplastic polyurethane/graphene strain sensor, with an intertwined-coil configuration, in response to the pulse [22]. (d) Resistance response of biocompatible gold nanoparticle/polyurethane (GNP/PU) strain sensor to the radial artery pulse [25]. (e) Wearable strain sensors together with a head mounted VR system. (f) The measured arterial pulse wave for 8 seconds. A close-up view of one cycle showing 3 peaks: systolic (Ps), inflection (Pi), dicrotic (Pd) peaks [23].	212
Figure 4.11: (a) Photograph images of a HNS strain sensor attached to wrist using adhesive tape to monitor pulse. (b) Electronic circuit diagram for measuring the resistance change of the HNS sensor due to geometrical deformation of the microchannel.	213
Figure 4.12: (a) Real-time pulse wave and small strain sensing performance, original signals measured (a) with and (b) without pulse detection. (c) A close-up view of one cycle showing three peaks: systolic (Ps), inflection (Pi), dicrotic (Pd) peaks.	214
Figure 4.13: An interactive electronic system with five nanowire-microfluidic hybrid sensors using a multichannel data-glove to control a robotic hand through a wireless communication. (Right) Controlling different configurations of robotic fingers by a human hand wearing the data-glove [41].	216

Figure 4.14 : (a) Design of uSkin for a fingertip (b) 3D printed fingertip with flexible PCB attached to it [33]. (c) Photographs showing experiment settings how Shimmers is used to measure wrist and forearm motion [36]. (d) Integrated rosette-shaped Graphite/Silk Fiber strain sensor for multidirectional motion detection and Responsive signals during cyclic bending-unbending motion of the wrist [49]. (e) Photographs of wearable sensor attached to the knee marked in the red box. (f) Responsive curves of wearable sensor on the knee, shows various motions as labeled [50].	218
Figure 4.15: (a) Three-point bending set-up (b) Representative calibration curve. Sensor is calibrated before being installed on the subject. Force output in Newton was synchronized with resistance variation to produce a calibration equation, which was used subsequently to convert the resistance variation data from all trials on finger/hand into units of force. The fit for this sensor was linear with an R^2 value of 0.9.	219
Figure 4.16: Relative resistance changes versus time of the finger motion on the tensile strain region.	220
Figure 4.17: (a) Diagram showing the placement of the sensors as well alphabet 'I' and 'L' on each peak represents which finger is bent at each region. (b) Real-time output of the sensor glove showing individual finger response.	221
Figure 4.18: (a) Photograph and (b) the layout of the sensors on the glove.	221
Figure 4.19: (a) Demonstration of real time tracking of the bending by the HNS stretch sensor glove at two different configurations. (b) Resistance response of Configuration 1 and Configuration 2. The particular case, Configuration 2, showing here tracks the ultralow sliding effect between the electrodes.	222
Figure 4.20: Real-time resistance responses of the strain sensor for monitoring hand motion for 10 minutes, the fatigue response after 6 minutes has been well recorded by the HNS sensor.	223
Figure 0.1: Symmetrical Three-point bend loading	235

General introduction

This work was carried out in the framework of a research project funded by the French National Research Agency (ANR) (Nanoheliflex) between the Laboratory of Analysis and Architecture of Systems (LAAS), an industrial partner Nanomade Lab, the Bordeaux Institute of Condensed Matter Chemistry (ICMCB), the Institute of Chemistry & Biology of Membranes & Nano-objects (CBMN), and the European Institute of Chemistry and Biology (IECB).

Necessity of the project. In the last few decades, the advancement of science and technology has greatly influenced health and medical applications. And the improvement in medical facilities has helped to improve the quality of life. In recent years, the nanotechnology-based devices have greatly assisted in medical field. Nanomaterial based devices has been used in medical field for e-skins, drug delivery, pressure sensing, physiological parameter monitoring, etc. [1].

It is estimated that in next 20 years the amount of elderly people will increase. Over 23% people are estimated to reach an age of 65 by 2035. This alarmingly calls for medical facilities, which are available in low cost and easily accessible manner for monitoring various health related problems. It is predicted that in next few years, there will be a considerable increase in medical market of around 500 billion USD. In addition, in the next 5 years the compound annual growth rate is estimated to increase by 14% investing in market for cancer diagnostic and cardiovascular problems [2].

Wearables are one popular choice for health care monitoring. Wearable devices can provide advantages in monitoring patient from a remote location, they are easy to use and their comfortable integration makes them strikingly attractive. This demands for future electronics to integrate the attributes of flexibility, in order to realize a more comfortable and efficient device. The ability to imitate and cover movable objects could be exploited in the development of wearable devices.

Scope of this project. The work on development of a flexible strain sensor for possible application of wearable device is based on various parameters like material availability, properties of the materials processed, the fabrication process and

characterization of the response output. This is essentially realized through a rational sensor design process i.e., properly selecting the hybrid material and treating through a fabrication recipe matching with a desired application with the objective to enhance the sensitivity response and strength.

Focus of this project. In this thesis, the focus is on the use of nanomaterials. Nanoparticles-based resistive strain sensors usually respond with an increase in resistance to force straining the material. The response is mainly due to changing tunneling distances between conductive nanoparticles placed on an insulating substrate. Such flexible sensors contain a nanoscale percolating conductive network elaborated into a non-conductive substrate. These percolation networks can be fabricated in the forms of 1D NP, 2D thin films, or 3D self-sensing structures.

For fabrication of these kinds of networks in this thesis, we make use of the dielectrophoresis technique. It is simple and versatile method, which has proven to be very effective in aligning and deposition. Overall, the electromechanical performance of the piezoresistive sensors can be adjusted by manipulating the deformation mechanism of the conductive network in micro or nanoscales.

The objective of this work is to develop strain sensors based on the use of assemblies of a novel nanomaterial consisting in 1D nanohelices coated with gold nanoparticles connected by ligands to achieve critical features such as high sensitivity to very low strain forces, high Gauge Factor values, reproducibility, stability and zero-hysteresis response.

Thesis layout. This thesis is organized into four sections:

Chapter 1: We start by introducing the strain sensing devices, their transduction and response mechanisms considering nanomaterials as strain sensing material and the reason behind the choice of 1D nanomaterial for strain sensing purposes. An overview of deposition techniques and more specifically alignment technique is presented. The chapter is completed with introduction on the performances and the characterization parameters of strain sensors.

Chapter 2: We presents unique property of 1D nanomaterials, designing approaches to develop interdigitated electrodes (IDE) on flexible substrates and their micro-fabrication strategies to improve the production output. Finally, the boundary conditions of 1D helical - nanomaterial alignment via dielectrophoresis on IDE is discussed.

Chapter 3: We demonstrate the sensing output of flexible electro-mechanical strain sensors using three-point bending setup. Further, to avoid rapid aging and increase the shelf life, devices are encapsulated. Effect of encapsulation on the response is examined. The strain sensors are characterized through various parameters such as sensitivity, linearity and dynamic stability.

Chapter 4: Finally, we demonstrate the relevance of our strain sensor as a biomedical device. An overview of the mechanical and electrical behaviors of the sensor is presented in order to validate their usefulness and readiness in wearable systems. The HNS sensors are tested for: (1) monitoring of human pulse waves (2) finger-lifting pressure analysis (3) angular motion detection.

Bibliography

- [1] M. Amjadi, K. U. Kyung, I. Park, and M. Sitti, "Stretchable, Skin-Mountable, and Wearable Strain Sensors and Their Potential Applications: A Review," *Adv. Funct. Mater.*, vol. 26, no. 11, pp. 1678–1698, 2016, doi: 10.1002/adfm.201504755.
 - [2] A. Nag and S. C. Mukhopadhyay, *Nanoparticles-based flexible wearable sensors for health monitoring applications*. Berlin: Springer, Springer Nature, 2019.
-

Chapter 1: Flexible strain sensors: state-of-the-art

Introduction

Object of interest. In the last decade, flexible devices have shown great potential in various fields. For future applications, such as electronic skin, flexible touch screens [1], etc. developed in soft electronics, flexible and biocompatible strain sensors are of supreme importance. The advancement in manufacturing and development of material science has kept up with the innovation in robotics [2][3], wearable electronics [4][5][6], epidermal electronic systems, human-machine interfaces, other biomedical devices[7], and the related systems. Associated with the rapid growth of intelligent robots and wearable equipment, various new-type devices based on flexible pressure sensors are in high-speed development, for applications in entertainment, games, cars, consumer electronics, industries, and health care fields, among others.

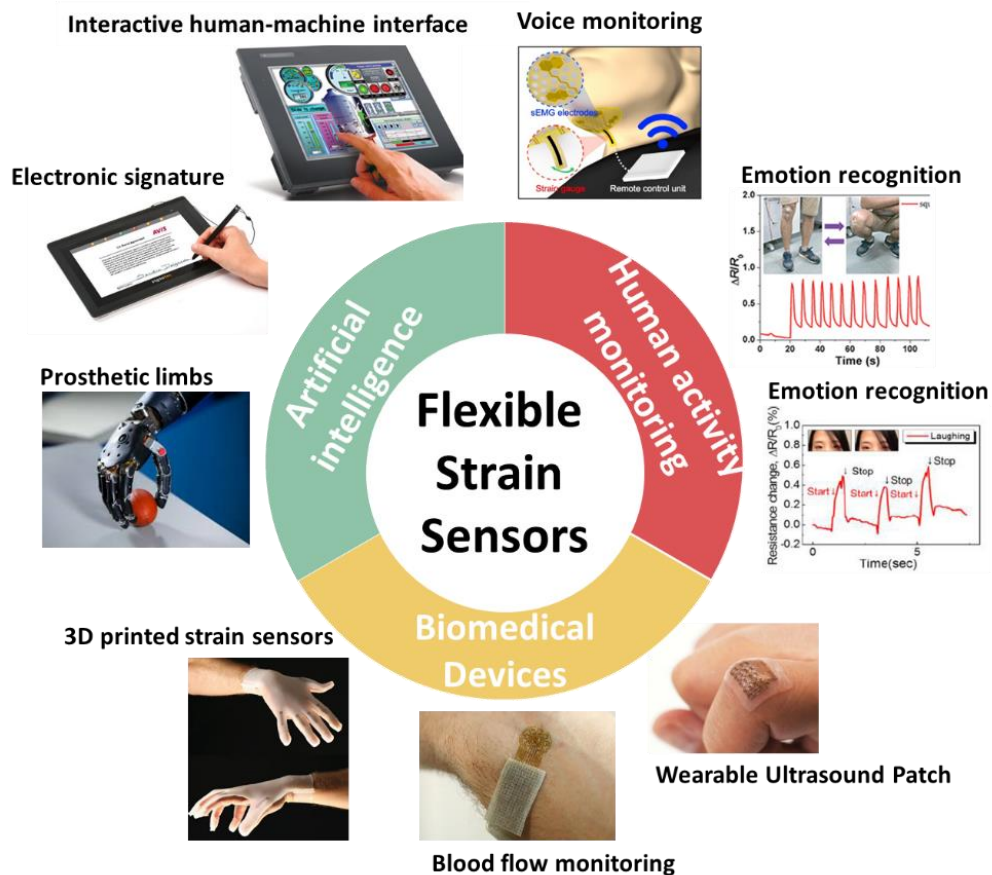


Figure 1.1: Flexible and stretchable strain sensors application

Strength. The flexible pressure sensors have a wide range of applications because they have excellent mechanical and electrical properties, such as high flexibility, high sensitivity, high resolution ratio, and rapid response [8][9][10][11]. The perception mechanisms of flexible pressure sensors can simply be divided into piezoresistivity, capacitance, and piezoelectricity. Flexible electronic skin (E-skin) sensing features with high sensitivity, high-resolution ratio, and fast response to temperature and pressure. The miniaturization of sensors and electronic circuits based on microelectronics has played a vital role in the development of wearable devices. The use of nanomaterials in electronics has enabled the development from today's rigid to flexible electronics and suggests the possibility of creating scalable electronic devices [12][13][11][14][15].

Material. Flexible sensing devices typically consist of active elements and a substrate. Many nanomaterials have been studied for the fabrication of flexible electronic devices. The electrically conductive/active materials widely used are metallic nanoparticles, nanowires [16], liquid metal, and carbonaceous components like carbon nanotubes, graphene, and other conductive polymers [17]. Among these materials, one-dimension nanomaterials exhibit unique benefits due to their inherent structural characteristics of their aspect ratio resulting in unique mechanical and electrical properties. Their morphology permits the assembly of a conductive percolation network, even with a small amount of material while still maintaining their performance. Simultaneously, 1D nanostructures can exhibit better mechanical properties, higher aspect ratio than corresponding spherical nanoparticles or massive materials, which is a key parameter for material design and allows better stability against material delamination or cracking problems [18].

Method of fabrication. The fact that flexible technology demands devices that are able to maintain their functional performance in both the original and the deformed states calls for flexible device configurations that can deliver the complex geometries and precisely scribed designs. Moreover, the array, including the alignment and predetermined location of nanomaterials, plays a crucial role in the fabrication of high-performance devices. The advantage of controlling the orientation of nanomaterials is to take advantage of their anisotropy, which is positively linked with the charge carrier

mobility. In contrast, electron transport may be adversely affected by disordered nanomaterial orientation. Therefore, assembling nanomaterials as desired to manufacture more promising devices [19]. However, to date, generating highly ordered alignment of nanomaterials at a large scale remains a major challenge that has restricted the applications of nanomaterials in advanced devices. Two techniques have been established to integrate nanomaterials, top-down and bottom-up fabrication, illustrated in Figure 1.2(b-c). Miniaturized devices such as mobile computers and cellular phones, are dependent on silicon-based nanotechnology and sophisticated ‘top-down’ type fabrication methods. However, this solid-state technology is likely to encounter size restrictions. Thus, more novel ‘bottom-up’ type nanofabrication techniques have recently been of interest as alternative manufacturing strategies. Bottom-up nanofabrication is driven by the self-assembling processes of constituent molecules. This approach is more moderate and fabricates large-scale nanomaterials from the nanoscale to micron to even centimeter size. One such bottom-up assembly technique is based on the mobility and interactions of particles caused by alternating electric fields, commonly referred to as Dielectrophoresis (DEP). The alternating current field allows manipulation and assembly of the particles. DEP has been used as a tool in the fabrication of complex particles, manipulation of living cells and microscopic sensors.

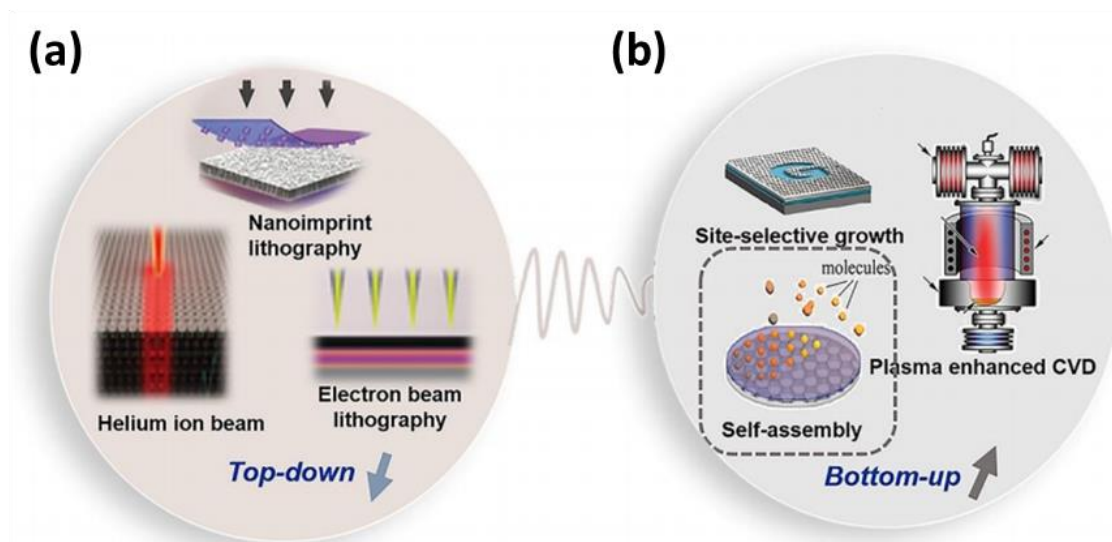


Figure 1.2: The illustration of top-down and bottom-up fabrication. In top down fabrication [20], materials with micron and centimeter dimensions, are cut into nanostructures via

photolithography, including nanoimprint lithography, electron beam lithography, helium ion beam lithography [21], and chemical oxidation. The bottom-up approach fabricates large-scale nanomaterials from the nanoscale to micron and even centimeter size. It mainly involves of in situ growth [22], chemical vapor deposition (CVD) [23], and self-assembly.

1.1 Strain Sensing Devices

Introduction. Sensor is a device that measures or detects an external physical stimulus, such as heat, pressure, light, motion or sound and converts it into an electrical signal. A strain sensor measures the applied strain on an object. In the latest years, many efforts are focused on flexible sensor fabrication. It has been useful in areas where sensors often need to work under high strain conditions and demand flexibility or stretchability. Conventional strain sensors are usually made of metals, metal alloys or piezoresistors. Due to limitation of material elasticity modulus, they tend to have reduced flexibility that have an impact when interfacing with nonplanar or deformable substrate. The advances in flexible and stretchable electronics expanded the capability of traditional rigid electronics [24][25][26]. Flexible electronics are classically composed of a thin inert substrate topped with a layer of active electronic components. In some applications, an additional layer is used for encapsulation and packaging. If the substrate is flexible as well as stretchable for better conformal fit to highly curved surfaces, the system would belong to the broader class of 'stretchable electronics' [27], Figure 1.3(a).

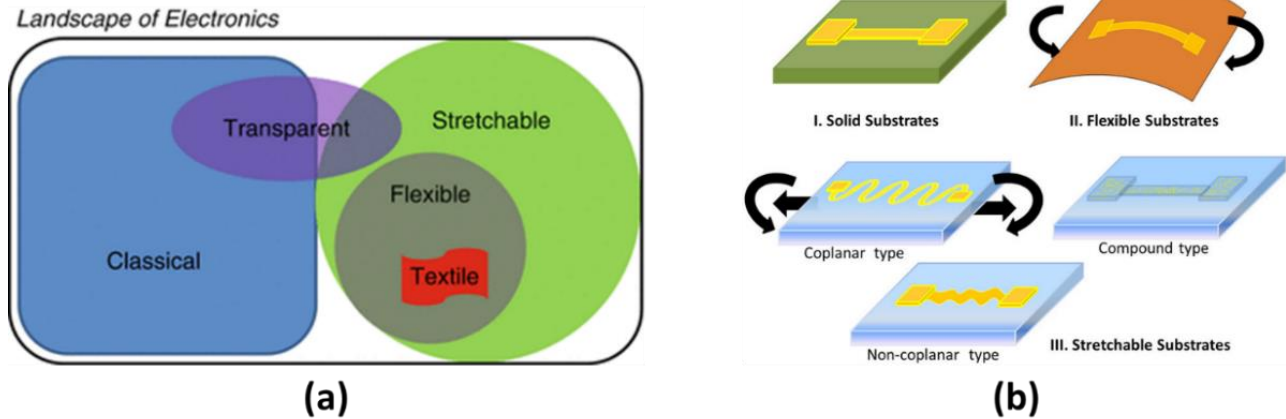


Figure 1.3: (a) Illustration shows classical, transparent, and stretchable regimes, Flexible electronics is subset of the stretchable electronics, and textile electronics is subset of the flexible electronics [27]. (b) Classification based on substrates type: Solid substrates, flexible substrates, and stretchable substrates [28].

The models of common substrates are as seen in Figure 1.3(b). Traditional electronic devices use **solid substrates**. Among the three substrates because of their high strength against bending, they tend to be most reliable. **Flexible substrates** show limited bendability and low stretchability. However, the stretchable property is not generally considered as their performance features. Hence, their lifetime will decrease drastically if subjected to prolong tensile or compressive strain. **Stretchable circuits** are divided generally into three types. They can sustain large bending and stretching movements, and have different applications from the other two. They can be placed on a non-planar surface. Because they are bent and stretched continually, their lifetime is low.

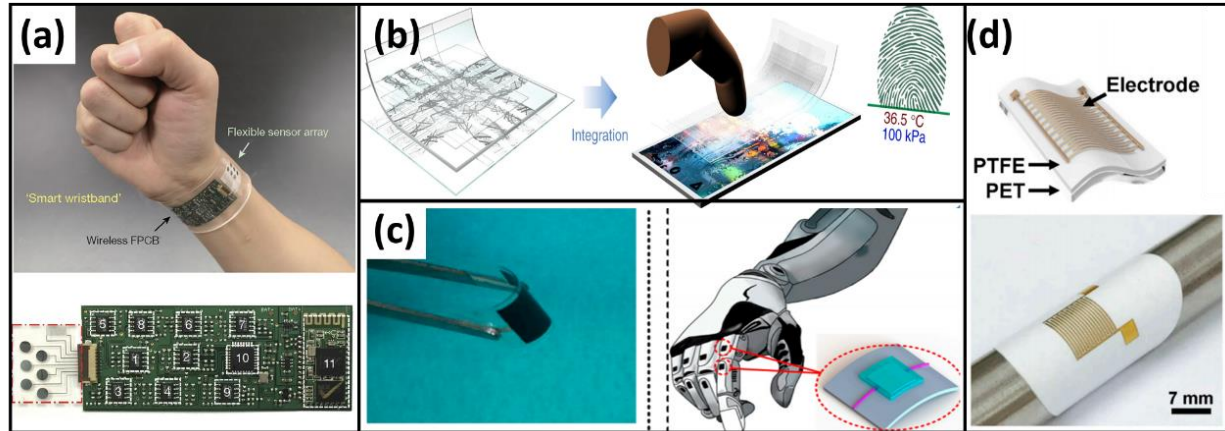


Figure 1.4: Examples of flexible electronics on bendable substrate (a) Photograph of flexible integrated sensing array for the purpose of perspiration analysis. Sensor fabricated on mechanically flexible polyethylene terephthalate (PET) [29]. (b) Schematics of multiplexed fingerprint sensor with multifunctional detection of finger pressure and skin temperature using AgNF–AgNW hybrid [30]. (c) Image flexible temperature sensor based on reduced graphene oxide and its possible application for robot skin [31]. (d) 3D schematics (top) and photograph (bottom) of a flexible hydrophilic polytetrafluoroethylene (H-PTEF) humidity sensor. To enhance mechanical stability of sensors, polyethylene terephthalate film (70 μm) is laminated beneath the thin H-PTEF film [32].

1.1.1 Stretchable devices

Introduction. Many strategies are used to make the electronic devices stretchable, including the direct use of intrinsically stretchable materials or constructing structure design strategies. **Application.** Soft stretchable strain sensors are in demand to measure movement on stretchable and curved surfaces, such as human motion detection, and blood pressure monitoring. Only a few stretchable strain sensors have been explored which can be placed in contact with human skin and of measuring high signal quality.

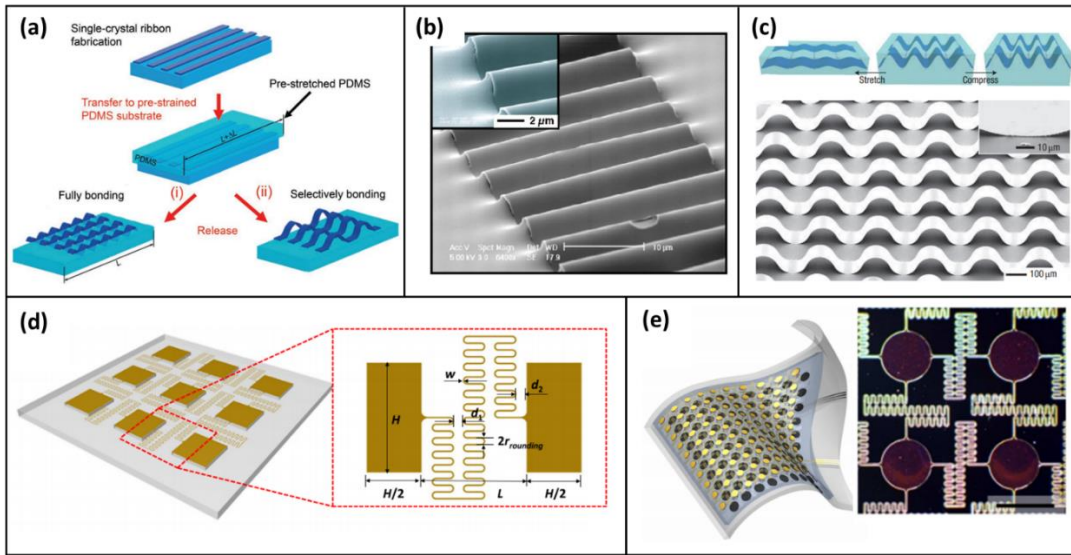


Figure 1.5: Structural stretchability examples: (a) Schematic illustration of wavy structures with two different bonding strategies on the elastomeric PDMS substrate, that are fully and selectively bonded onto the substrate [33]. (b) Atomic force micrographs of the 1D and 2D wavy ribbons fully bonded onto PDMS substrate [34]. (c) Response of 3D buckled nanoribbons to stretching and compressing (top). SEM image of a sample formed (below) [35]. (d) Design optimization of the 2nd order serpentine interconnects in an island-bridge structure [36]. (e) structure of stretchable battery, stretchable current collectors with an island-bridge structure [37].

Physical parameter. The required strain sensitivity does not need to be high to detect large strains. Though, such strain sensors must possess high stretchability along with a good stability [38]. It is extremely difficult to develop intrinsically elastic active materials. However, a possible way to obtain stretchable sensor is to use a stretchable structural design, which can sustain large elastic deformations [39]. Following are some examples:

- **Wavy structural configuration**, Figure 1.5(a-c). Unidirectional stretched configuration. The key of this strategy is to introduce an initial strain difference in the soft substrate (e.g., PDMS or ecoflex) and hard thin films (e.g., metal or semiconductor), either by thermally induced mismatch [40] or mechanical pre-strain [41][42].

- **Island-interconnect configuration**, Figure 1.5(d-e). It avoids the limitation of unidirectionality. The fabrication process of such a structure involves the transfer printing of 'island-like' semiconductor devices (e.g., silicon), connected with each other by planar 'bridge-like' metal interconnects, onto a biaxial pre-strained elastomeric substrate (e.g., PDMS), and the release of pre-strain which causes the bridges to lift vertically off the substrate and forms the arc-shaped structures. However, assembly process is complicated and the stability obtained is unsatisfactory.

- **Coiled fiber structure**. Unidirectional stretched configuration. Due to the simple structure, first coil fibers have reported less than 400% stretchability. Helical coil fibers are reported to be stretchable up to 800% [43][44].

Material. The fabrication of stretchable devices is the more challenging. Stretchable elastomers are often used as soft substrates in many electronic devices, such as predominant poly(dimethylsiloxane) natural rubber, styrene butadiene rubber, ethylene-propylene-diene monomer, polyurethane, thermoplastic polyurethane, etc., which can reversibly tolerate high deformations [45] [46]. However, this often results in high electrical resistivity of electronic devices but low electrical mobility. To overcome that various structure design strategies enable, as already mentioned, the use of common conductive bulk metals in stretchable electronic devices. It includes wavy structures, island-interconnect configuration, mesh structure, fractal design approach, origami and kirigami structural configurations, Figure 1.6.

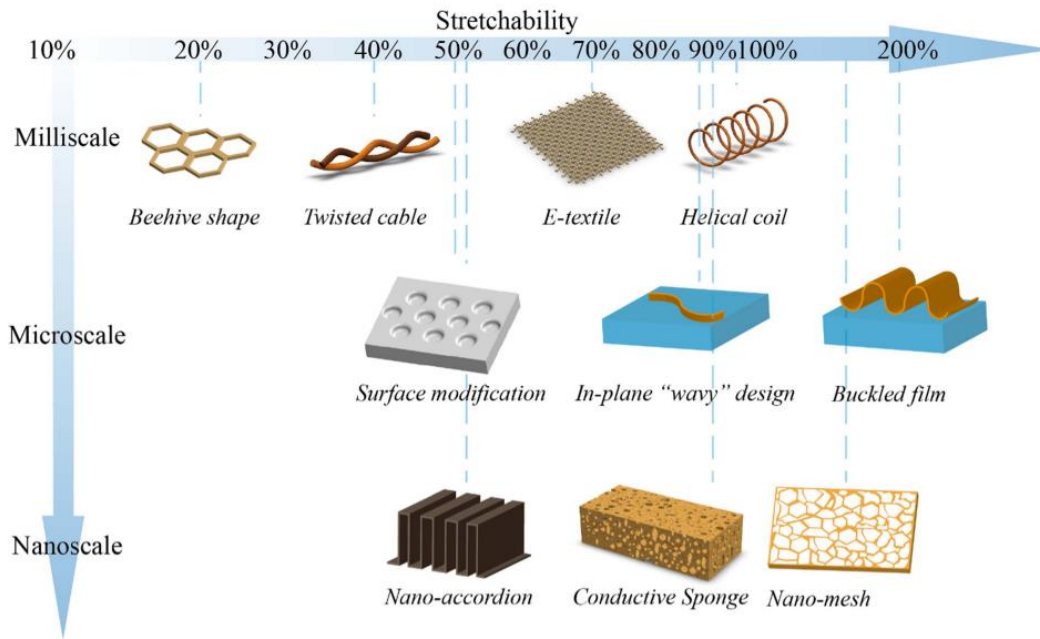


Figure 1.6: Various stretchable structure configuration on scale of increasing stretchability with respect to the scale of structure size [47][48].

1.1.2 Flexible devices

Introduction. Flexible electronics in comparison with conventional electronics use material component with wide range of response to bending or twisting. It is important in flexible electronics to work with sensor that has high sensitivity. **Application.** The flexible strain sensors have attracted significant attention for applications like wearable electronics, smart textiles as well as other applications concerning structural health monitoring of critical infrastructures highways, buildings, bridges, ships, aircraft, pipelines, particularly during hurricanes, earthquakes, and other natural disasters [38].

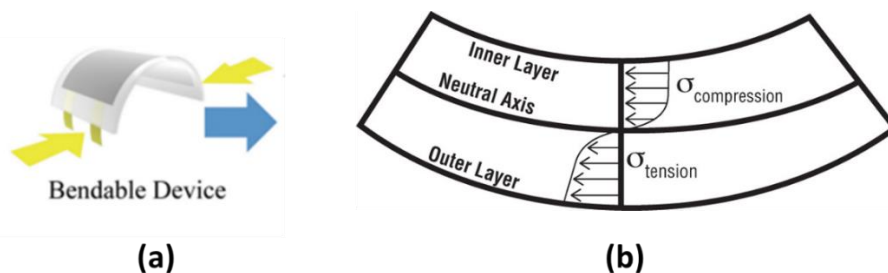


Figure 1.7: (a) Diagram of a bent strain device (b) Compression and tension zone created during the bending.

Physical parameter. Through an external bending moment, strain is generated in the film. The inner surface is in compression and the outer surface is in tension, Figure 1.7. The neutral plane is a surface within film, where the material is not under stress, either compressive or tensile. Flexible electronics relies on the basic idea that a substrate of thickness $2h$ can be bent with the radius of curvature (ρ) as long the strain, $\varepsilon = \frac{h}{\rho}$, developed does not exceed the yield strain (ε_c) of the film. Substrates of such devices should be comparatively inexpensive, mechanically robust and resist to creep, free from structural defects like pits and pinholes and electrically passive.

Material. Typical substrates for flexible electronics include polymers, thin foils of metal, fabrics, and even paper. Polymer substrates such as Kapton polyimide, Polyethylene terephthalate, Polytetrafluoroethylene and Polyethylene naphtholate used in various applications [27].

1.1.3 Conclusion

The following rapid prototyping addresses the crucial aspects toward the advancement of stretchable devices and flexible devices; summarized in Figure 1.8(b).

Deformation. In materials science, mechanical deformation due to external forces, categorized into (1) elastic or (2) plastic deformation, Figure 1.8(a). (1) Elastic deformation is recoverable change in shape of material after the stress is removed. (2) When the stress permanently deforms the material, it is plastic deformation. Therefore, only completely reversible mechanical and electrochemical behavior is acceptable, because any minor irreversible mechanical or electrochemical performance will eventually degrade the device. Consequently, stretching-deformation is more challenging than bending-deformation. Mainly due to the limited elastic – strain extensibility of the conventional electrode materials, these materials cannot accommodate large strain. Stretching leads to damage in flexible electrodes due to two processes: (1) the inorganic active material has an extremely low elastic strain, a slight stretching can break the electrode; (2) due to repeated deformation, and the active materials may lose electronic contact.

Thickness. To achieve remarkable bendability/flexibility, the thickness of the substrate can be sufficiently reduced. However, this approach is restricted only to near

flat substrates. In contrast, stretchable electronics are proficient in adhering to uneven surfaces, similar to human skin. To achieve more flexible, there are two other methods: (1) they must become ultrathin and ultra-light. An ultrathin structure can also expand flexibility range; (2) or they must be molded into different shapes to imitate various curved surfaces. Among these features, reversible elastic flexibility remains the main constraint.

Fabrication. Until now two main classes of materials often used for electrodes in electronic devices; one is well-known inorganic metals (Al, Au, Mo, Ti, and Ag) and metal oxide (ITO), and the other is organic conductive polymers (such as PEDOT: PSS). The realization of flexible, stretchable devices using conventional metal or semiconducting materials is challenging because they sustain very small strain value. However, from the perspective of fabrication the construction of a flexible device is easier than stretchable devices [49]. For the designed shape of the device to remain intact under bending or stretching conditions the substrate needs to be sufficiently elastic and the device must keep their performance during deformations [50].

One of the main objectives of this project is not in achieving highly stretchable devices with very large deformation. However, to integrate and test the nanomaterial with helical morphology over an adequately bendable substrate like PET, the focus lies on building a sensor with maximum sensitivity. Another objective of this project is to build a sensor with low or no hysteresis and long-term stability in their response, with cost efficient fabrication process and minimal material wastage. For flexible sensor, thickness is not a major constrain and therefore, the fabrication process becomes comparatively simpler.

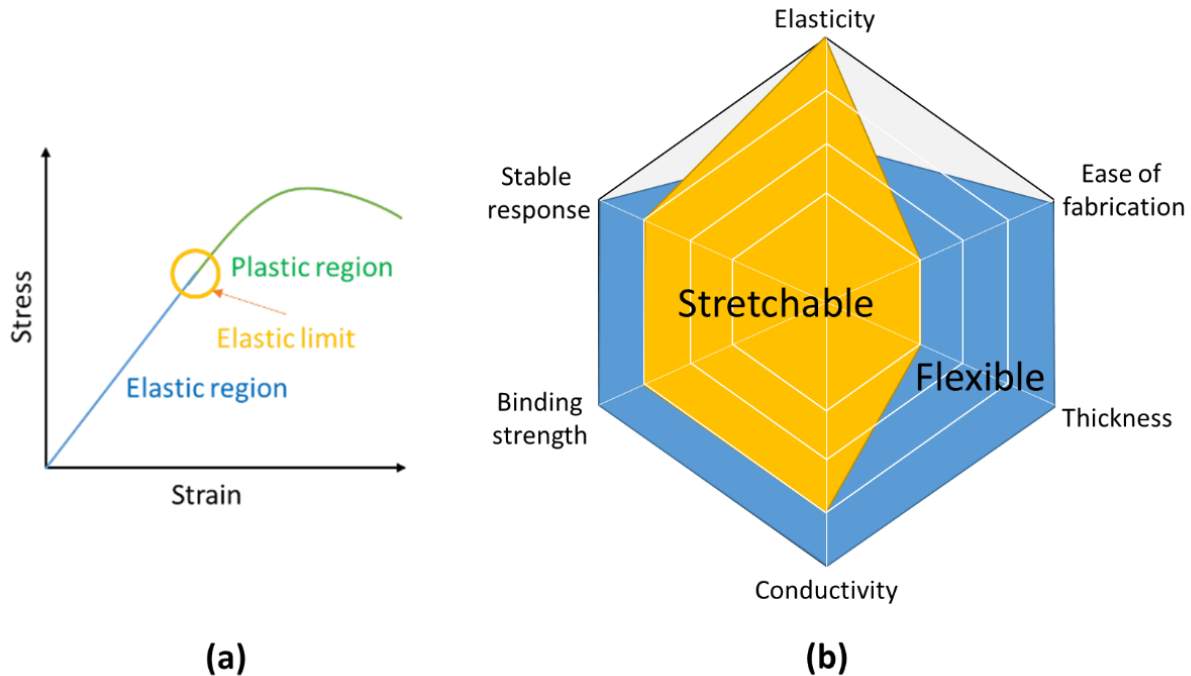


Figure 1.8: (a) Stress vs strain graph (b) Web chart summarizing various properties of stretchable and flexible strain sensor. In the four level of each property, higher/more marking corresponds to higher point. Example: The ease of fabrication scores 1point for stretchable strain sensor representing very low flexibility in fabrication.

1.2 Flexible Strain Sensor

1.2.1 Transduction mechanism

The current trend toward smart textiles and structural composites demonstrates that the embedded sensor platforms will be playing a key role in shaping the future of smart technologies. Strain sensors have been used for applications in machine learning (e.g., in soft robotics), as well as real-time structural health monitoring (SHM). The transduction mechanism of such sensors relies on the piezoelectric effect, a change in capacitance, or a change in resistance (piezoresistive effect). Based on working mechanisms it is categorized into: piezoresistive, capacitive and piezoelectric sensor, as seen in Figure 1.9.

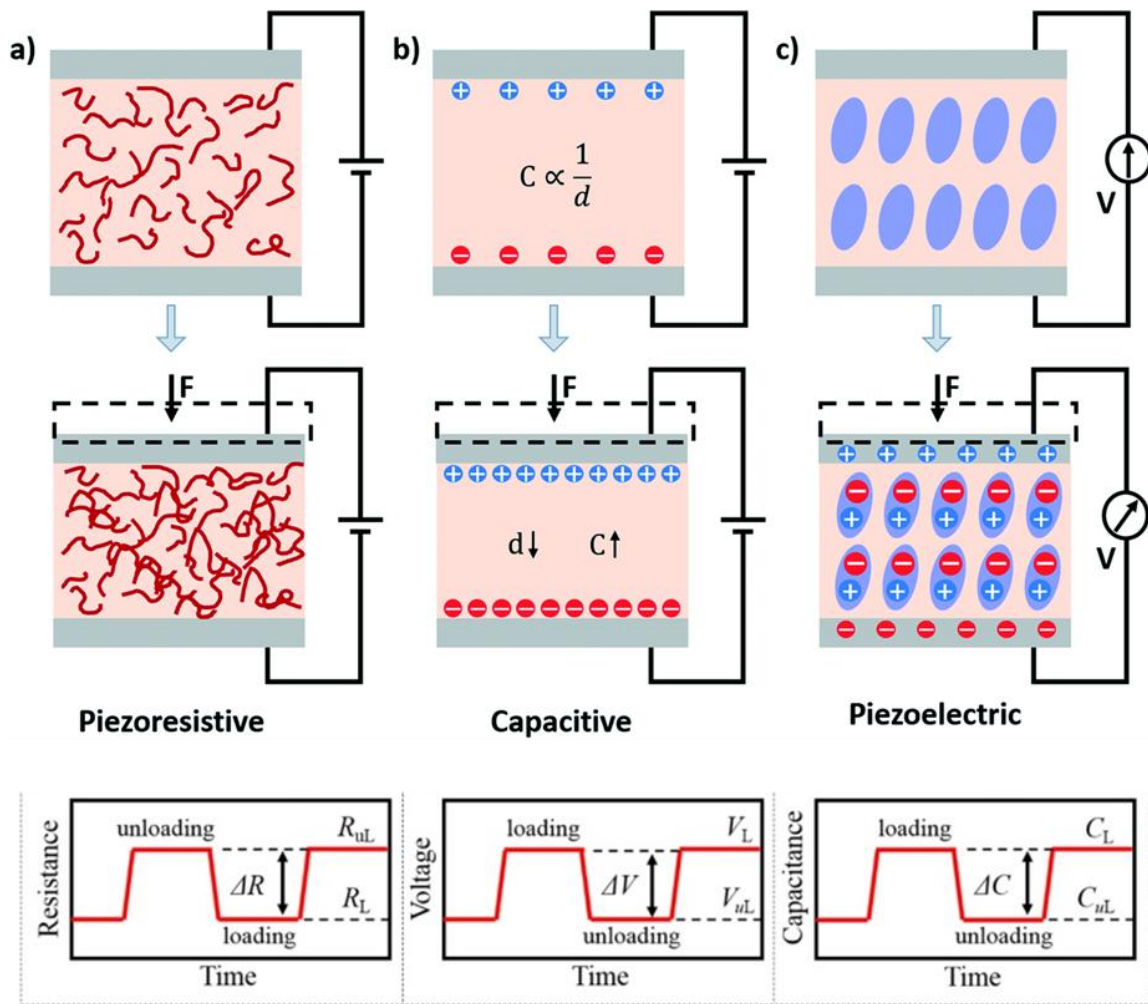


Figure 1.9: Schematics illustrating the different modalities of electromechanical sensors. (a) Piezoresistivity, (b) capacitance, (c) piezoelectricity. [51]

1.2.1.1 Capacitive pressure sensors

As for capacitive sensing, it relies on the charge storage and the capacitance change upon deformation. It measures changes in electrical capacitance by detecting changes in electrical capacitance caused by the movement of a deformable surface. A capacitor typically consists of two parallel conducting plates separated by a small gap. The capacitance is inversely related to the distance between plates. Changing the gap will cause a corresponding change in the capacitance. A mechanical deformation brings the electrodes closer and induces changes in the capacitance of the dielectric medium. Apart from the traditional parallel plate configuration, an interdigital configuration is widely used in capacitive sensors, Figure 1.10.

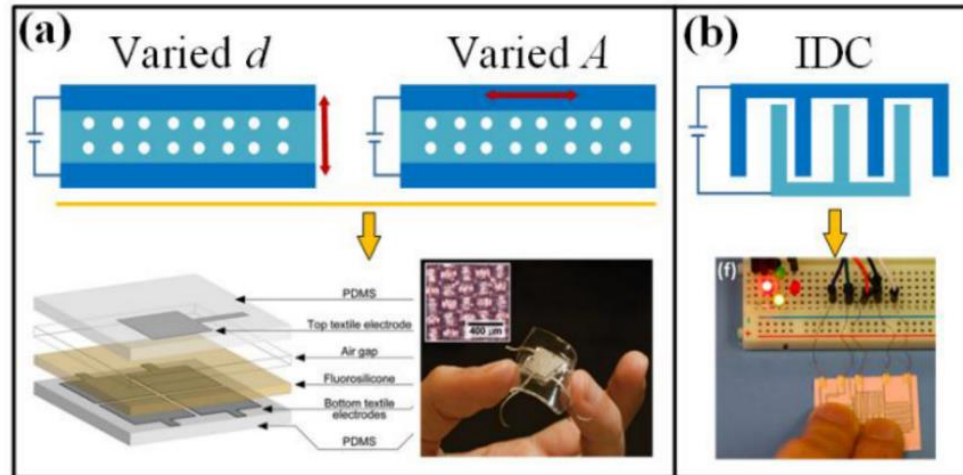


Figure 1.10: Capacitive sensing with (a) parallel plate configuration (b) interdigitated configuration [52]

Advantage. The capacitance-based sensors are advantageous in various aspects such as high strain sensitivity, temperature independence, low power consumption, and low signal to noise ratio. Sensitivities of these types of sensors can be improved by addressing the compressibility of the materials by using low modulus materials. Likewise, altering the surface of the electrode or dielectric layer with patterns and microstructures like dome-shaped, pyramidal, or interconnected hollow-spheres shows improved sensitivity [48]. **Disadvantage.** Cross talk between the taxels and complex circuitry is the disadvantageous characteristics of capacitance-based sensors.

1.2.1.2 Piezoelectric sensors

It uses materials, such as quartz crystals or specially formulated ceramics, which generate a charge across the faces when a pressure is applied. Dipole moments are observed from the deformation of the oriented crystalline structures. A charge amplifier converts this created charge to an output voltage proportional to the pressure. A given force results in a corresponding charge across the sensing element. Inorganic piezoelectric materials, such as ZnO, GaN and PZT, have been widely investigated to construct flexible strain/pressure sensors by coating or embedding them to flexible polymers. Piezoelectric nanomaterials, especially nanowires, feature excellent piezoelectricity and have been used in nanosensors, piezotronic devices and nanogenerators [53][54][55].

Advantage. This type of sensors shows rapid response, high sensitivity, low power consumption, and self-powering/energy harvesting characteristics. Conventional piezoelectric materials such as inorganic ceramics, single crystals, and lead zirconate titanate (PZT) possess high sensitivity

Disadvantage. Conventional piezoelectric materials are too brittle for the flexible/stretchable tactile sensors. The utilization of inorganic materials has inherent disadvantages, such as high processing cost and potential high toxicity (presence of lead in certain piezoelectric materials). Thus, the utilization of piezoelectric polymer materials in flexible sensors has attracted increasing interests. The drift of sensor output over time and its susceptibility to temperature are the major disadvantages in this type of sensors. However, this charge can leak away over time meaning that the sensor cannot be used to measure static pressure but can be of interest in dynamic mode.

1.2.1.3 Piezoresistive strain sensor

It relies on the piezoresistive effect, which occurs when the electrical resistance of a material changes in response to an applied mechanical strain. The change in resistance is directly proportional to the change in geometry and in resistivity of the sensing material with the applied strain. A significant variation of the resistivity can be induced because of the strain dependence on mobility and density of the charge carriers. Except for a metallic piezoresistance, the change in geometry is usually negligible.

Piezoresistivity is caused by a mechanical stress that modifies the band-gap, which in turn alters the mobility of the charge carriers. It is implemented either by (1) modifying the contract state of the conductive materials or (2) through tunneling effect. The former is observed in silicon, carbon nanotubes, and graphene-based piezoresistive sensors. While the latter is observed in conductive composite materials based on conductive nanoparticles, nanowires, nanotubes, and flakes as current tunneling through nanogap [48]. The crack-based sensors have super high sensitivity in tiny deformations. They trigger a great resistance variation to the film. Comparatively, the cracks cannot sustain large strains, and the measuring performance and device robustness will dramatically decline if the applied strain is out of a reasonable range.

Advantage. It is the common transduction principle, due to its high sensitivity, uncomplicated structure, and low cost. It has a wide range of detection, low energy consumption, and manageable readout mechanism. **Disadvantage.** The disadvantages associated with these types of sensors are their dependence on temperature, stability issues, and hysteresis effect.

Table 1: In the table ‘0’ being neutral and ‘++’ being maximum value or most positive for the corresponding category

	Resistive	Piezoelectric	Capacitive
Range	++	+	0
Sensitivity	0	+	++
Repeatability	+	0	++
Temperature stability	+	0	++
Design flexibility	+	0	++
Electrode degradation	0	+	+
DC response	+	0	+
Cost	0	++	++
Circuit complexity	0	0	++
Temperature range	<600°	<1000°	<400°
Advantage	<ul style="list-style-type: none"> ▪ Comparatively smaller structure ▪ Simple transducer circuit ▪ Simple construction ▪ High resolution ▪ No need for integration 	<ul style="list-style-type: none"> ▪ High frequency response ▪ High accuracy ▪ High sensitivity ▪ High dynamic range 	<ul style="list-style-type: none"> ▪ High sensitivity ▪ High spatial resolution ▪ Large dynamic range ▪ Temperature independent ▪ More robust
Disadvantage	<ul style="list-style-type: none"> ▪ Strong temperature dependence ▪ Hysteresis ▪ High power consumption ▪ Lack of reproducibility 	<ul style="list-style-type: none"> ▪ Poor spatial resolution ▪ Charge leakages ▪ Dynamic sensing only 	<ul style="list-style-type: none"> ▪ Electronically more complicated ▪ Needs integrated electronics ▪ Stray capacitance ▪ Hysteresis ▪ Susceptible to noise ▪ Cross-talk between elements

1.2.2 Responsive Mechanism

Depending on the type of material and fabrication process, each strain gauge sensor responds to the applied strain with different mechanism. Traditionally the response to the strain gauge originates from the geometrical effects and piezoresistivity of material

themselves [56][57]. Unlike common strain gauges, mechanisms such as disconnection between sensing elements, crack propagation in thin films, and tunneling effect have been utilized to develop flexible strain sensors.

1.2.2.1 Crack Propagation

Under very large strain, microcracks were generated in CNT, silver nanoparticle, gold nanowire, and graphene thin films coated on flexible substrates [58][59][60]. The size of microcracks and the density is increased by applied strain and upon the release of thin films, it would recover their initial states. Due to the separation of several microcrack edges, it creates limitation the electrical conduction passing through thin films. Moreover, the resistance of thin films is drastically increased by the applied strain. Upon release of the applied strain microcrack edges is reconnected, ensuring complete recovery of the electrical resistance.

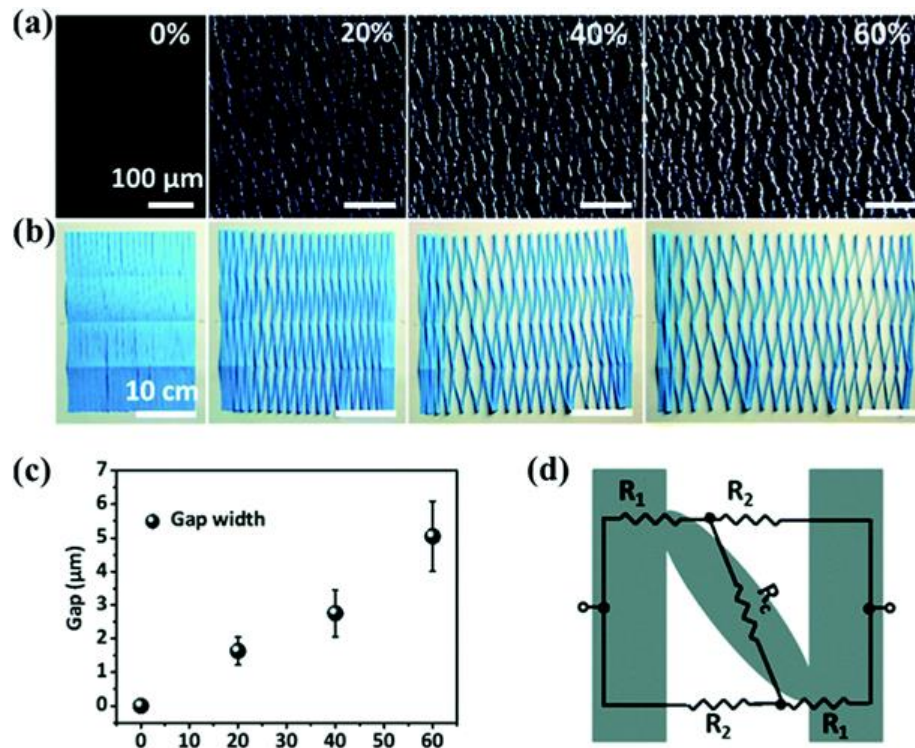


Figure 1.11: (a) Series of optical images of the CNT films/PDMS composites stretched from 0% to 60%. (b) Simulation using Chinese paper cuttings show the change of crack morphology from unstrained to strained states. (c) Average gap width versus strain loading (d) the resistance model of a sensing unit [61].

1.2.2.2 *Disconnection Mechanism*

In thin films made of nanomaterial conductive assembly within a percolation network, electrons can pass through overlapped nanomaterials. Bending/Stretching of thin films causes some connected nanomaterials to lose their overlapped area and electrical connection and, consequently, increases the electrical resistance [62][63][64]. Based on the disconnection mechanism, strain sensors have been reported of thin films formed of nanowire and graphene flakes coated on flexible support materials. When composite films are stretched, graphene flakes slid in the direction of the elongation which decreases the overlapped area between connected flakes and increases the contact resistance in the flake-flake junctions [57].

1.2.2.3 *Geometrical Effect*

Resistance of a conductor increases upon elongation in length and shrinkage in cross-sectional area. Dimensional change is the piezoresistive mechanism of commercially available metal-based resistive-type. In these conventional sensors, it is known that the resistance of the metallic film varies with induced strain by the generated geometry change. However, because of limited stretchability of metal thin film-based devices they are not suited for certain applications like in wearable and body motion monitoring applications. Moreover, their sensitivity is limited to gauge factor between 2 and 5.

1.2.2.4 *Piezoresistive Effect*

Change in the resistance of materials caused by the structural deformations is known as piezoresistivity. Piezoresistivity of some metals and metal alloys may increase the resistance of strain gauges by small order. Whereas, semiconductor materials such as silicon and germanium can improve the resistance change of sensors to several orders of magnitudes, induced by the change of the bandgap on inter-atomic spacing [65][66][67]. Therefore, semiconductors or nanoscale materials can be used to achieve a highly sensitive strain sensor. Nanomaterials such as individual CNT and nanowire (ZnONW) owing to their chirality and change in barrier height, respectively, showed ultrahigh piezoresistivity. Moreover, inhomogeneous electromechanical properties, and poor stretchability have prevented the extensive use of single nanowire, nanotube as

strain sensors. To overcome these shortcomings, several new approaches have been proposed i.e. by forming composites of functional nanomaterials and polymers [16][68][69].

1.2.2.5 Tunneling Effect

Crossing of electrons through a classically forbidden potential energy barrier is called tunneling. Electrons can tunnel through closely spaced adjacent nanomaterials. Under a certain cut-off distance between neighboring nanomaterials, electrons can path through thin layers and form quantum tunneling junctions. The cut-off tunneling distance depends on numerous factors such as type of conductive materials, insulating media, and processing parameters [70]. For example, cut-off distances of the AgNW–PDMS–AgNW and CNT–polymer–CNT channels were reported to be about 0.58 and 1–1.8 nm, respectively [71][72][73]. The tunneling cut-off distance was determined to be 2-3nm for two parallel graphene sheets insulated with polymers. Owing to highly crumpled nature of graphene sheets, this value is larger than the cut-off distances for AgNWs or CNTs. When an external strain is applied, it is more probable that entangled elastic nanomaterials will unfold rather than sliding in their axial directions, changing the tunneling resistance. This mechanism is unlike the disconnection mechanism where several connected junctions are separated due to the sliding of nanomaterials inside the polymer matrices [74].

1.2.3 Sensing Materials

Conventional strain sensors are generally made using piezoresistive materials, most commonly metals [75]. Rigid bulk materials like solid metals, semiconductors and polymers, can be used as films designed into special bendable structures or ultrathin films with thickness ranging from tens of nanometers to tens of micrometers [76]. Advances in materials science and micro-nanotechnology have transformed commercial brittle strain to soft sensors and robust strain sensors. Various flexible materials with excellent electrically conductive property such as liquid metals, metal nanowires/nanostructures [16][77][78][79], carbon black [80][81], CNT, graphene [56][82][83], ionic liquids [84] and hydrogels [85][86] have been used. An emerging approach for robust real-world applications of flexible sensors relies on nanoparticles (NPs) with diameters that range from 10 to 100 nm. Among the many reasons to exploiting NPs for flexible sensors is the

ability to control the NPs type, ability to vary the NPs' size, ability to cap the NPs, Figure 1.12. Their electromagnetic properties can be tuned readily by adjusting the NP size, shape, and separation.

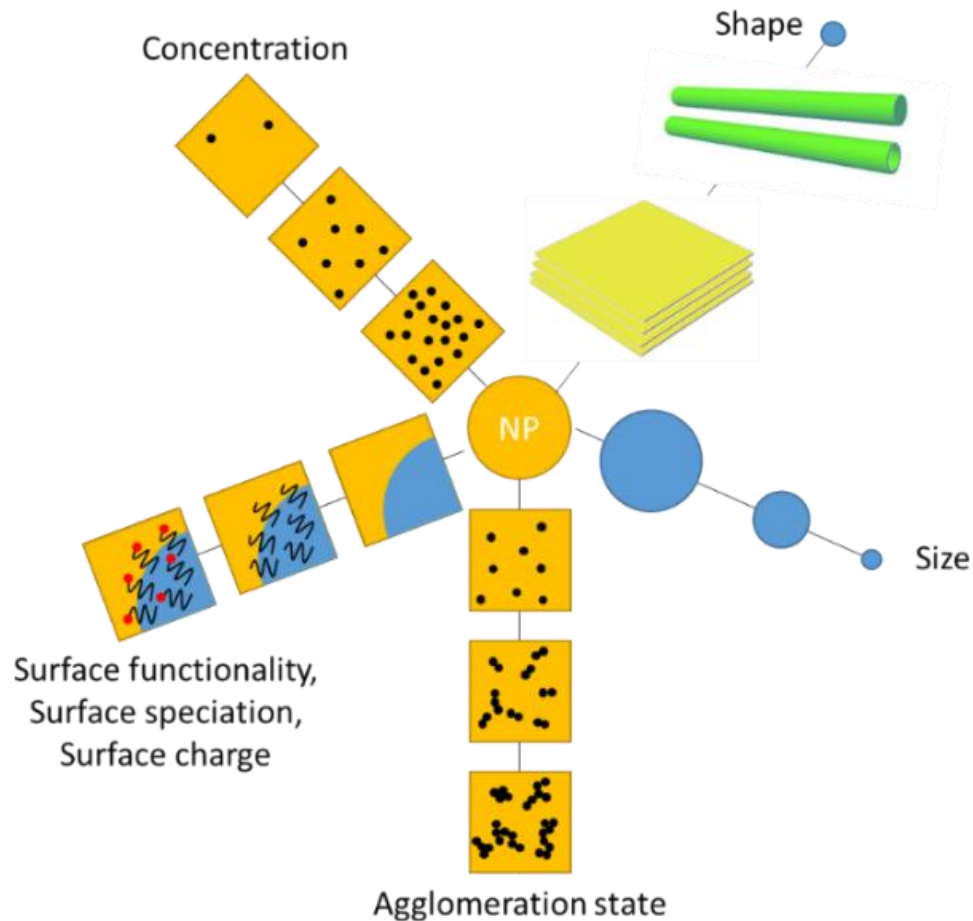


Figure 1.12 : Characteristics of the nanoparticles

1.2.3.1 Nanomaterial

Nanostructures range between 1 and 100 nm and can be organic, inorganic, composite, and carbon-based. Nanostructures have different shapes, sizes, structures and origins. They can be spherical, conical, spiral, cylindrical, tubular, flat, hollow, or irregular in shape. Classified depending on their dimensions into one of four categories, Figure 1.13 :

- **0D:** with a single characteristic nanoscale size, such as nanoparticles. Where length, height, and breadth parameters are fixed at a single point, for instance at a dot.

- **1D**: with a nanometric diameter and a high aspect ratio (nanotubes, nanowires). Where only one the parameter exists.
- **2D**: with only nanometric thickness (thin films, graphene), where parameters of length and breadth exist, for instance nanosheets.
- **3D**: this category includes all nanostructures that do not meet the previous classification because they have more complex geometries. In these structures all three parameters exist.

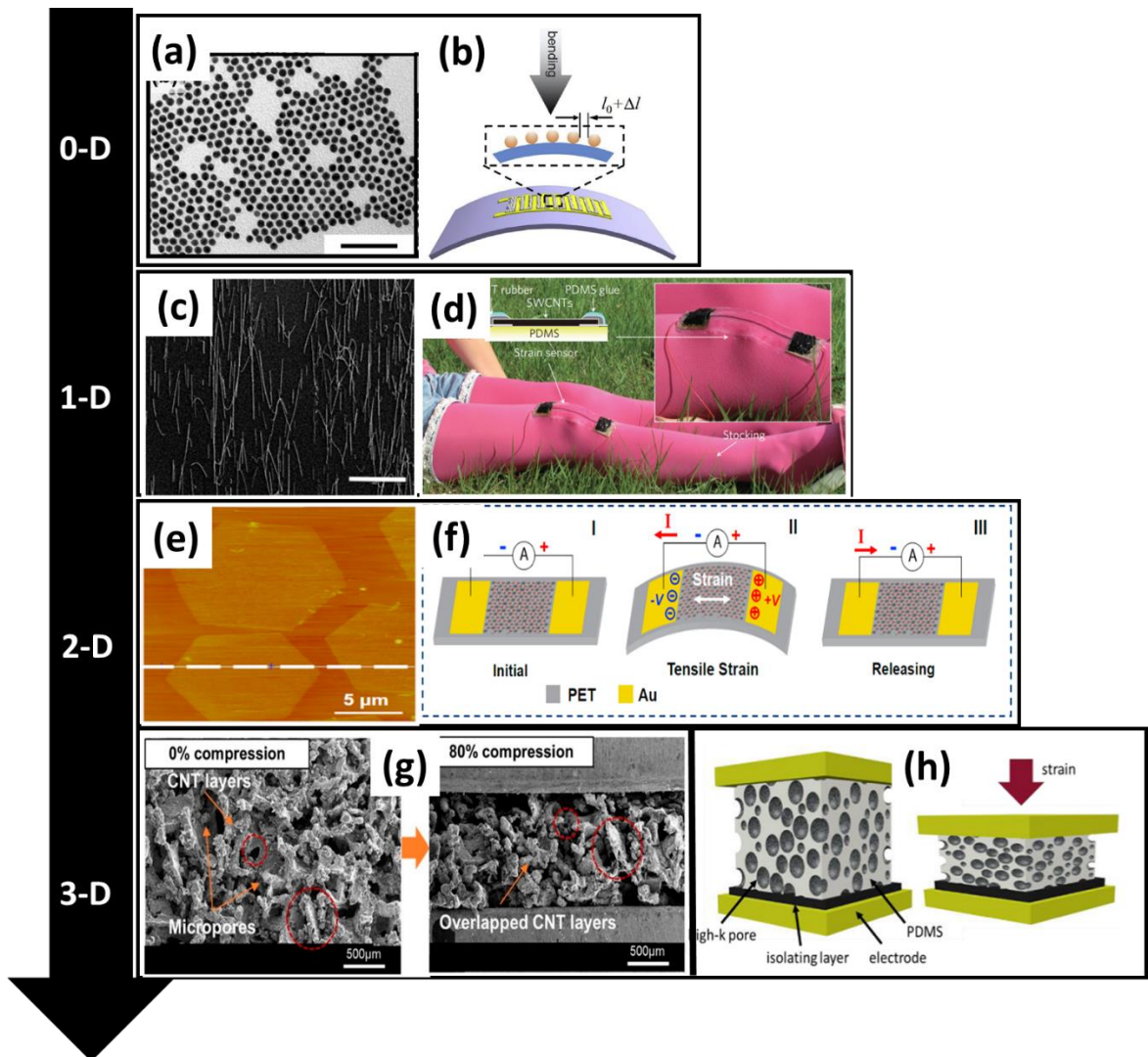


Figure 1.13 : Illustration of size distribution of nanoparticle – 0D, 1D, 2D, 3D. (a) TEM images of gold nanoparticle samples [87]. (b) Diagram of strain sensing measurement where inter-particle distance increased as the sensor is bending [88]. (c) SEM image of higher density aligned 1D AgNWs [89]. (d) Stretchable electric nanomaterial consisting

of aligned single-walled carbon nanotube (SWCNT) thin films for the application of human motion detection[62]. (e) *AFM image shows two-dimensional structure of lead iodide nanosheet.* (f) *Diagram showing the electricity generation process of a 2D piezoelectric device* [90]. (g) *Cross-sectional SEM images of flexible resistive pressure sensor based on a CNT network-coated thin porous PDMS sponge at compressions of 0% and 80%, showing the formation of overlapped CNT layers upon compression* [91]. (h) *Schematic showing application mechanical pressure to 3D porous device* [92].

The chemistry of metal NPs, particularly gold NPs, has been exploited for use in highly selective sensors [93][94][95][96]. The ability of preparing films of NPs with controllable porous properties has been explored extensively [97]. The presumed ability of NPs to allow easier, faster, more cost-effective fabrication of flexible sensors compared to those currently in use, which mostly rely on complicated, multistep processes makes their use very attractive [98]. The distance between the encapsulated NPs is controlled by choosing the encapsulating molecules or the assembly/deposition procedure. This allows a very good control over the interparticle distance. As example, two commonly used thiols capping agents are thioglycolic acid (TGA) and 3-mercaptopropionic acid (MPA). These two agents impart a negative surface charge and create nanoparticles with an extremely high colloidal stability [99][100]. NSs can either be deposited on flexible substrates at low temperatures as sensing cap-layers or they can be integrated into the composite of a flexible material. For sensing applications, one can obtain NPs with a hybrid combination of chemical and physical functions, which would have a great effect on the sensitivity and selectivity of the sensors [48].

1.2.3.2 One-dimension Nanomaterial

One-dimensional nanostructures have a particular aspect factor, as their diameter is very small compared to their length. 1D materials have the potential to be the building blocks for nano electronic devices. 1D nanostructures possess superior properties because of their facile and large-scale synthesis, and electronic tunability by molecular design. Several other advantages, such as good uniformity and dispersion, predefined electrical conductivity and high impact resistance. 1D-NS such as nanowires, nanofibers, nanorods, nanobelts and nanotubes, have attracted much attention in recent years.

Different categories of 1D nanostructures, includes polymeric, small molecule and inorganic species, have a prominent role due to their importance in terms of both fundamental studies in mesoscopic physics and technological applications in nanoscale device generation, summarized in Table 2.

Table 2 : One dimensional nanostructure characteristic

1D-NS	Categories	Properties
Nanowires Nanofibers Nanorods Nanobelts Nanotubes CNT	Polymeric	Flexible, facile and large-scale synthesis, electronic tunability by molecular design
	Small molecule	Easy to mold, drive, align uniformly
	Inorganic	Easy synthetic access, good uniformity and dispersion, predefined electrical conductivity, high impact resistance

Helical nanostructures. The objective of this study is to utilize one dimensional, helical nanostructure for building flexible strain sensor. The significance to use helical structure from a purely geometric point of view is that the helical geometry enables many possible applications through utilizing its unique nanoscale properties. For example, nanohelices resembling the shape of macroscopic springs will have improved mechanical properties under strain. Therefore, nanohelices with adjusted geometric parameters will fulfil the designs required from different device configurations depending on the target applications. The helical nanostructures with precise control over the geometric feature and artificially added multiple functionalities will find promising applications for next generation sensing and actuating units, optical and magnetic devices, energy conversion, robotics, biomedical diagnostics and therapy.

1.3 Nanomaterial assembly for nanoparticles and nanowires

Alignment of nanomaterial building blocks into ordered layer by bottom-up approaches, it is one of the key steps towards the fabrication of strain sensor [101][102][103]. The use of external means and electrical fields to control the particle arrangement has long been a powerful way for tailoring the mechanical and electronic

properties of materials in applications ranging from electro-mechanical systems over nanocomposites to electronic inks, Figure 1.14.

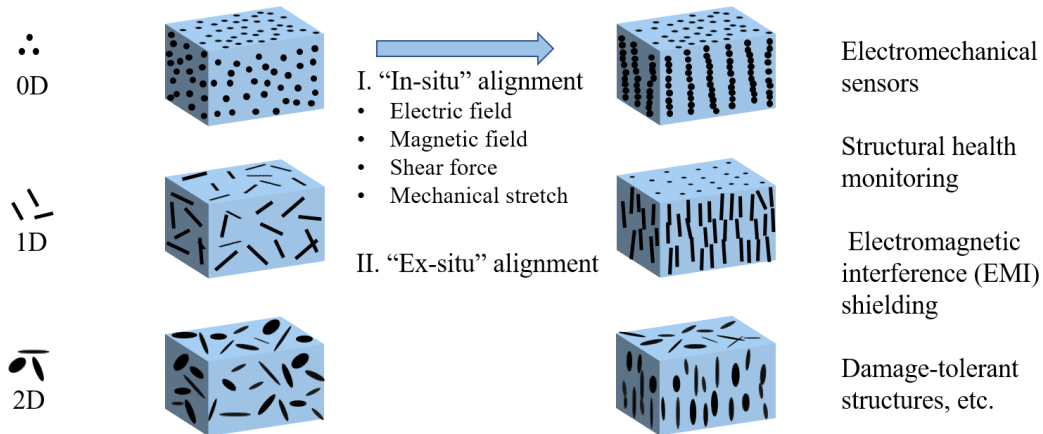


Figure 1.14 : Nanomaterial alignment on different dimensions [104].

More recently, external fields have emerged as key methods to direct the assembly of nanomaterials. Electric or magnetic fields are obvious candidates for field-directed assembly, proved to hold promise for scale-up. Various applications through aligned deposition on a flexible substrate have been achieved by techniques such as drop casting, inkjet printing, layer by layer, stamping method, self-assembly and electrodeposition [105][106][107]. The different approaches used to align nanomaterials based on different physical phenomena are briefly mentioned in the following section. They will be described in details in Chapter 2:

1.3.1 Chemically Driven

Chemical assembly is a powerful self-assembly method to create highly organized patterns or assemblies of specific objects. This technique exploits the covalent and non-covalent interactions of ligands covering the objects. Different techniques such as layer-by-layer electrostatic assembly, chemical structuring, and self-assembled molecular layers are the most commonly used modes [102][108]. Usually, an appropriate functionalization of objects and surfaces is prepared. These chemical functionalities surface leads to the assembly and organization of objects. More advanced techniques such as Dip-pen nanolithography and micro contact printing use chemical conjugation forces indirectly to attach objects to substrates [109].

1.3.2 Flow fields

Incorporating self-assembly with a flow include Langmuir-Blodgett, dip coating, flow coating and spin coating [110][111]. These methods are based on the use of fluidic forces on a solution containing a suspension of nanomaterial of interest. Though Langmuir-Blodgett's method is a complex method, it allows large-scale organization. In laminar flow conditions, 1D nanostructures are thus aligned in the direction of movement of the fluid to minimize viscous dissipation caused by shear stress. Other techniques working on similar principle as well includes: blowing, microfluidic channels, or capillary forces [112][113].

1.3.3 Shear force

The technique known as 'contact printing' principle is very simple and consists in directly exploiting the nanomaterial resulting from growth on a raw substrate, generally in the form of a forest of nanowires [114]. The growth substrate supporting a forest of nanowires is rubbed in a precise direction on a receiving substrate. The growth substrate can thus be planar (contact printing) or cylindrical (roll printing) while the receiving substrate can be structured beforehand by photolithography. The two substrates are placed side by side. Friction is obtained by applying pressure between the two substrates while moving them very slowly relative to each other. Thus, the aligned nanowires are in the direction of friction and directly transferred to the host substrate by Van der Waals interactions between the surface and the nanowires. The pressure maintained between the two substrates must be well controlled. This is the main limitation of this alignment technique. The yield obtained by this technique is improved by functionalizing the surface of the receiving substrate. Since the transfer takes place at room temperature, this shear force transfer process is compatible for various types of receiving substrates, from solid silicon to glass and flexible substrates.

1.3.4 Electric and Magnetic field

Electric and magnetic fields allow induced interactions to align. The fields take advantage of the charge or the polarizability of the nanomaterial and its functional groups. When these field-induced interactions overcome random Brownian motion, particles join to form chains and then assemble. Electric and magnetic field direction requires a constant balance between thermal energy and interaction energies. This involves using

electromagnetic forces to control the movement of the suspended particles in a fluid. Magnetic forces can be used in the case of nanomaterial having ferromagnetic properties.

The assembly is based on the mobility and interactions of nanomaterial caused by alternating electric fields (Dielectrophoresis). Indeed, the application of an alternating electric field allows the manipulation and assembly without the electro-osmotic or electro-chemical effects found in DC field systems.

Dielectrophoresis. It is based on the fact that when a polarizable particle is subjected to an electric field. Electric charges are induced and it create a dipole, which lines up with the electric field lines. The electric field directed assembly can therefore be used to position individual particle at a specific position while at the same time controlling their orientation. One of its advantages is that method can be self-limiting: the capture of nanostructures cancels the electric field, which eventually stops the phenomenon. Unlike electrophoresis, dielectrophoresis does not depend on the charge ration the size of the particles but their dielectric properties compared to that of the liquid in which they immersed. Dielectrophoresis has great potential for assembling, manipulating, trapping, sorting and characterize nanostructures suspended in a liquid.

1.4 Characterization platform

1.4.1 Performance parameters

The performance of strain sensors can be characterized by factors like sensitivity (or gauge factor), linearity, hysteresis, durability, response and recovery time, long term stability, electrical conductivity, fabrication cost, etc. Other specific ones like self-power, wireless communication, biocompatibility and biodegradability can be considered depending on the targeted applications. Sensor-to-sensor uniformity and hysteresis are of critical importance for any sensing application.

1.4.2 Sensitivity

The sensitivity or gauge factor is one of the main performance parameters and often used to measure the data for strain sensors under variable strains, which is the standard for quantifying the sensitivity. The sensitivity of a sensor is defined in terms of

the relationship between the input physical signal and the output electrical signal. It is the ratio between small change in electrical signal to the small change in physical signal.

Gauge Factor. When pressure or force is applied to a strain sensor, the relative change of the electrical resistance $\Delta R/R_0$ is a function of the applied strain ϵ . Strain (ϵ) is defined as the ratio of length deformation (ΔL) to the original length (L_0). The gauge factor corresponds to the sensitivity of a strain sensor and can be expressed as:

$$\text{Gauge Factor} = \frac{\Delta R}{\epsilon R_0} \quad (1)$$

For a linear variation, the gauge factor is therefore the slope of plot $\Delta R/R$ as a function of $\Delta L/L_0$

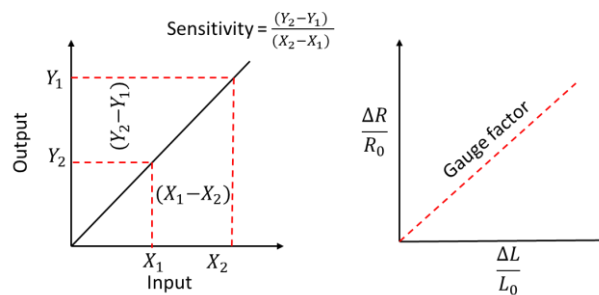


Figure 1.15: Gauge factor is the ratio of resistance variation to the length deformation

Example. Typically, the gauge factor for conventional strain sensors based on metal materials is between 2 to 5, mostly due to changes in length and cross-sectional area [65]. Compared to metallic foils, semiconductor devices can exhibit much larger gauge factor due to piezoresistive effects. Here, the changes arise due to the dependence of the bandgap on inter-atomic spacing [115]. However, neither metallic strain gauges nor semiconductor-based piezoresistors are suitable for highly flexible sensors. The former is restricted by its low gauge factor, and the latter is hindered by its high rigidity.

The measurement sensitivity can be affected by the sensing mechanism, structural configuration and functional material. A variety of alternative nanomaterial such as graphene, carbon nanotubes, metal nanoparticles and nanowires have been effective in increasing the sensitivity [116]. AuNP-based strain sensors increase their strain factors

with the size of the AuNPs, allowing a wide range of strain factors between 15 and 200 [117]. Recently nanographene films have been synthesized whose piezoresistive response is controlled by changing their growth parameters resulting in gauge factor over 300 [118]. The gauge factor has been tuned by conductive network morphological of CNTs to CB control strategies [119]. Tunneling effect and crack/gap structures in piezoresistive sensors have been effective in promoting sensitivity. Strain sensors based on nanoscale crack junctions working on the mechanism of disconnection-reconnection were able to achieved gauge value of 2000 [120]. Strain sensing fibers based on carbon nanotube exhibited a gauge factor of 425 (at 100% strain) [121]. Further, to improve the performance of sensors and to introduce multiple sensing capabilities, bio-inspired interlocked microstructure geometries [63], whisker arrays [122][123], silk and 2D/3D micro/nanostructures[124][82] have also been employed [125].

Table 3: The reported various flexible and stretchable strain sensors, with their performance in gauge factor values

Nanomaterial	Processing technique	Type of deformation	Properties	Ref.
Graphene	dip-coating	Tensile 104%	GF >100	[126]
Graphene	sprayed	Tensile 26%	GF = 1054	[127]
GnP/MWCNT mixture	Spray-vacuum filtration	Tensile 7.5%	GF = 181.36	[128]
silver nanoparticle	drop cast	Tensile 110%	GF = 268.4	[129]
Pd hexadecylthiolate	Micro molding	Tensile 0.09%	GF ~390	[38]
MXene/PU composite	wet-spinning	Tensile (max. at ≈ 152%)	GF ≈12900 GF ≈238 (at 50% strain)	[130]
Gold NP	Airbrush gun	Tensile (Cylindrical formers)	GF = 50-200	[131]

PEDOT: PSS with a commercial Polyurethane (Lycra)	drop casting	Tensile 10%, 50%	GF = 1,1.3	[132]
overlapped carbon nanotube	CVD-Roller Transfer	Tensile (125 – 145%)	GF = 42300	[64]
Multi-walled carbon nanotubes	Air-spray coating	Tensile (0 – 100%)	GF ~ 1.75	[74]
GWFs	Coated onto or embedded	Tensile (2 – 6%)	GF = (103 – 106)	[133]
Silver nanowire	Drop-casting	Tensile (max. at ≈ 70%)	GF = (2 – 14)	[16]
Fragmentized graphene foam	Drop-casting	Tensile (8.5% -77%)	GF = (15 – 29)	[134]
graphene and carbon nanotube	Selective laser pyrolyzation	Tensile (0 – 100%)	GF = 20 000	[135]
AgNW	drop-coating	Tensile (0 – 150%)	GF = 846	[136]
MWNT-PS microspheres	self-assembly	Tensile (0 – 100%)	GF = 1.35	[137]
Graphene nanoflakes decorated with MoS ₂	One-step carbonization	Tensile (0 – 37.5%)	GF = 1242	[138]
Graphene	CVD-grown	Tensile	<1.8% strain the GF was 2.4 >1.8% strain the GF was 4-14	[139]
Au film	electron-beam evaporation	Tensile (0 – 140%)	GF = (7.2 - 474.8)	[140]
MXene nanocomposite	anti-freezing, and self-healing	Tensile (0 – 350%)	GF = 44.85	[141]

organohydrogel (MNOH)				
conductive filler carbon black (CB) and one-dimensional carbon nanotubes (CNTs)	mixing-casting molding method	Tensile 10%	GF = 4.36(CNT) GF = 15.75(CB)	[142]
CNT@CNC	sputtered - stamped	Tensile (9 – 260%)	GF = (4.5 – 70)	[143]
SWCNT/hydrogel		Tensile (0 – 1000%)	GF = 1.51	[144]
graphite ink	screen printing	Two-point and four-point bending at 0.66%	GF = 19.3 ± 1.4	[145]
MCNP	drop casting	Three-point bending	GF = 250	[146]
titanium nitride thin-film	Sputtering	Three-point bending (Max. at <0.12%)	GF = 5.44	[147]
Gold	self-assembly	Four-point bending 0.6%	GF <135	[148]
1,9-nonanedithiol cross-linked gold nano-particle (GNP) films	layer-by-layer (LbL) spin coating-Contact Printing	Four-point bending	GF ~14 for 4 nm GF ~26 for 7 nm GNPs	[87]
PEDOT: PSS	Spin coating	Bending radius of 5 mm (0.14 - 0.4%)	GF = (3.4 - 17.5)	[149]
polymer/CNT	In situ polymerization	Clamped end of the beam	8 times higher than that of	[72]

			traditional strain gauges.	
Platinum nanoparticle	Atomic layer deposition	0.3%	gauge factor of 2 × 10 ⁴	[150]
Graphene	RPECVD	Bending (max. at < 0.4%)	GF ~ 300	[118]
SWCNTs	self-assembling(self-pinning)	Strain (2% - 15%)	161 ($\epsilon < 2\%$), 9.8 (Avg., $2\% < \epsilon < 15\%$), and 0.58 ($\epsilon > 15\%$)	[151]
silver (Ag) nanoparticles (NPs)	Aerosol Jet based additive printing method	Cantilever beam	3.15+0.086	[152]
graphene-based thin film	Spray deposition	<2%	GF >150	[57]
zinc oxide (ZnO)	Drop casting	Flexural <1% strain	GF >104	[153]
graphene-based elastomer(3DGP)	three-dimensional printing	Flexural 30%	GF = 448(30% strain)	[154]
tin-doped indium oxide	Assembly	Flexural	GF = (18-157)	[155]
CdSe NCs into Au NC matrix	Spin casting	Bended curvature of 1/6.25 mm ⁻¹ (0.2% - 1%)	GF = 5045	[156]
SWCNT/PVdF-HFP	blow-spinning	Bending machine (Minimum at 0.03%)	GF = 134	[157]
Platinum nanoparticle	Atomic layer deposition	Buckling and conformational contact	GF = 70 (at 0.5% strain)	[158]

		configurations 0 – 0.7%		
p-type SiNWs	ion beam implantation-wet etching process		GF = 47	[159]
Graphene	RPECVD		GF <600	[160]
polysilicon film	AIC process		GF = 77	[161]
ZnO	Bonding		GF = 1250	[66]
Platinum	Sputtering		GF = 75	[162]

1.4.3 Non-Linearity

A sensor is linear when the relative change in the electrical signal is linearly proportional to the applied strain. This slope defines the sensor's gauge factor. The linearity of the curve indicated the extend sensor's sensitivity will remain constant. The magnitude of linearity is evaluated with the coefficient of determination (R^2) derived by a linear regression. A higher value of R^2 indicates a stronger linear relationship. Simultaneously achieving sensitivity and linearity can be challenging, but it is not essential to have a high linearity. Most resistive-type strain sensors are linear with low strain ($\epsilon < 1\%$) and non-linear with high strain ($\epsilon > 1\%$). Piezoresistive sensors often exhibit varied gauge factor value in different strain ranges, which is induced by the nonlinear heterogeneous deformation and the different conduction mechanisms that take place. Highly sensitive strain sensors normally respond to the applied strain with a high nonlinearity and low stretchability. It is therefore still difficult to develop strain sensors with simultaneously ultrahigh sensitivity, flexibility and excellent linearity.

Example. The linearity of capacitive strain sensors is superior to that of resistive-type strain sensors. The nonlinear response of resistive strain sensors is because of nonhomogeneous microstructural and morphological changes in the sensing films. Many recently reported resistive strain sensors have shown linear response in two or three regions. Self-healing nanocomposite based strain sensor showed electromechanical response in two linear regions (0–800% and 800–1400%) [163]. Sensor based on the

PDMS elastomer showed high linearity up to the tested range (0–100%) of tensile strain [164]. CNT polymer nanocomposite based strain sensors typically exhibited nonlinear electromechanical response [165][166]. Sensors based on microcracks formation generally have poor linearity, which critically hinder their implementation in practical applications [58]. This may be attributable to the rapid increase in resistance when the sensory metal film breaks into cut-through forms with strain. In order to enhance the linearity, sensor based on super aligned carbon nanotube sheet has successfully shown linearity of $R^2 \approx 0.996$ [167]. Likewise, for sensors based on disconnection mechanism or tunneling effect, the transition from a homogeneous to an inhomogeneous percolation network, has been identified as the focal reason for non-linearity.

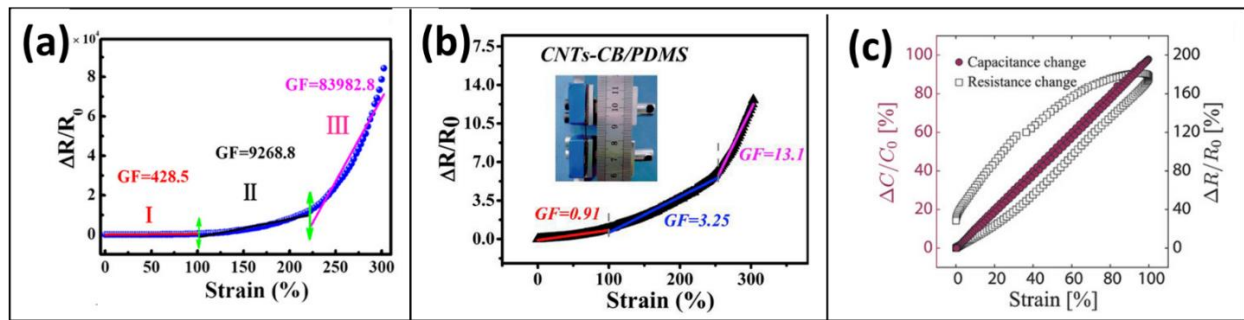


Figure 1.16: (a) Basic tensile electromechanical response of CNT/TPU sensor. Relative resistance changes of strain sensor with high sensitivity and linear response in three strain ranges [163]. (b) Relative resistance change of CNT-CB/PDMS strain sensor as a function of applied tensile strain shows a non-linear response [168]. (c) Measured sensor response under one cycle strain for 100% strain amplitude. As seen capacitive type exhibited linear sensor response ($R^2 = 0.9995$), while the resistive type exhibited nonlinearity and variable gauge factor. Sensors consist of a carbon black-filled elastomer composite [81].

1.4.4 Hysteresis

A consistent sensing performance in loading and unloading is critical. Hysteresis arises when sensor does not return to the same output as the input stimulus when cycled up and/or down, such as when using the sensors as an electronic skin or for measuring heartbeat [169]. The interfacial binding between sensing film and substrate is the essential parameter for hysteresis optimization. The interfacial sliding between nanomaterial filler and the polymer matrix, in a weak binding hampers the fully recovery of filler position, and

results in hysteresis [169][170]. Adversely, a weak adhesion is required to avoid the friction and fracture in nanomaterial fillers. Under small strain as the morphology of the conductive network almost remains unchanged, good reversibility and repeatability can be observed. A deteriorating trend of the relative change in resistance with increasing stretching/releasing cycle number and subsequent saturation is often observed. In addition, because of fatigue and plastic deformation under large strain, and fracture of sensing nanomaterials the degradation of the performance of strain sensors has been seen. These irreversible variations in resistance make the sensors less efficient. Capacitive-type strain sensors show less hysteresis than resistive and optical strain sensors. The reconnection of nanomaterials (tunneling contact) during the release cycle takes time and though they return to initial position they can be still irreversible. The carbon nanotube based strain sensors are reported to have higher hysteresis behavior compared to other nanomaterials [171][172]. Capacitive and optical strain sensors show negligible hysteresis [173] because of the fact that they do not need to rely on the formation of ohmic contact or tunneling conduction path between nanomaterial matrix. These connection pathways are often irreversible over repeated dynamic loading condition.

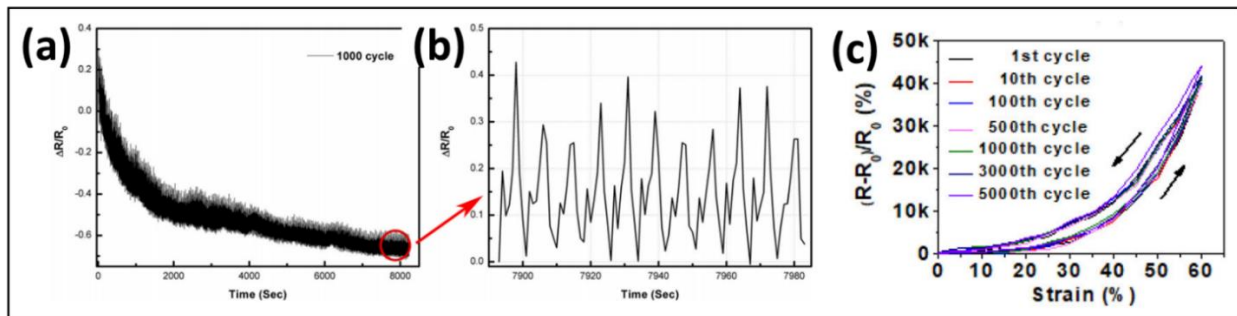


Figure 1.17 : (a-b) Long-term relative variation in resistance of the MWCNT/PDMS strain sensor when subjected to the 1000 cycles of stretching/releasing (from 0–10% strain) [174]. (c) Hysteresis loops of a Ti_3C_2Tx -AgNW-poly(dopamine)/ Ni^{2+} strain sensor subjected to 5000 stretching and releasing cycles [175].

1.4.5 Reproducibility and Dynamic Durability

Repeatability is the ability of the sensor to replicate the same output signal under the same conditions, when the same measurand is applied to it continually. The inability

of the sensor to perform the same value under identical condition causes this error. The assembled structures linked with processing strategies are more critical for the final sensing performances. Therefore, rational structure design, proper selection of materials and control of the connection types of sensing materials are effective routes to realize balanced performances.

Durability. It represents the long-term durability of the strain sensors during cyclic load with stable electrical response and mechanical integrity. It is especially important for sensors integrated on skin, textiles or touch screens. These applications undergo a very large number of complex and dynamic deformations and must be maintained during their use. Performance degradation can be led by irreversible deformation or fracture of the nanomaterial assembly. Highly durable strain sensors have been recently reported in which they have shown notable dynamic durability up to 20000 cycles [176][177][178][179][180][181]. Overall, resistive-type sensors generally respond to applied strain with high hysteresis and non-linearity when undergoing large deformation, especially in the case of nanocomposite-based sensors. But they show high sensitivities, therefore when operated under low deformations prove to be very reliable [182].

Apart to the above covered crucial performance parameters, a more recent research has demonstrated that several novel design parameters such as self-healing, self-powering, self-cleaning, transparency, biocompatibility, and biodegradability need to be considered as well to ensure a better application adaptability [125].

1.4.6 Characterization Set-up

Mechanical deformation can be induced by pressing, stretching, bending, and twisting which creates a parametric variation in the active sensing component. These distortions variation leads to change in physical distance between the active sensing elements. A strain gauge system consists of the following components, shown in Figure 1.18:

- Strain sensor
- Measuring instrument
- Power supply, alternating current generator

- Source Meter
- Recorder of changes in electrical quantities

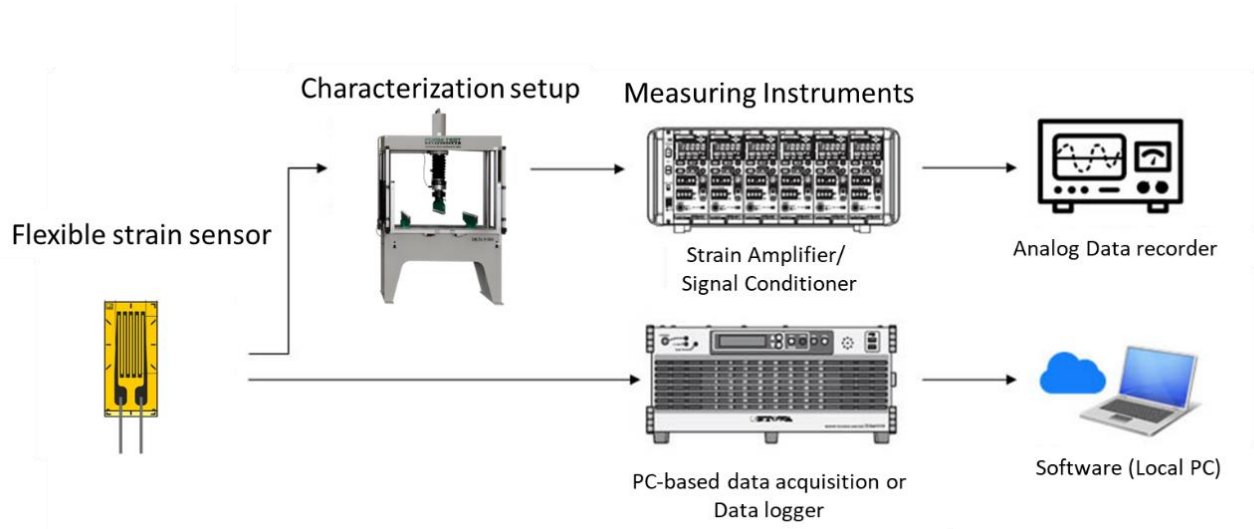


Figure 1.18 : Overview of strain measuring system

1.1.1. Tensile test

The geometric component of piezoresistivity originated from a change in dimension of a strained element. When a strain sensor experiences a tensile strain, it becomes longer and the cross-sectional area becomes smaller. Both of these situations contribute to the increase in the resistance, and vice versa for a compressive strain.

This resistance and length variation can be used to calculate the gauge factor. Tensile testing determines the behavior of a sample when an axial stretching load is applied. These types of tests can be performed under controlled atmosphere (heating or cooling). Tensile testing is commonly used to define the maximum load that a device can withstand. For a piezoresistive strain sensor, it would correspond to the maximum resistance variation under this maximum load.

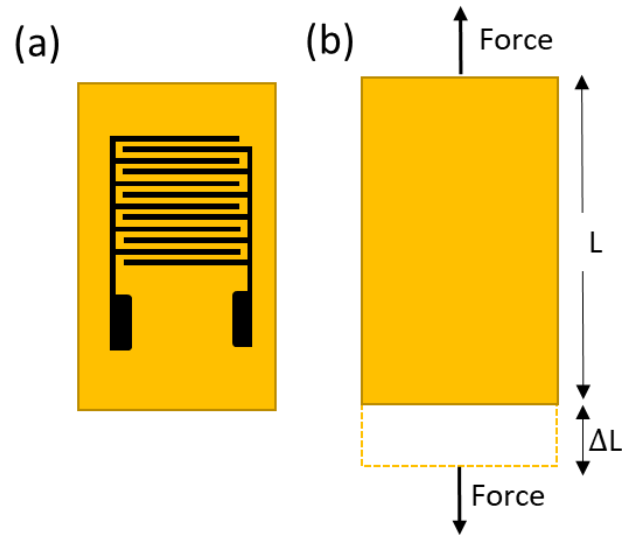


Figure 1.19 : Schematics of stretching

Use. The properties derived using the resultant stress/strain curve, include the modulus of yield strength, elasticity, and strain. It is used for characterizing stretchable electronics, electronic skins that can mimic its functions, by enabling conversion of various stimuli created by the human body and surrounding environment to electrical signals (strain, temperature, humidity, etc.)

Set-up. The set up consists of two clamps, one on top and one on bottom, as shown in Figure 1.20, fixed on ESM303 Motorized Tension / Compression Test Stand operated by the LabVIEW software. A similar set-up consists of stretching rig, 5944 Instron machine, motorized stage that has been used for stretching [183][184][185]. Flexible/stretchable sensor is held in position between clamps. The connection is established between electrodes to have a good contact between the sensor and the Source Meter.

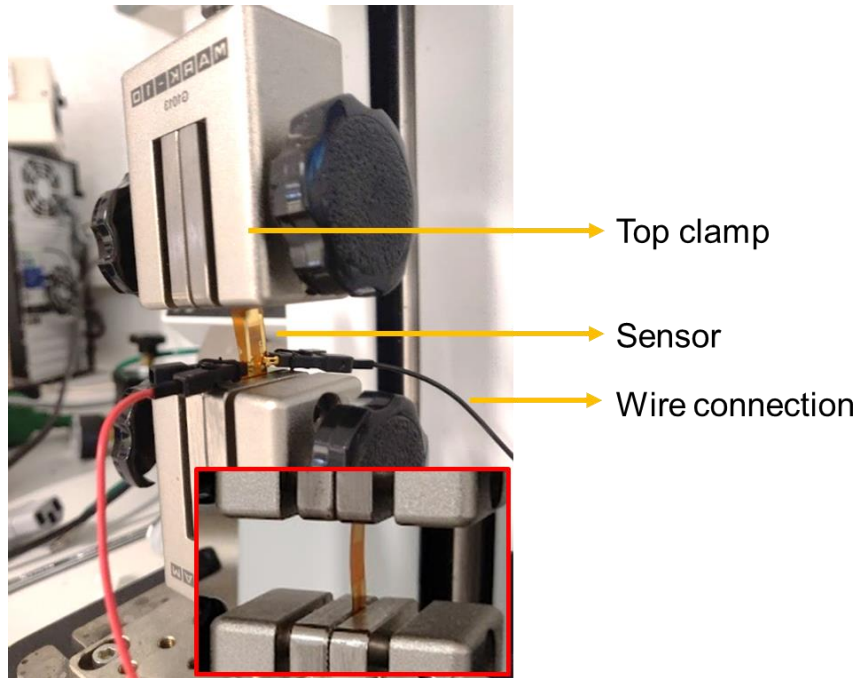


Figure 1.20 : Schematic set-up used for the tensile testing. In red is the zoom image of sensor closer to the clamp.

1.1.2. Flexural test

The flexure test measures the electrical change in active materials when subjected to a bending load. A flat rectangular specimen is loaded at two, three or four points, Figure 1.21. Two-point and three-point bending fixtures are commonly used. The main advantage of a three-point flexural test is the ease of the specimen preparation and testing.

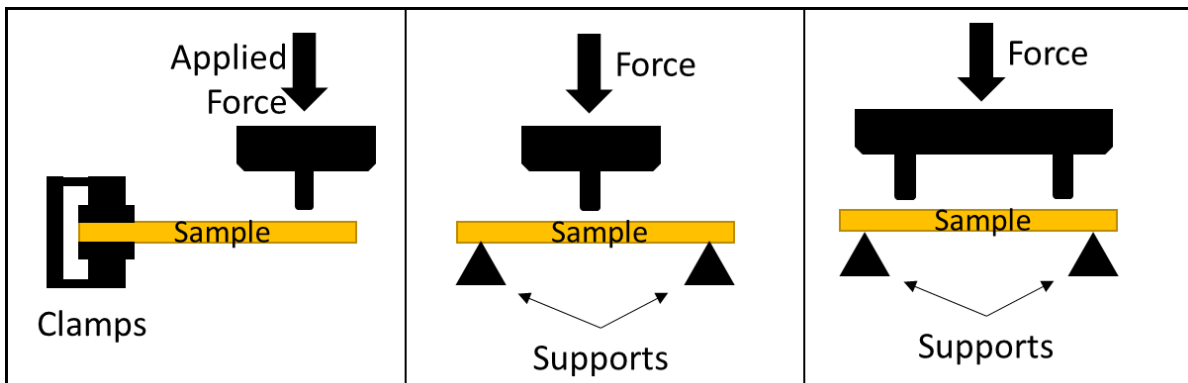


Figure 1.21 : (a) Cantilever beam or two-point bending (b) Three-point-bending (c) Four-point bending

Use. The three-point bending delivers values for the modulus of elasticity in bending and flexural stress–strain response of the material. **Setup.** The three-point bending technique makes use of a downward moving probe, which applies force at a constant speed, as shown in Figure 1.22.

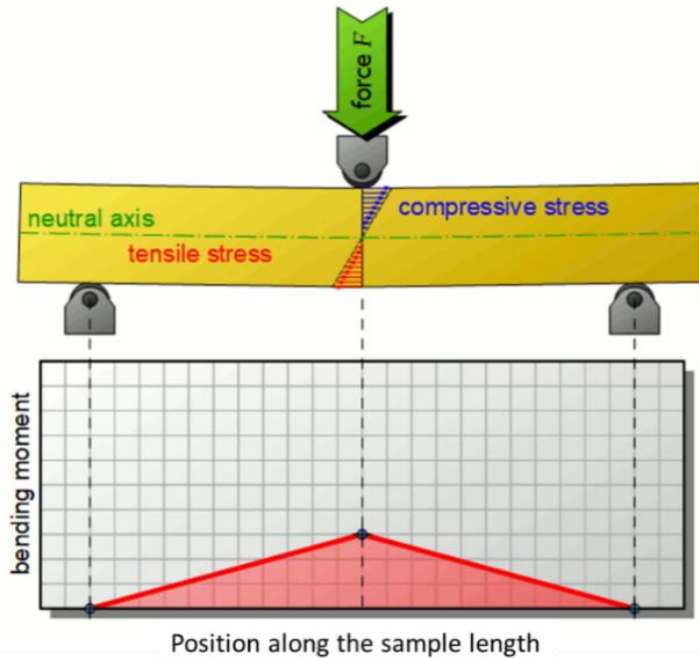


Figure 1.22 : Illustration of deformation by the 3-point bending load

Under an applied stress/ force, the substrate is bent. The outer (upper) surface is then subjected to compression, while the inner (lower) surface is under tension. The 3-point flexure test is the most commonly used for polymers while the 4-point flexure test is mostly used for wood and composites.

1.5 Conclusion

This first chapter has highlighted the need to obtain flexible strain sensors used in various fields [186][187][188][189]. However, the practical problems involving their sensitivity and stretchability remain as challenges. Stretchability is important for biomedical, mechatronic, sports, and entertainment applications [190]. However, achieving high stretchability is not within the scope of this work.

In this work, efforts are devoted to fabricating piezoresistive strain sensor based on dielectrophoresis of 1D - helical nanostructures on flexible polyimide substrate. The bottom-up approach and assembly are used to elaborate high performance sensors and offer a highly sensitive response to low strain values. Owing to the helical configuration of sensing material and the tunneling effect between adjacent gold nanoparticles, the strain sensor is hypothesized to have zero hysteresis response. This special configuration endowed strain sensor with an ability of have a quick recovery.

However, the sensors manufactured under the same conditions can have different properties, as a result, measurement reliability is compromised, and consequently the sensor cannot be used in a practical setting. When characterizing a strain sensor, sensitivity and linearity are the most supreme parameters, others consist of hysteresis and reliability. All these parameters should be considered for the development of flexible strain sensors.

In the later section, HNS sensor will be characterized using three point bending set-up, with objective to build strain sensor with (i) near zero hysteresis and zero-point drift and (ii) improve cycling performance. In order to avoid any mechanical/machine inaccuracy, the calibration of three-point bending system is presented as well. Strengths of strain sensor is tested as a biomedical device not only for subtle movements (such as distinguishing a pulse), but also large movements (such as recognizing the motion of fingers and wrists) as well. We believe that 1D – helical nanostructure is a promising material for low-cost, high-sensitivity, and long-stability sensors. Overall, we believe that HNS strain sensors can be a potential candidate in strain and pressure sensing related applications.

Bibliography

- [1] H. K. Kim, S. Lee, and K. S. Yun, "Capacitive tactile sensor array for touch screen application," *Sensors Actuators, A Phys.*, vol. 165, no. 1, pp. 2–7, 2011.
- [2] M. Cutkosky, R. Howe, and W. Provancher, "Handbook of Robotics, Chapter 19: Force and Tactile Sensors Chs.," *Handb. Robot.*, no. November, p. 1611, 2007.
- [3] Y. Huang, D. Fang, C. Wu, W. Wang, X. Guo, and P. Liu, "A flexible touch-pressure sensor array with wireless transmission system for robotic skin," *Rev. Sci. Instrum.*, vol. 87, no. 6, 2016.
- [4] T. Someya, T. Sekitani, S. Iba, Y. Kato, H. Kawaguchi, and T. Sakurai, "A large-area, flexible pressure sensor matrix with organic field-effect transistors for artificial skin applications," *Proc. Natl. Acad. Sci. U. S. A.*, vol. 101, no. 27, pp. 9966–9970, 2004.
- [5] T. Q. Trung and N. E. Lee, "Flexible and Stretchable Physical Sensor Integrated Platforms for Wearable Human-Activity Monitoring and Personal Healthcare," *Adv. Mater.*, vol. 28, no. 22, pp. 4338–4372, 2016.
- [6] K. Xu, Y. Lu, and K. Takei, "Multifunctional Skin-Inspired Flexible Sensor Systems for Wearable Electronics," *Adv. Mater. Technol.*, vol. 4, no. 3, pp. 1–25, 2019.
- [7] O. Erol, I. Uyan, M. Hatip, C. Yilmaz, A. B. Tekinay, and M. O. Guler, "Recent advances in bioactive 1D and 2D carbon nanomaterials for biomedical applications," *Nanomedicine Nanotechnology, Biol. Med.*, vol. 14, no. 7, pp. 2433–2454, 2018.
- [8] G. Schwartz *et al.*, "Flexible polymer transistors with high pressure sensitivity for application in electronic skin and health monitoring," *Nat. Commun.*, vol. 4, no. May, pp. 1858–1859, 2013.
- [9] X. Liao *et al.*, "Flexible and highly sensitive strain sensors fabricated by pencil drawn for wearable monitor," *Adv. Funct. Mater.*, vol. 25, no. 16, pp. 2395–2401, 2015.

- [10] Y. Li, Y. A. Samad, T. Taha, G. Cai, S. Y. Fu, and K. Liao, "Highly Flexible Strain Sensor from Tissue Paper for Wearable Electronics," *ACS Sustain. Chem. Eng.*, vol. 4, no. 8, pp. 4288–4295, 2016.
- [11] D. Jiang *et al.*, "Flexible Sandwich Structural Strain Sensor Based on Silver Nanowires Decorated with Self-Healing Substrate," *Macromol. Mater. Eng.*, vol. 304, no. 7, pp. 1–9, 2019.
- [12] S. Chen, Z. Lou, D. Chen, Z. Chen, K. Jiang, and G. Shen, "Highly flexible strain sensor based on ZnO nanowires and P(VDF-TrFE) fibers for wearable electronic device," *Sci. China Mater.*, vol. 59, no. 3, pp. 173–181, 2016.
- [13] J. Ren *et al.*, "Environmentally-friendly conductive cotton fabric as flexible strain sensor based on hot press reduced graphene oxide," *Carbon N. Y.*, vol. 111, pp. 622–630, 2017.
- [14] J. Lee *et al.*, "Transparent, Flexible Strain Sensor Based on a Solution-Processed Carbon Nanotube Network," *ACS Appl. Mater. Interfaces*, vol. 9, no. 31, pp. 26279–26285, 2017.
- [15] B. Hu, W. Chen, and J. Zhou, "High performance flexible sensor based on inorganic nanomaterials," *Sensors Actuators, B Chem.*, vol. 176, pp. 522–533, 2013.
- [16] A. Morteza *et al.*, "Highly stretchable and sensitive strain sensor based on silver nanowire-elastomer nanocomposite," *ACS Nano*, vol. 8, no. 5, pp. 5154–5163, May 2014.
- [17] B. Wang and A. Facchetti, "Mechanically Flexible Conductors for Stretchable and Wearable E-Skin and E-Textile Devices," *Adv. Mater.*, vol. 31, no. 28, pp. 1–53, 2019.
- [18] Z. M. Dang, M. S. Zheng, and J. W. Zha, "1D/2D Carbon Nanomaterial-Polymer Dielectric Composites with High Permittivity for Power Energy Storage Applications," *Small*, vol. 12, no. 13, pp. 1688–1701, 2016.
- [19] Y. Z. Long, M. Yu, B. Sun, C. Z. Gu, and Z. Fan, "Recent advances in large-scale

- assembly of semiconducting inorganic nanowires and nanofibers for electronics, sensors and photovoltaics,” *Chem. Soc. Rev.*, vol. 41, no. 12, pp. 4560–4580, 2012.
- [20] J. Yin, Y. Huang, S. Hameed, R. Zhou, L. Xie, and Y. Ying, “Large scale assembly of nanomaterials: mechanisms and applications,” *Nanoscale*, vol. 12, no. 34, pp. 17571–17589, 2020.
- [21] S. A. Cybart *et al.*, “Nano Josephson superconducting tunnel junctions in YBa₂Cu₃O_{7-δ} directly patterned with a focused helium ion beam,” *Nat. Nanotechnol.*, vol. 10, no. 7, pp. 598–602, 2015.
- [22] K. S. Kim *et al.*, “Large-scale pattern growth of graphene films for stretchable transparent electrodes,” *Nature*, vol. 457, no. 7230, pp. 706–710, 2009.
- [23] J. Fang, I. Levchenko, T. Van Der Laan, S. Kumar, and K. Ostrikov, “Multipurpose nanoporous alumina-carbon nanowall bi-dimensional nano-hybrid platform via catalyzed and catalyst-free plasma CVD,” *Carbon*, vol. 78. Elsevier Ltd, pp. 627–632, 2014.
- [24] H. Wang, H. Yang, S. Zhang, L. Zhang, J. Li, and X. Zeng, “3D-Printed Flexible Tactile Sensor Mimicking the Texture and Sensitivity of Human Skin,” *Adv. Mater. Technol.*, vol. 4, no. 9, pp. 1–8, 2019.
- [25] A. Chortos, J. Liu, and Z. Bao, “Pursuing prosthetic electronic skin,” *Nat. Mater.*, vol. 15, no. 9, pp. 937–950, 2016.
- [26] T. Someya, Z. Bao, and G. G. Malliaras, “The rise of plastic bioelectronics,” *Nature*, vol. 540, no. 7633, pp. 379–385, 2016.
- [27] M. A. Alam and S. Kumar, “Flexible Electronics,” in *Encyclopedia of Nanotechnology*, B. Bhushan, Ed. Dordrecht: Springer Netherlands, 2012, pp. 860–865.
- [28] H. Hocheng and C. M. Chen, “Design, fabrication and failure analysis of stretchable electrical routings,” *Sensors (Switzerland)*, vol. 14, no. 7, pp. 11855–11877, 2014.

- [29] W. Gao *et al.*, “Fully integrated wearable sensor arrays for multiplexed in situ perspiration analysis,” *Nature*, vol. 529, no. 7587, pp. 509–514, 2016.
- [30] B. W. An, S. Heo, S. Ji, F. Bien, and J. U. Park, “Transparent and flexible fingerprint sensor array with multiplexed detection of tactile pressure and skin temperature,” *Nat. Commun.*, vol. 9, no. 1, pp. 1–10, 2018.
- [31] G. Liu *et al.*, “A flexible temperature sensor based on reduced graphene oxide for robot skin used in internet of things,” *Sensors (Switzerland)*, vol. 18, no. 5, 2018.
- [32] H. Park *et al.*, “Enhanced moisture-reactive hydrophilic-PTFE-based flexible humidity sensor for real-time monitoring,” *Sensors (Switzerland)*, vol. 18, no. 3, 2018.
- [33] Y. Sun, V. Kumar, I. Adesida, and J. A. Rogers, “Buckled and wavy ribbons of GaAs for high-performance electronics on elastomeric substrates,” *Adv. Mater.*, vol. 18, no. 21, pp. 2857–2862, 2006.
- [34] H. Jiang, D. Y. Khang, J. Song, Y. Sun, Y. Huang, and J. A. Rogers, “Finite deformation mechanics in buckled thin films on compliant supports,” *Proc. Natl. Acad. Sci. U. S. A.*, vol. 104, no. 40, pp. 15607–15612, 2007.
- [35] Y. Sun, W. M. Choi, H. Jiang, Y. Y. Huang, and J. A. Rogers, “Controlled buckling of semiconductor nanoribbons for stretchable electronics,” *Nat. Nanotechnol.*, vol. 1, no. 3, pp. 201–207, 2006.
- [36] H. Fu *et al.*, “Lateral buckling and mechanical stretchability of fractal interconnects partially bonded onto an elastomeric substrate,” *Appl. Phys. Lett.*, vol. 106, no. 9, pp. 9–14, 2015.
- [37] S. Xu *et al.*, “Stretchable batteries with self-similar serpentine interconnects and integrated wireless recharging systems,” *Nat. Commun.*, vol. 4, pp. 1543–1548, 2013.
- [38] B. Radha, A. A. Sagade, and G. U. Kulkarni, “Flexible and semitransparent strain sensors based on micromolded Pd nanoparticle-carbon μ -stripes,” *ACS Appl. Mater. Interfaces*, vol. 3, no. 7, pp. 2173–2178, 2011.

- [39] L. Wen, F. Li, and H. M. Cheng, "Carbon Nanotubes and Graphene for Flexible Electrochemical Energy Storage: from Materials to Devices," *Adv. Mater.*, vol. 28, no. 22, pp. 4306–4337, 2016.
- [40] N. Bowden, "Spontaneous formation of ordered structures in thin films of metals supported on an elastomeric polymer," *Lett. to Nat.*, vol. 393, no. May, pp. 146–149, 1998.
- [41] J. Jones, S. P. Lacour, S. Wagner, Z. Suo, P. Lacour, and S. Wagner, "Stretchable wavy metal interconnects Stretchable wavy metal interconnects," vol. 1723, no. 2004, pp. 23–26, 2014.
- [42] J. Song, H. Jiang, Y. Huang, and J. A. Rogers, "Mechanics of stretchable inorganic electronic materials," *J. Vac. Sci. Technol. A*, vol. 1107, no. 2009, 2014.
- [43] Z. Lu, J. Foroughi, C. Wang, H. Long, and G. G. Wallace, "Superelastic Hybrid CNT / Graphene Fibers for Wearable Energy Storage," vol. 1702047, pp. 1–10, 2017.
- [44] H. Wang *et al.*, "Superelastic wire-shaped supercapacitor sustaining 850 % tensile strain based on carbon nanotube @ graphene fiber," pp. 1–10, 2017.
- [45] W. Wu, "Stretchable electronics: functional materials, fabrication strategies and applications," *Sci. Technol. Adv. Mater.*, vol. 20, no. 1, pp. 187–224, 2019.
- [46] J. H. Ahn and J. H. Je, "Stretchable electronics: Materials, architectures and integrations," *J. Phys. D. Appl. Phys.*, vol. 45, no. 10, 2012.
- [47] W. Dang, V. Vinciguerra, L. Lorenzelli, and R. Dahiya, "Printable stretchable interconnects," *Flex. Print. Electron.*, vol. 2, no. 1, p. 013003, Mar. 2017.
- [48] K. S. Kumar, P. Chen, and H. Ren, "Review Article A Review of Printable Flexible and Stretchable Tactile Sensors," vol. 2019, p. 32, 2019.
- [49] X. Wang, L. Dong, H. Zhang, R. Yu, C. Pan, and Z. L. Wang, "Recent Progress in Electronic Skin," *Adv. Sci.*, vol. 2, no. 10, pp. 1–21, 2015.
- [50] M. Park, J. Park, and U. Jeong, "Design of conductive composite elastomers for

- stretchable electronics,” *Nano Today*, vol. 9, pp. 244–260, 2014.
- [51] D. Liu and G. Hong, “Wearable Electromechanical Sensors and Its Applications,” in *Wearable Devices - the Big Wave of Innovation*, IntechOpen, 2019.
- [52] H. Q. Yan Liu, Hai Wang, Wei Zhao, Min Zhang and Y. Xie, “Flexible, Stretchable Sensors for Wearable Health Monitoring: Sensing Mechanisms, Materials, Fabrication Strategies and Features,” 2018.
- [53] Z. Chen *et al.*, “Flexible Piezoelectric-Induced Pressure Sensors for Static Measurements Based on Nanowires/Graphene Heterostructures,” *ACS Nano*, vol. 11, no. 5, pp. 4507–4513, 2017.
- [54] C. K. Jeong *et al.*, “Nanowire-percolated piezoelectric copolymer-based highly transparent and flexible self-powered sensors †,” 2019.
- [55] Z. Wang, X. Pan, Y. He, Y. Hu, H. Gu, and Y. Wang, “Piezoelectric Nanowires in Energy Harvesting Applications,” *Adv. Mater. Sci. Eng.*, vol. 2015, 2015.
- [56] J. Zhao, G. Y. Zhang, and D. X. Shi, “Review of graphene-based strain sensors,” *Chinese Phys. B*, vol. 22, no. 5, 2013.
- [57] M. Hempel, D. Nezich, J. Kong, and M. Hofmann, “A novel class of strain gauges based on layered percolative films of 2D materials,” *Nano Lett.*, vol. 12, no. 11, pp. 5714–5718, 2012.
- [58] T. Yang *et al.*, “Structural engineering of gold thin films with channel cracks for ultrasensitive strain sensing,” *Mater. Horizons*, vol. 3, no. 3, pp. 248–255, 2016.
- [59] W. Wu, Y. Xu, J. Zhang, W. Lu, and G. Song, “Enhanced Performance of a Soft Strain Sensor by Combining Microcracks with Wrinkled Structures,” *Phys. Status Solidi - Rapid Res. Lett.*, vol. 2000400, pp. 1–7, 2020.
- [60] Q. Zou, J. Zheng, Q. Su, W. Wang, W. Gao, and Z. Ma, “A wave-inspired ultrastretchable strain sensor with predictable cracks,” *Sensors Actuators, A Phys.*, vol. 300, 2019.
- [61] S. Wang *et al.*, “Network cracks-based wearable strain sensors for subtle and

- large strain detection of human motions,” *J. Mater. Chem. C*, vol. 6, no. 19, pp. 5140–5147, 2018.
- [62] T. Yamada *et al.*, “A stretchable carbon nanotube strain sensor for human-motion detection,” *Nat. Nanotechnol.*, vol. 6, no. 5, pp. 296–301, 2011.
- [63] C. Pang *et al.*, “A flexible and highly sensitive strain-gauge sensor using reversible interlocking of nanofibres,” *Nat. Mater.*, vol. 11, no. 9, pp. 795–801, 2012.
- [64] J. Lee, S. Pyo, D. S. Kwon, E. Jo, W. Kim, and J. Kim, “Ultrasensitive Strain Sensor Based on Separation of Overlapped Carbon Nanotubes,” *Small*, vol. 15, no. 12, pp. 1–7, 2019.
- [65] R. O’Donnell, “Prolog to Semiconductor Piezoresistance for Microsystems,” *Proc. IEEE*, vol. 97, no. 3, pp. 511–512, 2009.
- [66] J. Zhou *et al.*, “Flexible piezotronic strain sensor,” *Nano Lett.*, vol. 8, no. 9, pp. 3035–3040, 2008.
- [67] R. He and P. Yang, “Giant piezoresistance effect in silicon nanowires,” *Nat. Nanotechnol.*, vol. 1, no. 1, pp. 42–46, 2006.
- [68] Alamusi *et al.*, “Ultrasensitive strain sensors of multiwalled carbon nanotube/epoxy nanocomposite using dielectric loss tangent,” *Appl. Phys. Lett.*, vol. 103, no. 22, 2013.
- [69] W. Obitayo and T. Liu, “A review: Carbon nanotube-based piezoresistive strain sensors,” *J. Sensors*, vol. 2012, 2012.
- [70] C. Deng, L. Pan, C. Li, X. Fu, R. Cui, and H. Nasir, “Helical gold nanotube film as stretchable micro/nanoscale strain sensor,” *J. Mater. Sci.*, vol. 53, no. 3, pp. 2181–2192, 2018.
- [71] C. Li, E. T. Thostenson, and T. W. Chou, “Dominant role of tunneling resistance in the electrical conductivity of carbon nanotube-based composites,” *Appl. Phys. Lett.*, vol. 91, no. 22, pp. 91–94, 2007.
- [72] R. Pethig *et al.*, “Tunneling effect in a polymer/carbon nanotube nanocomposite

- strain sensor,” *Acta Mater.*, vol. 56, no. 13, pp. 2929–2936, 2008.
- [73] Alamusi, N. Hu, H. Fukunaga, S. Atobe, Y. Liu, and J. Li, “Piezoresistive strain sensors made from carbon nanotubes based polymer nanocomposites,” *Sensors*, vol. 11, no. 11, pp. 10691–10723, Nov. 2011.
- [74] M. Amjadi, Y. J. Yoon, and I. Park, “Ultra-stretchable and skin-mountable strain sensors using carbon nanotubes-Ecoflex nanocomposites,” *Nanotechnology*, vol. 26, no. 37, p. 375501, 2015.
- [75] J. C. F. Millett, N. K. Bourne, and Z. Rosenberg, “On the analysis of transverse stress gauge data from shock loading experiments,” *J. Phys. D. Appl. Phys.*, vol. 29, no. 9, pp. 2466–2472, 1996.
- [76] M. Park, Y. J. Park, X. Chen, Y. K. Park, M. S. Kim, and J. H. Ahn, “MoS₂-Based Tactile Sensor for Electronic Skin Applications,” *Adv. Mater.*, vol. 28, no. 13, pp. 2556–2562, 2016.
- [77] S. R. Kim, J. H. Kim, and J. W. Park, “Wearable and Transparent Capacitive Strain Sensor with High Sensitivity Based on Patterned Ag Nanowire Networks,” *ACS Appl. Mater. Interfaces*, vol. 9, no. 31, pp. 26407–26416, 2017.
- [78] J. H. Cho, S. H. Ha, and J. M. Kim, “Transparent and stretchable strain sensors based on metal nanowire microgrids for human motion monitoring,” *Nanotechnology*, vol. 29, no. 15, 2018.
- [79] M. D. Ho *et al.*, “Percolating Network of Ultrathin Gold Nanowires and Silver Nanowires toward ‘Invisible’ Wearable Sensors for Detecting Emotional Expression and Apexcardiogram,” *Adv. Funct. Mater.*, vol. 27, no. 25, pp. 1–9, 2017.
- [80] W. Zhang, Q. Liu, and P. Chen, “Flexible strain sensor based on carbon black/silver nanoparticles composite for human motion detection,” *Materials (Basel)*, vol. 11, no. 10, pp. 1–13, 2018.
- [81] J. Shintake, E. Piskarev, S. H. Jeong, and D. Floreano, “Ultrastretchable Strain Sensors Using Carbon Black-Filled Elastomer Composites and Comparison of

- Capacitive Versus Resistive Sensors,” *Adv. Mater. Technol.*, vol. 3, no. 3, pp. 1–8, 2018.
- [82] A. Nakamura, T. Hamanishi, S. Kawakami, and M. Takeda, “A piezo-resistive graphene strain sensor with a hollow cylindrical geometry,” *Mater. Sci. Eng. B Solid-State Mater. Adv. Technol.*, vol. 219, pp. 20–27, 2017.
- [83] A. Mehmood *et al.*, “Graphene based nanomaterials for Strain Sensor Application A-review,” *J. Environ. Chem. Eng.*, p. 103743, 2020.
- [84] S. H. Zhang, F. X. Wang, J. J. Li, H. D. Peng, J. H. Yan, and G. B. Pan, “Wearable wide-range strain sensors based on ionic liquids and monitoring of human activities,” *Sensors (Switzerland)*, vol. 17, no. 11, 2017.
- [85] H. Sun *et al.*, “Highly Stretchable, Transparent, and Bio-Friendly Strain Sensor Based on Self-Recovery Ionic-Covalent Hydrogels for Human Motion Monitoring,” *Macromol. Mater. Eng.*, vol. 304, no. 10, pp. 1–10, 2019.
- [86] H. Xu, Y. Lv, D. Qiu, Y. Zhou, H. Zeng, and Y. Chu, “An ultra-stretchable, highly sensitive and biocompatible capacitive strain sensor from an ionic nanocomposite for on-skin monitoring,” *Nanoscale*, vol. 11, no. 4, pp. 1570–1578, 2019.
- [87] B. Ketelsen *et al.*, “Fabrication of Strain Gauges via Contact Printing: A Simple Route to Healthcare Sensors Based on Cross-Linked Gold Nanoparticles,” *ACS Applied Materials and Interfaces*, vol. 10, no. 43, pp. 37374–37385, 2018.
- [88] B. Xie *et al.*, “A tunable palladium nanoparticle film-based strain sensor in a Mott variable-range hopping regime,” *Sensors Actuators, A Phys.*, vol. 272, pp. 161–169, 2018.
- [89] J. Dong, N. Mohieddin Abukhdeir, and I. A. Goldthorpe, “Simple assembly of long nanowires through substrate stretching,” *Nanotechnology*, vol. 26, no. 48, 2015.
- [90] H. B. Song *et al.*, “Lead iodide nanosheets for piezoelectric energy conversion and strain sensing,” *Nano Energy*, vol. 49, no. March, pp. 7–13, 2018.
- [91] S. Kim *et al.*, “Wearable, Ultrawide-Range, and Bending-Insensitive Pressure

- Sensor Based on Carbon Nanotube Network-Coated Porous Elastomer Sponges for Human Interface and Healthcare Devices,” *ACS Appl. Mater. Interfaces*, vol. 11, no. 26, pp. 23639–23648, 2019.
- [92] M. Pruvost, W. J. Smit, C. Monteux, P. Poulin, and A. Colin, “Polymeric foams for flexible and highly sensitive low-pressure capacitive sensors,” *npj Flex. Electron.*, vol. 3, no. 1, pp. 13–18, 2019.
- [93] N. Ben Messaoud, M. E. Ghica, C. Dridi, M. Ben Ali, and C. M. A. Brett, “Electrochemical sensor based on multiwalled carbon nanotube and gold nanoparticle modified electrode for the sensitive detection of bisphenol A,” *Sensors Actuators, B Chem.*, vol. 253, pp. 513–522, 2017.
- [94] J. Wang *et al.*, “Fabrication of a Sensitive Strain and Pressure Sensor from Gold,” 2020.
- [95] H. Moreira *et al.*, “Electron transport in gold colloidal nanoparticle-based strain gauges,” *Nanotechnology*, vol. 24, no. 9, Mar. 2013.
- [96] N. Elahi, M. Kamali, and M. H. Baghersad, “Recent biomedical applications of gold nanoparticles: A review,” *Talanta*, vol. 184, pp. 537–556, 2018.
- [97] J. Schuster *et al.*, “Spherical ordered mesoporous carbon nanoparticles with high porosity for lithium-sulfur batteries,” *Angew. Chemie - Int. Ed.*, vol. 51, no. 15, pp. 3591–3595, 2012.
- [98] M. R. Willner and P. J. Vikesland, “Nanomaterial enabled sensors for environmental contaminants,” *J. Nanobiotechnology*, pp. 1–16, 2018.
- [99] M. Daniel and D. Astruc, “Gold Nanoparticles : Assembly , Supramolecular Chemistry , Quantum-Size-Related Properties , and Applications toward Biology , Catalysis , and Nanotechnology,” 2004.
- [100] P. J. Vikesland and K. R. Wigginton, “Nanomaterial Enabled Biosensors for Pathogen Monitoring - A Review,” vol. 44, no. 10, pp. 3656–3669, 2010.
- [101] Y. Xing and P. S. Dittrich, “One-dimensional nanostructures: Microfluidic-based

- synthesis, alignment and integration towards functional sensing devices,” *Sensors (Switzerland)*, vol. 18, no. 1, p. 21, 2018.
- [102] S. Jambhulkar, W. Xu, D. Ravichandran, J. Prakash, A. N. Mada Kannan, and K. Song, “Scalable Alignment and Selective Deposition of Nanoparticles for Multifunctional Sensor Applications,” *Nano Lett.*, vol. 20, no. 5, pp. 3199–3206, May 2020.
- [103] J. Hong *et al.*, “Shape transformation and self-alignment of Fe-based nanoparticles †,” vol. 1, pp. 2465–2784, 2019.
- [104] S. Wu, S. Peng, and C. H. Wang, “Multifunctional polymer nanocomposites reinforced by aligned carbon nanomaterials,” *Polymers (Basel)*., vol. 10, no. 5, 2018.
- [105] M. Segev-Bar and H. Haick, “Flexible sensors based on nanoparticles,” *ACS Nano*, vol. 7, no. 10, pp. 8366–8378, 2013.
- [106] S. Bi, Z. Ouyang, Q. Guo, and C. Jiang, “Additive Effect for Organic Solar Cell Fabrication by Multi-Layer Inking and Stamping,” *J. Sci. Adv. Mater. Devices*, vol. 3, 2018.
- [107] L. Nayak, S. Mohanty, S. K. Nayak, and A. Ramadoss, “A review on inkjet printing of nanoparticle inks for flexible electronics,” *J. Mater. Chem. C*, vol. 7, no. 29, pp. 8771–8795, 2019.
- [108] Z. Yin *et al.*, “Aligned hierarchical Ag/ZnO nano-heterostructure arrays via electrohydrodynamic nanowire template for enhanced gas-sensing properties,” *Sci. Rep.*, vol. 7, no. 1, pp. 1–10, 2017.
- [109] S. Santra *et al.*, “Dip pen nanolithography-deposited zinc oxide nanorods on a CMOS MEMS platform for ethanol sensing,” *RSC Adv.*, vol. 5, no. 59, pp. 47609–47616, 2015.
- [110] S. Salomon, J. Eymery, and E. Pauliac-Vaujour, “GaN wire-based Langmuir-Blodgett films for self-powered flexible strain sensors,” *Nanotechnology*, vol. 25, no. 37, 2014.

- [111] G. Monastyreckis *et al.*, “Strain sensing coatings for large composite structures based on 2d mxene nanoparticles,” *Sensors*, vol. 21, no. 7, pp. 1–14, 2021.
- [112] G. Yu, A. Cao, and C. M. Lieber, “Large-area blown bubble films of aligned nanowires and carbon nanotubes,” *Nat. Nanotechnol.*, vol. 2, no. 6, pp. 372–377, 2007.
- [113] B. W. Messmore, J. F. Hulvat, E. D. Sone, and S. I. Stupp, “Synthesis, self-assembly, and characterization of supramolecular polymers from electroactive dendron rodcoil molecules,” *J. Am. Chem. Soc.*, vol. 126, no. 44, pp. 14452–14458, 2004.
- [114] C. García Núñez, F. Liu, W. T. Navaraj, A. Christou, D. Shakthivel, and R. Dahiya, “Heterogeneous integration of contact-printed semiconductor nanowires for high-performance devices on large areas,” *Microsystems Nanoeng.*, vol. 4, no. 1, 2018.
- [115] N. Lu, C. Lu, S. Yang, and J. A. Rogers, “Highly sensitive skin-mountable strain gauges based entirely on elastomers,” *Adv. Funct. Mater.*, vol. 22, no. 19, pp. 4044–4050, 2012.
- [116] Y. Cai *et al.*, “Stretchable Ti₃C₂T_x MXene/Carbon Nanotube Composite Based Strain Sensor with Ultrahigh Sensitivity and Tunable Sensing Range,” *ACS Nano*, vol. 12, no. 1, pp. 56–62, 2018.
- [117] N. M. Sangeetha, N. Decorde, B. Viallet, G. Viau, and L. Ressier, “Nanoparticle-based strain gauges fabricated by convective self assembly: Strain sensitivity and hysteresis with respect to nanoparticle sizes,” *J. Phys. Chem. C*, vol. 117, no. 4, pp. 1935–1940, 2013.
- [118] J. Zhao *et al.*, “Ultra-sensitive strain sensors based on piezoresistive nanographene films,” *Appl. Phys. Lett.*, vol. 101, no. 6, 2012.
- [119] K. Ke, P. Pötschke, N. Wiegand, B. Krause, and B. Voit, “Tuning the Network Structure in Poly(vinylidene fluoride)/Carbon Nanotube Nanocomposites Using Carbon Black: Toward Improvements of Conductivity and Piezoresistive Sensitivity,” *ACS Appl. Mater. Interfaces*, vol. 8, no. 22, pp. 14190–14199, 2016.

- [120] D. Kang *et al.*, “Ultrasensitive mechanical crack-based sensor inspired by the spider sensory system,” *Nature*, vol. 516, no. 7530, pp. 222–226, 2014.
- [121] J. Zhou, X. Xu, Y. Xin, and G. Lubineau, “Coaxial Thermoplastic Elastomer-Wrapped Carbon Nanotube Fibers for Deformable and Wearable Strain Sensors,” *Adv. Funct. Mater.*, vol. 28, no. 16, pp. 1–8, 2018.
- [122] S. Harada, W. Honda, T. Arie, S. Akita, and K. Takei, “Fully printed, highly sensitive multifunctional artificial electronic whisker arrays integrated with strain and temperature sensors,” *ACS Nano*, vol. 8, no. 4, pp. 3921–3927, 2014.
- [123] Q. Hua *et al.*, “Bioinspired Electronic Whisker Arrays by Pencil-Drawn Paper for Adaptive Tactile Sensing,” *Adv. Electron. Mater.*, vol. 2, no. 7, pp. 1–5, 2016.
- [124] T. Kim, J. Park, J. Sohn, D. Cho, and S. Jeon, “Bioinspired, Highly Stretchable, and Conductive Dry Adhesives Based on 1D-2D Hybrid Carbon Nanocomposites for All-in-One ECG Electrodes,” *ACS Nano*, vol. 10, no. 4, pp. 4770–4778, 2016.
- [125] L. Duan, D. R. D’hooge, L. Cardon, R. D. Dagmar, and L. Cardon, “Recent progress on flexible and stretchable piezoresistive strain sensors: from design to application,” *Prog. Mater. Sci.*, vol. 114, p. 100617, Oct. 2019.
- [126] H. Montazerian, A. Rashidi, A. Dalili, H. Najjaran, A. S. Milani, and M. Hoorfar, “Graphene-Coated Spandex Sensors Embedded into Silicone Sheath for Composites Health Monitoring and Wearable Applications,” *Small*, vol. 15, no. 17, pp. 1–12, 2019.
- [127] Y. F. Yang, L. Q. Tao, Y. Pang, and H. Tian, “An ultrasensitive strain sensor with a wide strain range based on graphene armour scales,” *Nanoscale*, vol. 10, no. 24, pp. 11524–11530, 2018.
- [128] S. Lu, J. Ma, K. Ma, X. Wang, and S. Wang, “Highly sensitive graphene platelets and multi-walled carbon nanotube-based flexible strain sensor for monitoring human joint bending,” *Appl. Phys. A Mater. Sci. Process.*, vol. 125, no. 7, pp. 1–11, 2019.
- [129] S. H. Min, A. M. Asrulnizam, M. Atsunori, and M. Mariatti, “Properties of

- stretchable and flexible strain sensor based on Silver/PDMS nanocomposites,” *Mater. Today Proc.*, vol. 17, pp. 616–622, 2019.
- [130] S. Seyedin, S. Uzun, A. Levitt, B. Anasori, and G. Dion, “MXene Composite and Coaxial Fibers with High Stretchability and Conductivity for Wearable Strain Sensing Textiles,” *Adv. Funct. Mater.*, vol. 1910504, pp. 1–11, 2020.
- [131] J. Herrmann, K. H. Müller, T. Reda, G. R. Baxter, B. Raguse, and G. J. J. B. De Groot, “Nanoparticle films as sensitive strain gauges,” *Appl. Phys. Lett.*, vol. 91, no. 18, pp. 1–4, 2007.
- [132] P. J. Taroni, G. Santagiuliana, K. Wan, P. Calado, and M. Qiu, “Toward Stretchable Self-Powered Sensors Based on the Thermoelectric Response of PEDOT:PSS/Polyurethane Blends,” *Adv. Funct. Mater.*, vol. 28, no. 15, pp. 1–7, 2018.
- [133] X. Li, R. Zhang, W. Yu, K. Wang, and J. Wei, “Stretchable and highly sensitive graphene-on-polymer strain sensors,” *Sci. Rep.*, vol. 2, pp. 1–6, 2012.
- [134] Y. R. Jeong, H. Park, S. W. Jin, S. Y. Hong, S. S. Lee, and J. S. Ha, “Highly Stretchable and Sensitive Strain Sensors Using Fragmentized Graphene Foam,” *Adv. Funct. Mater.*, vol. 25, no. 27, pp. 4228–4236, 2015.
- [135] R. Rahimi, M. Ochoa, W. Yu, and B. Ziaie, “Highly stretchable and sensitive unidirectional strain sensor via laser carbonization,” *ACS Appl. Mater. Interfaces*, vol. 7, no. 8, pp. 4463–4470, 2015.
- [136] Z. Z. Wang, L. Zhang, J. Liu, and C. Li, “Highly Stretchable, Sensitive, and Transparent Strain Sensors with a Controllable In-Plane Mesh Structure,” *ACS Appl. Mater. Interfaces*, vol. 11, no. 5, pp. 5316–5324, 2019.
- [137] Z. Su, H. Chen, Y. Song, X. Cheng, and X. Chen, “Microsphere-Assisted Robust Epidermal Strain Gauge for Static and Dynamic Gesture Recognition,” *Small*, vol. 13, no. 47, pp. 1–9, 2017.
- [138] A. Chhetry, M. Sharifuzzaman, H. Yoon, S. Sharma, X. Xuan, and J. Y. Park, “MoS₂-Decorated Laser-Induced Graphene for a Highly Sensitive, Hysteresis-free,

- and Reliable Piezoresistive Strain Sensor,” *ACS Appl. Mater. Interfaces*, vol. 11, pp. 22531–22542, 2019.
- [139] S. H. Bae, Y. Lee, B. K. Sharma, H. J. Lee, J. H. Kim, and J. H. Ahn, “Graphene-based transparent strain sensor,” *Carbon N. Y.*, vol. 51, no. 1, pp. 236–242, 2013.
- [140] Z. Song, W. Li, Y. Bao, and F. Han, “Breathable and Skin-Mountable Strain Sensor with Tunable Stretchability, Sensitivity, and Linearity via Surface Strain Delocalization for Versatile Skin Activities’ Recognition,” *ACS Appl. Mater. Interfaces*, vol. 10, no. 49, pp. 42826–42836, 2018.
- [141] H. Liao, X. Guo, P. Wan, and G. Yu, “Conductive MXene Nanocomposite Organohydrogel for Flexible, Healable, Low-Temperature Tolerant Strain Sensors,” *Adv. Funct. Mater.*, vol. 29, no. 39, pp. 1–9, 2019.
- [142] Y. Zheng, Y. Li, Z. Li, Y. Wang, and K. Dai, “The effect of filler dimensionality on the electromechanical performance of polydimethylsiloxane based conductive nanocomposites for flexible strain sensors,” *Compos. Sci. Technol.*, vol. 139, pp. 64–73, 2017.
- [143] S. Yang, C. Li, T. Cong, and Y. Zhao, “Sensitivity-Tunable Strain Sensors Based on Carbon Nanotube@Carbon Nanocoil Hybrid Networks,” *ACS Appl. Mater. Interfaces*, vol. 11, no. 41, pp. 38160–38168, 2019.
- [144] G. Cai, J. Wang, K. Qian, J. Chen, S. Li, and P. S. Lee, “Extremely Stretchable Strain Sensors Based on Conductive Self-Healing Dynamic Cross-Links Hydrogels for Human-Motion Detection,” *Adv. Sci.*, vol. 4, no. 2, 2017.
- [145] A. Bessonov, M. Kirikova, S. Haque, I. Gartsev, and M. J. A. Bailey, “Highly reproducible printable graphite strain gauges for flexible devices,” *Sensors Actuators, A Phys.*, vol. 206, pp. 75–80, 2014.
- [146] M. Segev-Bar, A. Landman, M. Nir-Shapira, G. Shuster, and H. Haick, “Tunable touch sensor and combined sensing platform: Toward nanoparticle-based electronic skin,” *ACS Appl. Mater. Interfaces*, vol. 5, no. 12, pp. 5531–5541, 2013.
- [147] N. D. Madsen and J. Kjelstrup-Hansen, “Three-point bending setup for

- piezoresistive gauge factor measurement of thin-film samples at high temperatures,” *Rev. Sci. Instrum.*, vol. 88, no. 1, 2017.
- [148] C. Farcau *et al.*, “Monolayered wires of gold colloidal nanoparticles for high-sensitivity strain sensing,” *J. Phys. Chem. C*, vol. 115, no. 30, pp. 14494–14499, 2011.
- [149] S. Takamatsu, T. Takahata, M. Muraki, E. Iwase, K. Matsumoto, and I. Shimoyama, “Transparent conductive-polymer strain sensors for touch input sheets of flexible displays,” *J. Micromechanics Microengineering*, vol. 20, no. 7, 2010.
- [150] E. Puyoo, S. Brottet, R. Rafael, and C. Malhaire, “Ultrahigh Sensitivity to Strain of Cracked Thin Films Based on Metallic Nanoparticles in a Dielectric Matrix,” *IEEE Sensors Lett.*, vol. 2, no. 3, pp. 1–4, 2018.
- [151] Z. Liu, D. Qi, P. Guo, Y. Liu, and B. Zhu, “Thickness-Gradient Films for High Gauge Factor Stretchable Strain Sensors,” *Adv. Mater.*, vol. 27, no. 40, pp. 6230–6237, 2015.
- [152] M. T. Rahman, R. Moser, H. M. Zbib, C. V. Ramana, and R. Panat, “3D printed high performance strain sensors for high temperature applications,” *J. Appl. Phys.*, vol. 123, no. 2, 2018.
- [153] B. Yin, X. Liu, H. Gao, T. Fu, and J. Yao, “Bioinspired and bristled microparticles for ultrasensitive pressure and strain sensors,” *Nat. Commun.*, vol. 9, no. 1, pp. 1–8, 2018.
- [154] K. Huang, S. Dong, J. Yang, J. Yan, Y. Xue, and X. You, “Three-dimensional printing of a tunable graphene-based elastomer for strain sensors with ultrahigh sensitivity,” *Carbon N. Y.*, vol. 143, pp. 63–72, 2019.
- [155] D. H. Lee *et al.*, “Highly sensitive and flexible strain sensors based on patterned ITO nanoparticle channels,” *Nanotechnology*, vol. 28, no. 49, 2017.
- [156] W. S. Lee, S. W. Lee, H. Joh, M. Seong, and H. Kim, “Designing Metallic and Insulating Nanocrystal Heterostructures to Fabricate Highly Sensitive and Solution

- Processed Strain Gauges for Wearable Sensors,” *Small*, vol. 13, no. 47. 2017.
- [157] D. H. Ho, S. Cheon, P. Hong, J. H. Park, and J. W. Suk, “Multifunctional Smart Textronics with Blow-Spun Nonwoven Fabrics,” *Adv. Funct. Mater.*, vol. 29, no. 24, pp. 1–9, 2019.
- [158] E. Puyoo, C. Malhaire, D. Thomas, R. Rafaël, and M. R’Mili, “Metallic nanoparticle-based strain sensors elaborated by atomic layer deposition,” *Appl. Phys. Lett.*, vol. 110, no. 12, pp. 2–7, 2017.
- [159] H. P. Phan *et al.*, “Piezoresistive effect of p-type silicon nanowires fabricated by a top-down process using FIB implantation and wet etching,” *RSC Adv.*, vol. 5, no. 100, pp. 82121–82126, 2015.
- [160] J. Zhao *et al.*, “Tunable piezoresistivity of nanographene films for strain sensing,” *ACS Nano*, vol. 9, no. 2, pp. 1622–1629, 2015.
- [161] I. Chuang, A. Michael, A. Soeriyadi, and C. Y. Kwok, “Aluminum Induced Crystallization of In-Situ Phosphorus Doped E-Beam Evaporated Silicon Films for High Gauge Factor Piezo-Resistors,” *IEEE Electron Device Lett.*, vol. 39, no. 6, pp. 889–892, 2018.
- [162] J. L. Tanner, D. Mousadakos, K. Giannakopoulos, E. Skotadis, and D. Tsoukalas, “High strain sensitivity controlled by the surface density of platinum nanoparticles,” *Nanotechnology*, vol. 23, no. 28, 2012.
- [163] L. M. Zhang *et al.*, “Self-Healing, Adhesive, and Highly Stretchable Ionogel as a Strain Sensor for Extremely Large Deformation,” *Small*, vol. 15, no. 21, pp. 1–8, 2019.
- [164] J. Guo, M. Niu, and C. Yang, “Highly flexible and stretchable optical strain sensing for human motion detection,” *Optica*, vol. 4, no. 10, p. 1285, 2017.
- [165] D. Cho *et al.*, “Three-Dimensional Continuous Conductive Nanostructure for Highly Sensitive and Stretchable Strain Sensor,” *ACS Appl. Mater. Interfaces*, vol. 9, no. 20, pp. 17369–17378, 2017.

- [166] Y. Chen, L. Wang, Z. Wu, J. Luo, and B. Li, "Super-hydrophobic, durable and cost-effective carbon black/rubber composites for high performance strain sensors," *Compos. Part B Eng.*, vol. 176, no. June, p. 107358, 2019.
- [167] K. H. Kim, S. K. Hong, S. H. Ha, L. Li, H. W. Lee, and J. M. Kim, "Enhancement of linearity range of stretchable ultrasensitive metal crack strain sensor: Via superaligned carbon nanotube-based strain engineering," *Mater. Horizons*, vol. 7, no. 10, pp. 2662–2672, 2020.
- [168] Y. Zheng *et al.*, "A highly stretchable and stable strain sensor based on hybrid carbon nanofillers/polydimethylsiloxane conductive composites for large human motions monitoring," *Compos. Sci. Technol.*, vol. 156, pp. 276–286, 2018.
- [169] S. Seyedin, P. Zhang, M. Naebe, and S. Qin, "Textile strain sensors: A review of the fabrication technologies, performance evaluation and applications," *Mater. Horizons*, vol. 6, no. 2, pp. 219–249, 2019.
- [170] H. Souri and D. Bhattacharyya, "Highly sensitive, stretchable and wearable strain sensors using fragmented conductive cotton fabric," *J. Mater. Chem. C*, vol. 6, no. 39, pp. 10524–10531, 2018.
- [171] H. Zhao *et al.*, "Carbon nanotube yarn strain sensors," *Nanotechnology*, vol. 21, no. 30, 2010.
- [172] E. T. Thostenson and T. W. Chou, "Real-time in situ sensing of damage evolution in advanced fiber composites using carbon nanotube networks," *Nanotechnology*, vol. 19, no. 21, 2008.
- [173] A. Leber, B. Cholst, J. Sandt, N. Vogel, and M. Kolle, "Stretchable Thermoplastic Elastomer Optical Fibers for Sensing of Extreme Deformations," *Adv. Funct. Mater.*, vol. 29, no. 5, pp. 1–8, 2019.
- [174] X. Fu, M. Ramos, A. M. Al-Jumaily, A. Meshkinzar, and X. Huang, "Stretchable strain sensor facilely fabricated based on multi-wall carbon nanotube composites with excellent performance," *J. Mater. Sci.*, vol. 54, no. 3, pp. 2170–2180, 2019.
- [175] X. Shi, H. Wang, X. Xie, and Q. Xue, "Bioinspired Ultrasensitive and Stretchable

- MXene-Based Strain Sensor via Nacre-Mimetic Microscale ‘brick-and-Mortar’ Architecture,” *ACS Nano*, vol. 13, no. 1, pp. 649–659, 2019.
- [176] D. Chen and Q. Pei, “Electronic Muscles and Skins: A Review of Soft Sensors and Actuators,” *Chem. Rev.*, vol. 117, no. 17, pp. 11239–11268, 2017.
- [177] Q. Zheng *et al.*, “Sliced graphene foam films for dual-functional wearable strain sensors and switches,” *Nanoscale Horizons*, vol. 3, no. 1, pp. 35–44, 2018.
- [178] Y. Wang, J. Hao, Z. Huang, G. Zheng, and K. Dai, “Flexible electrically resistive-type strain sensors based on reduced graphene oxide-decorated electrospun polymer fibrous mats for human motion monitoring,” *Carbon N. Y.*, vol. 126, pp. 360–371, 2018.
- [179] J. Zhou, H. Yu, X. Xu, F. Han, and G. Lubineau, “Ultrasensitive, Stretchable Strain Sensors Based on Fragmented Carbon Nanotube Papers,” *ACS Appl. Mater. Interfaces*, vol. 9, no. 5, pp. 4835–4842, 2017.
- [180] J. Ren, X. Du, W. Zhang, and M. Xu, “From wheat bran derived carbonaceous materials to a highly stretchable and durable strain sensor,” *RSC Adv.*, vol. 7, no. 37, pp. 22619–22626, 2017.
- [181] Y. Zhou, P. Zhan, M. Ren, and G. Zheng, “Significant stretchability enhancement of a crack-based strain sensor combined with high sensitivity and superior durability for motion monitoring,” *ACS Appl. Mater. Interfaces*, vol. 11, no. 7, pp. 7405–7414, 2019.
- [182] Z. Wang, X. Guan, H. Huang, H. Wang, W. Lin, and Z. Peng, “Full 3D Printing of Stretchable Piezoresistive Sensor with Hierarchical Porosity and Multimodulus Architecture,” *Adv. Funct. Mater.*, vol. 29, no. 11, pp. 1–8, 2019.
- [183] H. Devaraj, T. Giffney, A. Petit, M. Assadian, and K. Aw, “The development of highly flexible stretch sensors for a Robotic Hand,” *Robotics*, vol. 7, no. 3, pp. 1–13, 2018.
- [184] Y. Xin, J. Zhou, R. Tao, X. Xu, and G. Lubineau, “Making a Bilateral Compression/Tension Sensor by Pre-Stretching Open-Crack Networks in Carbon

- Nanotube Papers,” *ACS Appl. Mater. Interfaces*, vol. 10, no. 39, pp. 33507–33515, 2018.
- [185] E. R. Cholleti, J. Stringer, M. Assadian, V. Battmann, C. Bowen, and K. Aw, “Highly stretchable capacitive sensor with printed carbon black electrodes on barium titanate elastomer composite,” *Sensors (Switzerland)*, vol. 19, no. 1, pp. 1–18, 2019.
- [186] M. Amjadi, K. U. Kyung, I. Park, and M. Sitti, “Stretchable, Skin-Mountable, and Wearable Strain Sensors and Their Potential Applications: A Review,” *Adv. Funct. Mater.*, vol. 26, no. 11, pp. 1678–1698, 2016.
- [187] W. W. Jheng, Y. S. Su, Y. L. Hsieh, Y. J. Lin, and S. Der Tzeng, “Gold Nanoparticle Thin Film-Based Strain Sensors for Monitoring Human Pulse,” *ACS Appl. Nano Mater.*, vol. 4, no. 2, pp. 1712–1718, 2021.
- [188] H. Joh, S. W. Lee, M. Seong, W. S. Lee, and S. J. Oh, “Engineering the Charge Transport of Ag Nanocrystals for Highly Accurate, Wearable Temperature Sensors through All-Solution Processes,” *Small*, vol. 13, no. 24, pp. 1–11, 2017.
- [189] M. A. Hossain, S. Jeon, J. Ahn, H. Joh, J. Bang, and S. J. Oh, “Control of tunneling gap between nanocrystals by introduction of solution processed interfacial layers for wearable sensor applications,” *J. Ind. Eng. Chem.*, vol. 73, no. 2018, pp. 214–220, 2019.
- [190] A. Qiu, P. Li, Z. Yang, Y. Yao, I. Lee, and J. Ma, “A Path Beyond Metal and Silicon: Polymer/Nanomaterial Composites for Stretchable Strain Sensors,” *Adv. Funct. Mater.*, vol. 29, no. 17, pp. 1–21, 2019.

Chapter 2: Fabrication of flexible strain sensors

Introduction

In this chapter, we will describe in a first part the fabrication processes published in literature for the realization of flexible strain sensors. A second part will be devoted to the fabrication process that has been developed using 1D nanostructures with grafted gold nanoparticles as sensing material and dielectrophoresis as the deposition technique.

As shown in Figure 2.1, the basic components of a strain sensor consist of a sensing element (active materials), conductive electrodes and a mechanical substrate. Each component needs to be carefully considered to develop a sensor that possesses excellent sensing capabilities such as high sensitivity and good stability. The different components require very specific performances [1][2]. For instance, the sensing component demands a high sensitivity to transform an applied pressure stimulus into a high resistance change. For the conductive component, a very low resistivity is required with a high electrical stability under high strains. The mechanical substrate is required to be flexible and/or stretchable depending upon the aimed application of the resulting sensor device [3].

The active material is the sensing component of the device, which senses the external pressure stimulus. Active materials are embedded into or placed on the substrate [4][5][6]. An ideal active material should be chemically stable, compatible with large area processing techniques and must exhibit a high mechanical compliance. Conducting nanomaterials such as metallic nanoparticles and metallic or semiconducting nanowires are commonly used as sensing nanomaterials [7][8]. Carbon nanomaterials such as carbon black, carbon nanotubes and graphene flakes have been of interest because of their exceptional chemical stability, biocompatibility and good electrical and mechanical properties [9][10][11]. They are also easily compatible with high-throughput solution processing techniques on large areas.

Commonly used solution deposition techniques are spin-coating, dip-coating, vacuum filtration, inkjet printing and spray coating. Other techniques have also been developed to attain large-scale alignment such as contact and roll printing, Langmuir-Blodgett deposition as well as electric-field assisted techniques [12][13].

Electrodes ideally should possess excellent stability and maintain high conductivity under large strains. Thin-film metal electrodes are usually suitable for

flexible devices, for example Au on PI substrate, Ag or Cu on flexible substrate [14][15][16]. Their shape on the sensing area is of critical importance. The most used design patterns are interdigitated electrodes with small gaps.

The choice of mechanical **substrate** is more important in stretchable devices for strain above 10% than for flexible ones, usually designed for strain under 1%. Most common stretchable substrate material include PDMS, hydrogels, elastomers, etc. For flexible sensors, materials like Kapton, PET, PVC can be advantageously used.

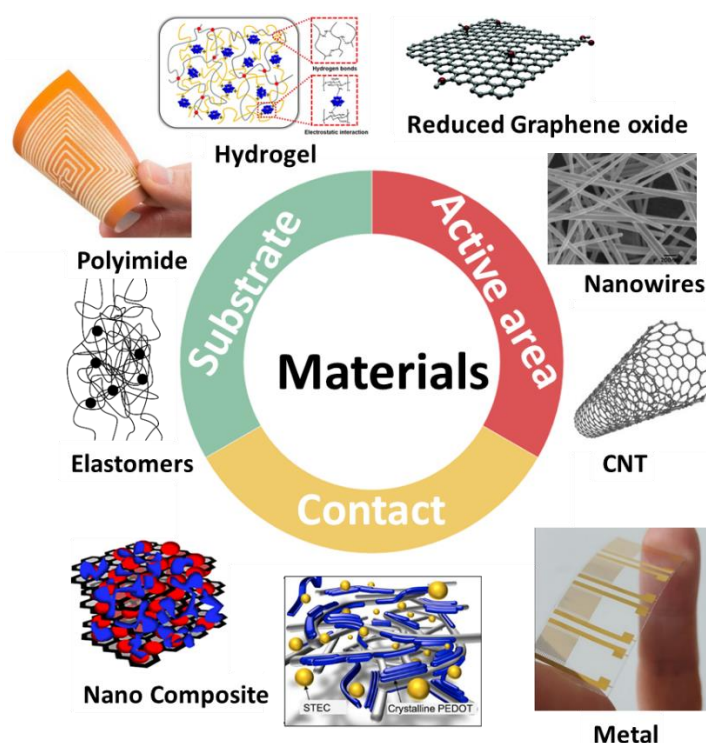


Figure 2.1 : Material overview for flexible and stretchable strain sensors.

In the following paragraphs, we will describe the different techniques used for depositing nanoparticles and 1D nanostructures on a substrate to fabricate strain sensors.

2.1 Techniques for nanoparticles deposition

Nanostructures range between 1 and 100 nm and can be organic, inorganic or composite. Nanomaterials can be classified depending on their dimensions into one of four categories: zero-dimensional (**0D**) nanoparticles and quantum dots; **1D** nanowires, nanotubes, and nanobelts; **2D** nanoflakes and nanosheets; and **3D** porous

nano-networks as shown in Figure 2.2. They can be spherical, conical, spiral, cylindrical, tubular, flat, hollow, or irregular in shape.


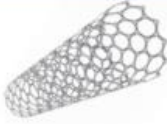

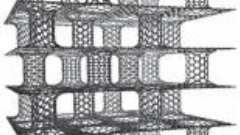
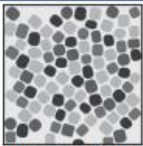
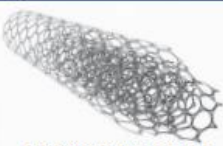
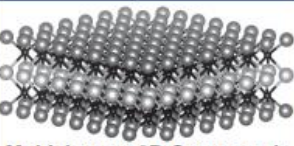
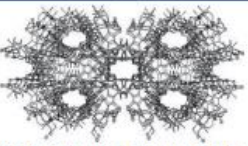
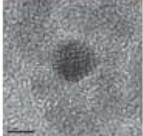


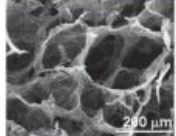
0D	1D	2D	3D
 Carbon Onion	 Single Wall Carbon Nanotube	 Graphene	 Pillared Graphene
 Nanoparticles	 Multiwall Nanotube	 Multielement 2D Compounds	 Metal-Organic Frameworks
 Quantum Dots	 Nanowires	 Nanoflakes	 Aerogels
Advantages			
Small in all dimensions Surfaces on all sites are accessible to electrolytes No bulk solid-state diffusion Can be integrated into multiple systems Can be used in stable inks for printing	Mechanical reliability Possibility to integrate with wearable devices Porous flexible freestanding films	Open 2D channels for ion transport; all surface is accessible enabling fast charge storage Compatible with flexible devices Small nanoflakes can be used in inks for printing	Can be used to create thick electrodes with large areal and volumetric storage properties
Limitations			
Agglomeration Do not densely and form only low density non-uniform structures Numerous points of contact lead to high resistance Poor chemical stability	Low packing density; cannot exhibit high volumetric performance Low yield and high cost of synthesis Diffusion pathways can be relatively long	Re-stacking Low out-of-plane electronic and ionic conductivity High cost of synthesis	Design Stability Manufacturing

Figure 2.2 : Advantages and limitations of geometrically different nanomaterials [17].

High surface area to volume ratios and facile surface functionalization, make nanomaterials highly sensitive to changes in surface chemistry and permit nano-sensors to achieve extremely low detection limits. The ability to control NPs type, to vary the NP's size, to cap the NPs proves to be very useful. Moreover, NPs can be prepared in films of controllable porous properties. This allows a control over inter-particle distance. Their electromagnetic properties can be tuned readily by adjusting the NP size, shape, and separation. The presumed ability of NPs allow easier, faster,

more cost – effective fabrication of flexible sensors compared to those currently in use, which mostly rely on complicated, multistep processes [18].

Another important parameter concerns the ligands with which tunneling conduction can take place in the nanoparticle network [19][20]. They are the key feature to obtain highly sensitive strain sensors. The type and the length of the ligands play a critical role to enhance the electromechanical properties of nanoparticles thin films [21][22][23].

However, the stability of the nanoparticles can be an issue as nanoparticles have a tendency to lower their very high surface energy, which originates from their high surface-to-bulk ratio. Bare nanoparticles tend to stabilize themselves by lowering the surface area through coagulation and agglomeration.

Coatings and thin films made from nanoparticles are used in various applications including displays, sensors, medical devices, energy storages and energy harvesting. There are multiple different coating methods available to deposit nanoparticles. The methods differ by their ability to control particle packing density and layer thickness, ability to use different particles and the complexity of the method and the instrumentation needed. In general, experimental parameters such as choice of solvent, particle concentration, and temperature will affect the deposition process, and must be tuned to yield a film with the desired thickness and morphology.

2.1.1 Drop cast method

As a simple low-cost method, drop casting is one of the most used techniques for depositing uniform good quality thin layers of almost any type of ‘liquid dispersed nanoparticles’ over a small area ($\sim 1 \text{ cm}^2$) on a substrate. It is capable of producing uniform good quality films over small areas and for a variety of materials and applications. It relies on the release of droplets with controlled size and momentum, which spread and wet the surface upon impact. Drop casting is better controllable. However, its applications are limited to films and coatings over a small area.

Fabrication. The fabrication process in drop casting starts by dispensing a solution containing the desired material (nanoparticles suspensions), onto a substrate. The droplets are left on the substrate for a sufficient amount of time to allow evaporation of solvent, under controlled conditions. The process leaves the desired solute on the substrate. A thin film is formed, which adheres to the substrate by Van

der Waal forces between the substrate and nano-particles of the film, Figure 2.3. Film thickness depends on the particle concentration in the liquid and the volume of the liquid dispersed; these parameters can be controlled easily to achieve desired number of (mono) layers on the substrate. Other variables that can determine the quality of the film structure include wettability of the solvent, evaporation rate and capillary forces associated with the drying process, etc. It is preferred to use volatile solvents, as these wet the substrate, and have negligible thin film instability (de-wetting) associated problems. Water, a common solvent, which has low vapor pressure and large surface tension, should be avoided as a solvent for drop casting.

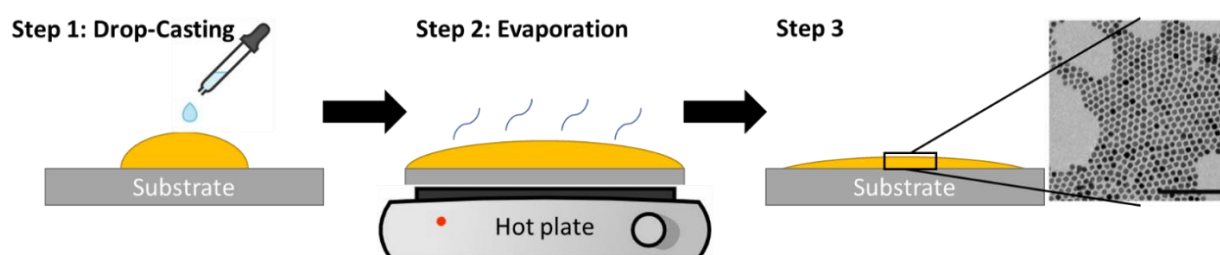


Figure 2.3: Schematic diagram of drop cast method. Step 1: A drop is poured onto a substrate; Step 2: the solution spreads spontaneously on the substrate and dries naturally or by using elevated temperature; Step 3: Resultant thin film. SEM image shows gold nanoparticle assemblies formed. reprinted from Ref.[24]. The scale bar is 100 nm.

Advantage. Drop casting is a low-cost method for preliminary level of testing, where homogeneity is not a very stringent requirement [25]. Desired thin films can be created by drop casting a mixture of materials, in a suitable solvent on the target substrate.

Disadvantage. However, the homogeneity of films obtained with drop casting technique is limited. Potential problem in film formation via drop casting is the ‘coffee ring effect’. It arises when suspension of particles in a liquid (e.g., coffee) is allowed to dry on a flat surface. It produces inhomogeneous deposition, as the solute tends to accumulate on the boundaries of the drop. The coffee ring effect is also observed due to the differential evaporation rates of the solution with dispersed particles density. The ring formation for a solute can be avoided by selecting appropriate combination of solvents [26], at temperature and humidity conditions leading to uniform film deposition. **An alternative method to avoid the coffee ring effect is the sweeping**

method. In Figure 2.4, a comparison between drop-casting and sweeping method displays uniformity of particle trapping achieved by the two methods; sweeping method shows superior trapping. Figure 2.4(c, g) and (d, h) shows the trapping of gold nanoparticles between electrode gap of thickness 130 nm and 150 nm respectively.

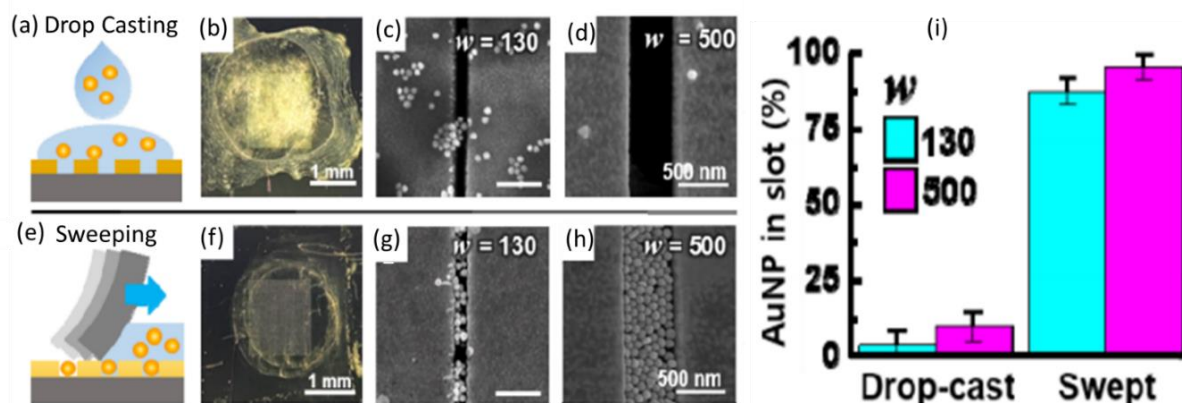


Figure 2.4: Schematic illustration of drop casting: ((a) - top line) vs the sweeping ((e) bottom line) techniques, (b) Microscopic image of AuNP after five-drop cast cycles. Corresponding SEM images of nano gap at (c) 130 nm and (d) 500 nm (f) Microscopic image of AuNP drop casted, followed by sweeping procedures. Corresponding SEM images of nano gap at (g) 130 nm (h) 500 nm, (i) Calculated AuNP ratio is nano gap by two techniques [27].

Another common problem associated with thin film deposition on a substrate is unwanted cracking of the films. Cracking occurs when a liquid film covering a solid substrate begins to dry. The difference in chemical composition (surface energies) between the substrate and drying film generates mechanical stress originating from the push and pull forces on the film and solid interface [28].

The maximum crack-free film thickness and area depend on the particle size, thickness of the deposition, film rigidity, nature of materials, and drying time. The stress at cracking varies inversely with the square root of the film thickness. Thinner films are capable of sustaining larger tensile (stretching) stresses before cracking [29].

2.1.2 Inkjet Printing

Inkjet printing is a direct printing method that makes use of liquid phase materials. Tiny droplets are jetted through a small orifice over a designated area with

high accuracy as shown in Figure 2.5(a). In conventional inkjet printing process, a sequence of sessile droplets is directly printed over a specific location on the substrates as can be seen in Figure 2.5(b, c). The droplets generated are governed by various parameters such as viscosity, surface tension and density of the particles in the printing ink. The resultant depositions show the signs of unwanted coffee-ring effect, Figure 2.6(a). It is because of a high solvent evaporation rate at the edges of the droplets after being printed.

Fabrication. Inkjet printing depends on the generation of a sequence of droplets on a specific location on the substrate. The liquid phase of a solute e.g., nanoparticles dissolved in solvents is dropped with high resolution without any extra wastage. The ink jetting (dropping) can be realized either by continuous-inkjet (CIJ) or by drop-on-demand (DOD) inkjet methods. Usually, CIJ is not favored in printing for manufacturing processes. Because the solvent is driven off in the curing process, this technology is considered not suitable for the environment. The DOD inkjet printing process has five stages: drop ejection, drop flight, drop impact, drop spreading and drop solidification. The minimum feature size depends on placement accuracy and substrate-ink interactions. A better understanding of these five stages benefits in improving the quality and decreases the line width of printed topographies [30].

After the jetted colloidal droplet is placed on substrate, the final deposition morphologies are governed by factors such as temperature of the substrate, wettability, surface roughness, humidity, particle size and concentration, etc. These factors significantly impact the resolution and performance of the printed patterns [31]. Other physical processes and constrains involved in inkjet technique are for instance: (1) droplet formation, (2) ink specifications, (3) droplet-droplet and droplet-substrate interactions, (4) solvent drying mechanism, impacts the quality of inkjet printing process.

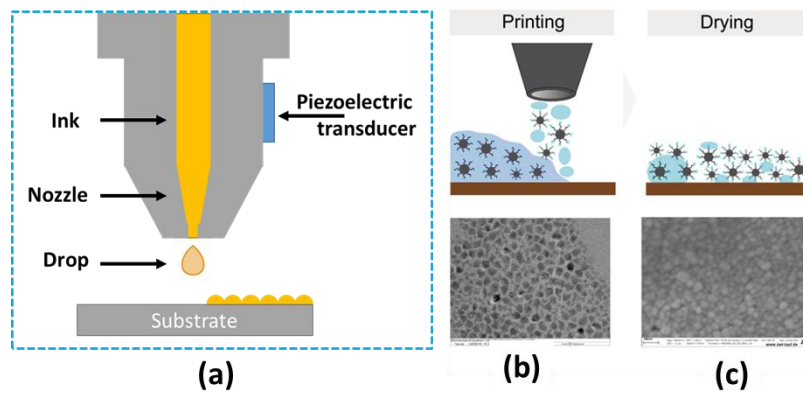


Figure 2.5: (a) Inkjet printing working principle (b) Processing steps for silver nanoparticle colloidal solutions (TEM image of nanoparticles on the carbon/copper grid). (c) SEM images: dried for 15 min. at 80 °C [32].

Advantage. In contrast to methods like photolithography, micro-contact printing, etc., inkjet printing is a low-cost technique, which makes it more attractive for printed electronics. It does not require mask; the material is directly deposited or dropped on the required area. It is a direct deposition tool. Inkjet printing is capable of printing with fine and smooth details. Ink-jet delivers a high-quality output. The technique offers a device manufacturing method with digital control on the printing process quality, via accurate deposition of ink on a predetermined position on the substrate. Moreover, precise control over the printing speed can be achieved. Various shapes and patterns can be printed and modified, by simply varying the drawings through CAD software of the printer system. Inkjet printing also allows multiple layer deposition for improving the functional outcomes of a device.

Disadvantage. One of the major limitations of inkjet-printing is the use of inks, which should obey strict rheological conditions with range of viscosity and surface tension. The print heads are prone to clogging and damage, and consequently being less durable. Limited concentration range of sensing material in an ink leads to multiple printing cycles to attain adequate packing density of the deposited material. Additional materials termed, as 'additives', are usually required to control the surface tension and viscosity. The stabilizing agents prevent agglomeration of nanoparticles that could adversely affect the sensing behavior of a printed device. To compete with other processes, higher printing speed is needed. Speed is improved by modifying drop frequency, number of nozzles, and material concentration in the ink and standoff distance. Ink bleeding is yet another problem associated with this method where ink is carried sideways producing blurring effect on some target substrates. [33]

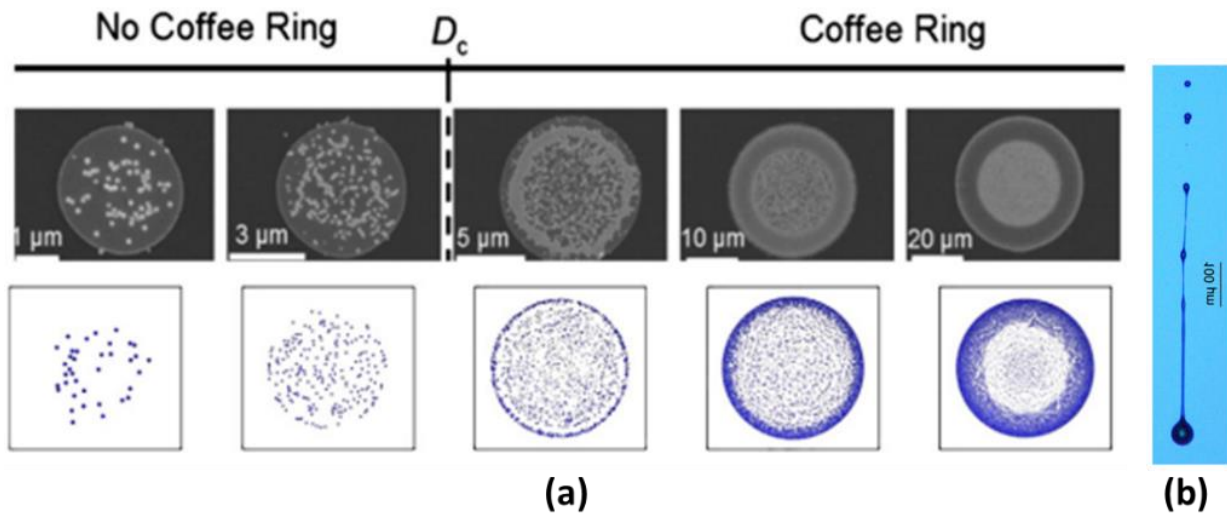


Figure 2.6 : (a) Coffee ring effect appears to be darker as the size of the drop increases. Smallest drop ($R = 1.5 \mu\text{m}$), medium sized drop ($R = 5 \mu\text{m}$), largest drop size ($R = 25 \mu\text{m}$). The critical diameter D_c for the transition between ring formation and no ring formation. [34] (b) Jet of ink emerging from a drop on-demand nozzle, along with unwanted secondary droplets called satellite drops. [35]

2.1.3 Spin Coating

On a laboratory scale, spin coating is the most used technique. To deposit thin films of functional materials on a substrate. It can be used with most classes of materials to grow uniform thin film. When a viscous solution of a material (particle form) in a solvent is spun on a smooth wafer, an even coating of the required the material film can be obtained. Centripetal force and surface tension of the liquid at high spin speeds, governs the quality of coating. Thickness of the spin-coated films after the solvent evaporation may range from a few nanometers to a few microns. The thickness of a spin-coated film is proportional to inverse of spin speed squared. However, it is mostly determined empirically, thickness also depends on evaporation rate of solvent and material concentration.

Fabrication. First step in spin coating is to cover the substrate with ink, Figure 2.7(a). Ink contains the desired material molecules dissolved in a solvent. As the substrate is rotated at high speed, it flings the majority of the ink off the substrate sides, Figure 2.7(b). Airflow then dries the solvent over the substrate. When the film dries fully, it leaves layer of desired material molecules on the surface, Figure 2.7(c). By

optimizing the solvent selection and its properties, the substrate, the temperature and the rotation speed, a fine control on film thickness and morphology can be realized. For the choice of solvents, liquids with low viscosity are preferred.

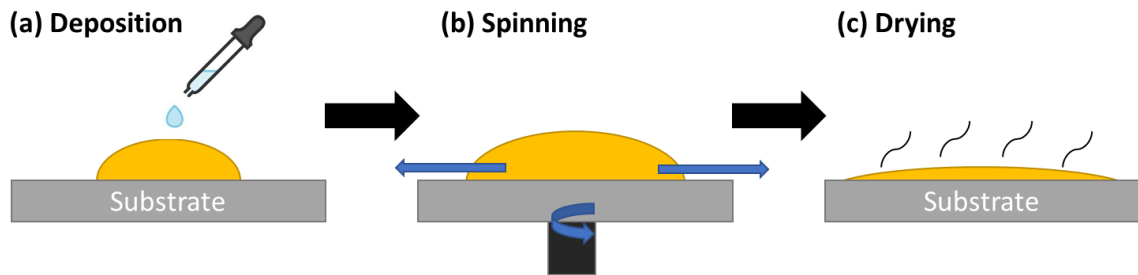


Figure 2.7: Schematic diagram of spin coating

Advantage. The main advantage of spin coating is its simplicity and relative ease of process set up. Resulting films are thin, uniform and reproducible. The process is mostly used for flat substrates. Because of the capability to have high spin speeds, the high airflow permits lower drying times. It results in high consistency at both macroscopic and nano-length scales. [36]

Disadvantage. One of the drawbacks of spin coating is that, it is inherently not a batch process. Multiple substrates cannot be processed simultaneously. The fast drying may lead to lower performance nanomaterials, which need longer time to self-assemble and/or crystallize. The actual material usage in a spin coating process is normally low (~ 10%), while the rest is simply flung from the sides. However, it is not usually an issue for research environments, but it is considered wasteful for in large-scale manufacturing [37].

2.1.4 Vacuum filtration

Filtration-assisted methods, including pressure, vacuum and evaporation-driven filtration. It is an approach employed to fabrication of membranes, especially freestanding membranes. It primarily has four steps: (i) dispersion of nanoparticles in a solution, (ii) vacuum filtering the nanoparticle suspension using filtration membrane; it forms a homogeneous film on the membrane, (iii) using a proper solvent to dissolving the filtration membrane, and (iv) moving the nanoparticle film onto a desired substrate. The resultant films are flexible and thus important for applications in flexible electronics and optoelectronics.

Fabrication. For vacuum filtration, the film forming material is uniformly dispersed in the solvent. Due to the fluxion function of the solvent molecules, the film material deposits uniformly on the substrate under appropriate vacuum filtration conditions. By controlling the volume of the filtered suspension, samples with various thickness of hybrid thin films can be prepared [38].

Figure 2.8 illustrates the process for fabricating thin film with tin nanoparticles. First the tin nanoparticles and conductive carbon suspension is placed in the funnel. When vacuum is applied, Figure 2.8(a), it causes the solvent to fall through the filter. It leaves behind only the trapped particles on top of the alumina filter. The resulting film on the alumina filter is placed in an aqueous solution of NaOH. The alumina filter dissolves in NaOH solution, leaving thin film on the surface. The NaOH solution is replaced by distilled water, Figure 2.8(b). Below this floating film, a copper foil is placed. By draining the distilled water, the copper foil is positioned below the floating electrode, Figure 2.8(c). The film undergoes pre-drying at 60°C followed by rinsing with water and drying again at 60°C. Finally, it is dried under vacuum at 120°C and then Ar purged.

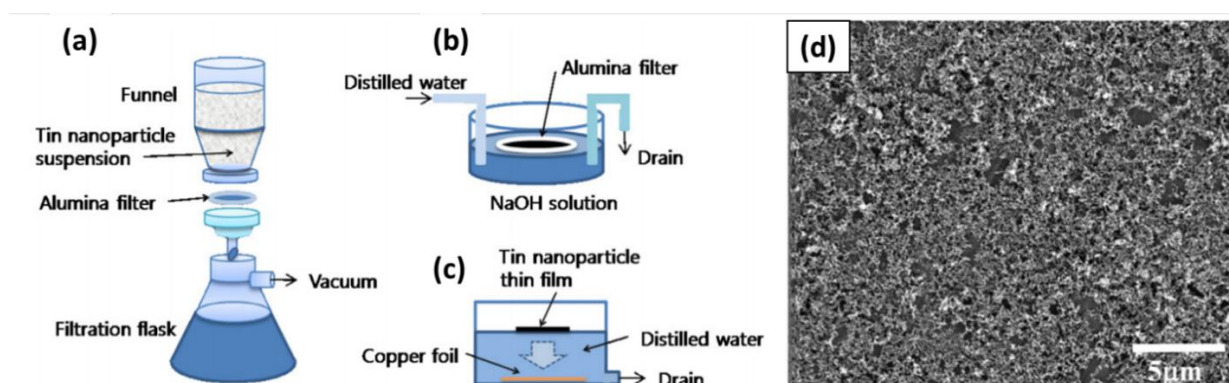


Figure 2.8 : (a-c) Schematic representation of the vacuum filtration procedure, (d) SEM image shows surface morphology of tin nanoparticle (having particle size ~50 nm) composite film prepared by vacuum filtration method [39].

Advantages. During the filtration process, the porosity of the filter membrane decreases gradually. This self-limiting process ensures a uniform film, which can be directly transferred to any substrate [40]. Vacuum filtration has the advantage that the thickness of the filtrated films can be simply controlled by the concentration and volume of the particles in the dispersion [41][42].

Disadvantages. Although it may have the advantage of simple operation, it is not easy to prepare a large-area membrane using vacuum filtration [43]. The technique can only produce randomly oriented nanoparticles. Drawbacks include limited film size of the filter. In addition, the necessity to transfer the film on substrate that is more suitable for certain specific applications.

2.2 Techniques to aligning 1D nanostructures

One-dimensional (1D) nanostructures, such as nanowires, nanofibers, nanorods, nanobelts and nanotubes, have attracted much attention in recent years. Many attempts made to align 1D nanostructures of numerous functional materials ranging from inorganic to organic types. 1D nanostructures possess specific properties because of their flexibility, high aspect ratio with anisotropic properties and electronic tunability. Perfectly aligned 1D nanostructures shows superior properties compared to its disordered counterpart. Providing promising applications in diverse fields. Well-aligned 1D nanostructure provides an effective electronic/ionic transport pathway.

1D materials have the capabilities to be the building blocks for nano-electro-mechanical devices with improved performances. Aligned nanostructures have a potential use in light-emitting diodes, solar cells, field-effect transistors, microcircuits and highly sensitive sensor and various other fields of nanotechnology. However, the main issue is to integrate these 1D blocks into functional devices.

The following section introduces a few alignment techniques for 1D nanostructures based on diverse approaches. Assembly strategies developed can be categorized as:

- 1) Directed growth method: starting from a pre-defined position, synthesizing and growing the 1D nanostructures/nanoobjects. This method controls both position and orientation of 1D-NS.

- 2) Directed assembly method: assembling already-made 1D nanostructures onto the desired substrate. Only orientation is controlled in directed assembly method. It is a low fabrication cost approach with pre-synthesized nanostructures. The latter process is a facile procedure. It provides better flexibility in choosing the substrates, building blocks and architecture. Thus, we mainly focus on the alignment of existing 1D-nanoobjects onto a substrate. This can be achieved using

various techniques like contact printing, convective flow, assembly assisted by magnetic field or electric field.

2.2.1 Contact printing

Contact printing technique is a method used for transferring various materials, such as polymers and nanomaterial, etc. to another surface. It allows the transfer in micrometer/nanometer sized patterns. This deposition method involves directional sliding of a growth substrate, consisting of nanomaterials, on top of a receiver substrate. During this process, nanomaterial is combed by sliding step, and are detached from the donor substrate as they are anchored by the van der Waals interactions with the surface of the receiver substrate; therefore, resulting in the direct transfer of aligned wires to the receiver substrate.

It leads to the detachment of oriented nanostructures from the growth surface towards the receiver substrate. The parameters need to be considered for an accurate transfer of nanomaterial ink are : the ink quality itself, surface modification of receiver substrate and the applied pressure during the contact printing process [44]. The density and alignment of transferred 1D nanostructure are affected by donor substrate area, speed and pressure applied.

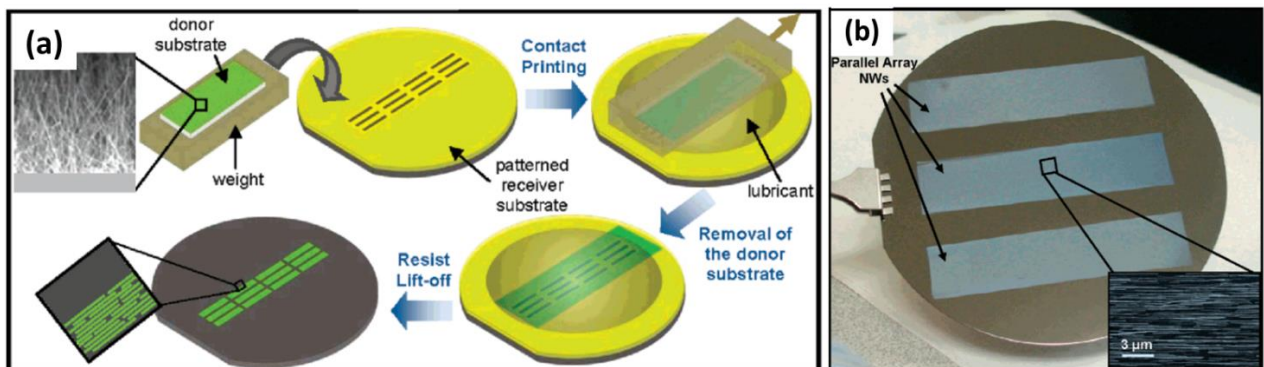


Figure 2.9: (a) Schematic of the process flow for Contact Printing. (b) SEM image of a wafer-scale nanowire printing. Large area and highly uniform parallel arrays of aligned NWs were assembled on a 4 in. Si/SiO₂ wafer by contact printing. [45]

Fabrication. Contact printing method involves directional sliding/rolling of a growth substrate (which can be flat or cylindrical) to a flat receiving substrate. Growth substrates consist of dense 1D nanostructures, Figure 2.9(a). These 1D NS/nanoobjects can be vertically grown on the substrate, by the chemical vapor deposition

(CVD). During the process of transfer of 1D-NW to receiver substrate, the NW are eventually detached from donor by the van der Waals interaction, Figure 2.9(a). An important aspect of this method is NW-NW friction during the process. It enhances the uncontrolled breakage and detachment of NW while hampering the alignment. Nonselective mechanical frictions can be lowered by using a lubricant. The use of lubricant serves as spacing between the two layers [45]. A well-controlled transfer is facilitated by the chemical binding interactions between the NW and the surface of the receiver substrate. To further enhance the NS density, one can consider complimentary surface functionalization of NW and receiver substrate. After the 1D-NW are printed, the patterned resist is removed by a standard lift-off process using acetone leaving behind the NW transferred on the substrate, Figure 2.9(b).

Advantage. The advantage of using contact printing includes:

- Ease and simplicity of creating patterns with micro-nano-scale topographies.
- Technique uses less energy
- Cleanroom is only required to make the master; this technique is able to operate without a constant use of cleanroom otherwise.
- An individual stamp can be used many times with slight degradation of performance. Multiple stamps can be produced from a single master.

Disadvantage. The contact-printing stamp can easily be deformed, producing printed structures that are unlike the original stamp structures. The change of the shape can occur during withdrawal from the master or during the substrate contacting procedure. The inking process is slow and adhesion of the ink to a hydrophobic surface could be another challenging step. The mobility of the ink is a problem, as it can cause lateral spreading to unwanted regions. Upon the transfer of the ink, spreading can influence the quality of desired pattern. During the transfer of nanostructures and annealing process, development of microscale cracks can be another critical issue.

In most experiments, poly(dimethylsiloxane) (PDMS) elastomer is used to perform the transfer from template to the substrate. The highly hydrophobic PDMS material limits the range of nanomaterial ink. However, hydrophobic nature can be changed by surface-treatment techniques [46].

2.2.2 Convective flow/Dip coating

Introduction. The dip coating technique is important within research and developments, for the fabrication of thin films. It is an effective and simple technique used across many different industries. The fundamentals of dip coating theory include the formation of wet film, thickness evolution and the drying dynamics. The major forces used for the dip coating process are force of inertia, viscous drag, gravitational force and surface tension.

Fabrication. Dip coating involves the deposition of a liquid film via the precise and controlled withdrawal of a substrate from a solution. This is typically done using an instrument known as a 'dip coater'. There are four different stages involved in the coating of thin films via dip coating - immersion, dwelling, withdrawal and drying, Figure 2.10(1-3). The substrate is lowered into a bath of solution, until it is mostly or fully immersed. A short delay occurs before the substrate is withdrawn. During the withdrawal process, a thin layer of the solution remains on the surface of the substrate. The two critical stages for determining the properties of the deposited film are the withdrawal and drying stages. Once fully withdrawn, the liquid from the film begins to evaporate and leaves behind a dry film. The final film thickness is determined by the interplay between the entraining forces, draining forces, and the drying of the film. The films are formed in one of three regimes (viscous flow, drainage, and capillary). The lower the speed, the thinner the resist film hereby formed. Speed of typically 3-20 mm/s is used. Further, a curing step may be performed for certain materials. This forces the deposited material to undergo a chemical or physical change.

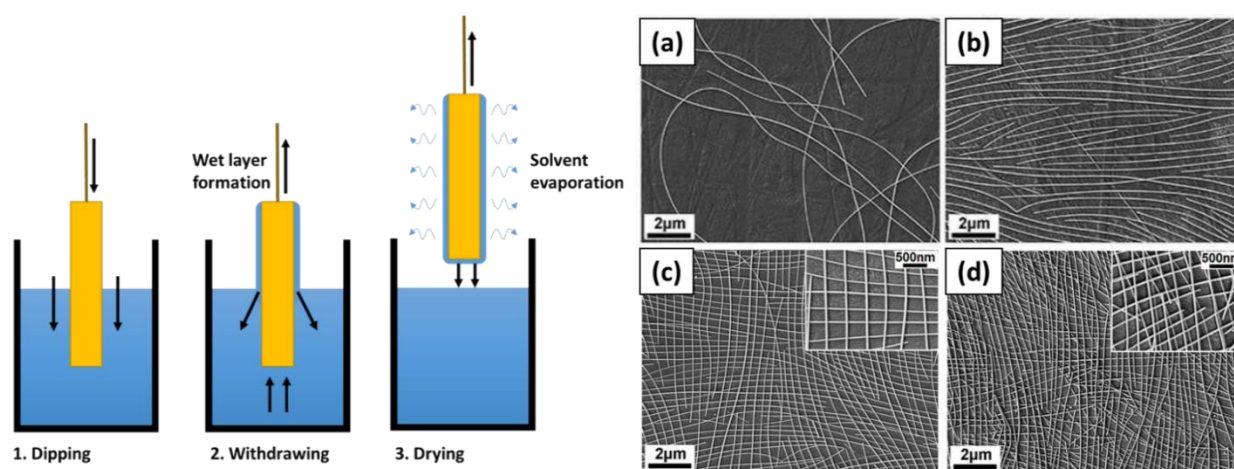


Figure 2.10 : Sequential stages of dip-coating techniques: (1) Substrate is dipped in the sol precursor, (2) Substrate is withdrawn at a constant speed, (3) To yield the

gelation layer, and solvent is let to dry. (a, b) SEM image of silver nanowire monofilm generated from one dip coating at water-bath temperature of room temperature (a) and 90°C (b). (c-d) SEM image of ordered multilayer silver nanowire of two(c) and three (d) orthogonal dip coating at water bath of 80°C [33].

A large variety of repeatable dip coated film structures and thicknesses can be fabricated by controlling many factors: functionality of the initial substrate surface, submersion time, withdrawal speed, number of dipping cycles, solution composition, concentration, temperature and environment humidity, Figure 2.10(a-d). The dip coating technique can give uniform, high quality films even on bulky substrates with complex shapes.

Advantage. The merits of dip coating are low cost and layer thickness can be easily adjusted. Even large scaled and arbitrary shaped substrates (e.g., stainless-steel panels) can easily be dip-coated. The attained resist film is very smooth, whereas the resist film thickness may change over the dimension of the substrate.

Disadvantage. Dip coating is a slow process. The forced coating of the rear side of the substrate can be either an advantage or a disadvantage. During the experiment, when the substrate is withdrawn at a certain speed, the particles tend to be deposited at the edge of the meniscus. If the evaporation rate is high, more material will be deposited at the meniscus edge, leaving thicker ridges across the substrate. The edge is pinned again when another meniscus is formed.

2.2.3 Langmuir Blodgett

Langmuir–Blodgett assembly method enables the formation of highly ordered monomolecular amphiphilic films at the interface between air and water. The subsequent film is then transferred to a solid support substrate. It can be used as a powerful technique to generate large-area monolayers of closely packed nanomaterials, Figure 2.11.

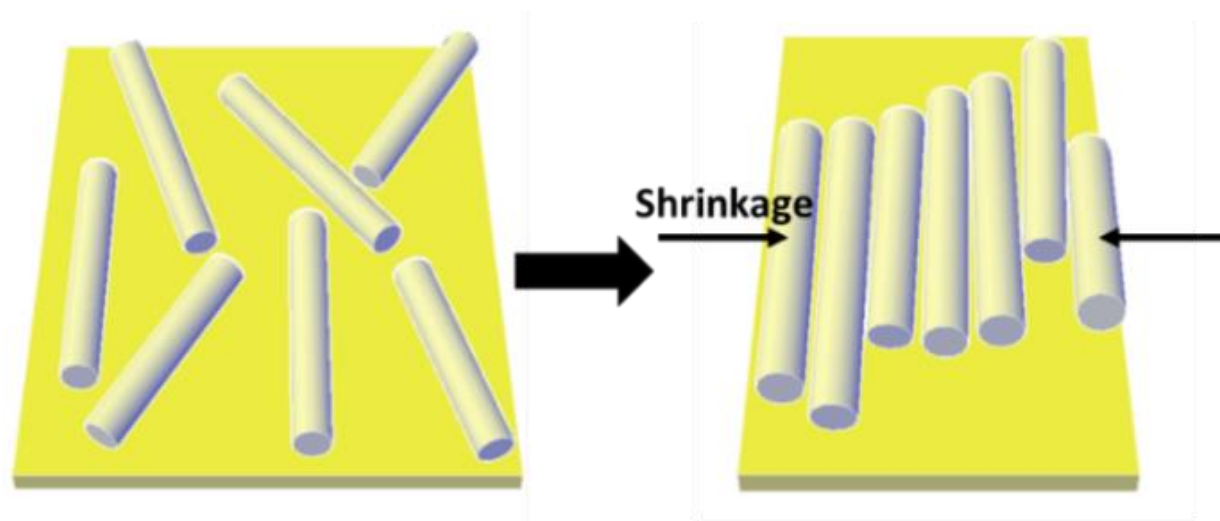


Figure 2.11: Schematic diagram of Langmuir–Blodgett technique

Fabrication. Langmuir films are generally composed of amphiphilic molecules, organized in a monolayer fashion at the liquid-gas interface. By spreading mixture of amphiphilic in a common solvent, films with mixed compositions can be prepared. In a LB trough on a water surface, nanowires are dispersed, Figure 2.12(a), resulting in a randomly distributed and loosely packed monolayer at the air-water interface. By applying lateral pressure using moveable barrier, Figure 2.12(a), using computer-controlled barriers, the slow compression creates densely aligned nanowires that are parallel to trough barrier, Figure 2.12(b-d). The film is then transferred to a desired substrate by horizontal or vertical lift-off; the resultant film can then be transferred from air-liquid interface to desired solid substrate.

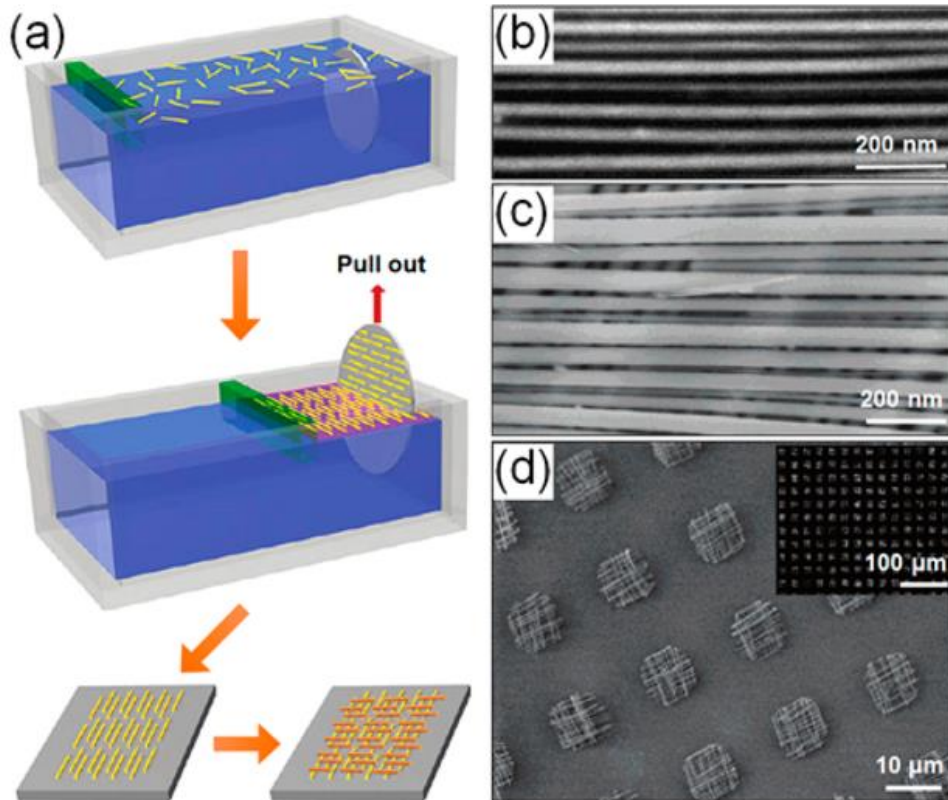


Figure 2.12 : (a) Photographs of Langmuir–Blodgett nanowire assembly process at different compression stages. SEM images (b, c) of a parallel nanowire array, and (c) crossed nanowire array. (d) SEM image at different magnifications for crossed nanowire array. [32]

Advantage. It is a promising technique for preparation of thin films. It provides precise control over the monolayer thickness. Langmuir-Blodgett technique enables a homogenous deposition of a monolayer over a larger area. It is possible to make multilayer structures by simply varying the layer composition.

Disadvantage. However, this technique does not have any industrial application at the moment because of the restricted substrate choice, only small and flat substrates can be covered by Langmuir- Blodgett films.

2.2.4 Magnetic Field Induction

It is a facile method to produce parallel fibers and multilayered grids driven by magnetic field. Magnetic field gradient produced by external magnets provides the means to manipulate and assemble the suspended nanoparticles in a solution. When a drop of organic/inorganic hybrid nanowire suspension is placed on the substrate and

exposed to a magnetic field. By the influence of the field gradient and forces exerted by neighboring nanowires, all the nanowires align along the magnetic field, Figure 2.13. Nanowires form a head-to-tail configuration under the influence of magnetic field [47]. Filler alignment line width and spacing can be tuned by varying the magnetic field frequency. In addition, the thermal fluctuations and magnetic moments can be well adjusted to control these pattern topographies.

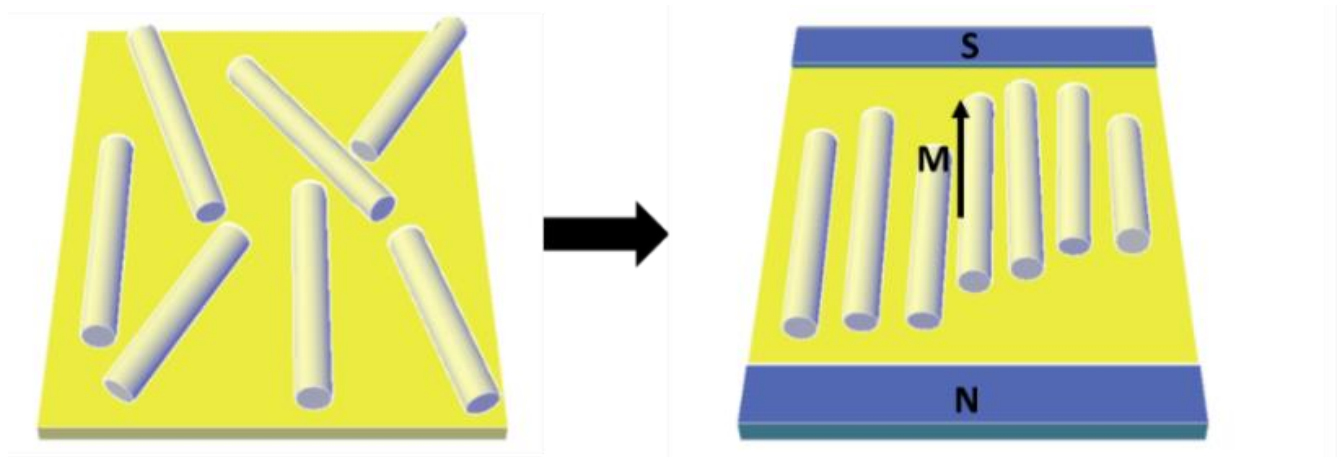


Figure 2.13: Schematic diagram of Magnetic induced

Fabrication. The method begins by placing a glass slide or a transparent plastic film in a container. The container is then filled with nanowires. Nanowires are decorated with magnetic particles and dispersed in ethanol or water. The container is placed on a permanent magnet. The position of the magnet is adjusted to enhance an apt combination of strong tangential (B_x) and weak normal (B_z) components of the magnetic field vector. Component B_x creates a magnetic torque on the nanowires that lines them up along the x-direction, Figure 2.14(a). The gradient of the magnetic field generates the force, which drives composite magnetic NW to the surface of the glass slide. Following the complete deposition, the excess solution is removed and a small amount of surfactant is added. The sample is left to dry while magnetic field is still applied. In order to form a second layer of grid the dried sample is placed in a container with fresh dispersion of NW. The horizontal component of magnetic field vector is rotated 90° and the second layer of nanowires is adsorbed on the surface, Figure 2.14(b). Figure 2.14(c-d) shows the corresponding SEM images.

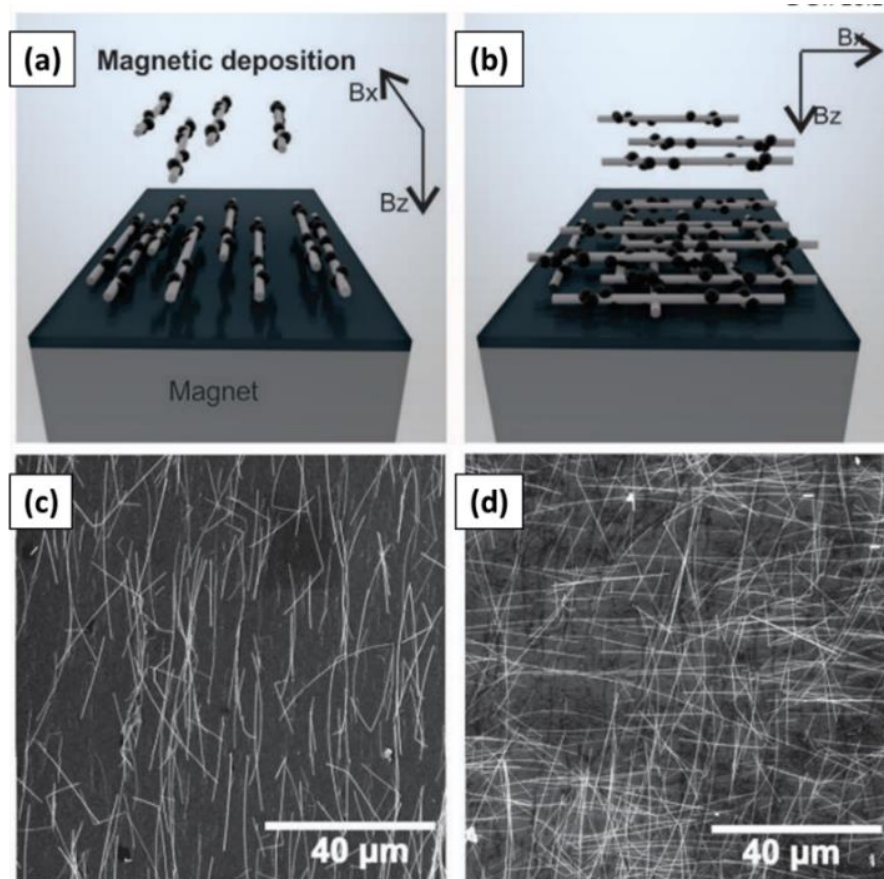


Figure 2.14: Fabrication of aligned network of nanowires: (a) Magnet is placed under the substrate and the inhomogeneous magnetic field directs nanowires towards the substrate. The tangential component of the magnetic field aligns nanowires (b) the second layer is deposited when the magnet is rotated 90° degrees; (c-d) Show the corresponding SEM images. [48]

Advantage. Under the influence of an external field, 1D nanoparticles align with their longitudinal axis oriented along the direction of the field lines. This ability of external field to direct the alignment of nanoparticles is particularly helpful for the assessment of anisotropic nanostructures, which demands orientation arrangement. Magnetic field application can attain multi-axis patterning with small fields and without migration, as long as nano-fillers are magnetically receptive. In comparison with the electric alignment, magnetic alignment has no limitation due to nano-filler migration or the requirements of high voltage.

Drawback. Complexity in fabrication of magnetic-force sensitive small nanostructures is the major drawback of the technique. The relative progress of alignment of 1D nanostructures by magnetic field is quite poor.

2.2.5 Nanoimprint lithography

Introduction. Nanoimprint lithography was invented as a low-cost, high-quality alternative to photolithography and e-beam lithography for high-resolution patterning. It was driven by limited resolution of optical lithography and highly expensive e-beam lithography. This technique is rapid and can be engaged to transfer the prefabricated topographical features from a mold to a flat polymeric film over large areas. Boundary conditions such as temperature or solvent vapors are important experimental parameters [49].

Fabrication. In nanoimprinting process, sample substrate is spin coated with a thin layer of imprint resist (thermoplastic polymer), Figure 2.15(a). Under a controlled pressure, a hard mold with topographical features is pressed into polymeric material layer, Figure 2.15(b). The pattern on the mold is pressed into the softened polymer film, which is heated above the glass transition temperature of the polymer. The mold is separated from the substrate after being cooled down, leaving the resist pattern on the substrate, Figure 2.15(c). A pattern transfer process, reactive ion etching, can normally be used to transfer the pattern in the resist layer to the underneath substrate, Figure 2.15(d). This results in a well-defined pattern in polymeric materials. This versatile technique popularly known as nanoimprint lithography (NIL), is used for a wide range of polymeric materials which includes conjugated polymers [50] [50] [49].

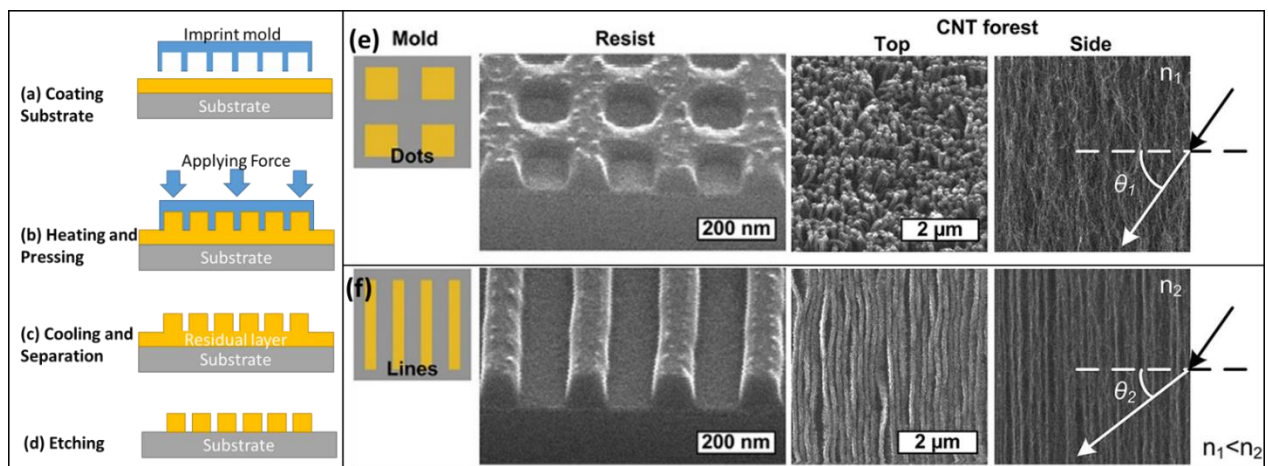


Figure 2.15: (a-d) Schematic diagram of nanoimprint lithography. (e, f) SEM images showing the resist structures after the imprint, sub-micrometer features of top and side surfaces of CNT [51].

Advantage. Nanoimprint lithography is considered as an enabling, cost-effective and simple process for pattern transfer. It is used for fabricating various micro/nano devices and structures. It provides the ability to pattern 3D large-area micro or nano structures. In comparison with conventional optical lithography, nanoimprint lithography is not limited by the factors such as wave diffraction, scattering, and interference in the resist, or backscattering from the substrates.

Disadvantage. Presently, the crucial challenge in nanoimprint lithography is the overlay alignment and the fabrication of the template with low level of defects to achieve higher yields. The other issues with NIL deposition are the anti-adhesion, defect inspection, and mold lifetime issues.

2.2.6 Spray alignment

Introduction. The key factors that determine the quality of a spray-coated layer are the size (order of a few microns in diameter) and dimensional uniformity of droplets in the spray and the droplet affect velocity. The deposition method is based on a spray-coating process under controlled conditions of the nozzle flow, droplet size, spray-coating angle, and temperature of the receiver substrate [52]. This alignment technique is versatile and applicable to various types of anisotropic materials.

Fabrication. If the spraying on a receiving surface is at 90° angle, resulting films show a homogeneous in-plane orientation, Figure 2.16(a). While spraying at smaller angles can causes a macroscopic directional surface flow of liquid on the receiving surface, Figure 2.16(b). Leads to films with substantial in-plane anisotropy with nanoscale objects, with anisotropic shapes used as components. The degree of orientation strongly depends on the distance away from the impact point along the flow direction, Figure 2.16(c-f).

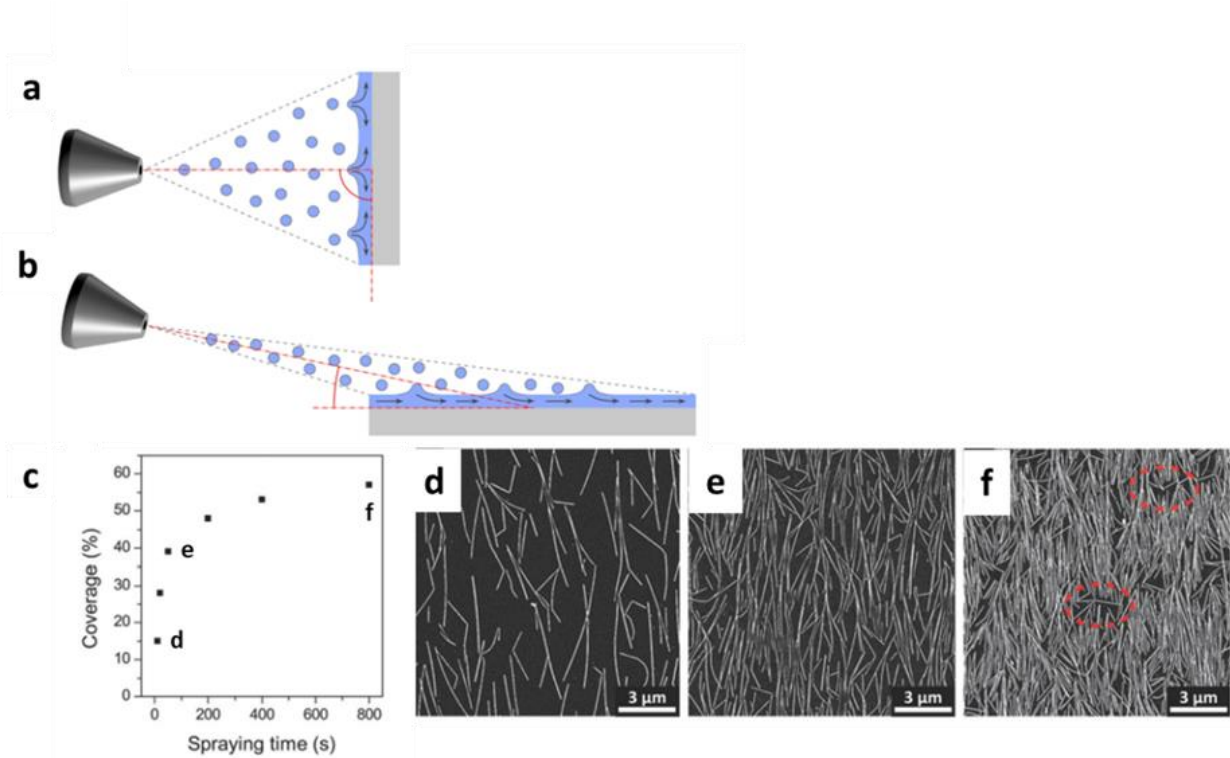


Figure 2.16 : (a) Schematically depiction of a spray jet in which the central axis of the spray cone is parallel to the surface normal. As a consequence, there is almost no macroscopically directed shear flow induced when spraying at a 90° angle against the receiving surface, especially when using small droplet speeds and when spraying from large distances. (b) The angle between the center of the spray jet and the surface is typically less than 20° (red lines), this technique is called Grazing incidence spraying. Spraying at this geometry produces a liquid flow on the surface in the spraying direction (away from the nozzle). [53] (d) surface coverage measured on SEM pictures as a function of the spraying time (d-f) SEM pictures of AgNW monolayers deposited for 10 s , 50 s and 800 s. [54]

Advantage. The cost-effectiveness of the spray-coating technique has a potential for immediate implementation in the industry and/or line productions. Spray coating operates on a different principle and it does not suffer from the thickness variation caused by the centrifugal force. For coating non-planar surfaces, spray coating presents some advantages over spin method. First, spray coating uses much less solution than spin coating. Secondly, the reproducibility of spray coating is better than spin coating. The thickness is repeatable over all cavities with the same size, regardless the position of cavities on the wafer. Spray coating has no thickness variation caused by directional effect of spinning. Even three-dimensional body (when

suitably mounted) can be spray coated with nanostructures. Substrates with pronounced topology are also easy to be spray-coated, and under optimized conditions, a good edge coverage can be attained.

Disadvantage. Since millions of droplets form the thin film. The film roughness is comparatively higher if the droplets loose too much solvent during flight. If the droplets are too solvent rich when they hit the substrate, the attained edge coverage will be poor since the resist needs to flow a little bit on the substrate before drying in order to convert from spheres to a flat film. The resist tries to minimize its surface and withdraws from edges. One always has to make a compromise between resist film smoothness and edge coverage.

2.2.7 Electric field induced alignment

The electric field induced alignment allows placement of 1D nanostructures in a desired region between the electrodes. The applied electric field induces dipole formation in conducting materials and forces them to move in the direction of the region with field gradient. It provides successful manipulation and alignment of nanostructures, Figure 2.17. The method is highly effective and have been explored with enormous interest to develop techniques for manipulating NS with high precision by means of electrostatic forces on large areas [55].

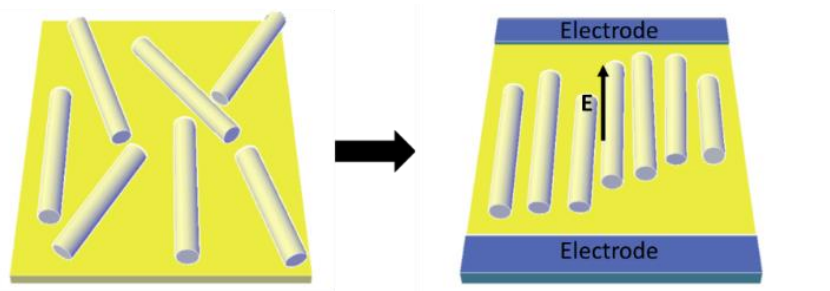


Figure 2.17: Schematic diagram of Electric field induction

Fabrication. In electric field driven self-alignment, a dipole moment induces resulting in the rotation at a certain angle providing alignment in the direction of electric field. These interactions depend on the inherent polarizability of the NS.

Another electric field induced technique is electrospinning that draws 1D nanofibers by use of high voltage (7-32 kV). This technique is capable of producing nanofibers in range of nanometer (nm) to micrometer (μm) with large variety of

materials. Several processing parameters like voltage, solution viscosity and conductivity, feed rate control the size of the nanofibers as well as their density. Use of direct current voltages with electrospinning provides a more powerful ability to align charged fibers compared to AC voltages. Electrospinning have been modified to achieve uniaxial alignment [56]. By replacing conventional collector electrode by two pieces, separated with a void gap, Figure 2.18(a). Because of electrostatic interactions, the fiber is made to form a parallel array between the void. By controlling the configuration of patterned electrodes, it is possible to stack the aligned nanofibers into multilayered films, Figure 2.18(b, c).

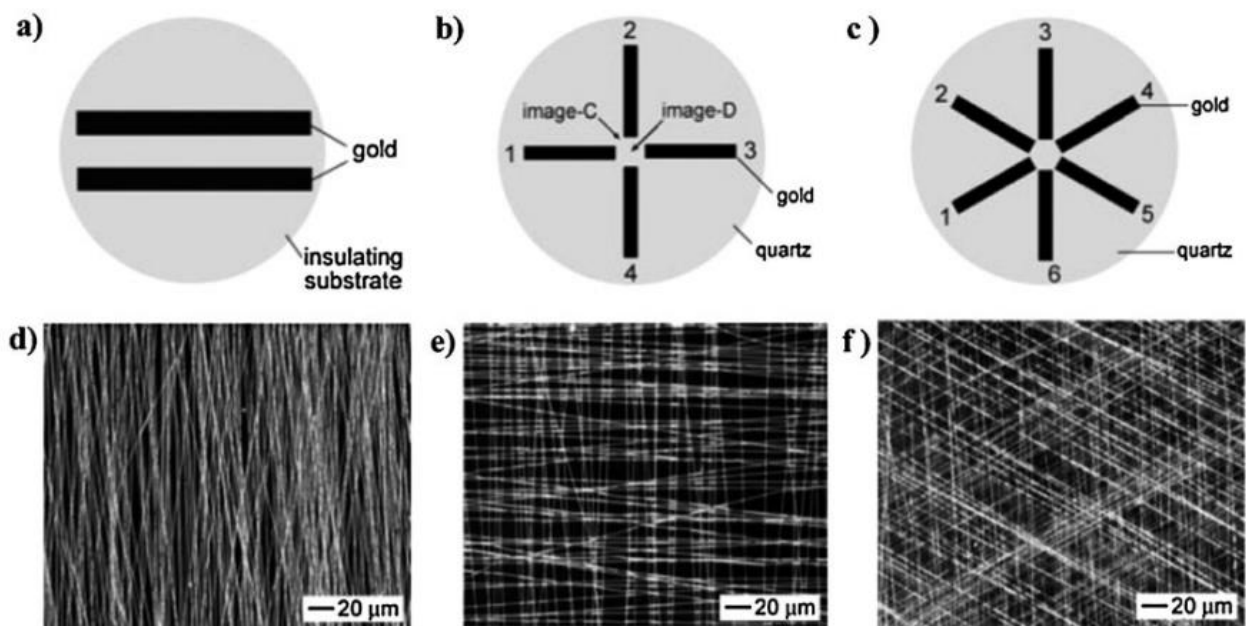


Figure 2.18 : (a) Schematic illustration of test pattern that comprised (a) two electrodes, (b) four electrodes, (c) six electrodes, (d-f) corresponding dark-field microscope graphs showing alignment of nanofibers. [56]

Another field-assisted assembly called Dielectrophoresis is a promising approach for manipulating polarizable nanomaterials. In particular, this method allows the precise deposition of individual nanostructures between prefabricated electrodes on a substrate. The electrodes on the substrate are used to generate the electric field in the suspension. The objects in suspension are then attracted to the high field gradient regions. DEP is a self-limiting assembly process. It requires careful balancing of the NSs surface area, hydrodynamic fluid flow and DEP forces. A complex set-up

coupled with precise control of the flow rate and electrical parameters (frequency, amplitude), can be difficult to implement on a larger scale.

Advantage. The electric field and magnetic field methods are easier to manipulate. It can quickly manipulate great quantities of 1D nanostructures over large areas. Electric field-assisted alignment is a promising method and is used by many research groups.

Disadvantage. Electric field induced alignment is difficult to apply though. The alignment is not very precise compared to other techniques. Another possible limitation as seen field-assisted assembly like dielectrophoresis is the requirement of prefabricated electrodes on the substrate. The aggregation present in the desired material solution hinders the dielectrophoresis assembly process.

Conclusion. 1D-nanomaterial alignment techniques could be categorized by observing the output from diverse approaches. The criteria of technique selection for alignment purposes are towards quick, feasible, apparatus-free and low-cost routes. **Electrospinning** and **Magnetic Field** make use of external forces onto the randomly dispersed nanomaterials to align them towards preferential direction in order to have low energy state, generally parallel to the applied field force. However, these approaches have a poor alignment yield. To improve the alignment yield, techniques like **NIL**, **LB method**, **Contact Printing** were developed. Such techniques could provide highly oriented 1D-NS and could be generated at large scale. Unfortunately, the position of alignment nanomaterials was upon random substrate. Aligned 1D nanomaterial films require post-treatments to be integrate onto the device.

As in the interest of this study, **Dielectrophoresis** technique helps reducing the post-treatment for device integration by not only aligning nanomaterial in desired directions but in the desired position as well. DEP does not require 1D nanomaterial to be conductive, charged or magnetic force sensitive, they must be polarizable. Table 4 shows the comparison between DEP and other 1D-alignment techniques.

Table 4 : Dielectrophoresis comparison with a few techniques; in the table '0' being neutral and '++' being most positive for the corresponding category

Criteria Technology	Experimental set-up			Material	Output	
	Set-up simplicity	Substrate size	Time for experiment	Material wastage	Alignment of resultant film	Post process
Drop Cast	No specific requirement	Not limited	+	++	Not aligned	Evaporation of excess solution
Inkjet printing	jet printers	Not limited	++	0	Not aligned	Evaporation of excess ink
Vacuum filtration	Vacuum pump	Limited	++	++	Not aligned	Transfer to a suitable substrate
Langmuir – Blodgett	LB Trough modules	Not limited	++	+	Aligned	Transfer to a suitable substrate
Dielectrophoresis	Electric field source	Not limited	0	0	Aligned	Removal of excess solution

2.3 Dielectrophoresis

Dielectrophoresis is altogether a different technique compared with electrophoresis. The latter is related to the motion of charged particles subjected to a uniform electric field while DEP is defined as the motion in a non-uniform electric field of uncharged and polarizable particles (ranging in size from 0.1 to 1000 μm) suspended in a solution, Figure 2.19. H.A. Pohl has been the first to conduct an experiment to demonstrate such motion by using small plastic particles suspended in an insulating liquid and under a non-uniform electric (AC/DC) field [57].

Among other alignment techniques, DEP is a very interesting and efficient approach for particle manipulation in microsystems due to its simplicity, the favorable scaling effects and its ability to induce both positive and negative forces. DEP can be generated using a direct (DC) or alternating (AC) field. The non-uniform field is obtained by means of properly designed electrodes. In such an electric field, the particle experiences different forces at each end. The difference in force at both ends creates a net force depending on the polarizability of the particle and the medium, which creates a dipole. The non-uniformity of the electrical field is therefore the key factor for the DEP technique.

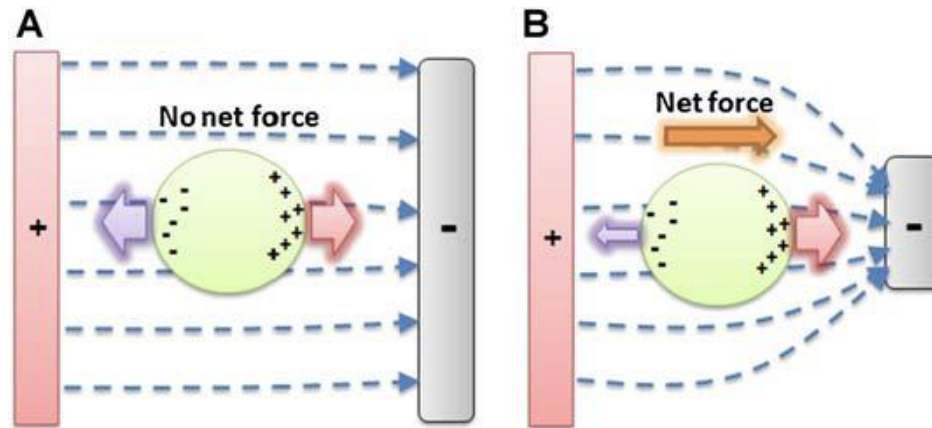


Figure 2.19 : Diagram of a positive dielectrophoresis (a) In uniform electric field, particle is symmetrically polarized resulting in zero amplitude net DEP force (b) In non-uniform electric field, particle is asymmetrically polarized, resulting in motion of the particle to an area with maximum electric field amplitude. [58]

2.3.1 Dielectrophoresis Force

In an inhomogeneous electric field, the motion of a particle is due to the interaction of the induced dipole moment of the particle and the spatial gradient of the electric field, Figure 2.20. DEP effects may also arise from spatial non-uniformities of both magnitude and phase of AC electric fields. The DEP force on a spherical particle can be formulated as:

$$F_{DEP} = 2\pi\epsilon_m R^3 K \nabla |\vec{E}|^2 \quad (1)$$

Where -

R is the particle radius

ϵ_m is the absolute dielectric permittivity ($\epsilon_r \epsilon_0$) of the surrounding medium

K is the Clausius-Mossotti factor related to the effective polarizability of the particle

E is the amplitude (rms) of the electric field, ∇ represents the gradient operator

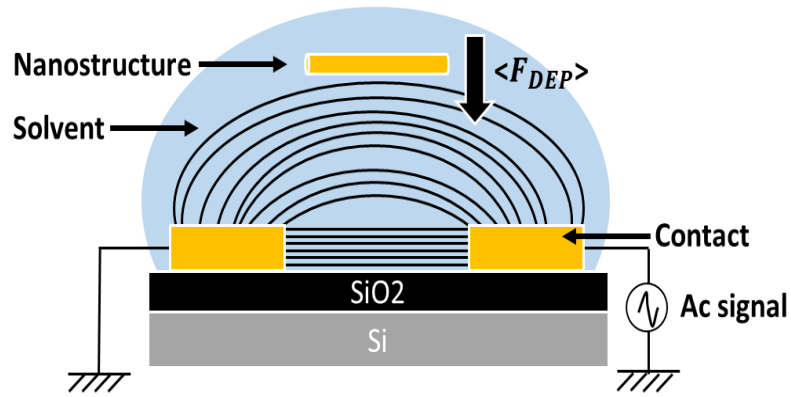


Figure 2.20 : Schematic representation of DEP alignment of 1D nanostructure.

Depending on the relative polarizability of the particle with respect to the medium, the particle will move either in the direction of the field gradient (positive DEP) or in the opposite direction (negative DEP). It is also interesting to consider the favorable scaling of the DEP force. If L represents the length that characterizes the electrical field variations and V the applied voltage, the order of magnitude of the DEP force is given by: $F_{DEP} = V^2/L^3$. It shows that if we decrease the length from 1cm to 100 μ m, the same DEP force can be obtained with an applied voltage reduced 1000 times. Very low voltage is therefore sufficient to generate a powerful DEP force.

2.3.2 Clausius-Mossotti factor $K(\omega)$

Clausius-Mossotti factor $K(\omega)$, is a frequency dependent factor, determined by using the complex dielectric (ϵ^*) permittivity of the medium and the particle. It is defined by [59]:

$$K(\omega) = \frac{(\epsilon_p^* - \epsilon_m^*)}{(\epsilon_p^* + 2\epsilon_m^*)} \quad (2)$$

In the above equation, ϵ_m^* and ϵ_p^* are the complex permittivities of the medium and the particle with $\epsilon_m^* = \epsilon_m - j\frac{\sigma_m}{\omega}$ and $\epsilon_p^* = \epsilon_p - j\frac{\sigma_p}{\omega}$

where ϵ_p , ϵ_m are the permittivity of the medium and the particle, respectively, σ_m and σ_p are the conductivities of the medium and the particle, respectively, and ω is the angular frequency. Certain key-points are worth noting:

- For spherical particles, values for $K(\omega)$ lie in the range $1.0 > [K] > -0.5$. [60][60][61]
- Positive or negative $K(\omega)$ values correspond to the polarizability of the particle being higher or lower, respectively, than that of the surrounding medium.

- When using the above form of $K(\omega)$, it is assumed that the particle is composed of homogeneous dielectric material that exhibits no conductive losses and carries no net charge.

2.3.2.1 Real $K(\omega)$

The complex $K(\omega)$ has two parts a real and an imaginary part. For the real part, the first limit is considered at low frequencies, $\omega \rightarrow 0$, giving the ionic contribution to the permittivity and Real $K(\omega)$ is expressed as:

$$Real K(\omega \rightarrow 0) = \frac{(\sigma_p - \sigma_m)}{(\sigma_p + 2\sigma_m)} \quad (3)$$

It is easy to verify that this limit can be positive if $\sigma_p > \sigma_m$ or negative if $\sigma_p < \sigma_m$, as shown in Figure 2.21.

The second limit is considered at higher frequencies, $\omega \rightarrow \infty$.

$$Real K(\omega \rightarrow \infty) = \frac{(\epsilon_p - \epsilon_m)}{(\epsilon_p + 2\epsilon_m)} \quad (4)$$

Here this limit can be negative if $\epsilon_p > \epsilon_m$ or positive where $\epsilon_p < \epsilon_m$.

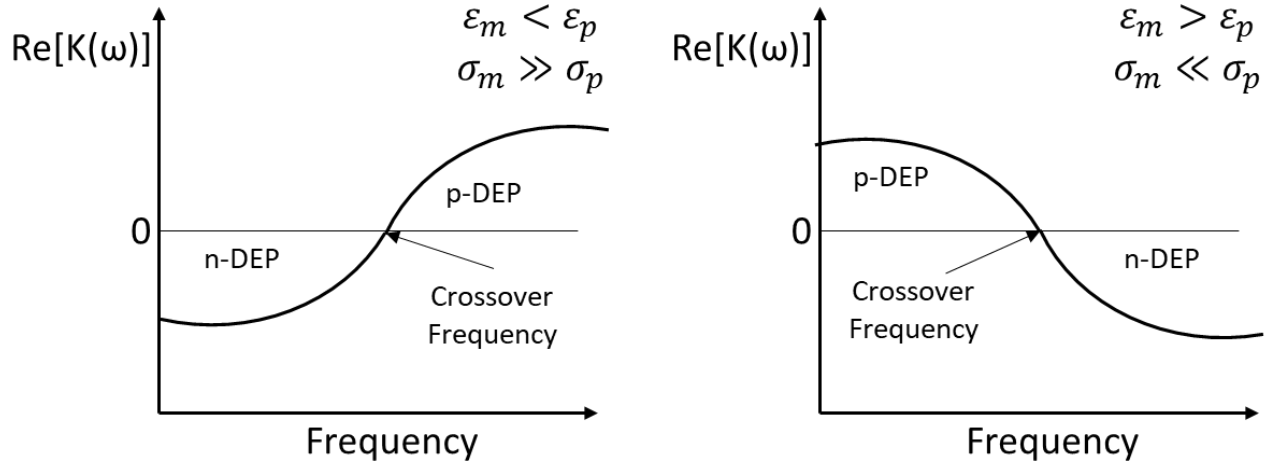


Figure 2.21 : Variation in Real part of Clausius-Mossotti factor, $Re [K(\omega)]$ with frequency when: (a) $\epsilon_m < \epsilon_p$ and $\sigma_m \gg \sigma_p$ (b) $\epsilon_m > \epsilon_p$ and $\sigma_m \ll \sigma_p$

4.1.1.1. Crossover frequency

At a particular frequency, the polarizability of the particle is identical to that of the suspending medium. In that case, there is no induced dipole. The net force is zero. This frequency is the crossover frequency where $K(\omega)$ equals zero. Several factors,

such as the electrode design, electric properties of the suspending medium, temperature, and the exact particle shape and size, may influence the measurement of crossover frequencies.

4.1.1.2. Imaginary part $K_i(\omega)$

The role of $K_i(\omega)$ in ac-electrokinetics (electrorotation and travelling wave DEP) is similar to the role of young's modulus in elasticity and viscosity in Newtonian fluid mechanics. The imaginary part of the Clausius-Mossotti factor, $K_i(\omega)$, is a crucial parameter in electrorotation and travelling wave DEP. The knowledge of imaginary $K_i(\omega)$ is fundamental from the academic point of view. It helps in calculating the torque and the force exerted on the particle for the electrorotation (ER) and travelling wave (twDEP) applications. It is an effective tool for the manipulation and characterization of particles and cells. [62]

2.3.3 Electrode configurations

The electric field gradient for DEP can be generated by using 2D or 3D electrode configuration. 2D electrodes are manufactured by conventional photolithography and metallization. 2D electrodes are planer and the field created mainly affects particles close to the surface. The 3D electrode configuration creates a field in the volume of the fluid. The applied force thus affects a larger number of particles with higher intensity. However, fabrication process for 3D electrodes is more complex. As shown in Figure 2.22, some examples of commonly used 2D electrode geometries are parallel or interdigitated, oblique, curved, in a matrix form, in quadrupole, etc. [63][64][65]

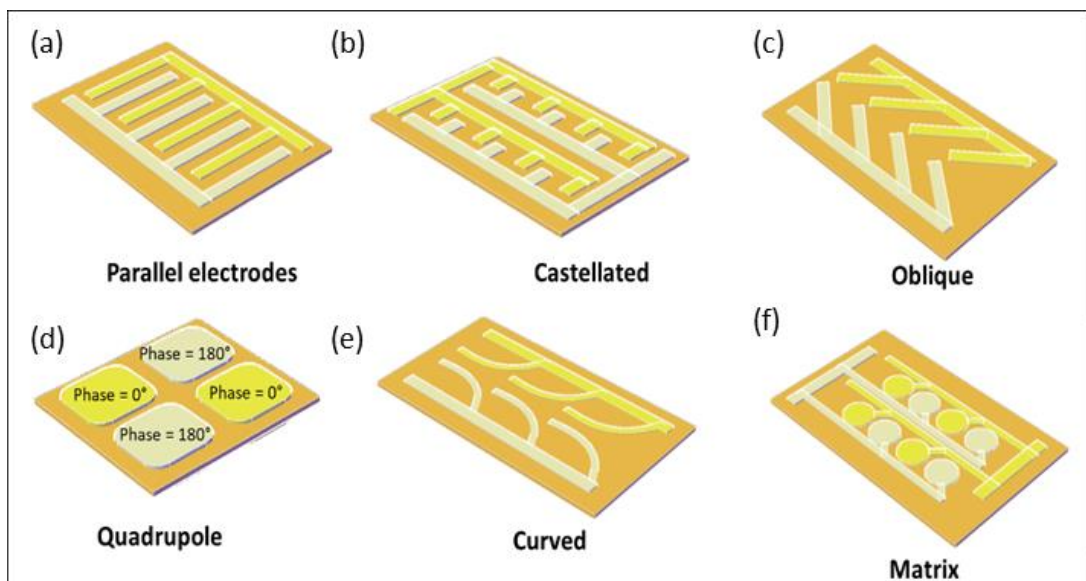


Figure 2.22: Examples for 2D electrode: (a) parallel or interdigitated, (b) crenellated, (c) oblique, (d) quadrupole, (e) curved, and (f) matrix

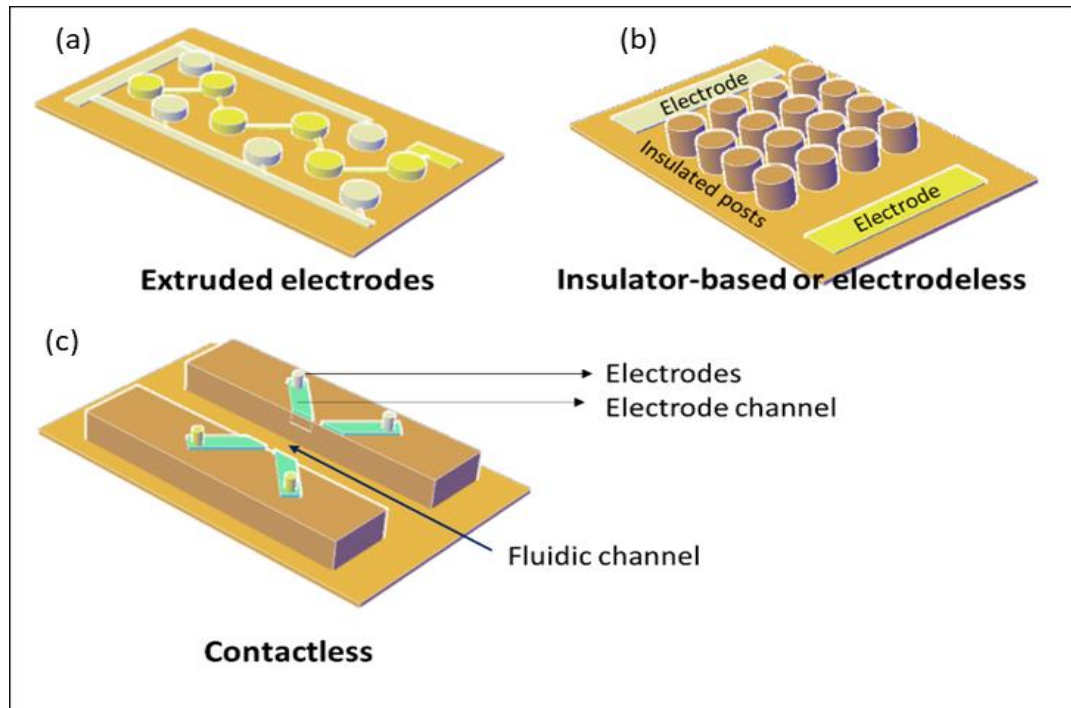


Figure 2.23: Examples for 3D electrode: (a) extruded, (b) insulator-based or electrodeless and (c) contactless

Commonly used geometries for 3D electrodes (Figure 2.23) are extruded, insulator-based or electrodeless and without direct contact with the fluid. Each electrode configuration allows the creation of localized areas with strong electric field gradients through which the suspended particles interact with the structures. Some electrode configurations are intended to be used in droplet systems, while the others will be more efficient if they are integrated within a micro channel. The following section is devoted to the operating regimes associated with the various types of electrodes.

2.3.4 Operating modes

Particles dispersed or already present in the solution can be handled in many different ways. Dielectrophoresis can be used to manipulate[66][58], transport[67], separate [61][68] and sort different types of particles[69]. The electrode configurations can preferably be associated with an operating regime as defined in the following.

2.3.4.1 Sorting

Sorting can be performed with help of a multiple frequency configuration. Particles are subjected to multiple electric fields of different frequencies created by adjacent electrodes [70]. Which makes particles are attracted to specific areas depending on the frequencies of the fields used. This allows particles with different dielectric properties to be assembled or located at different locations.

2.3.4.2 Electro-rotation

By using quadrupole electrodes and applying a 90° phase-shifted signal between the electrode pairs (pair is formed between the alternate electrodes), it is possible to rotate the particles. This offers ability to manipulate suspended particles remotely without direct contact and has significant potential for applications in micro total-analysis systems technology [71][64].

2.3.4.3 Separation and detection

Selective detection and rapid manipulation of particles via contactless methods is useful in research, drug discovery and delivery. The contactless process of manipulating and separating particles through the DEP method is based on the dielectric value of the particles and medium environment, subject to the input frequency applied. The ability of DEP to choose one type of particle has been introduced and progressively being performed in medical studies [72][72][73].

2.3.4.4 Direct Assembly

By using electrode arrays, it is possible to assemble nano-objects by positive DEP. These are attracted to the areas of strong fields, which often correspond to the inter-electrode spacing. This makes it possible to place precisely, a large number of objects, at the same time. [74][75]

2.3.5 External Impact factor of Dielectrophoresis

Experimental investigations of DEP suggest a difference between numerical expectation and experimental results. Every particle type solution reveals a near-unique profile of response, against applied electric field for given environmental conditions. Hence, the following stated boundary conditions are explicitly manipulated for aligning nanowires controlling the DEP response. When controlling and driving DEP experiments for aligning 1D nanostructures, the following parameters are of critical importance:

2.3.5.1 Effect of the magnitude and frequency of the ac voltage

The magnitude of the AC voltage determines the strength and gradient of the electric field. Increasing the magnitude of the AC voltage, the DEP force will increase. In addition, more NS will be attracted to the electrode gap in fixed time duration of the electric field. Resulting in more NS attracted to the electrode gap in fixed time duration of the electric field, Figure 2.24(a, b) in the case of carbon nanofibers.

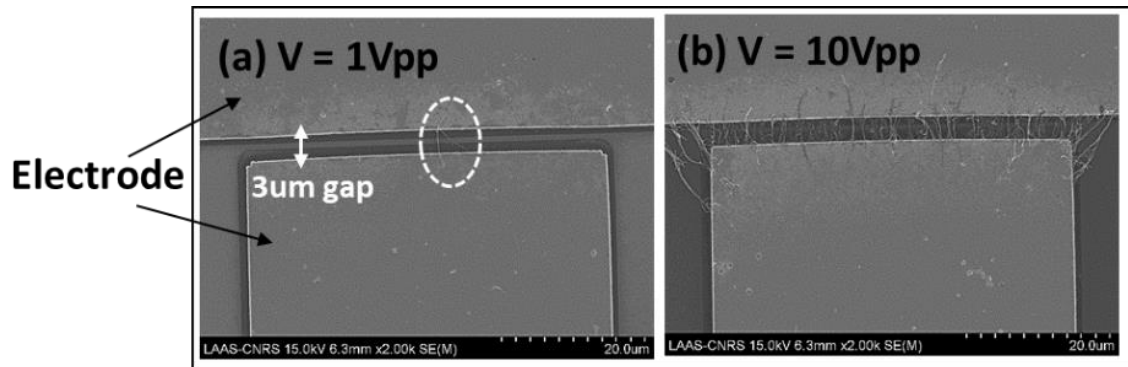


Figure 2.24 : Scanning electron micrographs of structures fabricated at two different voltage (a, b) using solutions 0.2 mg/ml of CNFs in water. The gap between the electrodes is 3 µm.

If instead of constant voltage, alternating voltage is applied the dielectric material will still be polarized. The frequency dependence of DEP force is determined by the frequency dependence of *Clausius-Mossotti factor* (K). It is unique to a particular particle type. Clausius-Mossotti (K) factor determines the sign of DEP force. If the value is greater than zero, the particle is more polarizable than the surrounding medium and will be attracted in maximum electric field intensity, showing pDEP trend. The opposite occurs when the Clausius-Mossotti (K) factor is less than zero, it is referred to as nDEP. Strong aligning effect is observed at lower frequency with Gold Helices, Figure 2.25 (a, b). The term “Gold helices” here is referred to gold nanoparticle of 10nm diameter, grafted on an inorganic helical template [76].

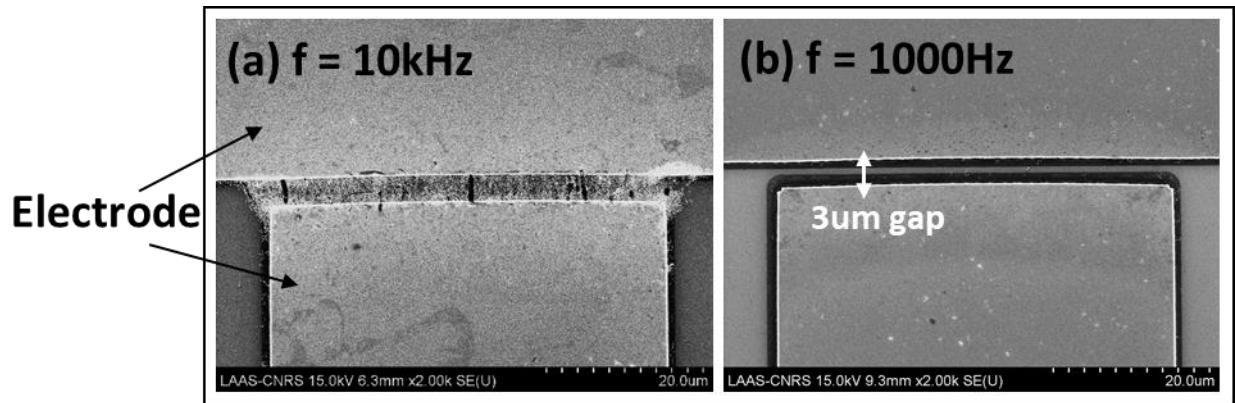


Figure 2.25 : Scanning electron micrographs of structures fabricated at two different frequency 10 kHz and 1000 kHz (c, d) Using solution of 0.01 mg/ml of gold nanoparticle grafter over inorganic silica nano helices. The gap between the electrodes is 3 μm .

2.3.5.2 Effect of the particle concentration

With the increase in concentration of the NS solution, more NSs will be attracted on the electrode region under fixed time duration of the electric field. On the contrary, as can be seen on Figure 2.26, as the solution concentration decreases, the bundles become thinner due to the lower availability of NSs in the solution. As a result, one can aim to deposit individual nanotube/nanostructure by simply using low concentration solution. Using narrow electrode gap ensures that the electric field in between the electrodes is extremely concentrated and directional.

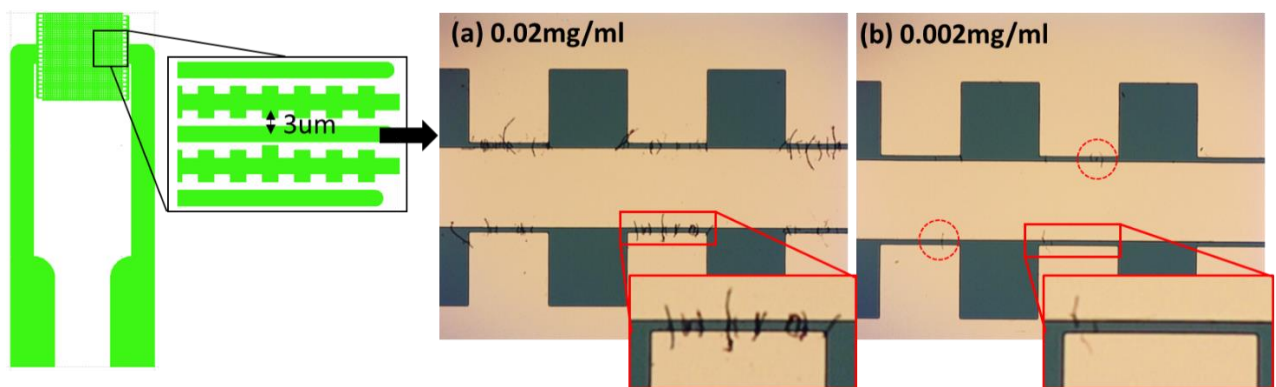


Figure 2.26 : SEM images of aligned nanofibers with the 3 μm -wide castellated electrode, solutions have two different concentrations: (a) 0.02 mg/ml, (b) 0.002 mg/ml. DEP boundary conditions: 5 V_{p-p} , 1 kHz, 6 s.

2.3.5.3 Effect of the NS dimensions and shape

For the precise alignment of nanowire, it demands an analysis of associated physical parameters, DEP frequency and electrode design. Equation (1) for DEP is only valid in case of an isotropic spheroid. Later in this study, manipulated objects were characterized by their cylindrical shape with a large aspect ratio that makes them quite far from the spherical model. In case of a prolate spheroid, it is approximated for a cylindrical particle. It permits for examining the DEP force on nanotube, nanofiber, nanowire like particles. Clausius-Mossotti factor for a prolate spheroid is different for each axis of particle. As a result, to determine the magnitude of DEP force along each axis, the electric field gradient is split into two components.

First scenario: Where the field gradient is oriented parallel to the nanowire, only the $K(\omega)$ along the long axis is consider in evaluating the magnitude and transitional DEP force. For the reason that, DEP force has only a single component aligned along the length of nanotube.

$$K(\omega - \text{longaxis}) = \frac{(\varepsilon_p^* - \varepsilon_m^*)}{(\varepsilon_m^*)} \quad (5)$$

where $\varepsilon_{p,m}^*$ is the complex permittivity as defined above in Clausius-Mossotti factor section.

Second scenario: Where the field gradient is perpendicular to the nanowire, only the $K(\omega)$ along the short axis is consider in evaluation of the magnitude of DEP force. Because DEP force has only a single component perpendicular to long axis of nanotube.

$$K(\omega) = 2 \frac{(\varepsilon_p^* - \varepsilon_m^*)}{(\varepsilon_p^* + \varepsilon_m^*)} \quad (6)$$

Third scenario: Where the field gradient is neither parallel nor perpendicular to the nanowire, $K(\omega)$ along both short-axis and long-axis is considered in evaluating the magnitude and direction of DEP force. From these equations, it is possible to predict the trajectory of a nanowire subjected to a positive DEP force.

Raychaudhuri et al. have traced the evolution of the direction of the DEP force as a function of the position of nanowire with respect to the electric field gradient in which it is immersed [77]. It can be seen from these graphs, reproduced in Figure 2.27, where the two forces along the long and short axes combine to give a resulting DEP force whose direction depends on the frequency used. It is evident, from the Figure 2.27(b), that at lower frequencies the DEP force will be dominated by long - axis components. While, at higher frequencies the dominance of long – axis becomes less significant.

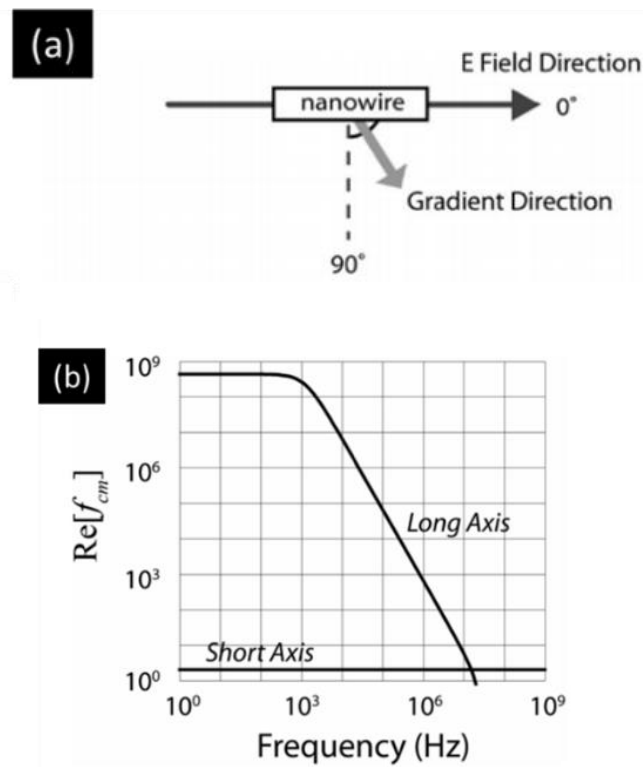


Figure 2.27: (a) Influence on the nanowire orientation as a function of direction of electric field gradient. (b) Clausius-Mossotti factor according to the long and short axis as a function of frequency, for InAs wires suspended in deionized water.

2.3.6 Synthesis of 1D nanohelices with grafted nanoparticles

Following section gives a brief overview of the 1D Nanohelical material and their synthesis; overall, the details of the nanomaterial solution that will undergo DEP deposition for fabrication of active sensing area of strain sensor are presented. A complete elaborate description can be found in These of Antoine Amestoy [78].

Gold nanoparticle (AuNP) are covalently grafted onto nano-helices by an amide bond. Before grafting onto the ribbons, the nanoparticles are functionalized by ligands such as SH-PEG7-COOH (PEG) and Mercaptopropionic Acid (MPA). In later sections, this 1D nanomaterial is simply referred to as Helical Nano-Structures (HNS). The fabrication is more elaborately explained through following three steps:

1) Synthesis of inorganic silica nanohelices

Organic nanohelices are obtained from the self-assembly of the gemini cationic surfactant ($C_2H_4-1,2-((CH_3)_2N^+C_{16}H_{33})_2$) with a chiral tartrate counter ion ($C_4H_4O_6^{2-}$) referred to as 16-2-16 tartrate. The resulting supramolecular assembly is then used as a support for the sol-gel reaction of tetraethyl orthosilicate (TEOS) which leads to the formation of hybrid nanostructures with an organic core and a silica shell. The organic core is removed by washing in different organic solvents to obtain the silica nanohelices.

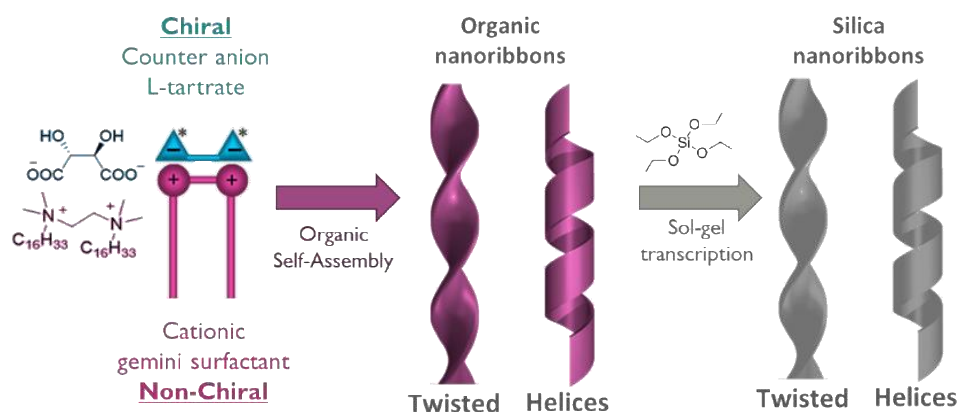


Figure 2.28 : Reaction scheme of the manufacturing process of silica nanohelices.

2) Functionalization of gold nanoparticles

In this study, 10 nm diameter Au-NPs are synthesized following the protocol established by Slot and Gueuze [79]. The metal precursor is potassium tetrachloroauric acid ($KAuCl_4$), sodium citrate and tannic acid both acts as reducing and stabilizing agents. To prepare 100 mL of a colloidal suspension of Au-NPs at 0.1 mg/mL, 2 solutions are prepared.

Solution A: 1 mL of a 1% by weight aqueous solution of $KAuCl_4$ in 80 mL of Milli-Q water.

Solution B: 4 mL of 1 wt% aqueous sodium citrate solution, 0.1 mL of 1 wt% aqueous tannic acid solution and 16 mL of Milli-Q water.

The two solutions are heated to 60 °C separately for 15 min, then solution B is poured into solution A. When the solution turns red, the flask is heated to 100 °C for 1 h and then cooled to room temperature. At this stage, AuNPs are stabilized by electrostatic interactions with a mixture of tannic acid and citrate. However, they can easily aggregate with the addition of salt, a change of temperature or a change of solvent. So, to avoid aggregation, they are modified with different thiol (R-SH) ligands. AuNPs are functionalized either with PEG, mercaptopropionic acid (MPA) or with different ratios of PEG – MPA mixture. It is useful to note that electron tunneling occurs generally over distances of up to 1 to 3 nm.

For functionalization with PEG or PEG – MPA mixture, 8 mL of tannic acid and citrate stabilized AuNPs are arranged in tubes. The tubes are centrifuged at 21,000 g for 20 min to remove 1.5 mL of supernatant. 0.5 mL of a 1 mM PEG solution or PEG – MPA mixture of total concentration 1 mM in water is added to each of the tubes, this is followed by a 10 min sonication. The tubes are shaken at 400 rpm on a tray overnight at 4°C. After the reaction AuNPs are precipitated by centrifugation at 21,000 g for 20 min, 1.5mL of supernatant is removed and the tubes are all combined. Finally, the modified AuNPs are dispersed in 0.5 mL of Milli-Q water, corresponding to a mass concentration of 3.2 mg/mL (134 nM).

The functionalized nanoparticles are nomenclature as PEG@AuNP and MPA@AuNP for AuNPs functionalized with PEG and MPA respectively and PEG_xMPA_{1-x}@AuNP for AuNPs functionalized with different ratios of PEG and MPA.

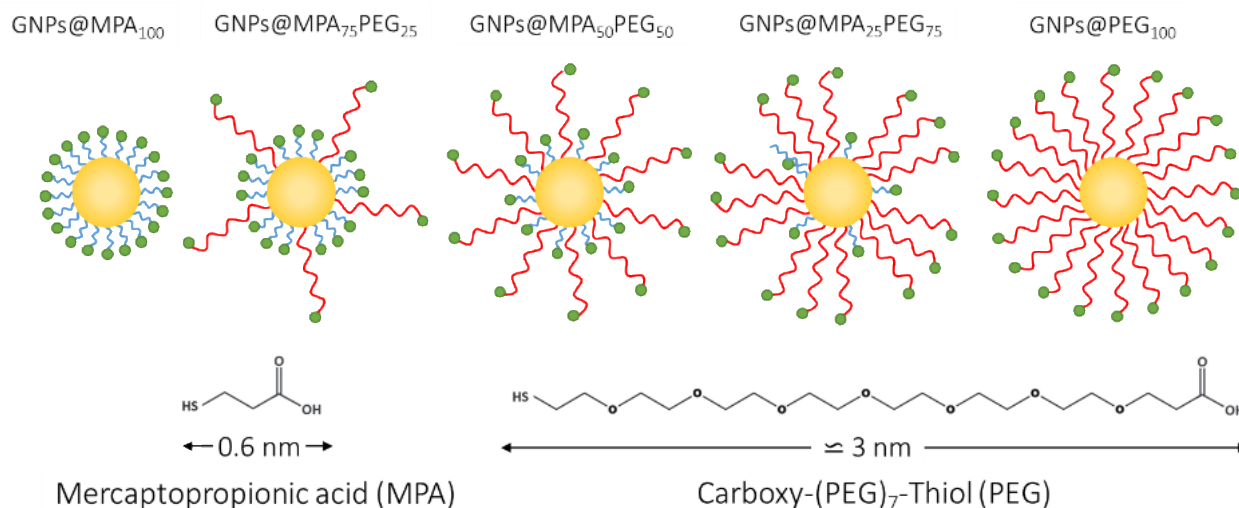


Figure 2.29 : (a) Schematic of gold nanoparticles functionalized with different ratios of mercaptopropionic acid (MPA) and SH-PEG-COOH (PEG).

3) Grafting the gold nanoparticles on the inorganic silica nanohelices

The assembly of AuNPs on the surface of the nanohelices is done by activation of the carboxylic groups present on the surface of the AuNP under the conjugate action of 1-Ethyl-3-(3-dimethylaminopropyl)-carbodiimide (EDC) and N-hydroxysuccinimide (NHS). An aqueous solution of EDC (1.2 mM) and NHS (6.0 mM) is added to the AuNPs suspension ($V = 0.5 \text{ mL}$, $C = 134 \text{ nM}$), obtained previously. The suspension is dispersed using an ultrasonic bath for 10min and then stirred for 2h at 4°C .

To $50\mu\text{L}$ functionalized nanohelices suspension in about 1mg/mL ethanol is added to the activated AuNPs. The HNS (i.e., activated AuNP grafted on nanohelices) are recovered by low-speed centrifugation and re-dispersed in water until the supernatant is clear. The HNS are, at the end, dispersed in water. If after dispersion, the aggregation of the HNS remains, it is possible to use a Vibra Cell 75186 at high intensity sonicator equipped with a 6 mm probe, for 10 seconds in 'pulsed' mode (1 s on/ 1 s off) at a power of 65 W and a frequency of 20 kHz.

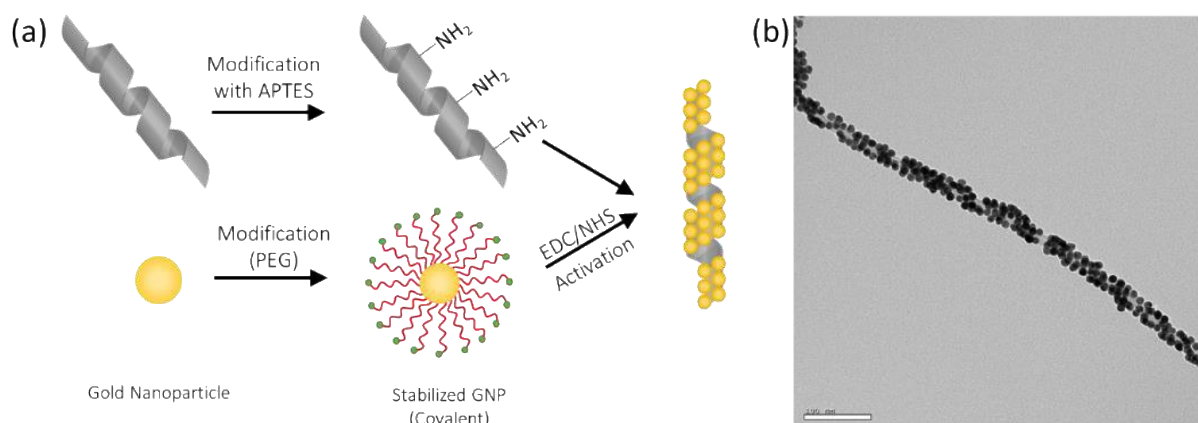


Figure 2.30 : (a) Reaction scheme for the fabrication of nano-helices @Au-NPs. (b) TEM image of a nano-helices @Au-NPs.

The size and nature of the ligand influences the quality of grafting onto twisted helices and final suspension. If the ligand is smaller, like MPA, it might reduce the tunneling barrier, but it would increase the possibility of AuNP aggregation in the solution, which results in the aggregation of nanohelices. To overcome this, one of the possible ways can be to use a combination of ligands, like PEG + MPA, in different ratios. PEG helps in stabilizing the NP and in preventing the aggregation while MPA ligand decreases the inter-particle distance. In general, the length of nanostructure is around 1-2 μm . AuNP used for grafting purposed are 10 nm in diameter. NS are dispersed in water or ethanol, in this study most of the solutions prepared were with water.

2.4 Device Fabrication

The following section describes the experimental steps towards the fabrication of flexible strain sensor, Figure 2.31. It gives information on the clean-room fabrication procedures of metallic castellated electrodes over a flexible substrate and how the DEP procedure was optimized to obtain localized deposition with aligned 1D nanostructures. Discussion is centered on approach towards selecting the most relevant DEP parameters. Problems associated with the fabrication of strain sensor are also mentioned.

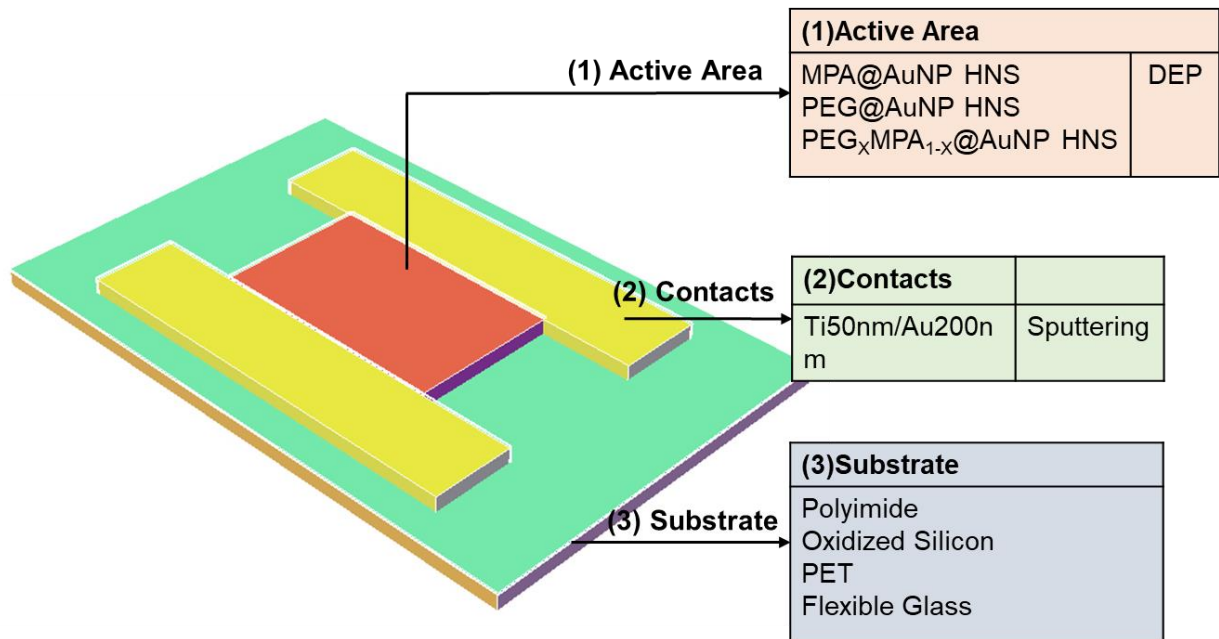


Figure 2.31 : Diagram of flexible strain sensor labeled with the techniques of fabrication and material used in this study.

2.4.1 Fabrication process for the interdigitated electrodes

Contact and Substrate. In order to deposit and characterize the active sensing material, interdigitated electrodes (IDEs) are fabricated. Two electrode designs are used, shown in Figure 2.32. The first design, Figure 2.32(a), has two long castellated electrodes with minimum separation gap of 3 μm . This electrode design has 10-alignment sites, which permits individual monitoring of each site. This design of electrode is used for characterization purposes mainly for SEM – AFM measurements and for testing DEP parameters. The second electrode design, Figure 2.32(b), is used for the fabrication of strain sensor. It possesses 720-alignment sites. The total IDE area is 16 mm^2 , it provides larger active sensing region.

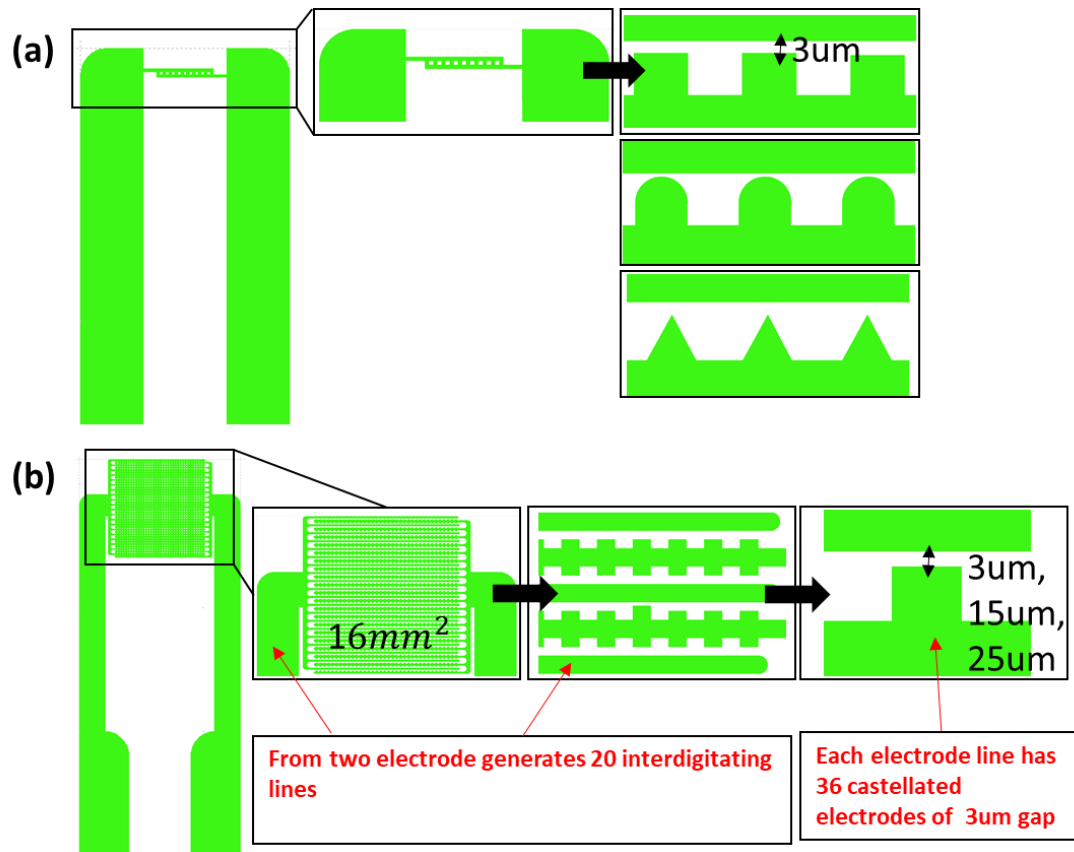


Figure 2.32 : (a) 10-alignment site design with three different castellated shapes, (b) 720-alignment site design to use for strain sensing purposes

For the choice of substrate two different materials are used: (1) oxidized silicon - a stiff substrate and (2) polyimide film that works as a soft substrate. In the subsequent fabrication steps, the 'active material' is deposited between the IDE by using DEP technique. As mentioned, two types of wafers, facilitate the mechanical characterization under a wider range of strain. IDEs over oxidized silicon wafer are better candidates for morphology analyses by using Scanning Electron Microscope (SEM). While electrode formation over polyimide (PI) substrate has more complex fabrication process as compared to the process on hard wafers.

In order to fabricate IDE over PI film, an additional procedure for attaching/sticking the PI film to standard a silicon wafer is required. The silicon wafer provides a hard base to PI film, which makes it easy to spin-coat photoresist, perform exposure and deposit metal uniformly. However, at higher baking temperatures (>90°C) PI film has tendency to peel off the silicon wafer, making it difficult to keep PI film firmly stuck over the silicon wafer.

The fabrication process for the IDE on a silicon p-type wafer (SiP) and a flexible polyimide (PI) substrate is further described:

1) Fabrication Process for IDE on Polyimide Film:

The fabrication process for interdigitated electrodes on flexible polyimide film is illustrated in Figure 2.33. In this case, a p-type silicon wafer is used as a hard substrate to facilitate the fabrication steps with the polyimide film; any other type of silicon wafer can also be used (for example a glass substrate).

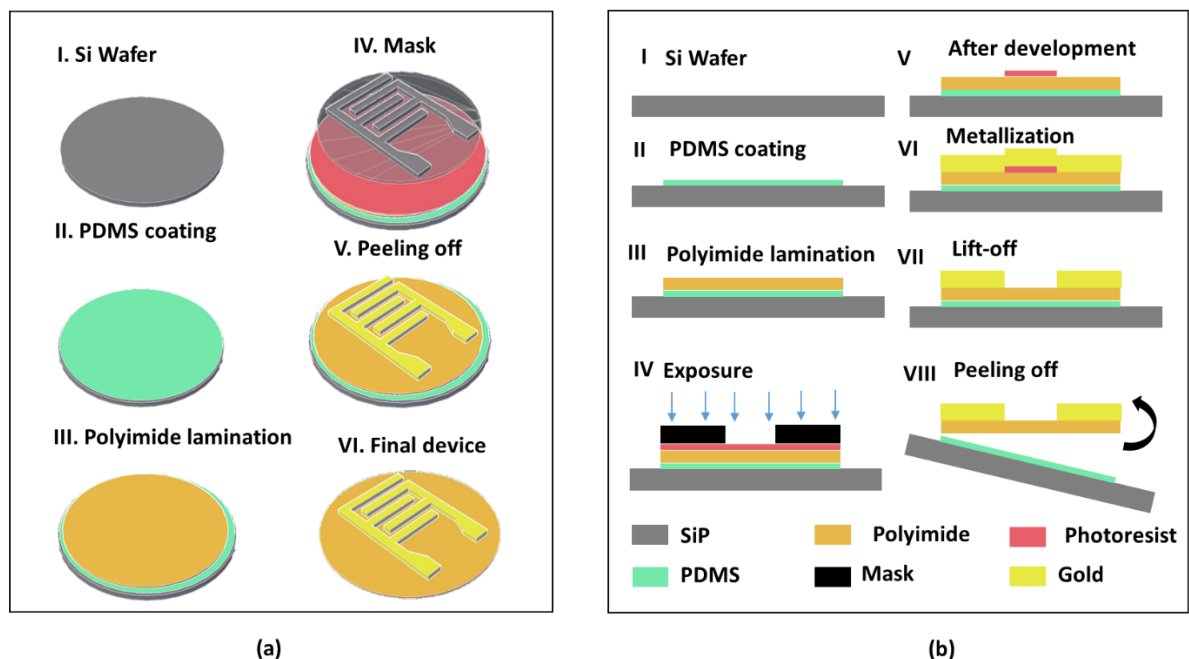


Figure 2.33 : Step-by-step fabrication process for interdigitated electrodes on polyimide: (a) Top view, (b) Cross-sectional view; In the cross-sectional view: (I) 4" p-type silicon wafer, (II) PDMS layer spin-coated on the silicon wafer, (III) Polyimide (PI) lamination, (IV) Deposition of a negative photoresist (PR) layer (nLOF) and transfer of the mask pattern onto the PR layer, (V) Development for 30 seconds (VI) Sputtering of a bilayer of Ti/Au (50 nm/200 nm), (VII) Lift-off and (VIII) Delamination and cutting of the PI layer.

The substrate preparation for selected 4-inch silicon p-type wafers (SiP) consists of O₂ plasma treatment for 5 min at 800 W (TEPLA). At this stage, it is important that the wafers are free from any contamination (dirt, scum, silicon dust, etc.). The backside of the wafer is laminated with a vinyl tape to avoid any PDMS deposition

in subsequent fabrication steps. The purpose of PDMS deposition (Figure 2.33(a)), on hard substrate is to promote adhesion between the wafer and the PI film.

PDMS (polydimethylsiloxane) coating consists of a combination of 10 g Silicone Elastomer (SYLGARD 184) and 1 g of hardener. The mixture is stored in vacuum for sufficient time to get rid of any bubbles present inside which is experimentally observed 15 -20 minutes under vacuum. The bubble-free PDMS solution is then spin-coated (Figure 2.34) onto the silicon wafer at a speed of 5000 rpm for 30 s, Figure 2.33(b-II).

The vinyl film from the backside of the PDMS coated silicon wafer is removed after deposition followed by a wafer annealing for 60 s at 120°C. The purpose of vinyl film is to avoid PDMS sticking on the backside. The process is followed by plasma functionalization of PDMS-SiP for 2 minutes at 60 W in O₂ plasma (TEPLA).

Polyimide substrate lamination: As shown in Figure 2.33(b-III) the next step is the lamination of the wafer with the polyimide film (PI). For this purpose, a polyimide film with a thickness of 127 μm is prepared and cut in the shape of 4" wafers. The PI film is cleaned thoroughly with ethanol, methanol and xylene, in the stated order, followed by rinsing in deionized (DI) water. The cleaned film is dried by using nitrogen gun and kept inside an oven for 12 hours at 120°C.

The PI film retained in the oven in the previous step is now rolled under pressure, over the PDMS coated wafers using SHIPLEY 360, shown in Figure 2.34. The process is carried out at a rolling speed of 0.5 m/min with rolling pressure of 2-3 bar at room temperature. The step ensures that no bubbles are trapped between the two layers as the presence of bubbles may lead to delamination under high temperature (>80°C) during subsequent processes. The rest of the IDE fabrication process on flexible PI film, i.e. IDE patterning and NS deposition, is similar to fabrication of IDE on hard silicon wafer with a SiO₂ layer on top.

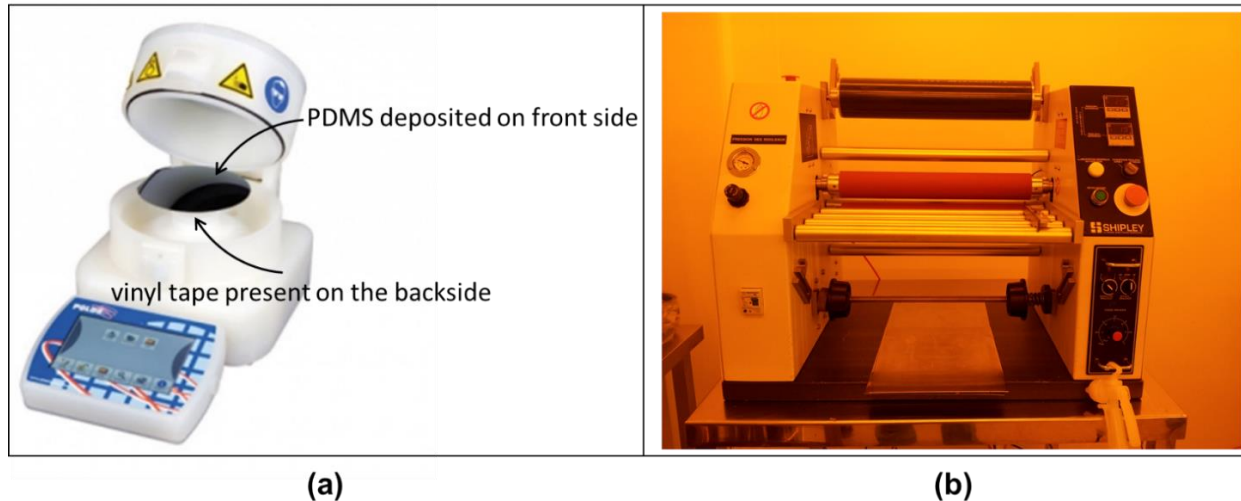


Figure 2.34: (a) Labeled image Spin coater for PDMS deposition (b) Manual laminator model ML 360 is designed to provide reliable lamination

2) Si-SiO₂ Hard Substrate preparation:

For IDE fabrication on hard substrate a p-type silicon (<111>) wafer of thickness $525\ \mu\text{m}$ and resistivity between $7\text{-}12\ \Omega\cdot\text{cm}$ is used. The wafer is thermally oxidized to grow an oxide layer of thickness $600\ \text{nm}$. The SiO₂ layer is used as an insulating base for the IDE and also reduces the parasitic device capacitance, thus enhancing the performance of the final device. The wafers are cleaned in oxygen plasma at 800W for 5 minutes. The subsequent fabrication steps such as photolithography and metallization are common for both - the hard-oxidized silicon substrate and soft PI film supported on a hard substrate as illustrated in Figure 2.33(b) step III – VIII.

Photolithography:

In order to enhance the adhesion between photoresist (PR) and silicon oxide wafer, a HMDS surface treatment (Obducat) at $800\ \text{W}$ has been performed on the wafer prior to photolithography process. It is followed by coating, baking and dissolution of the negative photoresist (using automated EVG lithography equipment), to obtain a $2.5\ \mu\text{m}$ -thick uniform coating of negative PR (nLOF) on the oxidized silicon wafers. The IDE patterns on the chrome mask are transferred onto the wafer surface by an UV exposure of 9 seconds (MA150) followed by the immersion of wafers in a developer

solution (MFCD26). The optimized process ensures good resolution, edge sharpness and process reproducibility.

About the photo Mask. The design of IDE pattern is as shown in Figure 30(b). Photo masks are designed using CleWin® software. The pattern of IDEs is described as a combination of a pair of twin electrodes connected together in a series of tooth and comb-like structures. The separation gap between the intertwined fingers has been optimized to 3 μm . Structures with gaps of 1 μm , 2 μm , 3 μm , 10 μm , 15 μm , and 25 μm have also been fabricated and characterized; 3 μm gap and higher is preferred for the ease of fabrication and good line and edge definition. Lift off process between the electrode gaps is easier at wider separations. These electrodes will be later used to perform dielectrophoresis, in general smaller the electrode gap is, stronger is the electric field experienced between. Hence, 3 μm is used for faster nanostructure bridge formation. The intertwined finger design for the electrodes is optimized with reference to DEP process requirements. Accordingly, the castellated electrode pattern as shown in Figure 30(b) is preferred. The tooth like structure provides better precision during DEP process. The castellated electrodes fabricated by lift-off process results in cleaner structure definition; these are resolved better and have lesser leakage or cross-linking artefacts. Compared with the comb-like pattern, parallel electrode fingers were not well resolved and post lift-off steps usually end with short circuits.

In the case of the PI/PDMS wafers, manual development process is preferred as it facilitates better monitoring and avoidance of delamination of PI films off the PDMS layer coated on the silicon wafers during the baking process. Similar to steps mentioned earlier, a 2.5 μm layer of negative PR (nLOF) is spin coated on the PI surface (by using LabSpin6 BM) at 5000 rpm and at acceleration 5000 rpm/s for 30 s. The wafer is baked at 100°C for 60 s to semi-harden the PR layer. If PI film delaminates in this step, it can simply be roll - pressed onto the same wafer (using SHIPLEY 360). Next, it is exposed to UV light for 9 seconds. For development, wafers are immersed in developer (MFCD26) and slowly stirred for 30-45 seconds followed by a thorough rinse in DI water. A longer development time indicates inadequate exposure and developer driven process; smaller dimensions may not be realized in such a case.

Metallization: The metallization step (Figure 2.33(b)-step VI) consists of Ti (50 nm) – Au (200 nm) sputter deposition. It is followed by a lift-off process where wafers

are immersed in acetone for 2 hours to remove the metal deposited over unwanted areas. After a rinse cycle in fresh acetone and DI water, wafers are annealed for 20 minutes at 250°C in N₂ ambient (by using Si (T-RRD)).

Wafer cutting: At this stage, PI films are simply peeled off the PDMS coated silicon wafers. As shown in Figure 2.35(a), on a 4" wafer we can achieve over ~48 interdigitated electrodes which need to be shaped into individual chips of size and dimensions as shown in Figure 2.35(b). Once ID electrodes are cut, these are tested for unwanted connectivity or improper lift-off, and validated by electrical characterization. Figure 2.35(c) shows three types of IDE structures fabricated on hard oxidized silicon wafer, glass substrate and on PI film. The structures are now ready for the dielectrophoresis step.

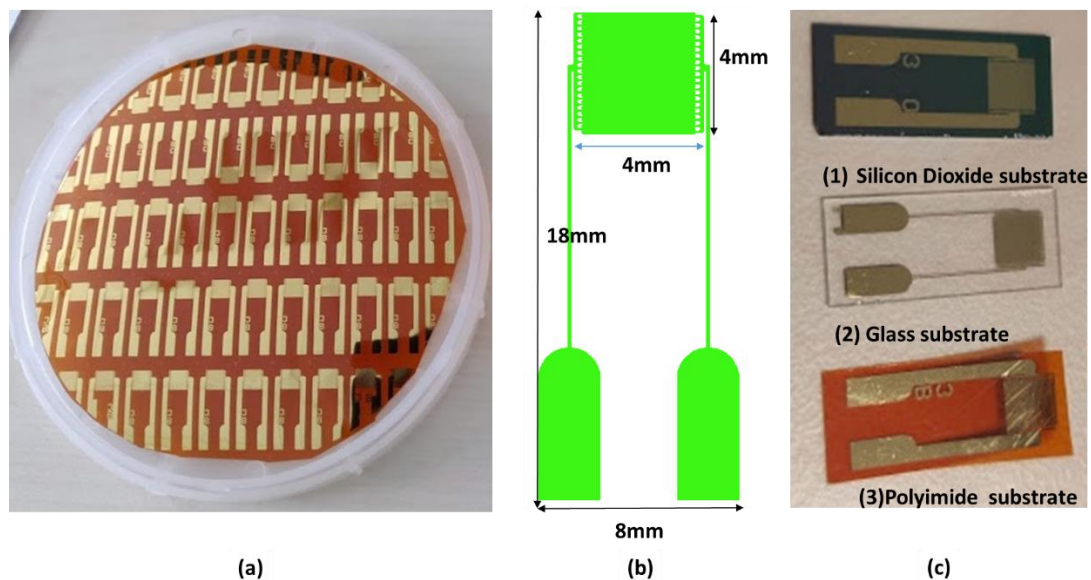


Figure 2.35 : (a) PI substrate with IDE (b) Dimensions of individual chip (c) IDE over (1) Silicon Dioxide substrate (2) Glass Substrate (3) polyimide substrate.

Problems associated with PI film lamination:

- Non-uniform PI film lamination over the silicon wafer:

Air bubbles trapped between silicon wafer and PI film may cause non-uniform film lamination and further lead to improper mask alignment. Therefore, silicon wafer and PI film are thoroughly cleaned to remove any dust or dirt particle to avoid any unwanted non-uniformity. Decreasing the rolling speed during lamination and taking special care along the edges helps in non-uniformity reduction.

- Delamination of PI film during fabrication steps:

Due to poor adhesion the PI films may peel off during high temperature processing steps such as baking/annealing at 100°C. To avoid temperature induced delamination the pre-bake step (after spin coating the PR) is carried out at lower temperature (~80°C) and for increased time. In addition, the PDMS coated silicon wafer surface is treated with HDMS, prior to PI film lamination.

- Improper lift-off between the electrodes or no adhesion of gold on PI:

Figure 2.36(a) shows IDE structures on PI film where the fine-patterned interdigitated part is completely missing. The problem is related to optimization of the development time for photoresist and inferior adhesion of gold on PI. The development time of PR is optimized in steps of a few seconds after the initial time step of 30 seconds, followed by an examination under optical microscope. Figure 2.36(b) and (c) show the structures after the process optimization. Coarse and fine geometries both are well resolved, Figure 3(b).

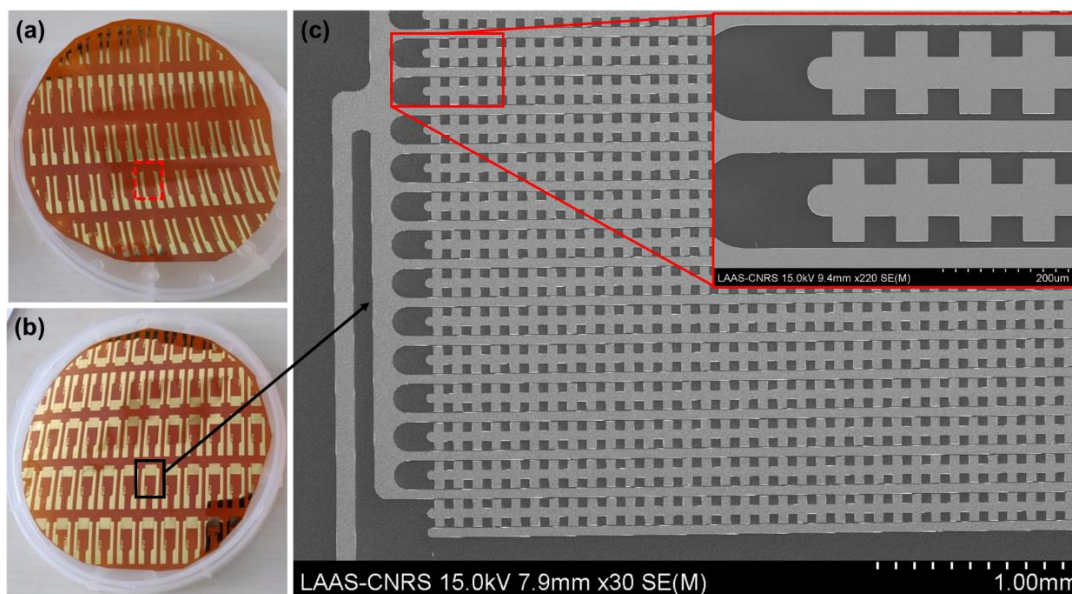


Figure 2.36: (a) Interdigitated part is lost during lift-off because of over-development (b) structures after process optimization (c) Magnified SEM image of well-resolved interdigitated part.

Because of improper lift off and non-uniformity in film, the output of successful IDE fabricated in a single 4-inch wafer is never 100%. In Figure 2.37, an example of one 4-inch wafer is shown with crossed IDE that are not usable because of the

improper lift-off. Either the design is not properly realized from the square shaped mask to almost circular wafer or gold is not properly removed from unwanted places.



Figure 2.37 : Output of a 4-inch wafer with proper 3 μm gap separation between IDE is never 100%.

2.4.2 Fabrication process for the 'active area'

In this part, details of dielectrophoresis set up and procedure to assemble nanostructures using AC-DEP technique are summarized. This study is carried out by positive-DEP. The experimental set-up consists of a source meter (Keithley 2450) connected to the IDE through two metal probes, Figure 2.38. The potential drop across the electrode gap is monitored through an in-house program in LabVIEW software developed by Fabrice Mathieu, research engineer at LAAS. It provides the change in impedance values across the two electrodes in real-time during the experiment.

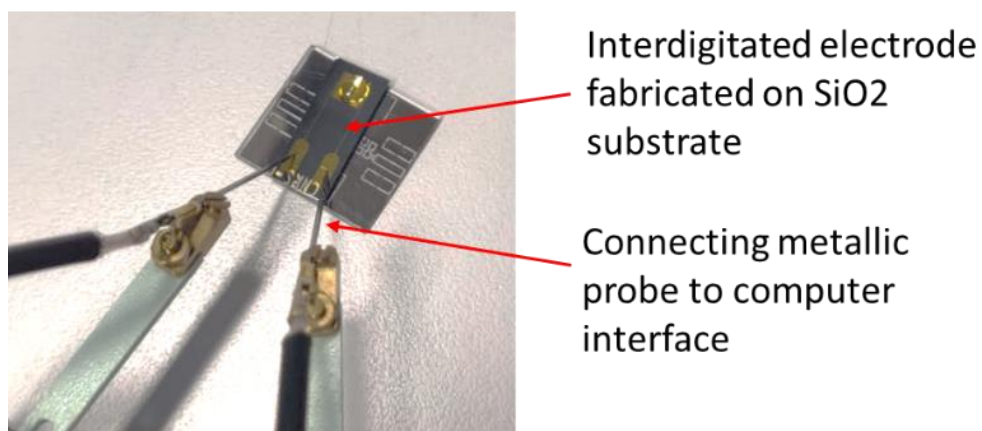


Figure 2.38 : Image showing the placement of connecting probe on IDE

2.4.2.1 Instrumental setup for DEP

The major advantage of DEP is the ability to have the desired particles in the created droplet. First a 10 μL droplet of MPA functionalized gold-helices of concentration 0.01 mg/mL in water is dropped using a micropipette on the IDE fabricated earlier, covering the IDE area as shown in Figure 2.39(a). The required electric field is established by a 10 – 100 kHz sinusoidal signal of 10 V (peak -to- peak) applied across the electrodes (Figure 2.39(b)), from a source-meter (Keithley 2450). The applied AC signal generates a field gradient between the comb-like electrodes. The positive DEP force thus exerted on the dispersed gold-helices, align them along the electric field lines as shown by SEM micrograph in Figure 2.39(a), step-4. The aligned nano-structures establish an interconnection between the IDE. The AC signal is switched off after 30 – 60 seconds and the excess solution is removed with the help of another syringe. It is followed by rinsing of the sample with ethanol and annealing at a temperature of 45°C for 60 seconds.

If the electrodes are fabricated over a PI substrate, a higher temperature cannot be used as it may damage the PI substrate and generate a short circuit. All the experiments have been conducted at room temperature. The experimental procedure is as illustrated in Figure 2.39.

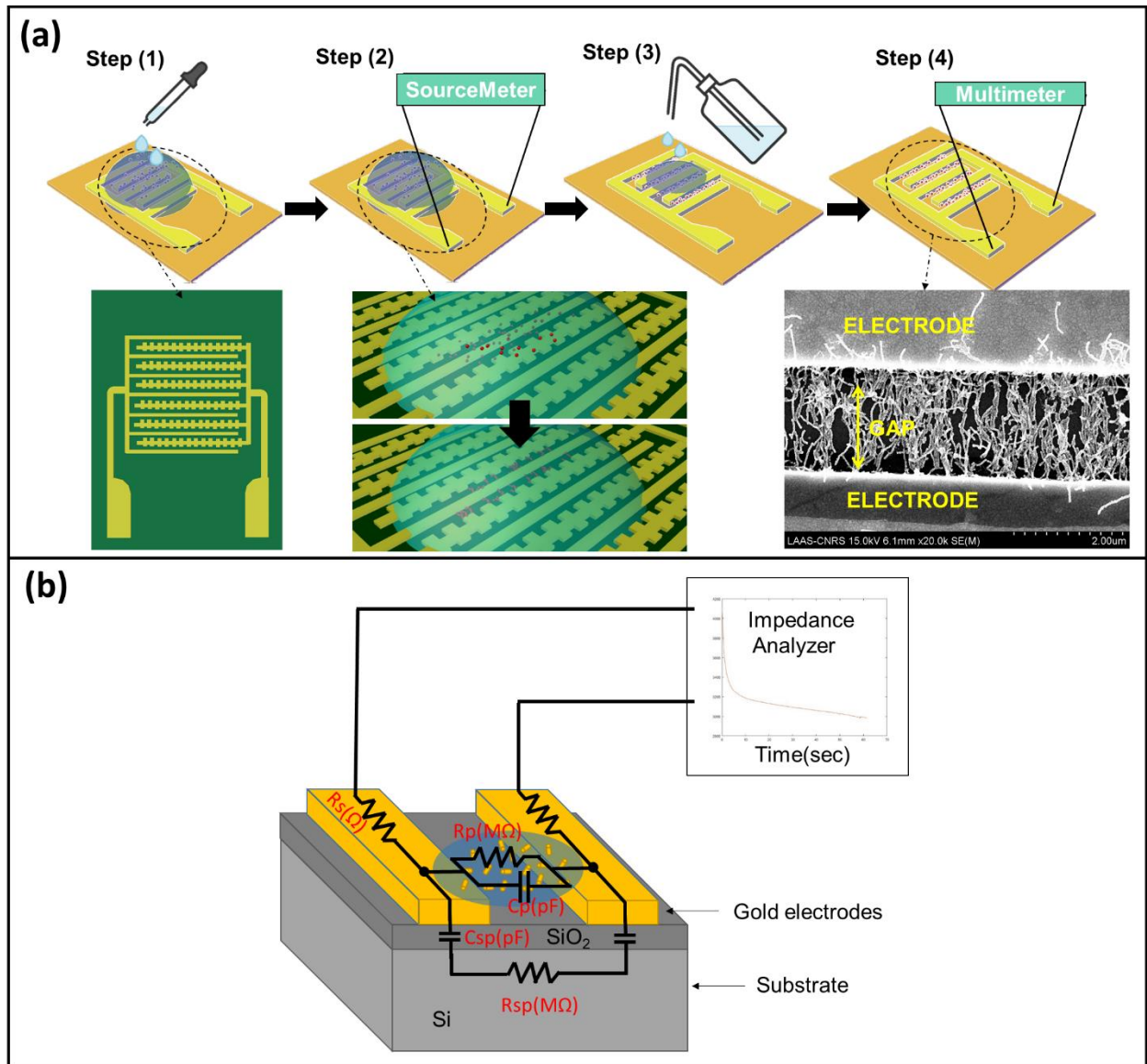


Figure 2.39 : (a) Schematic of Dielectrophoresis: Step 1. Droplet of solution placed over IDE, Step.2 $10 V_{p-p}$ applied between the IDE, Step.3 Sample is cleaned off the excess solution, Step 4. SEM picture of aligned gold helices across the electrode gap, Sample (Sensor chip) is now ready for electrical and mechanical characterization (b) Impedance analyzing system.

It is possible to re-use the IDE where DEP has already been performed. Performing DEP multiple times can help to achieve the desired resistance, Figure 2.40. The resistance is a relevant way to estimate the number of nanostructures deposited on the IDE. Additionally, our industrial partner of this project Nanomade, has provided us with the resistance range value suitable for their fabricated strain sensors. The set range is from 10 k to 100 kΩ.

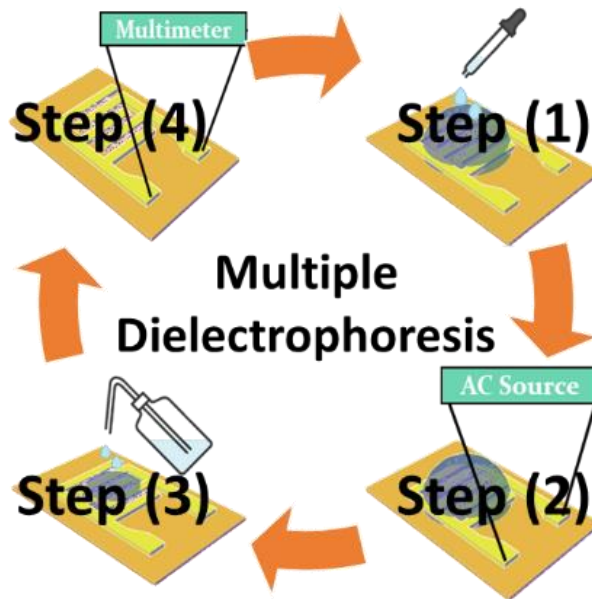


Figure 2.40 : Multiple dielectrophoresis is performed to tune the resistance within the appropriate range for the strain sensor.

The necessary parameters are summarized in Table 5. The deposited nanostructures establish an electric conduction path between the electrodes that is very sensitive to strain. The aligned gold-helices between the gaps after DEP are stable and cannot be removed off the IDE.

Table 5. **Boundary conditions of DEP for Gold Helices**

Solution sample: Gold functionalized with MPA ligand grafted on inorganic silica helices				
Concentration	Voltage	Time range	Frequency range	Measured resistance range
0.001 $\mu\text{L}/\text{mL}$	$\pm 10\text{ V}$	5 – 180 seconds	10 – 100 kHz	10 – 100 $\text{k}\Omega$

In order to get a better understanding of the effect of DEP boundary conditions on the deposition and alignment, the electrical and morphological properties of the devices are characterized. Gold-helices used in this study align directly between the electrodes, Figure 2.41, in a very short period, a few seconds to a few minutes, after the electric field is switched on and remain intact even after rinsing with ethanol/water. It is a faster process in comparison to techniques that require additional evaporation time or film transfer, as in case of vacuum filtration for example. The amount and concentration of nanoparticles in the solution used is also significantly lower.

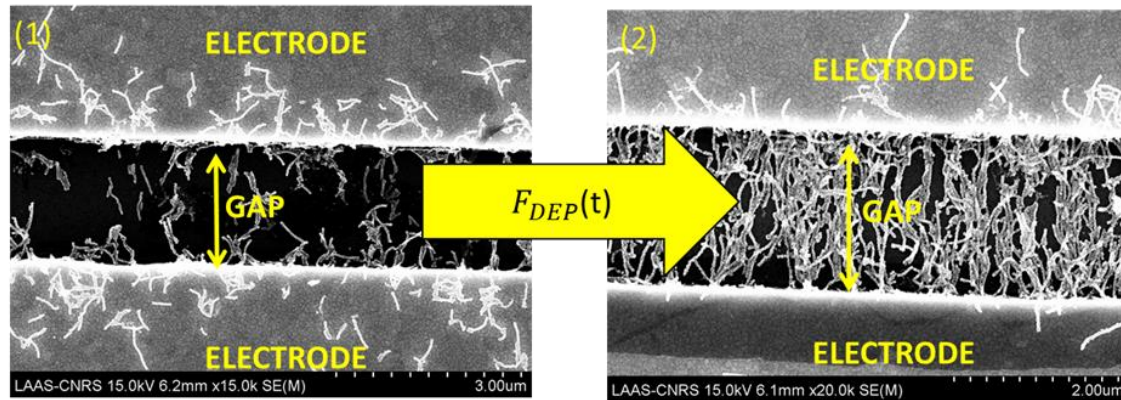


Figure 2.41 : SEM image show the deposition of Gold Helices between 3 μm gaps (1) Initial state of DEP showing dispersed Gold Helices around the electrode (2) In later state of DEP, earlier scattered particles are now well aligned and forming a bridge between the electrode.

2.5 Discussion

2.5.1 Dielectrophoresis comparison with Drop-Casting

Comparison with Drop-casting method. SEM micrographs in Figure 2.42 present a comparison of DEP and drop-cast method. DEP was performed for 300 seconds at 30 kHz frequency with MPA gold functionalized HNS. Post – DEP, IDE is washed with ethanol and annealing for 60 seconds at 90°C. In case of Drop-casting, it is performed for 10 minutes followed by evaporation of solution.

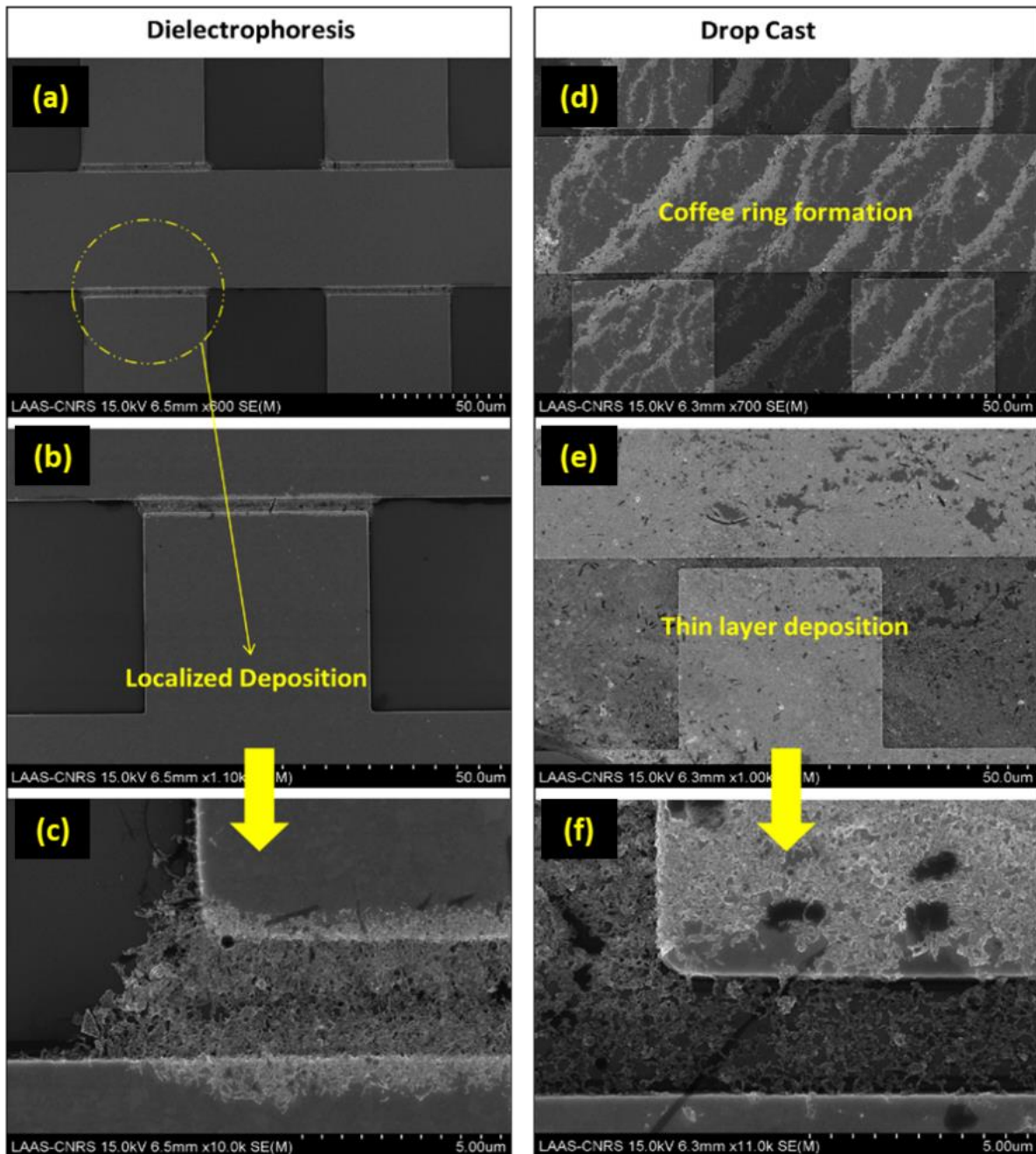


Figure 2.42 : Dielectrophoresis vs Drop-Cast; (a-c) Results of DEP deposition; (d-f) Results of Drop-Cast.

As seen in Figure 2.42(b) one of the major drawbacks of the drop-cast method is the differences in evaporation rates across the substrate that leads to variations in film thickness and internal structure. Figure 2.42(e), show that the deposition is dense but uniformity is poorer. Deposition over the electrode is not useful. DEP needs lesser amount of time to deposit the NS and lower concentration of nanoparticles in the solution. As shown in Figure 2.42(c), for DEP distribution is more localized. Figure

2.42(d) summarizes the experimental ease of DEP in comparison to various other techniques already discussed above.

2.5.2 Helical nanostructures

For Gold Helices, a few batches were prepared in ethanol and some others in deionized water. Each batch had a different combination of functionalizing ligand for AuNP (discussed in *Synthesis of 1D nanohelices with grafted nanoparticles*) the functionalizing ligand provides the nanoparticles with colloidal stability and favor the electrical conduction path within the nanoparticles network. As shown in Figure 2.43, changing the ligand from PEG to MPA has a strong impact on the deposition morphology.

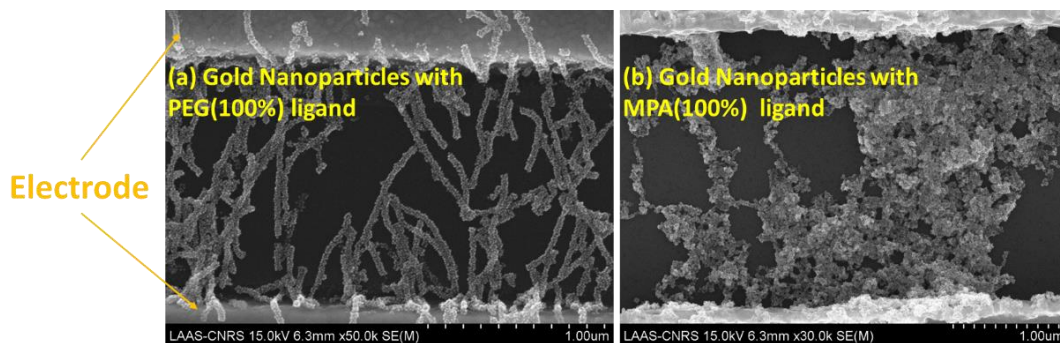


Figure 2.43 : SEM image of various nanoparticles deposition using DEP at same boundary condition. (a) Dense deposition of helical nanostructure made with only PEG ligand attached to AuNP, (b) Clustered deposition of helical nanostructure made with only MPA ligand attached to AuNP.

From a mechanical point of view, one of the main advantages of helical nanostructures is that they resemble mechanical springs. Long helical nanostructures are ‘high aspect ratio structures’, and provide excellent mechanical stretchability and electrical conductivity in the nanowire-like web structures. The structures enable full inter-networking; provide high conductive pathways even at low density with added advantage of ‘stress release’ during mechanical elongation. Reversible sliding [80] or stretching allows the network of helical nanostructures to maintain electrical connectivity, while being stretched to strains greater than the fracture strain for individual nanowires. Coiling of the structures helps in zero-degradation to the helix conductivity after repeated strain cycles. For example, ref. [2] mentioned that the

stretchability arising from a spring structure is 20 times higher than the pure carbon nanotube yarn in straight form, while still sustaining good strength.

2.6 Dielectrophoresis boundary conditions

Certain DEP boundary conditions for deposition of HNS on IDE has been more focused upon. It helps to control the deposition density and to establish conditions for DEP that, overall, creates an efficient flexible strain sensing device.

1. One of the parameters: the alternating electric field can prominently influence the morphology of the resulting nanoparticle assemblies. It implies that larger the voltage input, the stronger the electric field gradient and as a result faster and denser the HNS deposition (considering positive DEP scenario) on IDE.
2. HNS deposition can differ in terms of their deposition outlook when different frequencies input values are used, i.e., if it is positive DEP or negative DEP or crossover frequency situation. The HNS quantity deposition is estimated in terms of device's total resistance.
3. Time of deposition is another parameter. It is possible to increase or decrease the deposition time to have more or lesser HNS deposited between the IDE.
4. Finally considered that all the above parameters are well – calibrated and a DEP deposition is made, if the resulting device does not have the desired resistance value; it is possible to simply make multiple DEP deposition over the same IDE area to achieve the desired results.

Few boundary conditions are more briefly explained using SEM images in the following section:

2.6.1.1 Frequency

1. Deposition Morphology

Different frequency regimes associated with specific morphologies are identified using IDE with 10 castellation sites i.e., 10 deposition sites, Figure 2.44(a). It is clarified using three selected frequency range, Figure 2.44(b).

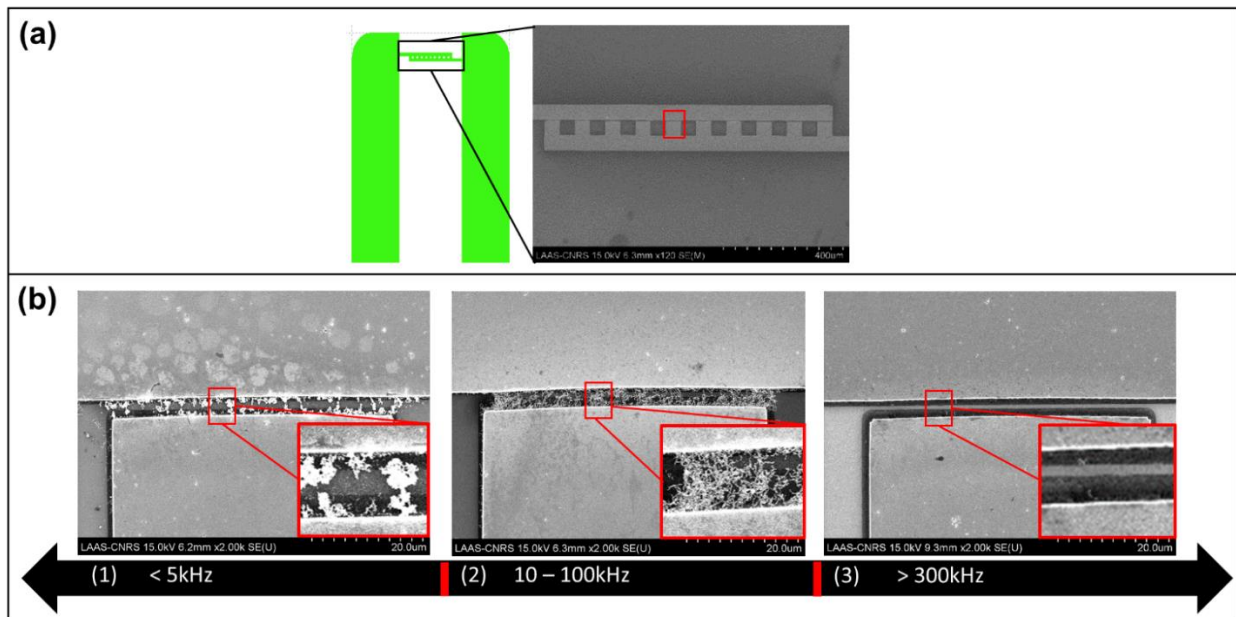


Figure 2.44: (a) Schematic diagram and SEM image of IDE with 10 castellations (b) Deposition morphology at three frequency regimes: (1) Aggregated and scattered deposition observed at lower frequencies (2) Uniform deposition at frequency range 10 - 100 kHz (3) Very low and almost no deposition observed at higher frequencies

Looking at the morphology, Figure 44(b), it can be hypothesized that below < 5 kHz the aggregated particles are attracted more, while at 10-100 kHz deposition appears more uniform. Because the objective is to prepare a uniform network HNS, frequencies 10 – 100 kHz are preferred. Additionally, it is observed that at frequencies greater than 30 kHz, the impedance drop with time is sufficiently slower, giving the benefit of controlling the experiment. Impedance is monitored in real-time using LabVIEW software. Impedance drop signifies the increase in density of NS deposited between the IDE.

2. Device Resistance

In addition to morphological observation, measuring resistance also provides with useful information, Figure 2.45. At 1 kHz, the measured resistance of this device was 10Ω . While at 50 kHz, it measured to be $400k\Omega$. At 100 kHz, IDE had no alignment of HNS and hence electrodes remained unconnected.

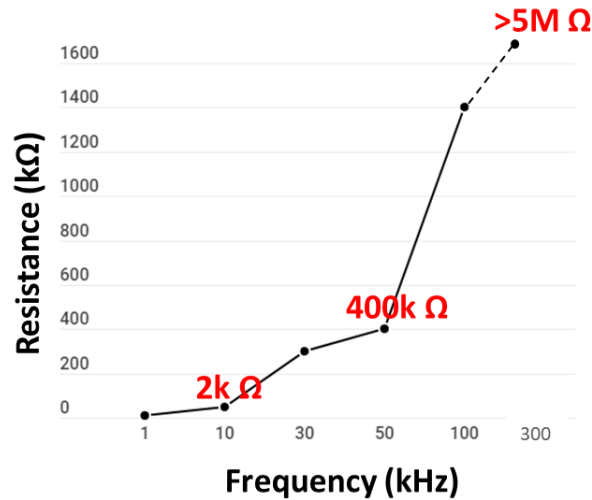


Figure 2.45: Resulting device resistance vs input DEP frequency relation is almost linear.

Later in Chapter – 3, the significance and effect of a certain resistance value towards the performance of sensing device is explained. As for the objective during HNS deposition via DEP is concerned, aim is always to achieve a resistance value between $[500, 20 \text{ k}] \Omega$. This implies that frequency between 10 kHz – 100 kHz stimulates ideal HNS deposition between the IDE, Figure 2.46(a, b). Above 300 kHz, there was no measurable resistance variation, Figure 2.46(c). As shown in Figure 2.46, each experiment is performed for 30 seconds.

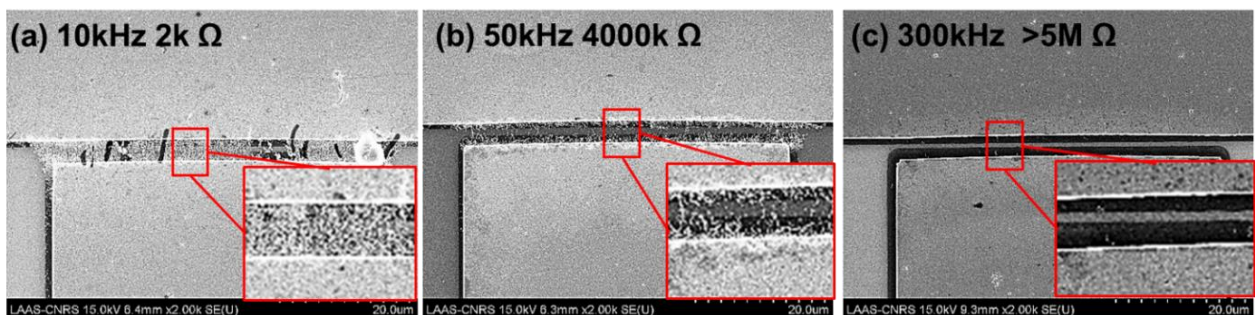


Figure 2.46 : SEM images of deposition made at: (a) 10 kHz frequency (b) 50 kHz frequency (c) 300 kHz frequency.

Resistance value increases with increasing frequency at fixed 30 seconds of deposition time. Lower frequency requires lesser time to achieve desired resistance range i.e., 10k – 100k Ω . While higher frequencies require more time. This could be explained in relation to the previous section on Clausius-Mossotti factor $K(\omega)$. It can be assumed that HNS experiences a positive DEP at frequency below 100 kHz.

Linearity of frequency and deposition rate implies that from 10 kHz to 100 kHz, DEP is at a transition phase from positive to negative, Figure 2.21. At 300 kHz there is almost no deposition signifying that DEP has reached a crossover frequency stage. Results and hypothesizes above are only specific to HNS.

The solution should be completely homogeneous for each experiment of DEP, but particles tend to aggregate. Experimentally it has been observed that, the morphology i.e., deposition density and device resistance are not completely reproducible, due to the solution inhomogeneity and aggregation.

2.6.1.2 Deposition time

By tuning the time and relative strength of the DEP force, the number of captured HNS between the electrodes can be controlled, Figure 2.47. For HNS, a time range of 10 s – 300 s is sufficient to achieve desirable results in terms of the resulting resistances. Time to achieve a chosen deposition density/resistance, also depends on the concentration and composition of the solution.

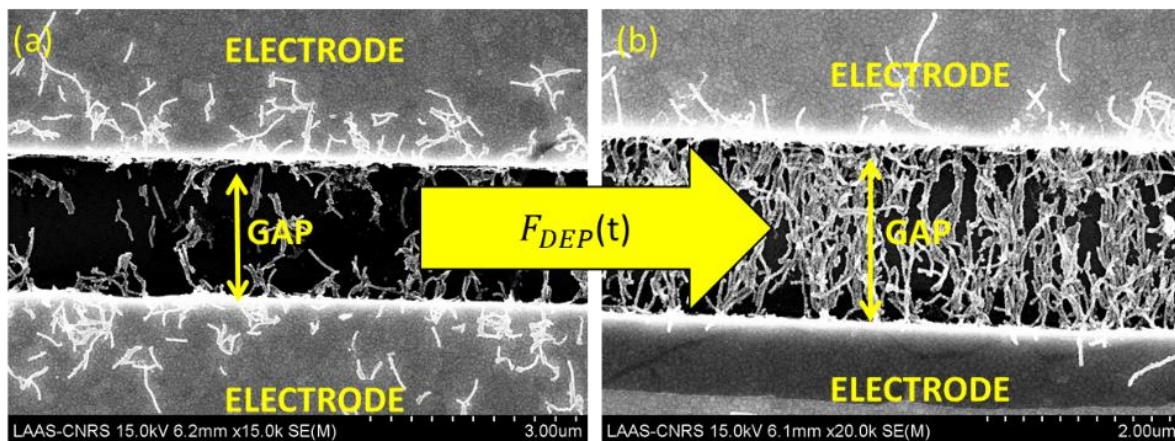


Figure 2.47 : Scanning electron microscope image of DEP process at (a) t seconds and (b) $t + \Delta t$ seconds, density increased because of longer time during which the DEP force is applied

2.6.2 Dielectrophoresis Challenges

2.6.2.1 Solution Aggregation

During dielectrophoresis process, large aggregates/agglomeration in solution can create short circuit. That can block the field force from attracting the dispersed NS. As explained using Figure 2.48, the two otherwise different sample have similar

resistance value ($<50 \Omega$). The morphology of Sample (a) is uniform and dense than Sample (b). Sample (b) had an abrupt 'stoppage' in between the experiment.

DEP does not occur when there is a complete connection formed between the electrodes. As a result, the sample had to be discarded. Aggregation increases with aging of the solution. Presence of the agglomerates in a solution deteriorate their electrical and mechanical properties and decrease their homogeneity.

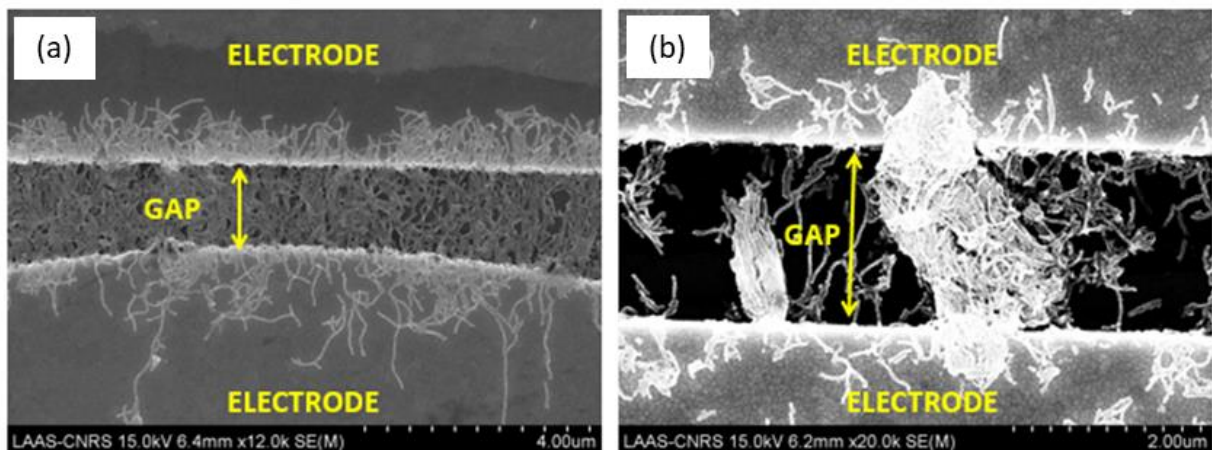


Figure 2.48 : SEM image of (a) Uniform DEP deposition (b) Incomplete DEP process hindered in presence of aggregate.

Ultra-sonication of these sediment solutions breaks the long strands creating smaller strands, which tend to aggregate again over time.

2.6.2.2 Unpredictability

Using a non-homogeneous solution for DEP deposition creates unpredictability in the amount of HNS deposited from one sample to the another. Reason for that is size dependency of particle during DEP i.e., larger the size of particle more attracted it will be towards the maximum of non-uniform electric field. Hence, in a non-uniform solution larger aggregate will be deposited first followed by the smaller nanoparticles. This can further create a difference in overall performance of the device. It is required that prior to a dielectrophoresis deposition solution is well sonicated and proper vortex mixing is done.

2.7 Conclusion

A flexible strain sensor has been built using a simple, dielectrophoresis alignment technique to form conductive paths between interdigitate electrodes on a flexible substrate, using a solution based on helical nanostructures.

Helical Nanostructure. Active sensing material used is: covalently grafted functionalized gold nanoparticle (AuNP) on nanohelices by an amide bond. The AuNP were functionalized by ligands such as SH-PEG7-COOH (PEG) and Mercaptopropionic Acid (MPA). Simply referred to as Helical Nano-Structures (HNS).

Technique. Dielectrophoresis technique has been compared with Drop-Cast deposition. DEP is efficient in time and make it possible to obtain an alignment of the HNS during deposition with lesser wastage of HNS during deposition. The electrical performances of the strain sensors are easily tunable by controlling the density of HNSs on the IDE. By adjusting the deposition parameters, the amount and alignment of HNS can be modified to increase the resistance of the Strain Sensing device. Resistance is an important parameter when sensitivity and stability of sensor device are concerned; this will be discussed in more details in next chapter, Chapter – 3. The goal of this chapter was to analyses the theoretical and experimental parameters of DEP, which provides more control on deposition density. Effect of boundary conditions such as voltage, frequency and deposition time has been discussed, by (1) looking at morphology through SEM and (2) measuring the final resistance of the device. Additionally, it has been experimentally observed that there is a possibility to carrying out multiple DEP over the same sample in order to gain desired results. DEP input voltage was fixed at 10 V_{p-p}, HNS were operate at 30 kHz frequency for 30 seconds. However, frequency and time were the two parameters most explored and varied from one experiment to another for purpose of obtaining expected deposition.

However, it is emphasized that the solution should not have any aggregation. HNS solution tends to aggregate. Prior to each deposition HNS solution underwent sonification and/or vortex. During DEP experiment, it was observed that a non-homogeneity of HNS solution generated non-uniformity in deposition network and as a result, it adversely effects the device performance.

Next step is to analyze the mechanism of resulting strain sensors, their response to low strain and their stability. The mechanical analyses and

characterization in accordance with the theoretical expectations for validation purposes. The details on strain sensor characterization methods are followed by a discussion on the generated results.

Bibliography

- [1] J. He *et al.*, “Recent advances of wearable and flexible piezoresistivity pressure sensor devices and its future prospects,” *J. Mater.*, vol. 6, no. 1, pp. 86–101, 2020.
- [2] N. Wen *et al.*, “Emerging flexible sensors based on nanomaterials: recent status and applications,” *J. Mater. Chem. A*, vol. 8, no. 48, pp. 25499–25527, 2020.
- [3] M. Amjadi, K. U. Kyung, I. Park, and M. Sitti, “Stretchable, Skin-Mountable, and Wearable Strain Sensors and Their Potential Applications: A Review,” *Adv. Funct. Mater.*, vol. 26, no. 11, pp. 1678–1698, 2016.
- [4] A. Morteza *et al.*, “Highly stretchable and sensitive strain sensor based on silver nanowire-elastomer nanocomposite,” *ACS Nano*, vol. 8, no. 5, pp. 5154–5163, May 2014.
- [5] S. R. Kim, J. H. Kim, and J. W. Park, “Wearable and Transparent Capacitive Strain Sensor with High Sensitivity Based on Patterned Ag Nanowire Networks,” *ACS Appl. Mater. Interfaces*, vol. 9, no. 31, pp. 26407–26416, 2017.
- [6] Z. Yang *et al.*, “Graphene Textile Strain Sensor with Negative Resistance Variation for Human Motion Detection,” *ACS Nano*, vol. 12, no. 9, pp. 9134–9141, 2018.
- [7] J. Lee *et al.*, “A stretchable strain sensor based on a metal nanoparticle thin film for human motion detection,” *Nanoscale*, vol. 6, no. 20, pp. 11932–11939, 2014.
- [8] F. Xu and Y. Zhu, “Highly conductive and stretchable silver nanowire conductors,” *Adv. Mater.*, vol. 24, no. 37, pp. 5117–5122, 2012.
- [9] S. Huang *et al.*, “Stretchable Strain Vector Sensor Based on Parallely Aligned Vertical Graphene,” *ACS Appl. Mater. Interfaces*, vol. 11, no. 1, pp. 1294–1302, 2019.
- [10] T. Yan, Z. Wang, Y. Q. Wang, and Z. J. Pan, “Carbon/graphene composite nanofiber yarns for highly sensitive strain sensors,” *Mater. Des.*, vol. 143, no. 2017, pp. 214–223, Apr. 2018.

- [11] T. Yamada *et al.*, “A stretchable carbon nanotube strain sensor for human-motion detection,” *Nat. Nanotechnol.*, vol. 6, no. 5, pp. 296–301, 2011.
- [12] B. Ketelsen *et al.*, “Fabrication of Strain Gauges via Contact Printing: A Simple Route to Healthcare Sensors Based on Cross-Linked Gold Nanoparticles,” *ACS Applied Materials and Interfaces*, vol. 10, no. 43, pp. 37374–37385, 2018.
- [13] X. Wang, J. Sparkman, and J. Gou, “Strain sensing of printed carbon nanotube sensors on polyurethane substrate with spray deposition modeling,” *Compos. Commun.*, vol. 3, no. September 2016, pp. 1–6, Mar. 2017.
- [14] T. Han *et al.*, “Gold/polyimide-based resistive strain sensors,” *Electron.*, vol. 8, no. 5, 2019.
- [15] D. Jung *et al.*, “A soft pressure sensor array based on a conducting nanomembrane,” *Micromachines*, vol. 12, no. 8, pp. 1–11, 2021.
- [16] J. L. Tanner, D. Mousadakos, P. Broutas, S. Chatzandroulis, Y. S. Raptis, and D. Tsoukalas, “Nanoparticle strain sensor,” *Procedia Eng.*, vol. 25, pp. 635–638, 2011.
- [17] J. K. Carrow and A. K. Gaharwar, “Bioinspired polymeric nanocomposites for regenerative medicine,” *Macromol. Chem. Phys.*, vol. 216, no. 3, pp. 248–264, 2015.
- [18] M. R. Willner and P. J. Vikesland, “Nanomaterial enabled sensors for environmental contaminants,” *J. Nanobiotechnology*, pp. 1–16, 2018.
- [19] E. Aslanidis, E. Skotadis, E. Moutoulas, and D. Tsoukalas, “Thin film protected flexible nanoparticle strain sensors: Experiments and modeling,” *Sensors (Switzerland)*, vol. 20, no. 9, pp. 25–27, 2020.
- [20] J. Herrmann, K. H. Müller, T. Reda, G. R. Baxter, B. Raguse, and G. J. J. B. De Groot, “Nanoparticle films as sensitive strain gauges,” *Appl. Phys. Lett.*, vol. 91, no. 18, pp. 1–4, 2007.
- [21] T. N. Ly and S. Park, “Wearable strain sensor for human motion detection based on ligand-exchanged gold nanoparticles,” *J. Ind. Eng. Chem.*, vol. 82, pp. 122–129, 2020.

- [22] W. S. Lee, S. Jeon, and S. J. Oh, "Wearable sensors based on colloidal nanocrystals," *Nano Converg.*, vol. 6, no. 1, 2019.
- [23] S. W. Lee, H. Joh, M. Seong, W. S. Lee, J. H. Choi, and S. J. Oh, "Engineering surface ligands of nanocrystals to design high performance strain sensor arrays through solution processes," *J. Mater. Chem. C*, vol. 5, no. 9, pp. 2442–2450, 2017.
- [24] J. Park, H. Zheng, W. C. Lee, P. L. Geissler, E. Rabani, and A. P. Alivisatos, "Direct observation of nanoparticle superlattice formation by using liquid cell transmission electron microscopy," *ACS Nano*, vol. 6, no. 3, pp. 2078–2085, 2012.
- [25] M. Cavallini, "Status and perspectives in thin films and patterning of spin crossover compounds," *Phys. Chem. Chem. Phys.*, vol. 14, no. 34, pp. 11867–11876, 2012.
- [26] H. Li *et al.*, "Preventing the coffee-ring effect and aggregate sedimentation by: In situ gelation of monodisperse materials," *Chem. Sci.*, vol. 9, no. 39, pp. 7596–7605, 2018.
- [27] Y.-S. Ryu, D.-K. Lee, J.-H. Kang, S.-H. Lee, E.-S. Yu, and M. Seo, "Ultrasensitive terahertz sensing of gold nanoparticles inside nano slot antennas," *Opt. Express*, vol. 25, no. 24, p. 30591, 2017.
- [28] F. Spaepen, "Interfaces and stresses in thin films," *Acta Mater.*, vol. 48, no. 1, pp. 31–42, 2000.
- [29] H. N. Yow, M. Goikoetxea, L. Goehring, and A. F. Routh, "Effect of film thickness and particle size on cracking stresses in drying latex films," *J. Colloid Interface Sci.*, vol. 352, no. 2, pp. 542–548, 2010.
- [30] G. Cummins and M. P. Y. Desmulliez, "Inkjet printing of conductive materials: A review," *Circuit World*, vol. 38, no. 4, pp. 193–213, 2012.
- [31] K. N. Al-milaji, "Material Interactions and Self-Assembly in Inkjet Printing," 2019.
- [32] O. Kravchuk, R. Lesyuk, Y. Bobitski, and M. Reichenberger, "Sintering Methods of Inkjet-Printed Silver Nanoparticle Layers," in *Nanooptics*,

- Nanophotonics, Nanostructures, and Their Applications*, 2018, pp. 317–339.
- [33] P. Sundriyal and S. Bhattacharya, “Inkjet-Printed Sensors on Flexible Substrates,” pp. 89–113, 2018.
- [34] T. Breinlinger and T. Kraft, “A simple method for simulating the coffee stain effect,” *Powder Technol.*, vol. 256, pp. 279–284, 2014.
- [35] G. D. Martin, S. D. Hoath, and I. M. Hutchings, “Inkjet printing - The physics of manipulating liquid jets and drops,” *J. Phys. Conf. Ser.*, vol. 105, no. 1, 2008.
- [36] N. Amdy Makhoulouf, Abdel Salam Abu-Thabit, *Advances in smart coatings and thin films for future industrial and biomedical engineering applications*. Elsevier Science Publishing Co Inc, 2019.
- [37] “Spin Coating: Complete Guide to Theory and Techniques.” [Online]. Available: <https://www.ossila.com/pages/spin-coating>.
- [38] X. Song, S. Liu, Z. Gan, Q. Lv, H. Cao, and H. Yan, “Controllable fabrication of carbon nanotube-polymer hybrid thin film for strain sensing,” *Microelectron. Eng.*, vol. 86, no. 11, pp. 2330–2333, 2009.
- [39] J. H. Lee, B. S. Kong, Y. K. Baek, S. B. Yang, and H. T. Jung, “Tin nanoparticle thin film electrodes fabricated by the vacuum filtration method for enhanced battery performance,” *Nanotechnology*, vol. 20, no. 23, 2009.
- [40] W. Gao and J. Kono, “Science and applications of wafer-scale crystalline carbon nanotube films prepared through controlled vacuum filtration,” *R. Soc. Open Sci.*, vol. 6, no. 3, 2019.
- [41] O. Kanoun *et al.*, “Flexible carbon nanotube films for high performance strain sensors,” *Sensors (Switzerland)*, vol. 14, no. 1, pp. 10042–10071, Mar. 2019.
- [42] Y. Zhou, L. Hu, and G. Grüner, “A method of printing carbon nanotube thin films,” *Appl. Phys. Lett.*, vol. 88, no. 12, pp. 14–17, 2006.
- [43] M. M. Cheng *et al.*, “Recent developments in graphene-based/nanometal composite filter membranes,” *RSC Adv.*, vol. 7, no. 76, pp. 47886–47897, 2017.
- [44] B. Su, Y. Wu, and L. Jiang, “The art of aligning one-dimensional (1D)

- nanostructures,” *Chem. Soc. Rev.*, vol. 41, no. 23, pp. 7832–7856, 2012.
- [45] Z. Fan *et al.*, “Wafer-Scale Assembly of Highly Ordered Semiconductor Nanowire Arrays by Contact Printing,” *NANO Lett.*, vol. 8, pp. 20–25, 2008.
- [46] A. Perl, D. N. Reinhoudt, and J. Huskens, “Microcontact printing: Limitations and achievements,” *Adv. Mater.*, vol. 21, no. 22, pp. 2257–2268, 2009.
- [47] J. Haibat *et al.*, “Preliminary demonstration of energy-efficient fabrication of aligned CNT-polymer nanocomposites using magnetic fields,” *Compos. Sci. Technol.*, vol. 152, pp. 27–35, 2017.
- [48] O. Trotsenko, A. Tokarev, A. Gruzd, T. Enright, and S. Minko, “Magnetic field assisted assembly of highly ordered percolated nanostructures and their application for transparent conductive thin films,” *Nanoscale*, vol. 7, no. 16, pp. 7155–7161, 2015.
- [49] H. Schiff and A. Kristensen, *Nanoimprint Lithography – Patterning of Resists Using Molding*. Springer, Berlin, Heidelberg, 2010.
- [50] L. Jiang, H. Dong, and W. Hu, “Controlled growth and assembly of one-dimensional ordered nanostructures of organic functional materials,” *Soft Matter*, vol. 7, no. 5, pp. 1615–1630, 2011.
- [51] S. J. Park *et al.*, “Modulation of the effective density and refractive index of carbon nanotube forests via nanoimprint lithography,” *Carbon N. Y.*, vol. 129, pp. 8–14, 2018.
- [52] O. Assad, A. M. Leshansky, B. Wang, T. Stelzner, S. Christiansen, and H. Haick, “Spray-coating route for highly aligned and large-scale arrays of nanowires,” *ACS Nano*, vol. 6, no. 6, pp. 4702–4712, 2012.
- [53] R. Blell *et al.*, “Generating in-Plane Orientational Order in Multilayer Films Prepared by Spray-Assisted Layer-by-Layer Assembly,” *ACS Nano*, vol. 11, no. 1, pp. 84–94, 2017.
- [54] H. Hu, M. Pauly, O. Felix, and G. Decher, “Spray-assisted alignment of Layer-by-Layer assembled silver nanowires: A general approach for the preparation of highly anisotropic nano-composite films,” *Nanoscale*, vol. 9, no. 3, pp. 1307–1314, 2017.

- [55] H. Sung and M. Choi, “n,” *KONA Powder Part. J.*, vol. 30, no. 30, pp. 31–46, 2012.
- [56] D. Li, Y. Wang, and Y. Xia, “Electrospinning Nanofibers as Uniaxially Aligned Arrays and Layer-by-Layer Stacked Films,” *Adv. Mater.*, vol. 16, no. 4, pp. 361–366, 2004.
- [57] R. Pethig, “Dielectrophoresis: Status of the theory, technology, and applications,” *Biomicrofluidics*, vol. 4, no. 2, p. 022811, 2010.
- [58] C. Zhang, K. Khoshmanesh, A. Mitchell, and K. Kalantar-Zadeh, “Dielectrophoresis for manipulation of micro/nano particles in microfluidic systems,” *Anal. Bioanal. Chem.*, vol. 396, no. 1, pp. 401–420, 2010.
- [59] A. Mortadi, A. El Melouky, E. G. Chahid, R. El Moznine, and O. Cherkaoui, “Studies of the clausius–Mossotti factor,” *J. Phys. Stud.*, vol. 20, no. 4, pp. 4001-1-4001–4, 2016.
- [60] R. Pethig, “Review-where is dielectrophoresis (DEP) going?,” *J. Electrochem. Soc.*, vol. 164, no. 5, pp. B3049–B3055, 2017.
- [61] P. R. C. Gascoyne, J. Vykoukal, G. P. RC, and V. Jody, “Particle separation by dielectrophoresis,” *Electrophoresis*, vol. 23, no. 13, pp. 1973–1983, 2002.
- [62] Y. Y. Lin and U. Lei, “Measurement of the imaginary part of the clausius-mossotti factor,” *Proc. 16th Int. Conf. Miniaturized Syst. Chem. Life Sci. MicroTAS 2012*, pp. 368–370, 2012.
- [63] M. R. Buyong, A. A. Kayani, A. A. Hamzah, and B. Y. Majlis, “Dielectrophoresis manipulation: Versatile lateral and vertical mechanisms,” *Biosensors*, vol. 9, no. 1, 2019.
- [64] H. Zhang, H. Chang, and P. Neuzil, “DEP-on-a-chip: Dielectrophoresis applied to microfluidic platforms,” *Micromachines*, vol. 10, no. 6, pp. 1–22, 2019.
- [65] K. Khoshmanesh, S. Nahavandi, S. Baratchi, A. Mitchell, and K. Kalantar-zadeh, “Dielectrophoretic platforms for bio-microfluidic systems,” *Biosens. Bioelectron.*, vol. 26, no. 5, pp. 1800–1814, 2011.
- [66] J. Kadaksham, P. Singh, and N. Aubry, “Manipulation of particles using

- dielectrophoresis," *Mech. Res. Commun.*, vol. 33, no. 1, pp. 108–122, 2006.
- [67] P. Singh and N. Aubry, "Transport and deformation of droplets in a microdevice using dielectrophoresis," *Electrophoresis*, vol. 28, no. 4, pp. 644–657, 2007.
- [68] M. P. Hughes, "Strategies for dielectrophoretic separation in laboratory-on-a-chip systems," *Electrophoresis*, vol. 23, no. 16, pp. 2569–2582, 2002.
- [69] J. G. Kralj, M. T. W. Lis, M. A. Schmidt, and K. F. Jensen, "Continuous dielectrophoretic size-based particle sorting," *Anal. Chem.*, vol. 78, no. 14, pp. 5019–5025, 2006.
- [70] M. Urdaneta and E. Smela, "Multiple frequency dielectrophoresis," *Electrophoresis*, vol. 28, no. 18, pp. 3145–3155, 2007.
- [71] A. D. GOATER and R. PETHIG, "Electrorotation and dielectrophoresis," *Parasitology*, vol. 117, no. 7, pp. 177–189, 1999.
- [72] N. A. Rahman, F. Ibrahim, and B. Yafouz, "Dielectrophoresis for biomedical sciences applications: A review," *Sensors (Switzerland)*, vol. 17, no. 3, pp. 1–27, 2017.
- [73] E. O. Adekanmbi and S. K. Srivastava, "Dielectrophoretic applications for disease diagnostics using lab-on-a-chip platforms," *Lab Chip*, vol. 16, no. 12, pp. 2148–2167, 2016.
- [74] Y. Liu, J. H. Chung, W. K. Liu, and R. S. Ruoff, "Dielectrophoretic assembly of nanowires," *J. Phys. Chem. B*, vol. 110, no. 29, pp. 14098–14106, 2006.
- [75] K. H. Bhatt and O. D. Velev, "Control and Modeling of the Dielectrophoretic Assembly of On-Chip Nanoparticle Wires," *Langmuir*, vol. 20, no. 2, pp. 467–476, 2004.
- [76] J. Cheng *et al.*, "GoldHelix: Gold Nanoparticles Forming 3D Helical Superstructures with Controlled Morphology and Strong Chiroptical Property," *ACS Nano*, vol. 11, no. 4, pp. 3806–3818, 2017.
- [77] S. Raychaudhuri, S. A. Dayeh, D. Wang, and E. T. Yu, "Precise semiconductor nanowire placement through dielectrophoresis," *Nano Lett.*, vol. 9, no. 6, pp. 2260–2266, 2009.

- [78] A. Amestoy, "Synthèse de nanohélices hybrides par auto-assemblage de type 'bottom up' pour la fabrication de capteurs de déformation flexibles," L'UNIVERSITÉ DE BORDEAUX, 2020.
- [79] J. W. Slot and H. J. Geuze, "A new method of preparing gold probes for multiple-labeling cytochemistry," *Eur. J. Cell Biol.*, vol. 38, no. 1, p. 87—93, 1985.
- [80] J. Wu, J. Zang, A. R. Rathmell, X. Zhao, and B. J. Wiley, "Reversible sliding in networks of nanowires," *Nano Lett.*, vol. 13, no. 6, pp. 2381–2386, 2013.

Chapter 3: Mechanical Characterization

Introduction

In the previous chapter, the theoretical and experimental considerations regarding the deposition of Helical Nanostructures (HNS) through Dielectrophoresis (DEP) technique over interdigitated castellated electrodes were presented. The fabrication of interdigitated electrodes (IDE) was described as well.

In this chapter, first the necessary steps towards a complete calibration of mechanical test bench are presented. The results of mechanical analyses and characterization of fabricated HNS are compared with the theoretically expected results for validation purposes. The details on strain sensor characterization methods are followed by a discussion on the obtained results. At the end of this chapter, the possibility of using HNS devices as multimodal sensors is discussed.

3.1. Measurement protocols

An overview of the characterization set-up is presented. In the following section the three-point bending bench, HNS sensors preparation and placement are described in detail.

3.1.1. Flexural Test Setup

The deformation sensor is characterized using a Mark 10 ESM three-point bending bench. Three-point bending is used to evaluate the sensitivity of strain sensor; their fabrication process has been explained in the previous chapter. The measurement of the change in resistance during deformation is done with a Keithley 2450 connected to the electrodes using alligator clips. The deformation force is applied by a tip moving from top to bottom, while the substrate is held by two supports as shown in Figure 3.1. The set-up consists of three-point bending fixture, a commercial mechanical testing apparatus ESM303 with a Force Gauge Model M5-2 designed for tension and compression forces. The rate of descent of the tip can be varied from 0.5mm/min to 1,100 mm/min. The applied force is controlled with a capacity ranging from 0.5 N to 10 kN. The accuracy is $\pm 0.1\%$ of full scale with a resolution of 1/5000.

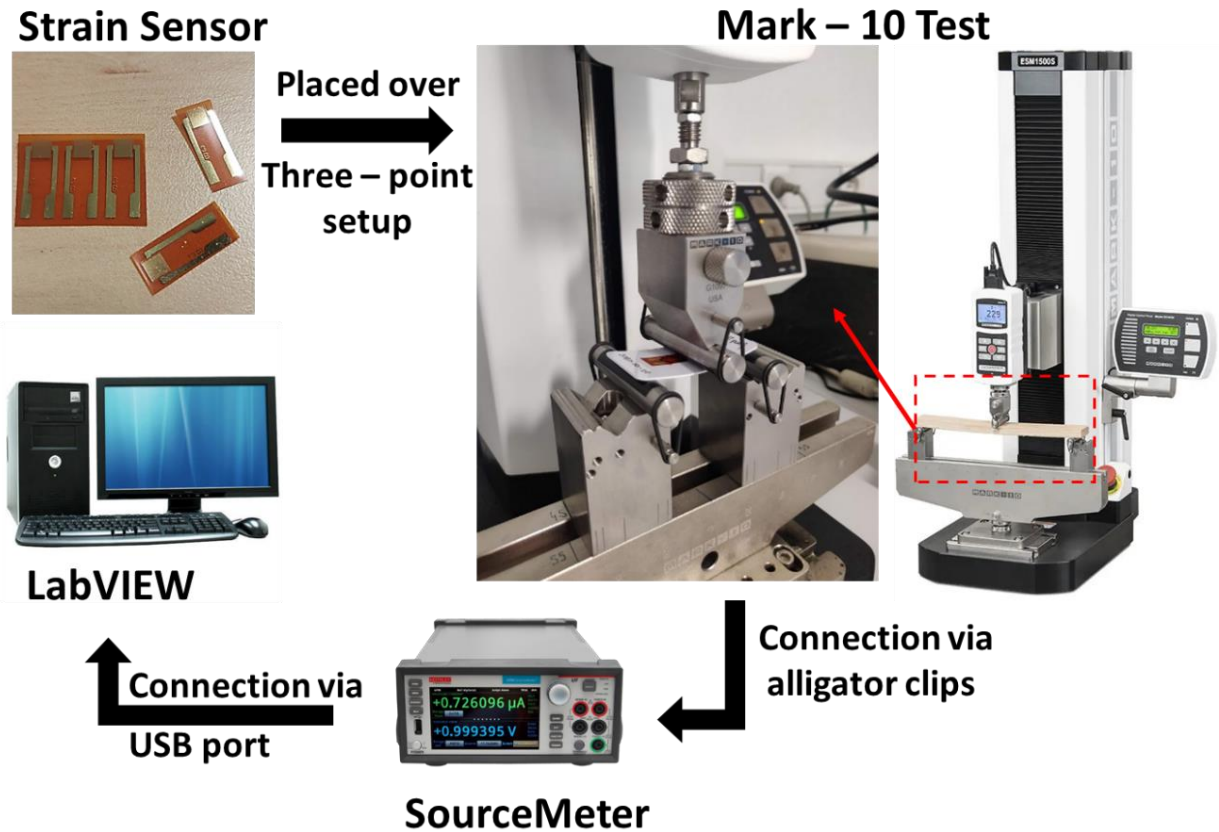


Figure 3.1: Three point bending setup: HNS sensors are placed over two supporting points by use of an additional base-substrate under HNS Kapton sensors. Electrical connections are made via alligator clips to the Sourcemeter and output data is observed and recorded through LabVIEW software.

The sample is placed over the support points and connected to the Keithley 2450 Sourcemeter. A force is applied upward and downward at a constant speed of 50 mm/min with a two-second dwell time. Speed and dwell time are adjusted as per the need of experiment. The sampling rate is set to a minimum, 10 kHz. The optimized parameters are as shown in Figure 3.2(b).

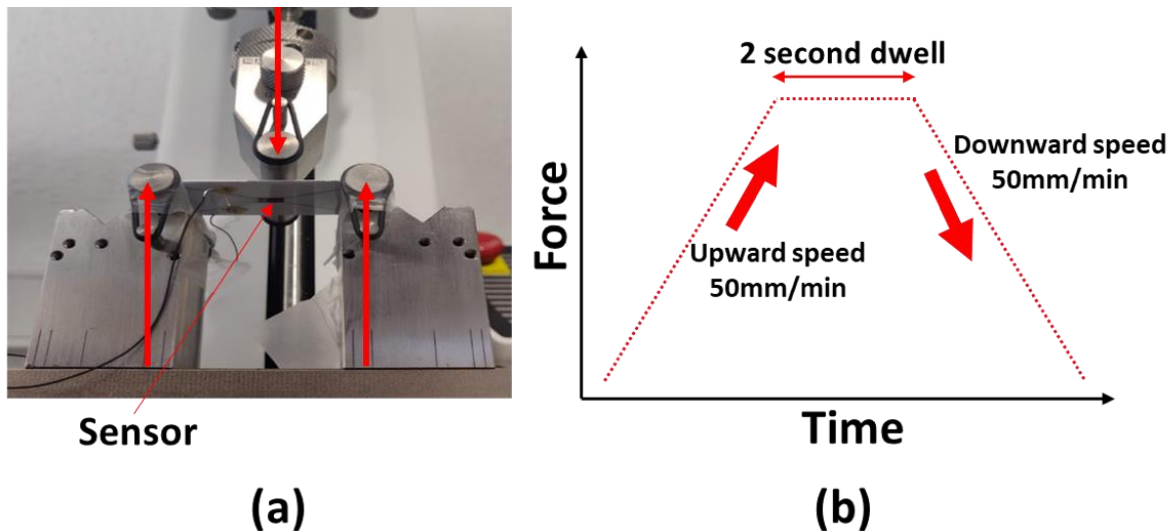


Figure 3.2 : (a) Strain sensor placed facing downwards on a three-point bending machine. (b) Graph shows input parameter i.e., speed of the probe and dwell time for three-point bending.

3.1.2. Sample Preparation

The response of the sensors to the deformations is evaluated by using the measurement bench and a dedicated protocol. The protocol consists in gluing the sensor on a reference support and then measuring the resistance variations with the three-point support. The flexible strain sensors fabricated on Kapton measure 18 mm in length, 8 mm in width with a thickness of 0.1 mm. Kapton based sensors are neither rigid enough nor long enough to be directly placed on the two supporting points of the three-point bending setup. For three point-bending characterization, sensors required a more rigid mechanical substrate for which three different base-substrates are used: thin glass slide (60 mm x 24 mm x 0.14 mm), thick glass slide (76 x 25 x 1 mm) and PVC (53.75 mm x 28.65 mm x 0.76 mm).

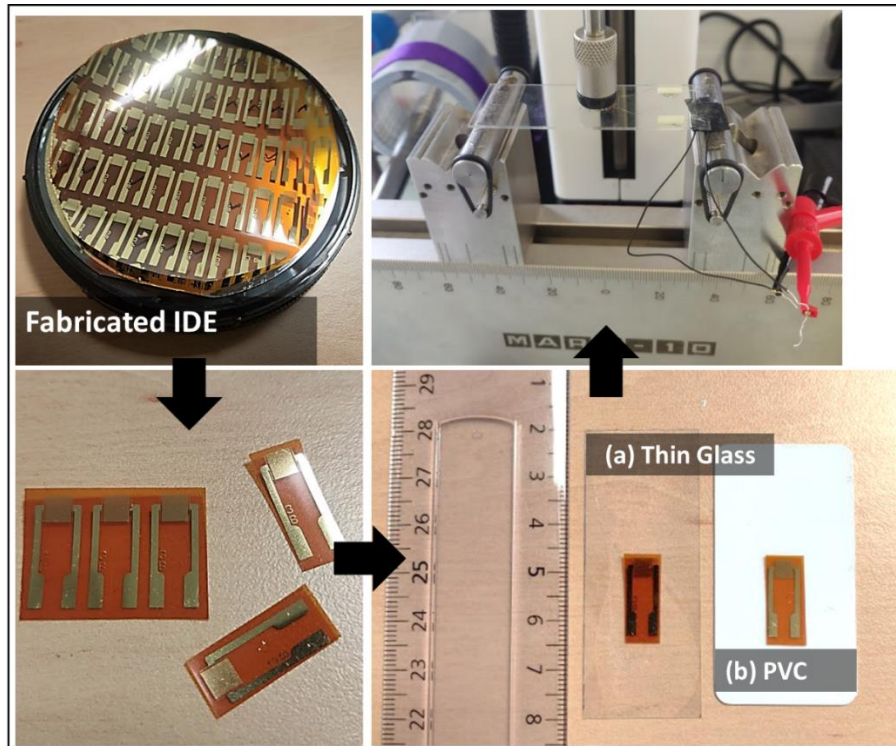


Figure 3.3: Sample preparation: 4inch wafer sized Kapton film, with many individual IDE is first cut. One fabricated IDE sample is 18 mm long and 8 mm wide, with an active area of interdigitated electrode of 16 mm². Single IDE is glued to glass or PVC base-substrate and later placed over two supporting points on three-point bending setup.

3.2. Calibration Protocol

The three-point bending test is controlled using LabVIEW program, developed by Nanomade (Industrial Partner) and Nicolas Mauran, engineer at LAAS-CNRS. The objective is to measure the displacement (or deflection) of the substrate as a function of the applied force. Significant input parameters involve the force range and number of cycles, among various other parameters. The software interface shows output values of the resistance change, applied force and corresponding deflection, as shown in Figure 3.4.

The raw data is processed using MATLAB to estimate the relation between change in resistance (ΔR) versus strain (ϵ) and to estimate the GF value.

$$GF = \frac{\Delta R/R_0}{\epsilon} \quad (3.1)$$

Here R_0 is the unstrained resistance of strain sensor.

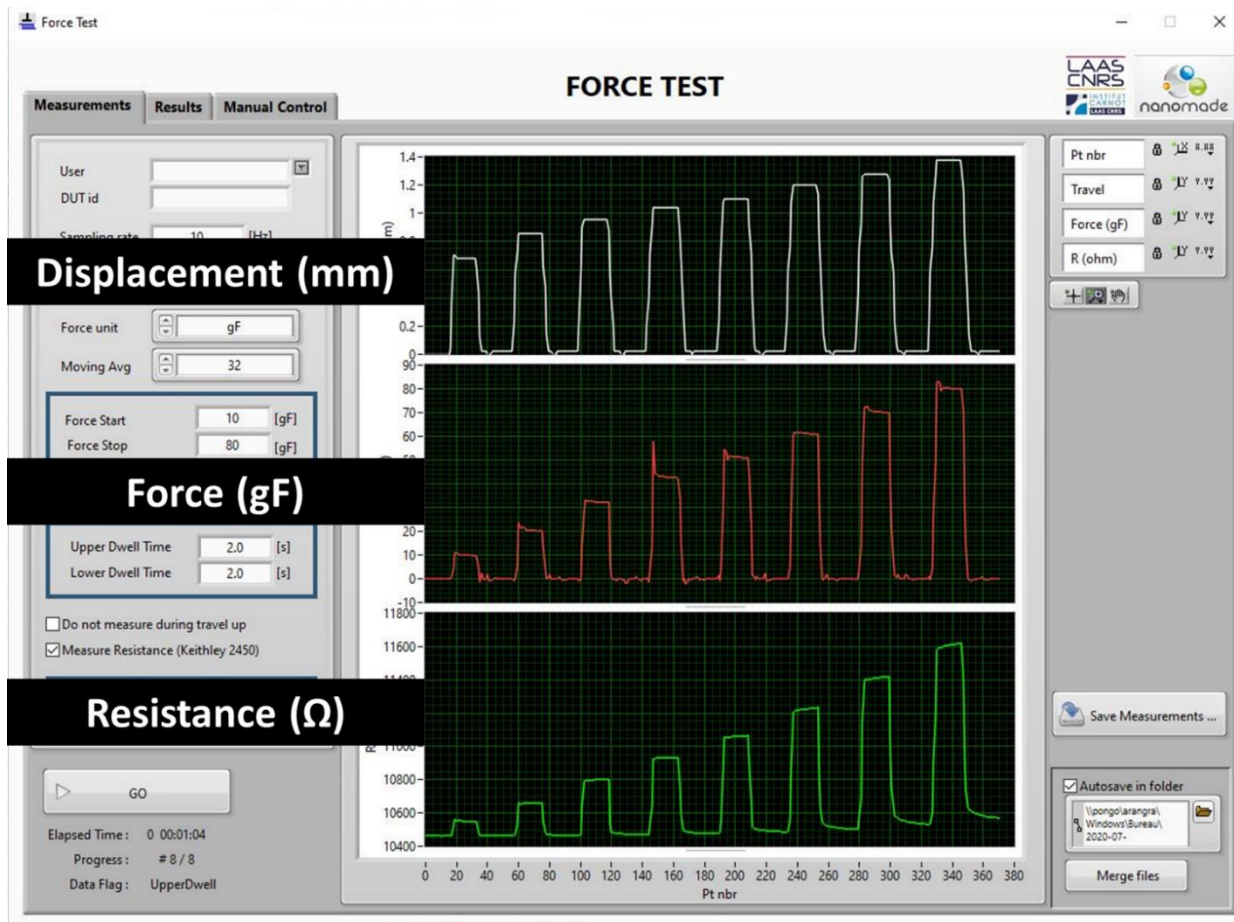


Figure 3.4 : LabVIEW software interface showing eight complete loading and unloading cycles.

The strain, ε , can be estimated through the following three methods:

1. **Knowing the applied force** Strain can be calculated by directly using the applied Force (F) value as written in Eq. (3.2) but it implies the knowledge of the young's modulus (E) of the mechanical substrate.

$$\varepsilon = 3(h + 2e) \frac{Fx}{Ebh^3} \quad (3.2)$$

Here h represents the thickness of supporting substrate, e represents the HNS sensor thickness, x is the distance between the point of the applied load and the support (shown in **Figure 0.1**) and b is the width of the sample.

In this work, this approach was not considered during the characterization of the strain sensors for the reasons later discussed.

2. **Knowing the displacement** Strain can also be calculated by using Eq. (3.3), which uses the resulting displacement (δ) for a given applied force to the strain sensor. The full set of calculations to obtain this expression is detailed in Appendix 1.

$$\varepsilon = \frac{6(h + 2e)\delta}{L^2} \quad (3.3)$$

This approach was initially used, however during the test, as shown in Figure 3.5, an undesirable change in displacement can create an inconsistency in strain calculated using displacement or force. The following graph is obtained by using data recorded for a constant input force of 0.8 N, at a speed of 50 mm/min.

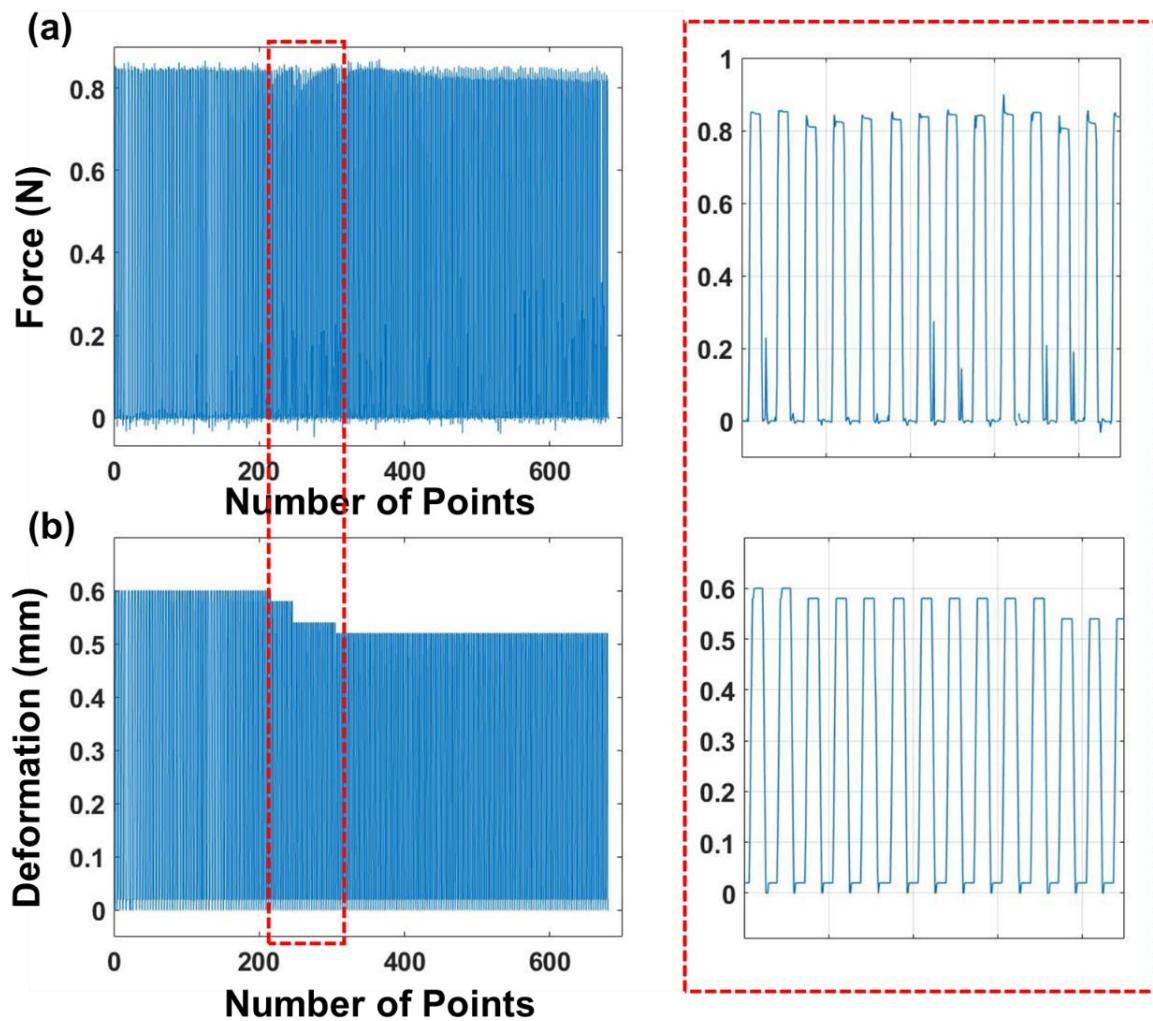


Figure 3.5: Inconsistency in applied uniform (a) Force (N) and the resulting (b) Deformation (mm).

Discrepancy, as shown in Figure 3.5, arises due to mechanical instabilities of the testing apparatus or the system fault. Some errors that reduced the confidence in a measurement during the procedure are further discussed:

- One of the common errors caused by machine/system related instabilities is shown in Figure 3.6(a). This non-linear nature of recorded displacement/deflection is with reference to the applied force (Figure 3.6(a)), where the data are collected through cyclic force sweep from 0.98 N to 7.85 N. From one cycle to next, ideally it is expected to have only a slight increase in value of applied force. However, a value for force, at which the deformation has a sharp anomalous change, as recorded in Figure 3.6(a), may possibly be considered as an inaccuracy caused by a software error or a mechanical instability.
- Another common error is introduced by the difference in travelling length of the probe which can also be seen as a difference in starting position of force probe, Figure 3.6(b). The system records this additional travelling distance as a part of 'deformation' during the characterization of the strain sensor. Therefore, one has to be cautious about the starting position as this value can change from one test to another. From an experimental point of view, the force probe only needs to gently touch the surface of the sensor, when beginning the experiment, without inducing any strain that could have an influence of the characterization protocol.

During the treatment of the data threshold force could be set to 0.01 N, in order to consider length value only after the force has passed the value of 0.01 N to be certain that it is in contact with the sensor. This could be one of the methods to measure the true deformation.

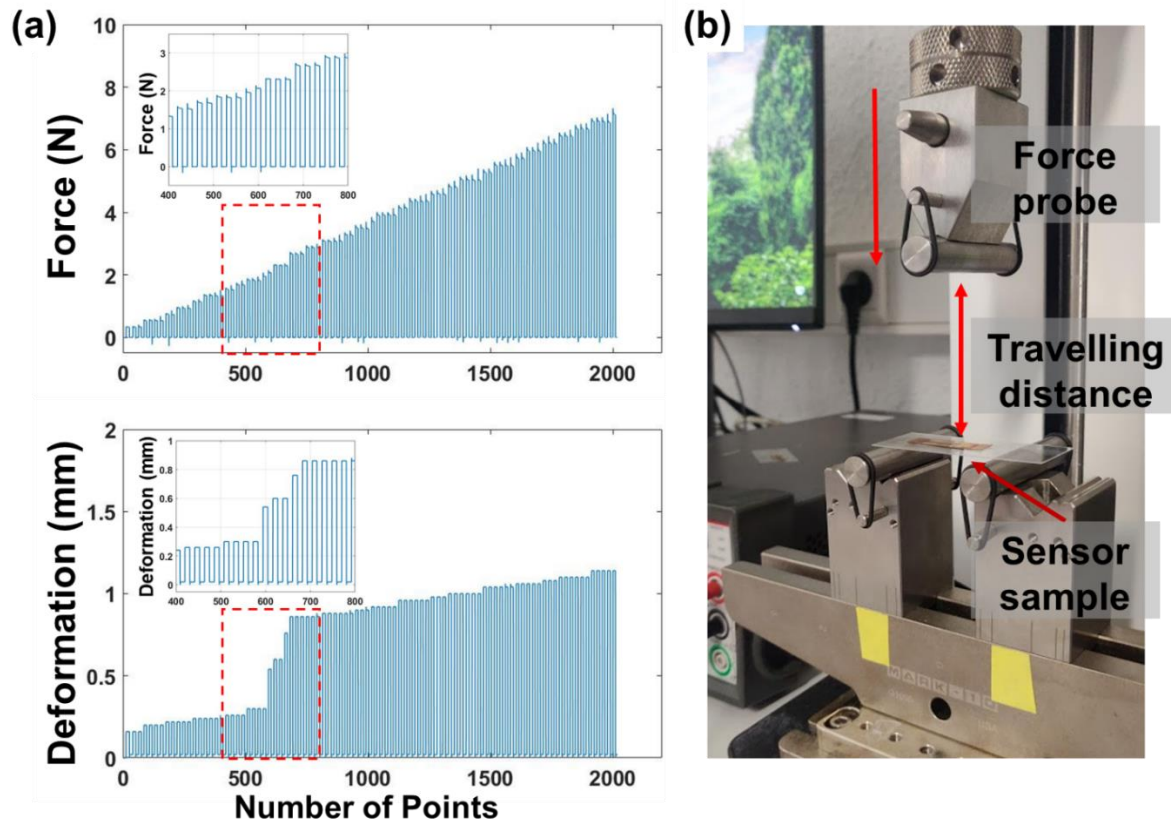


Figure 3.6 : (a) Force, length vs number of points recorded. (b) Image showing the three-point bending set-up, force probe moves in downward direction to approach the sensor sample.

To avoid the apparatus induced errors and provide accurate measurements, the use of a strain sensor with known GF was chosen to establish the relation between an applied force and the generated strain for a device under test. It is the most reliable and easiest way to obtain the force-strain curve for a given substrate.

3.2.1. Strain Calculation

The calibration method, used in this study, is based on the Force – Strain relation curve, Figure 3.7(a). This relation is established by means of 70 μm -thick commercial sensors with a known GF of 2 (comidox BF120-3AA 120 Ω). There is a 40% difference in thickness between the commercial sensors used for calibration and our Kapton-based sensors ($\sim 100 \mu\text{m}$) built for this study. This difference is important as it can lead to a non-negligible error in the estimation of the GF as the induced strain for a given applied load is dependent upon the stiffness of the substrate and therefore

upon its elastic modulus and thickness. Nonetheless, in our case, the stiffness of the mechanical holder (glass, PVC, etc.) is high enough to compensate the difference between the commercial sensor thickness with the thickness of our Kapton-based sensors.

Using Eq. (3.1), where resistance variation is accurately measured for the device-under-test (acquired by using LabVIEW) and GF is known to be 2, the ‘m’ value is derived, (Figure 3.7(a)). The slope ‘m’ is the relation between the calculated strain and the applied force for various supporting substrates, like glass slide with two different thicknesses and PVC, Figure 3.7(b).

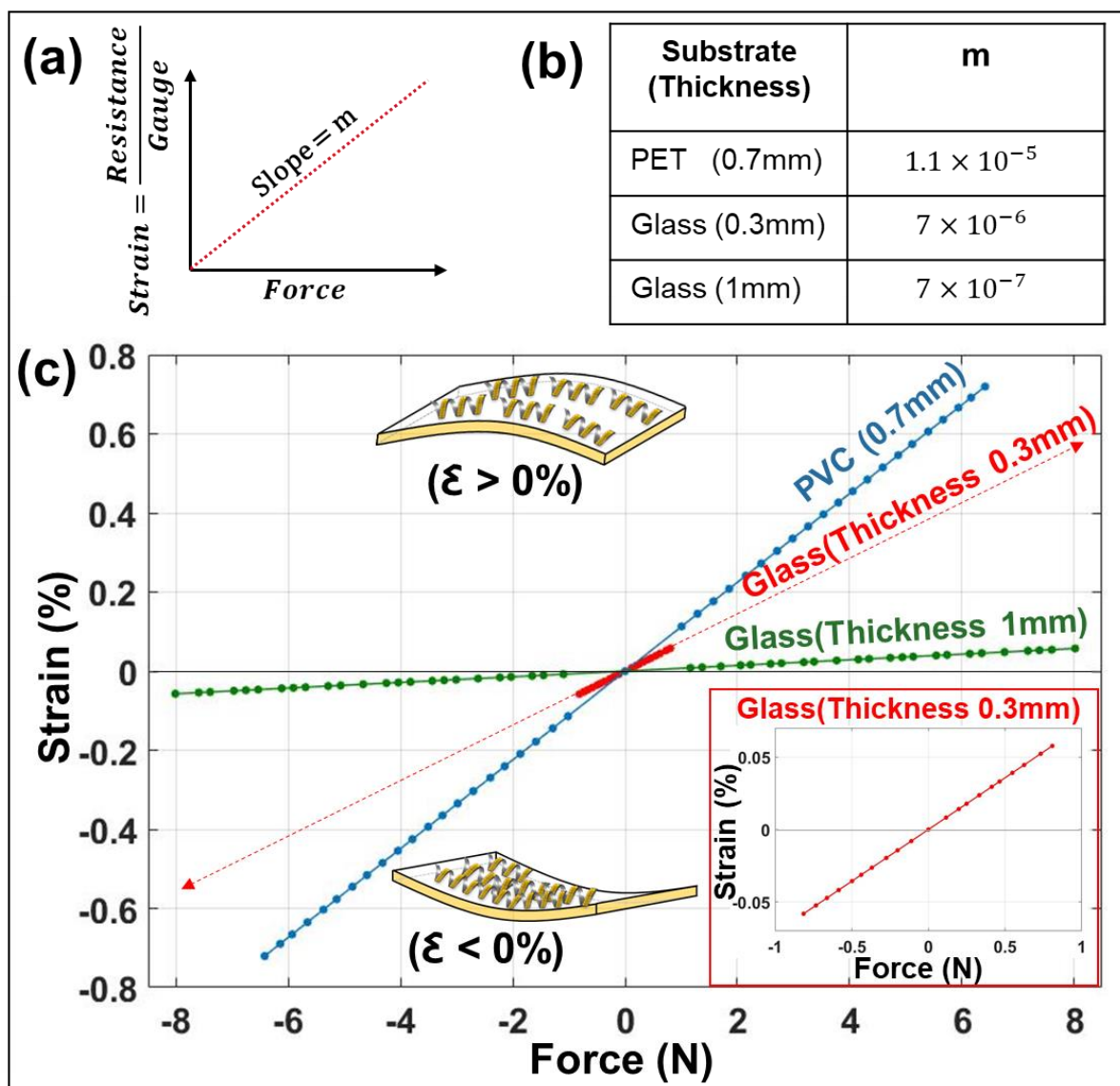


Figure 3.7: (a) Schematic explanation of proportionality factor ‘m’ between applied force and generated strain. (b) Value of slope m for different support substrate. (c)

Strain and Force relation for three different substrates established using commercial sensor.

As shown in Figure 3.7(c), the applied force for PVC and thick glass slide ranged from 0.98 N to 7.85 N. Thin glass slide cannot withstand force more than 0.88 N and therefore the range is kept between 0.10 to 0.78 N. These three substrates were used as mechanical support for our Kapton-based sensor and selected as ease of material availability.

3.2.2. Electrical connection and encapsulation layer

Ideally, the electrical connection and the encapsulation layer should not have any influence on the strain measurements. It is imperative to verify that the additional encapsulation layer does not degrade the performance of the sensor and that the sensing layers remain unaffected. It may also be noted that adding an encapsulation layer before performing characterization tests is essential to prevent the sensors from being damaged as the force probe could be in contact with the deposited sensing nanomaterial.

- As shown in Figure 3.8(a), by using toothless alligator clips, electrical connections are formed. For sensors where toothless clips are not an option such as commercial sensors because of their small size, metallic wires are soldered on the electrode pads, as shown in Figure 3.8(b). To form the connection between the sensor chips and the sourcemeter, soldering wire is not always feasible. The heat applied to the sensor chip to solder the wire should be as low as possible as it can damage the sensing element.

To address the influence of the type of electrical connection on the variation of the sensor output, the following graph of the resistance variation vs strain is generated. The two coinciding slopes lines shown in Figure 3.8(a) proves that the sensor response and sensitivity remain unaltered by the use of either method for connection. This makes it promising to use toothless alligator clips as an alternative method to avoid wire bonding.

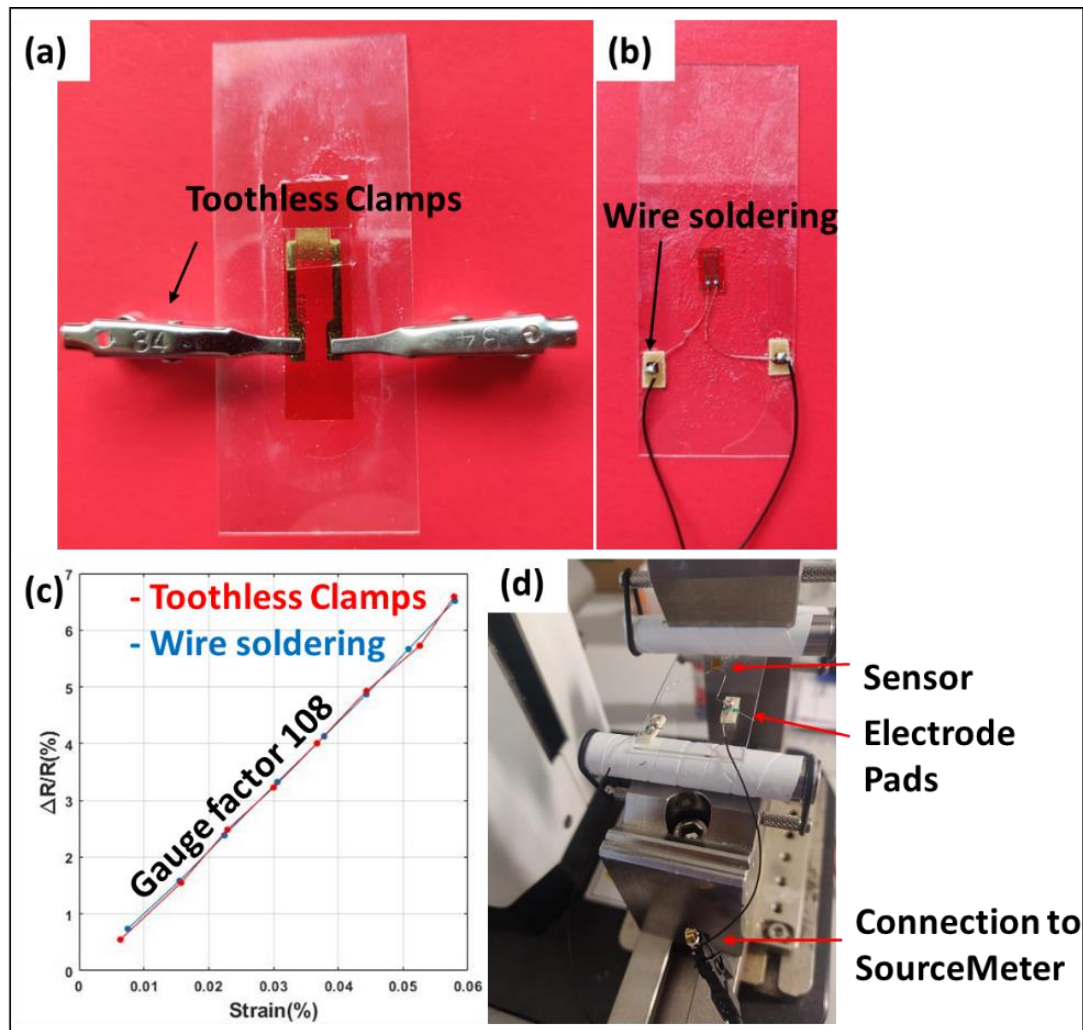


Figure 3.8: Possible ways to connect sensor to Keithley 2450 Source Meter by (a) crocodile clamps and (b) soldering wires on commercial sensors where adding clamps is not possible. (c) Comparison between two different means for the electrical connection of the sensor.

- Further, to create a sensor that is not susceptible to changes in the environment, it is encapsulated with a thin film (Dupont™ Kapton). Encapsulation protects it from various types of foreign substance, moisture, dust, ensuring its electrical stability on the long term. In order to verify that the strain sensing capability remains unaffected by the addition of the encapsulated film, a range of tensile strain from 0.01 to 0.08 % is applied to the HNS sensor. The resistance variation is plotted first for a bare sensor (red) and then for a similar sensor after being encapsulated (blue) as shown in Figure 3.8. In both cases, the slope is almost identical, that excludes a potential degradation of the sensor due to a mechanical action of the encapsulation layer on the sensor surface at least for a range of strain between 0.01 to 0.08 %.

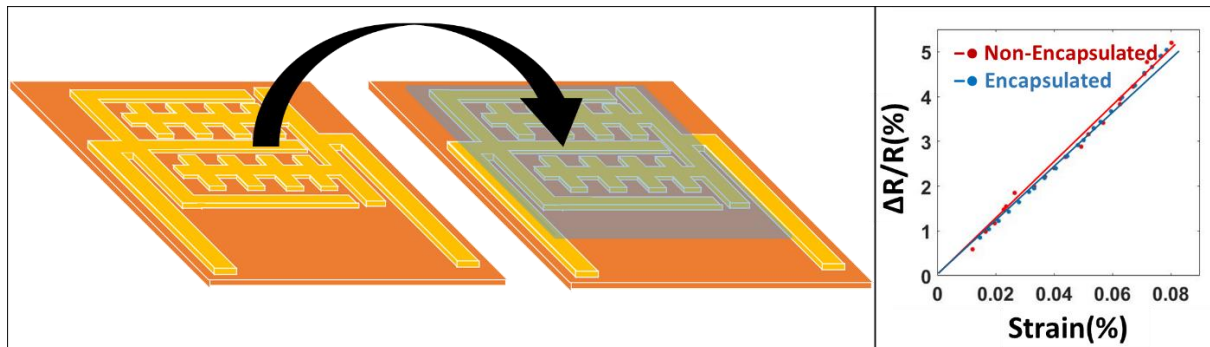


Figure 3.9: Calibration Figure: Relative resistance variation as a function of induced strain ε (%) for bare strain sensor (red) and same sensor after encapsulation (blue), where the points and lines show the experimental and linear data fit respectively.

3.3. Performance Characteristics

The strain sensors are characterized through various parameters such as sensitivity, linearity, dynamic stability, hysteresis, temperature and humidity response, Figure 3.10. In the past decade, the use of strain sensor built over flexible substrates for the applications such as e-skin has attained great importance [1][2]. Despite recent improvements, there is an emergent demand for high-flexibility, high-sensitivity and low-power strain gauges capable of sensing low strains in extreme conditions. Conventional strain sensors are simple in design; however, their fabrication procedures are not. The cost as well is not suitably low for real applications. To overcome this problem naturally flexible, low-cost materials and new designing have been investigated [3]. New materials such as nanoparticles and composites are investigated to assess their suitability in fabricating such sensors [4].

In this section, the optimization results of HNS sensors are presented. A new type of flexible conductive nanomaterial consisting of gold nanoparticles grafted on helical nanostructures that deform when strained, in a manner similar to the structural deformation of a spring, is discussed.

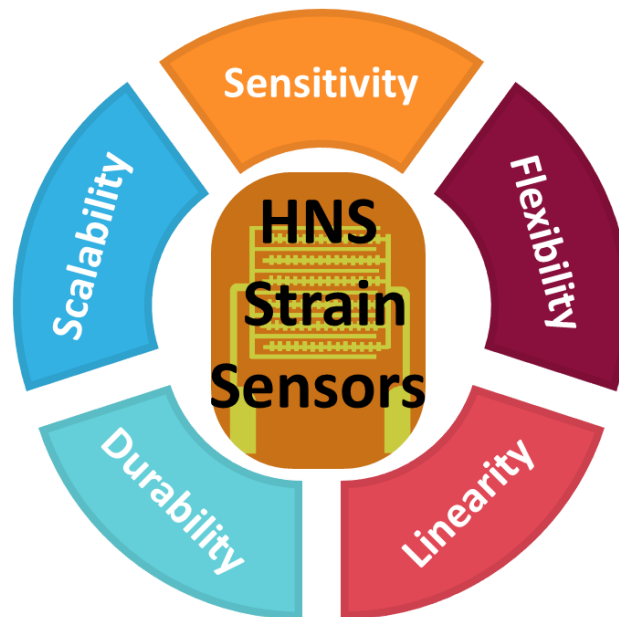


Figure 3.10: The features of HNS-based strain sensors that need to be evaluated.

3.3.1. Sensitivity

A sensor is required to have appropriate sensitivity range and strain detection limit for the desired and foreseen applications. An ultralow detection provides the sensors with the capacity to detect subtle strain changes caused by cardiac pulsation for example, which is critically important for real-time health monitoring [5]. Reported sensors ($\epsilon > 0.3$) so far monitor only large deformations, they cannot sense small strains ($\epsilon < 0.05$) with high precision [6]. For e-skin sensors, it is important to detect very small deformation [7][8][9]. At the same time, enhancing GF remains one of the major challenges.

One of the most common types of strain gauge sensor is a patterned metallic foil on a substrate. Deformation in the device leads to dimensional variations in the foil causing an electrical resistance change. The resistance change is mostly due to changes in length and the cross-sectional area. The GF of these metallic foils is between 2 to 5. For a more precise measurement, semiconductor gauges are preferred over metal foils. As an example, the gauge factor for p-type (110) single crystalline silicon can reach up to 200. On the other hand, most of the semiconductor materials used in strain sensing devices are brittle and can bear only a small strain range.

Most of the reported semiconductor strain sensors depend on costly, time-consuming and sophisticated fabrication methods or materials synthesis. Moreover, devices which make use of bio-inspired designs or require intimate integration with the human body demand curved shapes and/or flexible responses to deformations. To overcome this issue, one of the strategies is the manipulation of the geometric design including wavy structure configuration, mesh structure, origami, etc. [10][11].

Another emerging strategy is the development of new nano/micro-structured materials, which enhances the sensing performance. In this study, gold nanoparticles grafted on HNS have been introduced as a new conductive material.

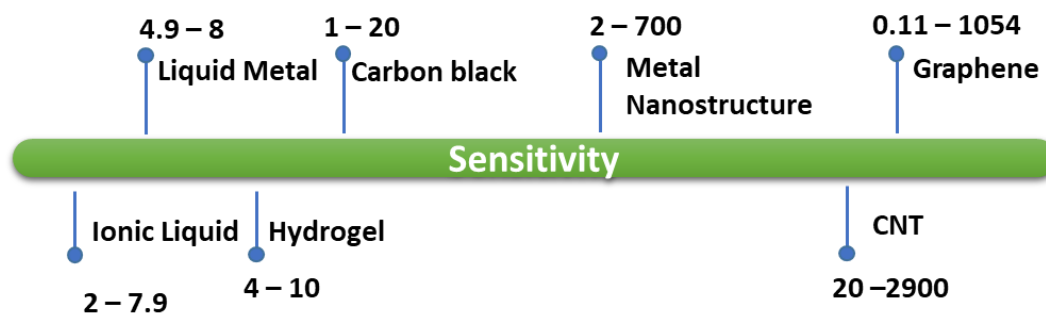


Figure 3.11: Gauge factors for various materials used for strain sensors.

HNS as sensing material The sensitivity of strain sensors depends on various factors, including sensing elements, sensing mechanism, and fabrication process [12]. The variation of the nanomaterial concentration and orientation can be useful in tuning of the electromechanical properties of the strain sensor. Tanner et al., presented a vacuum technique for nanoparticle deposition that permitted controlling the electrical resistance of the film, showing semiconductor like behavior when arrays of nanoparticles cover the surface below a certain threshold value, the behavior is metal-like if the deposition density is above this threshold [13]. They found that the highest sensitivity is obtained for intermediate density values, which is likely due to a tunneling and hopping current.

In this study, HNS separate upon bending, leading to the increase of the tunneling resistance between adjacent HNS and consequently the reduction of the electrical conductance. The tunneling resistance greatly influences the sensor

conductivity and strain sensitivity as well. As can be explained through three different scenarios (illustration in Figure 3.12(a, b)):

In the first case, the electrical conductivity is very low since there are only a few nanostructures (NSs) deposited on the surface of the sensor, as shown in Figure 3.12(c). In this assembly, only a small amount of NSs is close to each other. Although there is no complete conductive path formed by contacting NSs when bent, the electrical conductivity increases gradually due to tunneling effects among neighboring NSs. As the amount of NSs further increases, a complete electrically conductive path is formed.

In this second case, the electrical conductivity increases remarkably. This process is termed the percolation progression.

In the third case, any further addition of HNS will create even more electrically conductive paths, complete conductive network can be seen in Figure 3.12(c), and the electrical conductivity increases gradually. [14]

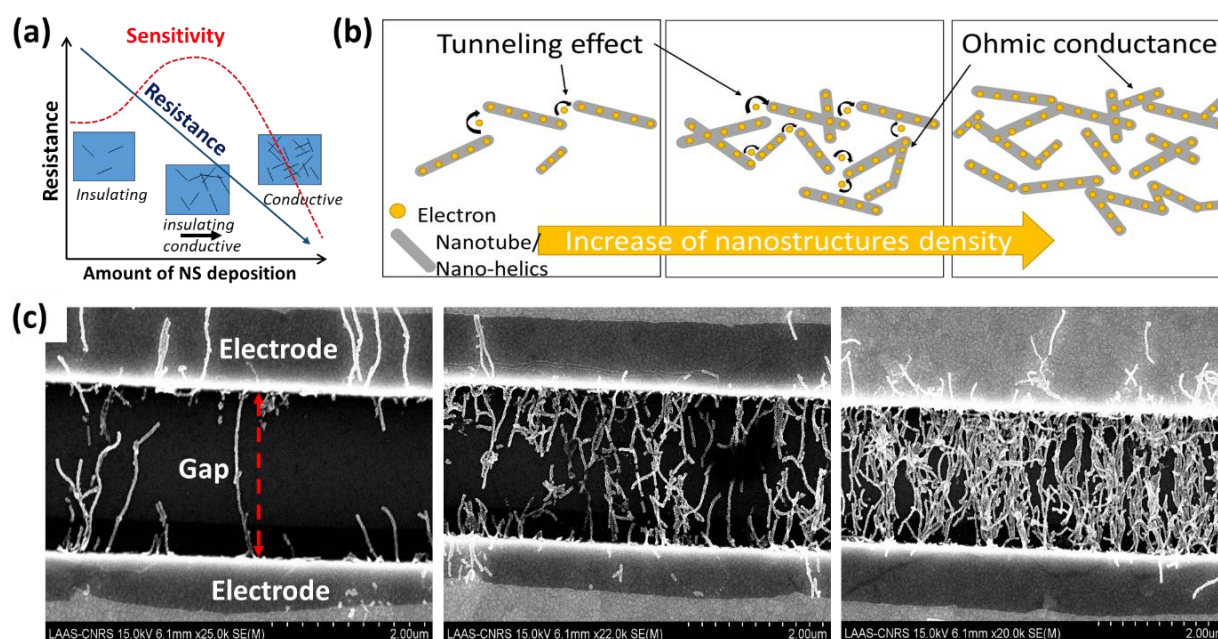


Figure 3.12: (a) Graph showing the significance of deposition via DEP, Resistance, and Gauge Factor. (b) Schematic illustration of the conductive mechanism. (c) SEM image of HNS between two gold electrodes separated by a 3 μm gap (bottom).

Experimental Method: The schematic in Figure 3.13 presents multiple-dielectrophoresis (DEP) deposition used to achieve the desired resistance with

precision. It shows the trend of subsequent DEP depositions over the same IDE sample. Each DEP deposition time is 5 seconds. It presents a possibility to slowly increase the concentration of HNS between IDE electrodes and thus decrease the resistance. It allows measuring the corresponding GF over a wide resistance range for the same device. Moreover, the method permits the reuse the same IDE sample. Multiple conductive layer deposition with lower amount of HNS density in each step can be helpful in: (1) monitoring the sensitivity response, (2) in stabilizing the response (discussed in later section), and (3) helps in addressing and overcoming the non-repeatability in DEP from one deposition to another. Non-repeatability usually arises because of non-homogeneity in the nanomaterial solution used.

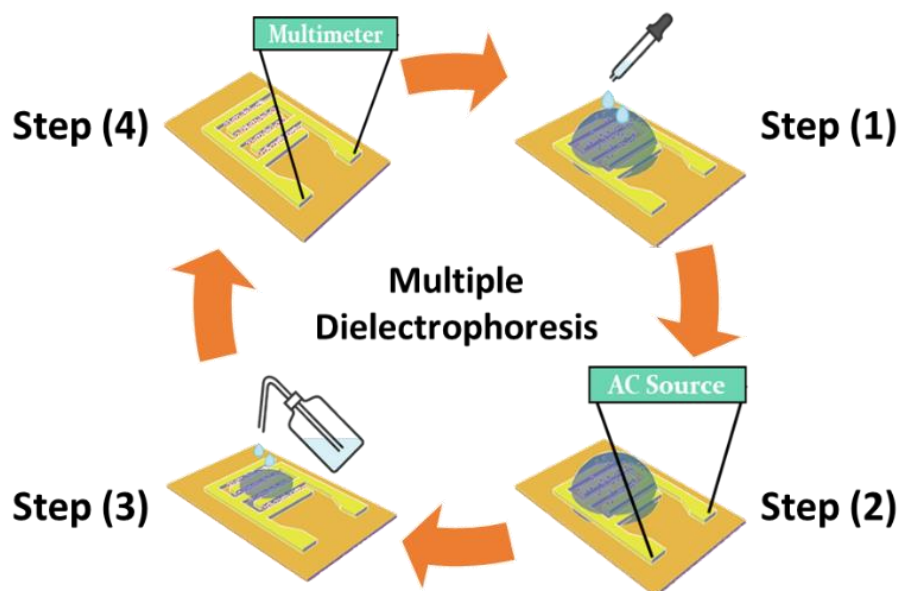


Figure 3.13: Schematic of Multiple depositions.

In the following paragraphs, the sensitivity of strain sensors using HNS is discussed using the same approach as presented by Tanner et al [13]. They demonstrate platinum nanoparticles films with low to medium nanoparticle area coverage would enhance the gauge factor, while the reverse is observed for medium to high coverage, Figure 3.14(a, b). Herrmann et al. anticipated that films with fewer and larger gold-nanoparticle aggregates would produce more sensitive strain gauges than those made up of smaller nanoparticles. This would mean that clustering of nanoparticles might actually enhance the gauge factor [15].

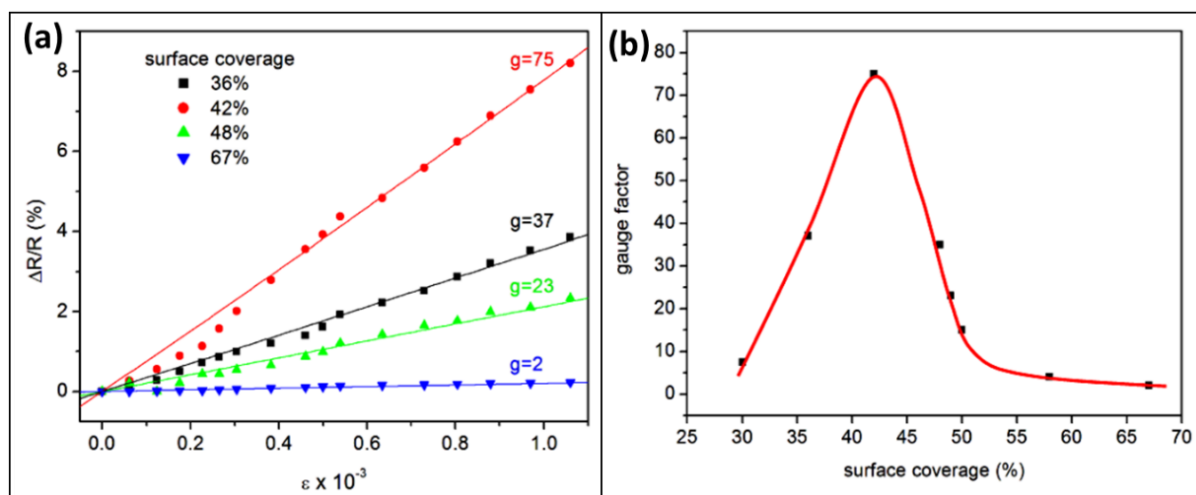


Figure 3.14: Influence of the nanoparticle density on the strain sensitivity. (a) relative resistance change as a function of strain of nanoparticle films of various platinum nanoparticle densities (b) the gauge factor as a function of surface coverage [13].

1D Nanostructure density in this study is simply quantified by measuring the resistance value of the final device. The relative resistance change versus strain for strain sensors based on different resistance values is shown in Figure 3.15(a). Through Figure 3.15(b), it is clear that an optimal GF can be obtained by adjusting the 1D nanostructure density deposited on the interdigitated electrodes.

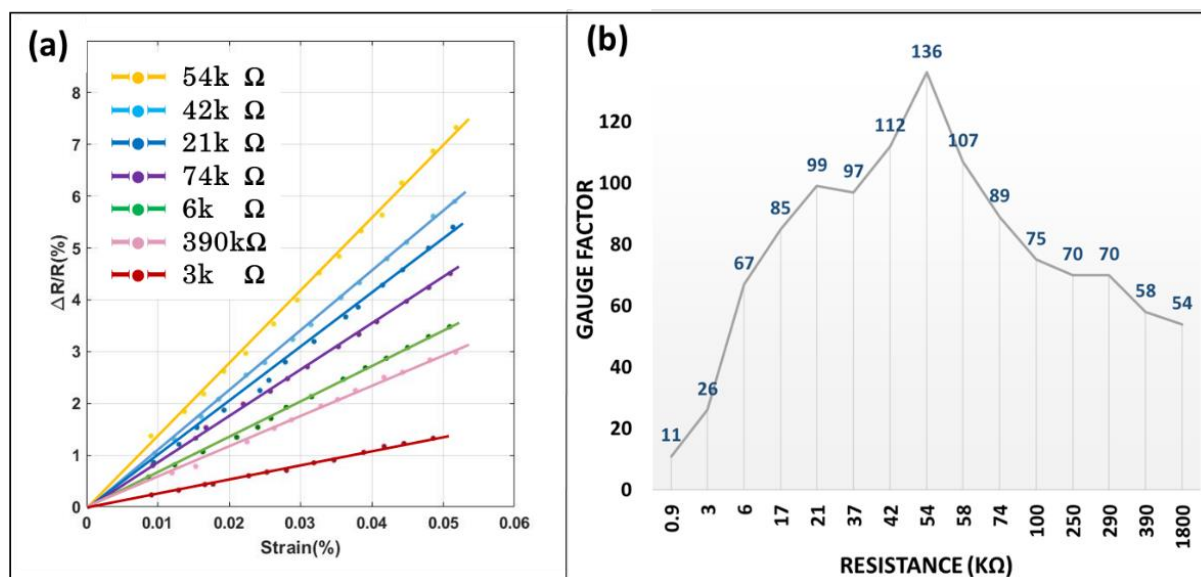


Figure 3.15: (a) Set of sensors at different resistance value and their resistance variation response to strain. (b) Change in Gauge Factor value obtained from sensors at different resistances (k Ω).

In order to further study the above-mentioned points, a periodic force pressure of 0.78 N is applied on sensors mounted over a thin glass slide. It is observed that when the resistance is roughly over or under the range [500, 20 k Ω], the response of relative resistance to strain in real time is not stable. This has been shown through a set of three sensors with different resistances. The resistance of Sensor (1) is the highest at 70 k Ω , Sensor (2) is at 2.74 k Ω while the resistance of Sensor (3) being the lowest at 58 Ω .

Case (1) High resistance values correspond to small quantities of HNS deposited between the electrodes. Thus, there is a low number of conduction paths, which may explain the relatively high signal-to-noise ratio of sensors as can be seen in Figure 3.16. A significant baseline drift can be clearly observed due to the presence of very few HNS which are neither connected nor stable, with each bending cycle they shift for their initial position on the surface sensor and this leads to a poor stability.

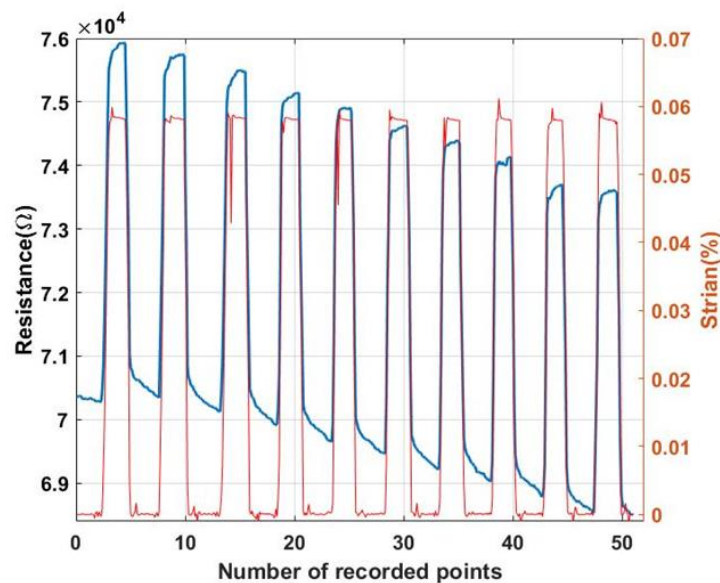


Figure 3.16: Resistance cycles of Sensor (1) with initial resistance of 70 k Ω , i.e., smaller amount of HNS present between the electrode. The calculated gauge factor of 115. Blue line represents the resistance variation and red represents the strain variation.

Case (2) The decrease in resistance of the sensors is accompanied by an increase in sensitivity with a better stability, Figure 3.17. The decrease in resistance reflects a denser deposition of HNS, which signifies a greater number of conduction paths between the electrodes and therefore a more stable and less noisy signal.

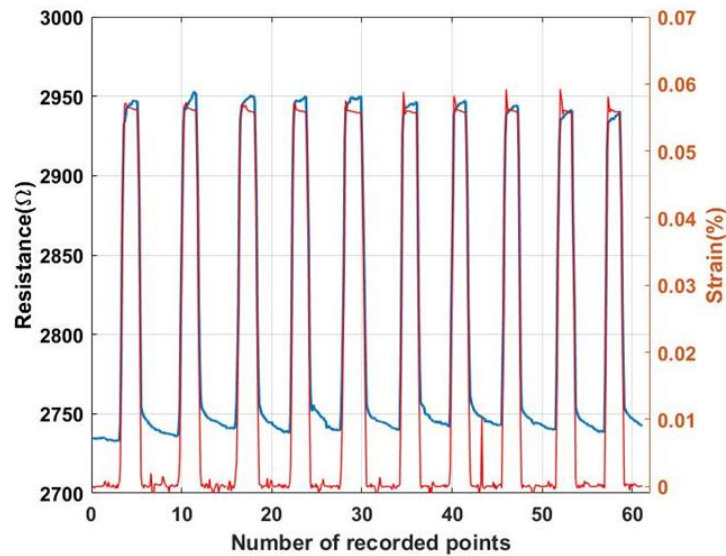


Figure 3.17: Resistance cycles of Sensor (2) with initial resistance of $2.5 \text{ k}\Omega$ and calculated gauge factor of 119. Device with optimized amount of deposition show no drift during the cycling response. Blue line represents the resistance variation and red represents the strain variation.

Case (3) Finally, the decrease in sensitivity with increased number of deposits can be explained by the increase in conduction paths as shown in Figure 3.18. With a reduction of the inter-particle distance, the conductivity increases. Moreover, with the increase in the deposition density, the system gradually moves from a 2D to a 3D configuration. The set of percolation paths is no longer only in the plane (x,y), but in space (x,y,z). In this case, the lower electron confinement also contributes to decrease the gauge factor.

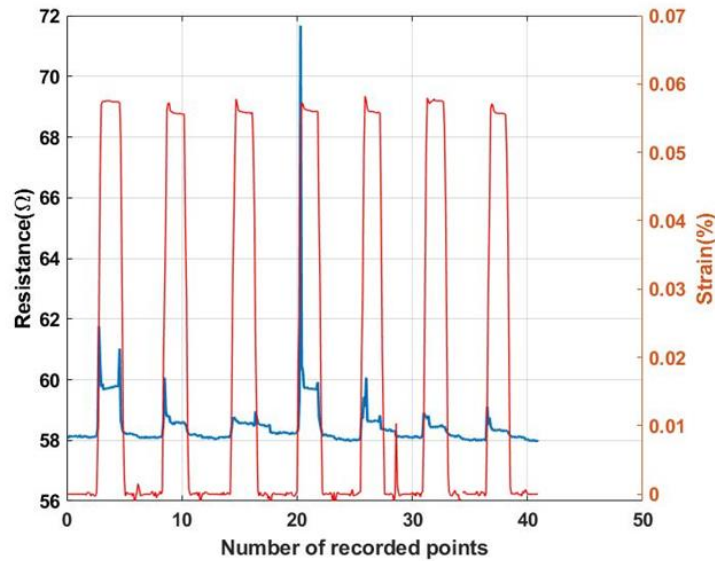


Figure 3.18: Resistance cycles of Sensor (3) with initial resistance of 58 Ω . The extremely dense deposition is the reason device is not able to detect small strain values accurately. Substrate straining is not enough to induce modification to the inter-particle distances. Blue line represents the resistance variation and red represents the strain variation.

Overall, the relation between resistance and sensitivity of our HNS strain sensor is a bell curve (Gaussian function), Figure 3.19.

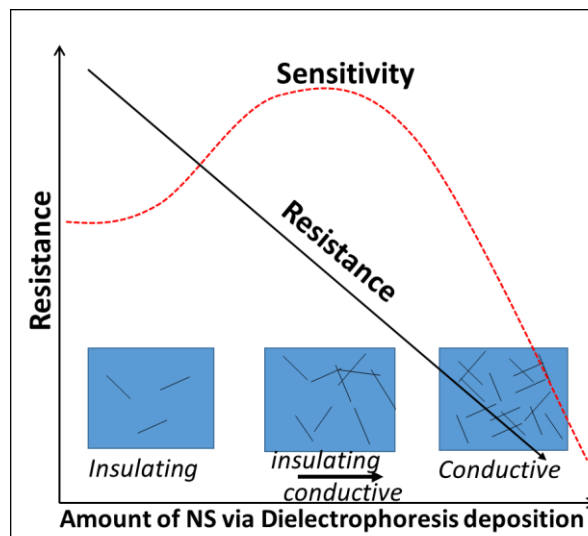


Figure 3.19: The significant relation between deposition via DEP, device resistance and Gauge Factor.

Further, to confirm the role of resistance not only on GF but also on the stability of a sensor, two sensors with different resistance values $\sim 70\text{ k}\Omega$ and $\sim 400\text{ k}\Omega$ having a similar GF equal to 40 are studied. As shown in Figure 3.20, at lower strain, the sensor resistance response is observed to be more stable for the one with the lowest resistance ($70\text{ k}\Omega$). The major disadvantage of strain gauges with high resistance is weak robustness, because at low density of HNS the breakage of a conduction path is more damaging than in the case of sensor containing denser HNS, implying a large number of conduction paths.

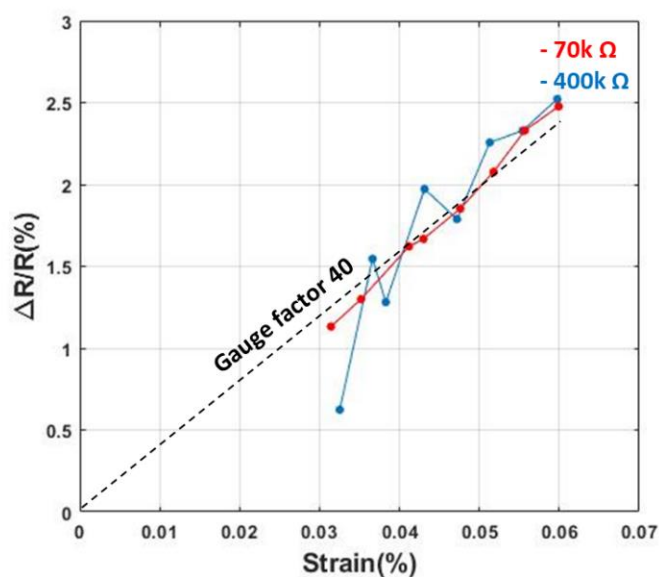


Figure 3.20: Two sensors with resistance $\sim 70\text{ k}\Omega$ and $\sim 400\text{ k}\Omega$ having a similar gauge factor 40.

A comparison of calculated GF, in the Figure 3.21, shows higher sensitivity for the HNS sensors and Nanomade sensors compared to commercial strain sensor. HNS based sensors are characterized on a three-point cyclic deformation bench with increasing deformation. The force applied to the sensor ranges from 0.10 N – 4.90 N. The resistance is measured during cycling and the relative change in resistance is plotted as a function of time under the corresponding deformation curve. Overall HNS sensors have a better sensitivity than Nanomade and commercial sensors, possible reason of this is the unique design of HNS themselves. The tunneling effect between functionalized AuNP plays an important role in enhancing the device sensitivity. While helical morphology providing a better recovery after bending.

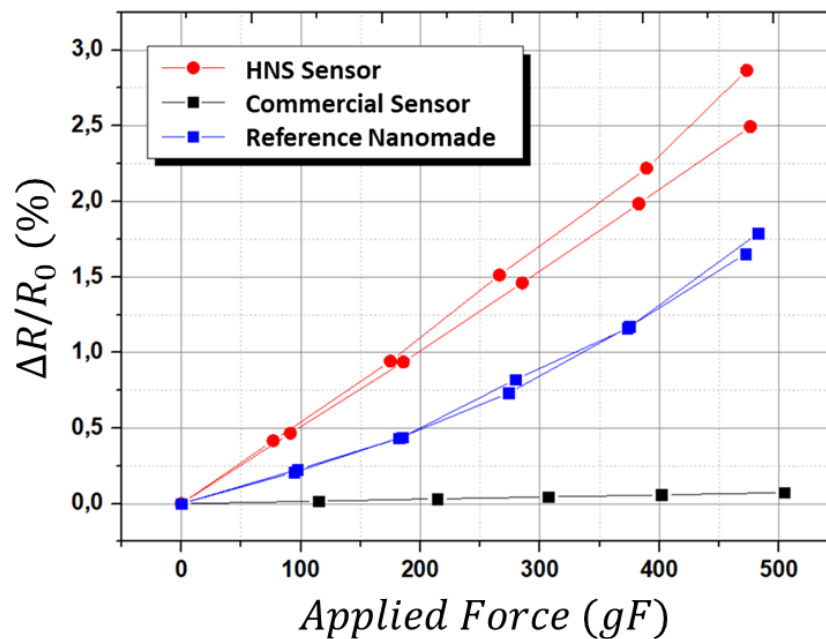


Figure 3.21: Comparison of HNS sensors (red) to commercial sensors (black) and strain sensors fabricated by Nanomade (blue). Two curves on HNS sensor and Nanomade sensor represents two trials to measure the resistance variation over similar sensor.

Conclusion The relative change in electrical resistance in the case of strain gauges with Sensor (1) is nearly three times greater than that of Sensor (3) as shown in Figure 3.16, Figure 3.18. The layer of HNS in contact with the substrate follows the deformation of the substrate. The upper layers allow the creation of conduction bridges between the NS far from the underlying layer to allow direct conduction, and participate in the overall conduction. As soon as a greater number of HNS is added in contact with the substrate, a loss of sensitivity is observed which leads to a less important variation of the electrical resistance with relative bending. The sensitivity of the Sensor (1), Sensor (2) and Sensor (3) gauges were 115, 119 and <20 respectively. These results show that there is a zone of optimal resistance in case of HNS that allows finding the best gauge factor, which lies in our case within range 500 to 20k Ω . It helps in building a more stable sensor that can retain its initial resistance or resting resistance even after a series of bending tests.

Further, it is established the use of HNS allows the detection of even smaller deformations with comparatively higher sensitivity. Deformations as low as 0.002% could be detected with a satisfactory signal-to-noise ratio, Figure 3.22.

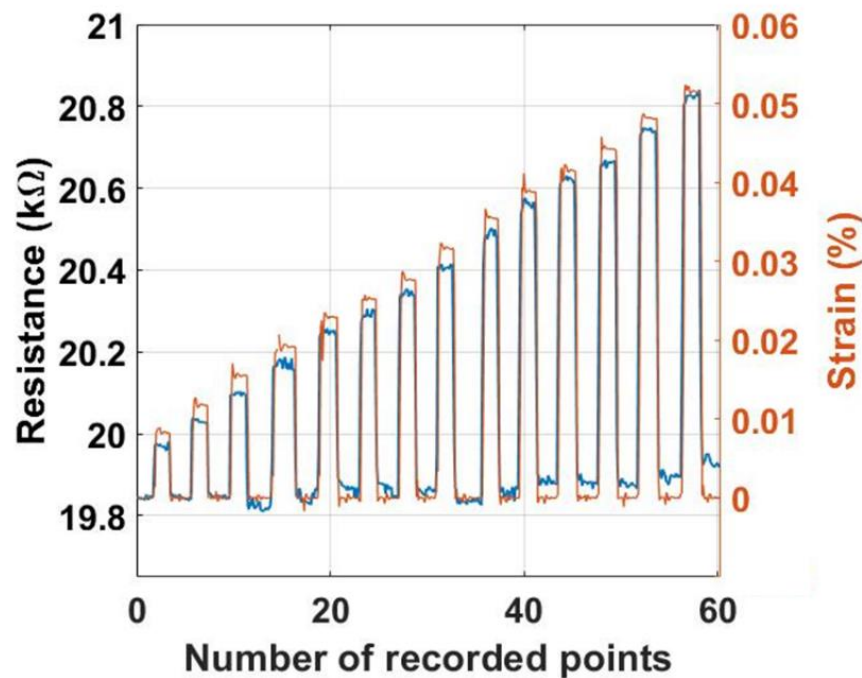


Figure 3.22: Resistance response of the strain sensor to the cycle of bending/releasing with low strain variation (0.01 - 0.05%).

3.3.2. Linearity

Development of a strain sensor that possesses both high sensitivity and linearity is still a huge challenge. Nonlinearities add difficulty to calibrate and process the data from the output signal and linear response of strain sensor is highly desired.

A highly flexible strain sensor typically is nonlinear or shows linearity when considering different regions. Usually after a nonhomogeneous morphological change, a strain sensor responds in a nonlinear manner to the applied strain. In particular, microcrack generation and propagation in a thin film lead to nonhomogeneous changes in piezoresistance [16][17]. For the similar reason of morphological changes in the sensing films, resistive type strain sensors also tend to have a nonlinear response to bending over a wide range of strain but the majority of recently reported resistive-type strain sensors have shown linear response in more than one regions [18]. Here, an assumption can be made that with wide range of strain and using higher strain values, a sensor tends to degrade faster. In linear, low deformation regime, the resistance of the sensor quickly returns to its nominal value and shows no hysteresis, which permits to make cycling measurements and study the stability. The non-linear regime tends to have greater deformation, in which the resistance increases

exponentially with the deformation. However, this increase is accompanied by a hysteresis phenomenon and the return to the resistance before deformation (R_0) is very slow or does not occur in some cases. Strain sensors based on the formation of disconnection and microcrack mechanism exhibit higher sensitivities in comparison to those with other sensing mechanisms, but at the same time exhibits high nonlinearity.

In this study, sensitivity and linearity of the sensors can be tuned by simply adjusting the number of HNS deposited by DEP. For instance, for low-strain applications, to detect minimal changes in strain, a lower density of HNS is more appropriate, whereas a higher density of HNS is better for high-strain applications to detect a wider range of strain. Experimental results, as can be seen in Figure 3.23, show the relative change in resistance as a function of strain applied on two different substrates with the calculated corresponding GF of the HNS sensor. $\Delta R/R_{\text{initial}}$ increased monotonously when the sensor is bent. For low strain tests ($\epsilon < 1\%$), the sensors are glued on $300\ \mu\text{m}$ thick glass substrates and for high strain tests ($\epsilon > 1\%$) the sensors are glued on $800\ \mu\text{m}$ thick PVC substrates. Using the calibration previously described, the bending strain range has been evaluated:

- For glass slide as a base-substrate from $0.02 - 0.08\%$
- For PVC as base-substrate from $0.1 - 0.8\%$.

A positive deformation value ($\epsilon > 0\%$) corresponds to an extensional deformation, where the HNS move away from each other, leading to an increase in the resistance of the sensor. A negative strain ($\epsilon < 0\%$) is a compression strain, where the HNS move closer together, resulting in a decrease in sensor resistance.

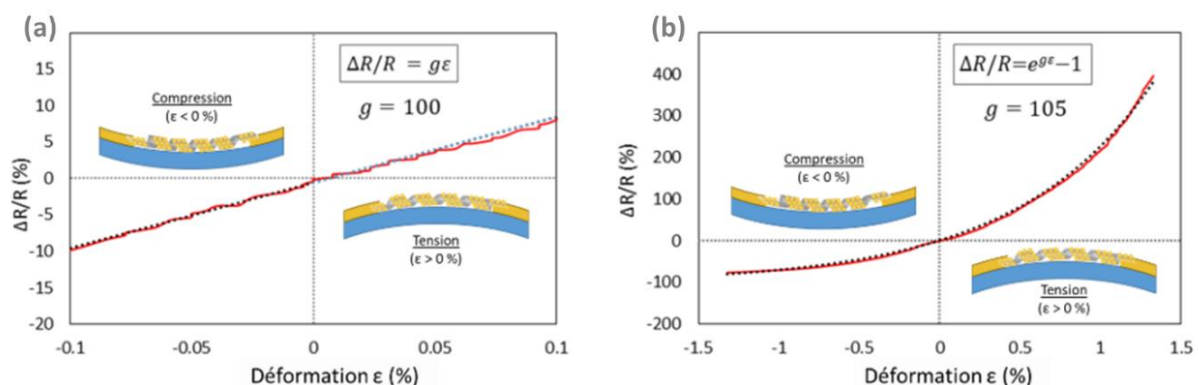


Figure 3.23: Relative variation of the resistance $\Delta R/R_0$ as a function of the applied strain for HNS based strain sensors, (a) Glass as base-substrate, the sensor shows

linear response at low strain. (b) PVC as base-substrate, the sensor shows non-linear trend seen at higher strain [19].

Within the limit of small deformations, the response becomes linear. At high deformation ($\epsilon \geq 0.4\%$), a non-linear change in electrical resistance is observed, Figure 3.23(b). This variation is representative of a change in conduction by tunneling in the nanoparticle assembly. As the interest of this project is to detect ultralow strain values, HNS sensors are operated under linear region.

3.3.3. Durability and Stability

An important aspect of the sensors is their stability over time. Dynamic durability signifies the ability of the strain sensor to recover its original properties during long-term bending–release cycles. Generally, performance degradation of strain sensors is often associated with plastic deformation of polymer substrates or generation of fractures in nanoparticle assemblies. A durable strain sensor holds a stable response and mechanical integrity during long-term cyclic loads. It is an essential requirement for wearable strain sensing applications where they are to accommodate large and dynamic strains over long time periods.

The subsequent experiment tests the sensor sample for long term cycling, the tensile speed is 50mm/min and the maximum force applied is 0.49N. However, either due to the machine or the software error the force during final cycles became 0.54N. This shift in force value can be seen in resistance variation response as well, in Figure 3.24. In each cycle, the sensor sample experiences the maximum strain for 2 seconds. This procedure then is repeated for 2200 cycles [20]. The sensor resistance variation shifts a bit in the second half of the cyclic response; however, the variation ratio remains the same. The following graph performed for 2200 cycles at an average strain of 0.51 N. To estimate the performances of the sensor on the long-term bases, mechanical cycling is performed by applying a 0.5 N force (~0.03%) at 1 Hz.

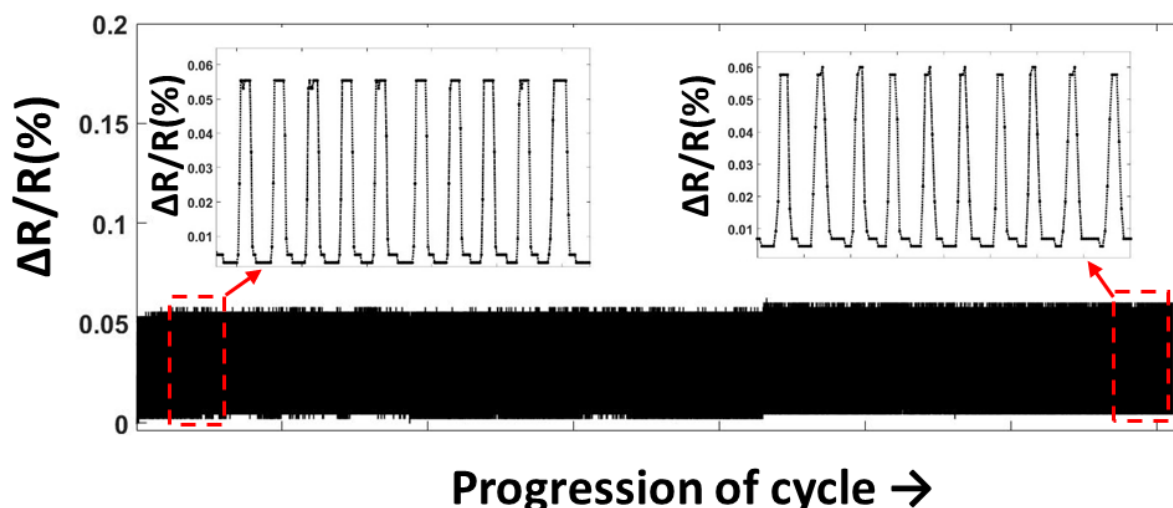


Figure 3.24: Durability of HNS under 2200 cycles with low tensile deformation. $\Delta R/R_0$ as a function of multiple bending and releasing cycles with 0.06% strain. $\Delta R/R_0$ refers to the relative resistance variation under bending and release, R_0 is the resistance in the relaxed state. Resistance variation shifts by 3% in the second half of the bending cycle; however, the ratio remains the same.

To go further in the mechanical ageing measurements, several series of cycles were performed at Nanomade by Fabrice Severac and Estelle Mazaleytrat, engineers at Nanomade, using a Key Life Test Machine (ZL - 2806) shown in Figure 3.25(a). The sensitivity is measured using three-point bending set-up after each set of cycles. The results as shown in Figure 3.25(b) show that HNS sensors retain their sensitivity even after 2 million cycles with an insignificant change in sensitivity. As mentioned earlier it has been observed that the fabricated sensors with resistance between 500 – 22k Ω have stable cyclic response because of the optimized amount of HNS composing the sensing part. Sensors are encapsulated and it also helps them to retain their resistance (R_0) value for long period, unless they suffer abnormally high physical damage.

The helical nanostructures on which the nanoparticles are grafted, are likely to have a positive effect on the stability and durability thanks to their spring like structure. It leads to less damage on the active sensing area during long term deformation and bending overall increasing the life period of a sensor.

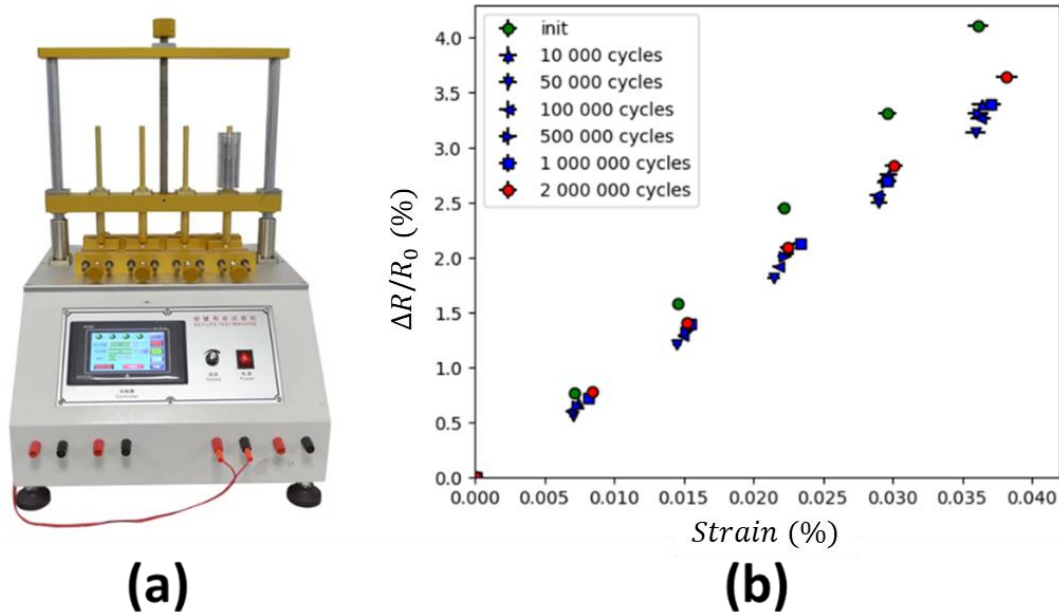


Figure 3.25: (a) Equipment to test measurement for mechanical aging: Key Life Test Machine (ZL – 2806). (b) Relative resistance variation as a function of applied force after different pulsing strain cycles of 0.03%. Init refers to measurement before subjecting to cycling test. ΔR refers to the resistance differences under bending and release (Picture and figure from Nanomade).

3.3.4. Hysteresis

Hysteresis is generally caused by friction and structural change in the materials. Upon dynamic loading, high hysteresis behavior leads to the irreversible sensing performance of sensors. Usually, elastic materials have higher hysteresis. This is because elastic materials need longer recovering time, especially when higher force is applied [21]. Under cyclic loading, high hysteresis behavior leads to the non-monotonic reaction of a strain sensor. Hysteresis is an important factor where strain sensors are frequently exposed to dynamic loading conditions. Resistive strain sensors rely on the formation of connections that is ohmic contact or tunneling conduction between nanomaterials. Though they return to the original position, this mechanism is often the cause of irreversibility over repeated bending and releasing cycles [22].

When the binding is weak, upon bending nanomaterials alter over the substrate and cannot rapidly slide back to their original positions. During the bending cycle, a weak binding would delay the recovery of nanomaterials to their initial positions which

leads to a high hysteresis effect. As can be assumed through this, strong interfacial bonding between the active sensing nanomaterial and substrate minimizes the hysteresis [23].[23]. While at the same time, if the interfacial binding is very strong, in resistive type strain sensor, friction force present in between can lead to fracture of nanomaterials at the releasing cycle. Therefore, it is extremely essential to have an optimal adhesion between rigid nanomaterials and flexible substrate materials to have minimum hysteresis output [12][24].

To test hysteresis response, HNS sensors were subjected to a force range of 0 to 0.49 N for continuous 10 bending cycles at the lowest speed possible of 1 mm/min. At the same time recording the resistance as a function of time at a sampling rate of 10 Hz. The results obtained are shown in Figure 3.26.

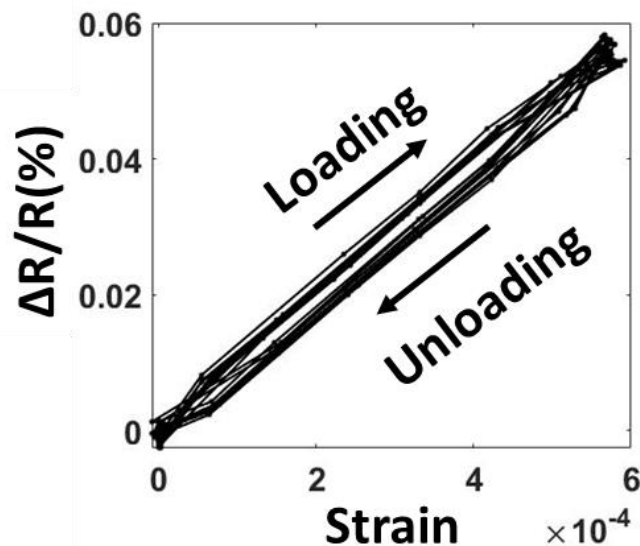


Figure 3.26: Resistive change at 10 bending cycles for HNS based strain sensor.

Realized on an identical substrate, the sensors based on nanoparticles show a significant hysteresis effect (Figure 3.27, red), while those based on HNS show no hysteresis (Figure 3.27, blue). This demonstrates that HNS allow to suppress the hysteresis effect. The original resistance of the sensor is fully recovered after releasing it from strain. As a result, the high sensitivity and accuracy of strain sensors can be maintained.

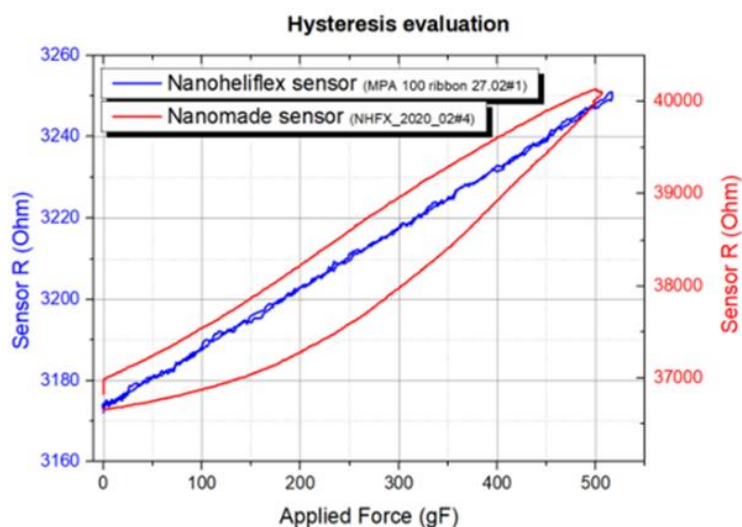


Figure 3.27: Comparison of hysteresis between HNS sensor (blue) and Nanomade (red) fabricated sensor that clearly show the advantage of using HNS to reduce or even suppress the hysteresis (Figure from Nanomade).

The helical nanostructures on which the nanoparticles are grafted have a positive effect on the durability, compared to sensor from Nanomade where the nanoparticles are directly deposited on the IDE via inkjet. It agrees well with the hypotheses or the assumption we have made, that the intrinsic mechanical properties of the HNS structure allow a faster return to their initial position after deformation. Additionally, HNS active area composition is a well aligned HNS network, which when deformed tends to damage less, implying negligible hysteresis. This allowed to limit or even suppress the latency phenomenon observed with nanoparticle assemblies.

3.3.5. Response Time

Apart from the concerns on strain range and gauge factor, fast response time is also a crucial vital feature. Sensors have illustrated diverse response times ranging from 0.2 to 320 ms [12][25]. As example, ecoflex elastomer show slower response time in comparison to PDMS-based resistive strain sensors due to ultra-softness of material, providing low recovery [26]. Natural-fiber-based strain sensors tend to have a short response time which make them a suitable candidate for wearable applications [27][28].[27][28]. Generally, strain sensors based on nanocomposites have shown longer recovery time, because of the existence of friction between conductive fillers

and polymer matrices. During the release cycle the friction force increases the time of recovery in this conductive network [12].

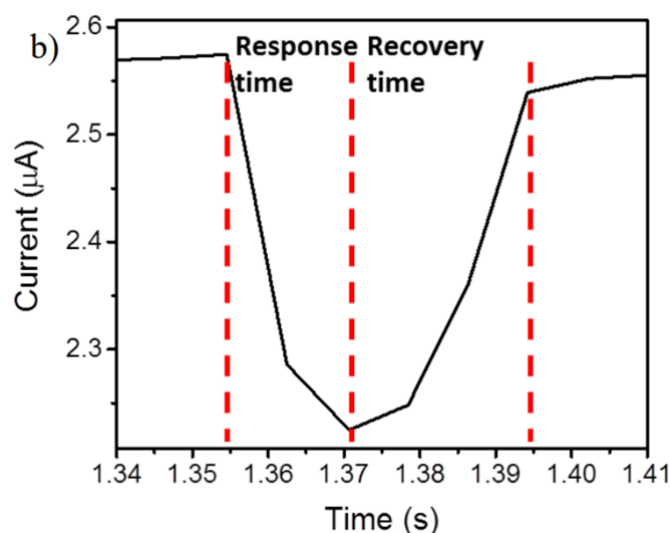


Figure 3.28 : Response (16.1 ms) and recovery time (23.5 ms) test for AuNPs–TEG network based strain sensor [29].

HNS strain sensors were tested by clamping the two ends of Kapton film and tapping on the sensor, Figure 3.29(a). The plot of the real-time current change of the HNS sensor is shown in Figure 3.29(b). It is seen that resistance change is achieved in about ~120 ms, indicating that the response time should be less than 120 ms. In the releasing stage, the sensor takes more time than the loading stage to go back to its initial state due to structural relaxation.

Another crucial performance parameter of a strain sensor, especially under cyclic loads, is recovery time, which could be in the order of sub-seconds to a few seconds. The capacitive-type strain sensor has a relatively shorter recovery time compared to that of a resistive type one [30]. In this case it is noted to be ~440 ms. The fast self-healing process is vital as it ensures quick recovery of the sensor and avoids the degradation of the device performance after being released to the relaxed state.

Overall, HNS strain sensors exhibited very fast response with a response time and a recovery time of 0.12 s and 0.44 s respectively, implying a very efficient self-healing response of HNS network.

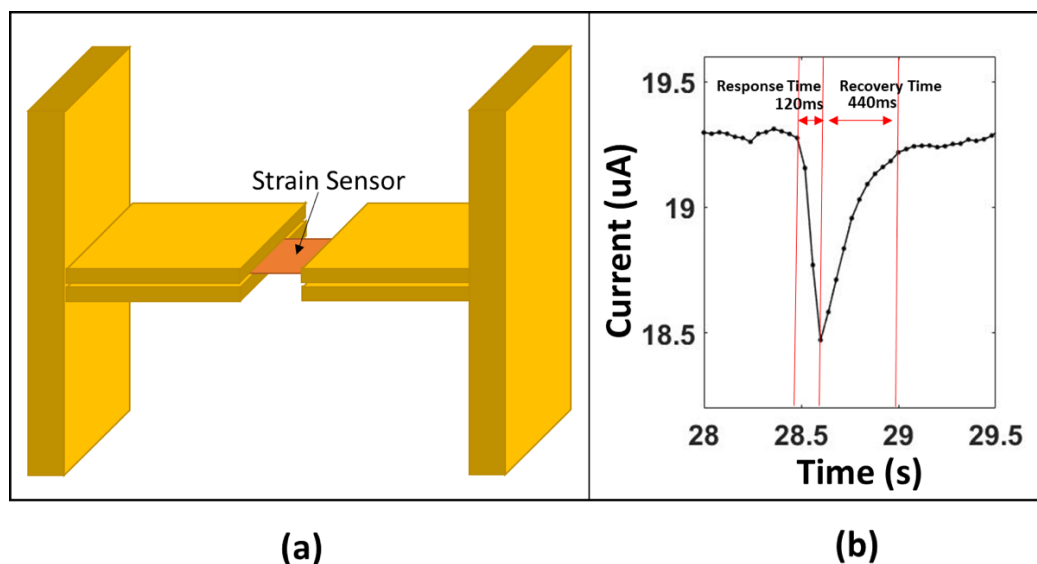


Figure 3.29: (a) Illustration of 'Response time' setup. (b) Response time measurement when a pressure is suddenly applied and then removed.

3.3.6. Vibration test

It is useful to know the dynamic response of the HNS, i.e., the natural frequencies and damping ratio. The effect of vibration on the device was tested by a slight tap on one end of the Kapton sheet while fixing the other one, as seen in Figure 3.30. The current of the device was recorded with an applied bias voltage of 0.5 V.

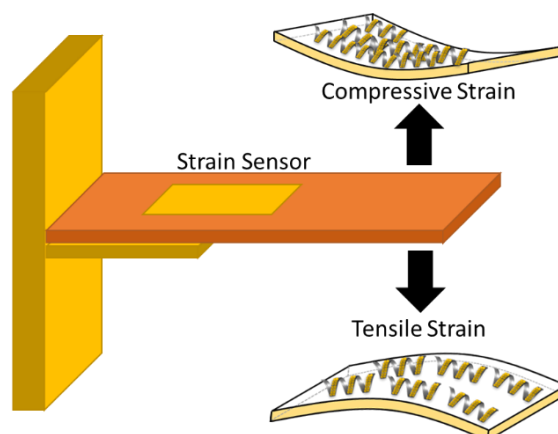


Figure 3.30: Illustration of the vibration test setup.

The amplitude of the strain variation decreased over time due to the damping of the vibration, Figure 3.31(a). The current signal of vibration is modeled by the underdamped vibration equation, Eq. (3.4) [29].

$$I = A \cos(2\pi f_0 t - \Phi) \exp(-2\zeta f_0 t) + I_0 \quad (3.4)$$

where A stands for the amplitude, f_0 for the natural frequency, Φ for the phase, ζ represents the damping ratio and I_0 is the current offset. The logarithmic decrement δ is defined as the natural log of the ratio of the amplitudes of any two successive peaks (Eq. (3.5)):

$$\delta = \frac{1}{n} \ln \frac{x(t)}{x(t+nT)} \quad n = 1 \quad (3.5)$$

$$\delta = 0.693$$

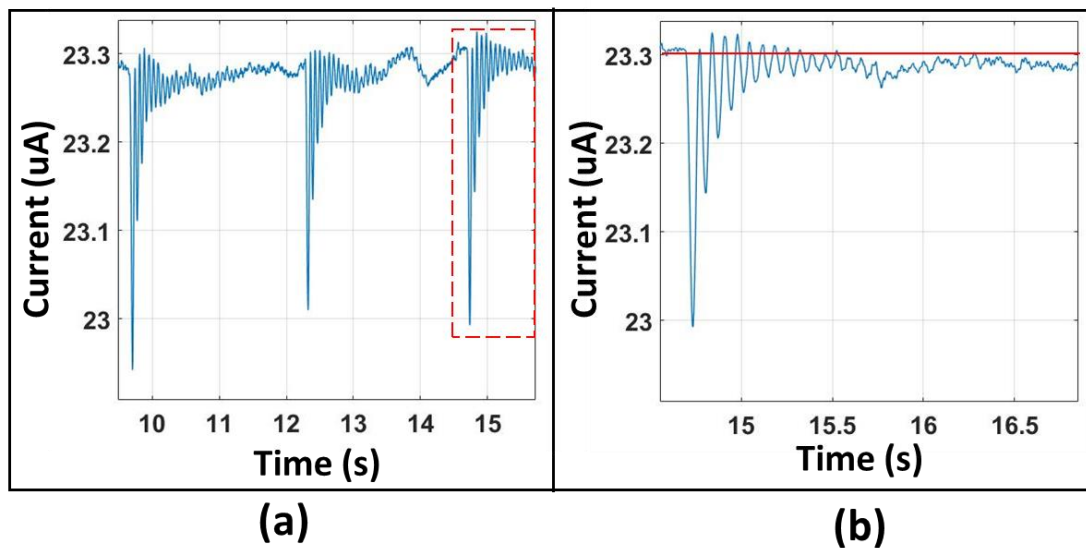


Figure 3.31: (a) Current response to vibration signal (b) Magnification of the signals in the red square in (a)

The damping ratio is then found ($\zeta = 0.109$) from the logarithmic decrement by:

$$\zeta = \frac{1}{\sqrt{1 + \left(\frac{2\pi}{\delta}\right)^2}} \quad (3.6)$$

The damping ratio can be used to find the natural frequency f_n ($f_n = 14.08$ Hz) of vibration of the system from the damped natural frequency f_d ($f_d = 14$ Hz)

$$f_n = \frac{f_d}{\sqrt{1 - \zeta^2}} \quad (3.7)$$
$$f_d = \frac{1}{T}$$

Results were comparable to those published by Huang. et al, they measured natural frequency to be 10.25 Hz and damping ratio to be 0.12 for strain sensor based on AuNP-TEG network [29] as shown in Figure 31 for a comparable sensor in terms of dimensions and materials used.

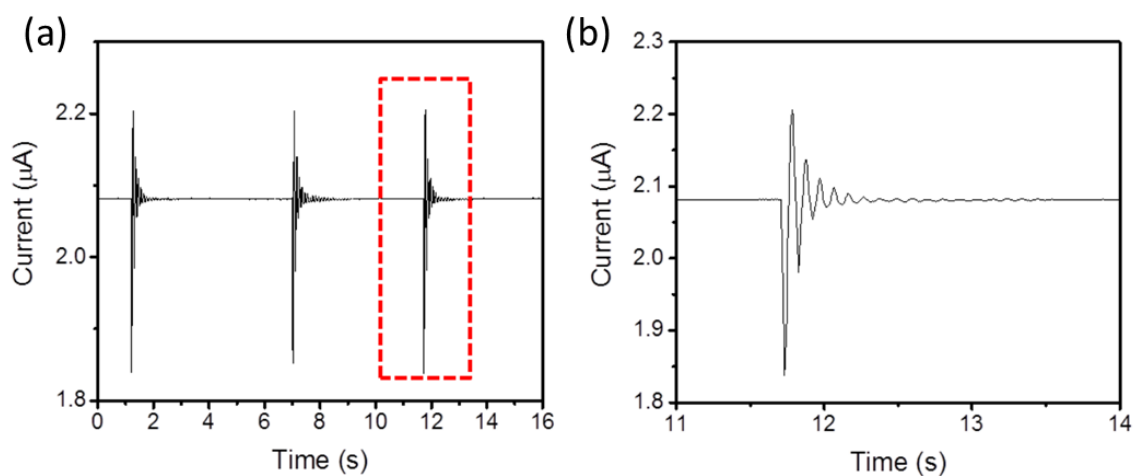


Figure 3.32: (a) Electrical response to vibration signal. (b) Magnification of the damping signals in the red square in (a) [29].

3.4. Conclusion

This chapter has addressed the mechanical analysis of the HNS based strain sensors. By making an estimation of quantity of HNS present between the IDE through device resistance, an interesting strategy to tune and enhance the GF of strain sensors has been presented based on multiple DEP deposition steps. While the helical nanostructure is the key contribution to no hysteresis response, high stability and durability. The grafting gold nanomaterials over a helical spring-like base made it possible to achieve mechanical properties rivalling those of the metallic nanoparticle networks. The intrinsic mechanical properties of the HNS structure allow a faster recovery after deformation. A higher structural integrity is also achieved through HNS sensors.

A novel strain sensor is realized that can measure ultralow strain up to 0.01%, with high durability (2M cycles at 1% strain) and fast response. These important features permit the HNS based devices to be used for real world applications, i.e., daily movements of the human body, structural health monitoring and data gloves. This will be addressed in the next chapter.

Bibliography

- [1] J. Park, Y. Lee, M. Ha, S. Cho, and H. Ko, "Micro/nanostructured surfaces for self-powered and multifunctional electronic skins," *J. Mater. Chem. B*, vol. 4, no. 18, pp. 2999–3018, 2016.
- [2] C. Mattmann, O. Amft, H. Harms, G. Tröster, and F. Clemens, "Recognizing upper body postures using textile strain sensors," *Proc. - Int. Symp. Wearable Comput. ISWC*, pp. 29–36, 2007.
- [3] R. Pethig *et al.*, "Tunneling effect in a polymer/carbon nanotube nanocomposite strain sensor," *Acta Mater.*, vol. 56, no. 13, pp. 2929–2936, 2008.
- [4] A. Morteza *et al.*, "Highly stretchable and sensitive strain sensor based on silver nanowire-elastomer nanocomposite," *ACS Nano*, vol. 8, no. 5, pp. 5154–5163, May 2014.
- [5] H. Li *et al.*, "A highly stretchable strain sensor with both an ultralow detection limit and an ultrawide sensing range," *Journal of Materials Chemistry A*, vol. 9, no. 3, pp. 1795–1802, 2021.
- [6] H. Liu *et al.*, "Electrically conductive polymer composites for smart flexible strain sensors: a critical review," *J. Mater. Chem. C*, vol. 6, no. 45, pp. 12121–12141, 2018.
- [7] S. Gong *et al.*, "Highly Stretchy Black Gold E-Skin Nanopatches as Highly Sensitive Wearable Biomedical Sensors," *Adv. Electron. Mater.*, vol. 1, no. 4, pp. 1–7, 2015.
- [8] W. Feng *et al.*, "Sensitive Electronic-Skin Strain Sensor Array Based on the Patterned Two-Dimensional α -In₂Se₃," *Chem. Mater.*, vol. 28, no. 12, pp. 4278–4283, Jun. 2016.
- [9] T. Q. Trung, N. T. Tien, D. Kim, M. Jang, O. J. Yoon, and N. E. Lee, "A flexible reduced graphene oxide field-effect transistor for ultrasensitive strain sensing," *Adv. Funct. Mater.*, vol. 24, no. 1, pp. 117–124, 2014.
- [10] C. Pang *et al.*, "A flexible and highly sensitive strain-gauge sensor using reversible interlocking of nanofibres," *Nat. Mater.*, vol. 11, no. 9, pp. 795–801, 2012.
- [11] S. J. Park, J. Kim, M. Chu, and M. Khine, "Highly Flexible Wrinkled Carbon Nanotube Thin Film Strain Sensor to Monitor Human Movement," *Adv. Mater.*

- Technol.*, vol. 1, no. 5, 2016.
- [12] M. Amjadi, K. U. Kyung, I. Park, and M. Sitti, "Stretchable, Skin-Mountable, and Wearable Strain Sensors and Their Potential Applications: A Review," *Adv. Funct. Mater.*, vol. 26, no. 11, pp. 1678–1698, 2016.
- [13] J. L. Tanner, D. Mousadacos, K. Giannakopoulos, E. Skotadis, and D. Tsoukalas, "High strain sensitivity controlled by the surface density of platinum nanoparticles," *Nanotechnology*, vol. 23, no. 28, 2012.
- [14] Alamusi, N. Hu, H. Fukunaga, S. Atobe, Y. Liu, and J. Li, "Piezoresistive strain sensors made from carbon nanotubes based polymer nanocomposites," *Sensors*, vol. 11, no. 11, pp. 10691–10723, Nov. 2011.
- [15] J. Herrmann, K. H. Müller, T. Reda, G. R. Baxter, B. Raguse, and G. J. J. B. De Groot, "Nanoparticle films as sensitive strain gauges," *Appl. Phys. Lett.*, vol. 91, no. 18, pp. 1–4, 2007.
- [16] J. Lee *et al.*, "A stretchable strain sensor based on a metal nanoparticle thin film for human motion detection," *Nanoscale*, vol. 6, no. 20, pp. 11932–11939, 2014.
- [17] X. Li, R. Zhang, W. Yu, K. Wang, and J. Wei, "Stretchable and highly sensitive graphene-on-polymer strain sensors," *Sci. Rep.*, vol. 2, pp. 1–6, 2012.
- [18] L. M. Zhang *et al.*, "Self-Healing, Adhesive, and Highly Stretchable Ionogel as a Strain Sensor for Extremely Large Deformation," *Small*, vol. 15, no. 21, pp. 1–8, 2019.
- [19] A. Amestoy, "Synthèse de nanohélices hybrides par auto-assemblage de type 'bottom up' pour la fabrication de capteurs de déformation flexibles," L'UNIVERSITÉ DE BORDEAUX, 2020.
- [20] W. Xu, T. Yang, F. Qin, D. Gong, Y. Du, and G. Dai, "A sprayed graphene pattern-based flexible strain sensor with high sensitivity and fast response," *Sensors (Switzerland)*, vol. 19, no. 5, Mar. 2019.
- [21] D. J. Lipomi *et al.*, "Skin-like pressure and strain sensors based on transparent elastic films of carbon nanotubes," *Nat. Nanotechnol.*, vol. 6, no. 12, pp. 788–792, 2011.
- [22] S. Xu *et al.*, "Biocompatible Soft Fluidic Strain and Force Sensors for Wearable Devices," *Adv. Funct. Mater.*, vol. 29, no. 7, pp. 1–14, 2019.
- [23] S. Seyedin, P. Zhang, M. Naebe, and S. Qin, "Textile strain sensors: A review of the fabrication technologies, performance evaluation and applications,"

- Mater. Horizons*, vol. 6, no. 2, pp. 219–249, 2019.
- [24] L. Duan, D. R. D’hooge, L. Cardon, R. D. Dagmar, and L. Cardon, “Recent progress on flexible and stretchable piezoresistive strain sensors: from design to application,” *Prog. Mater. Sci.*, vol. 114, p. 100617, Oct. 2019.
- [25] Y. Zhao *et al.*, “Ultra-sensitive and durable strain sensor with sandwich structure and excellent anti-interference ability for wearable electronic skins,” *Compos. Sci. Technol.*, vol. 200, no. September, p. 108448, 2020.
- [26] M. Amjadi, Y. J. Yoon, and I. Park, “Ultra-stretchable and skin-mountable strain sensors using carbon nanotubes-Ecoflex nanocomposites,” *Nanotechnology*, vol. 26, no. 37, p. 375501, 2015.
- [27] H. Souri and D. Bhattacharyya, “Highly sensitive, stretchable and wearable strain sensors using fragmented conductive cotton fabric,” *J. Mater. Chem. C*, vol. 6, no. 39, pp. 10524–10531, 2018.
- [28] H. Souri and D. Bhattacharyya, “Highly stretchable and wearable strain sensors using conductive wool yarns with controllable sensitivity,” *Sensors Actuators, A Phys.*, vol. 285, pp. 142–148, 2019.
- [29] C. B. Huang *et al.*, “Highly Sensitive Strain Sensors Based on Molecules–Gold Nanoparticles Networks for High-Resolution Human Pulse Analysis,” *Small*, vol. 17, no. 8, 2021.
- [30] T. Wang, Z. Ouyang, · Fei Wang, and Y. Liu, “A review on graphene strain sensors based on fiber assemblies,” *SN Appl. Sci.*, vol. 2, 123AD.

Chapter 4: Temperature
& humidity tests,
Preliminary results for
wearable strain sensors

Introduction

This chapter focuses on applications of flexible strain sensors that were developed with helical nanostructures (HNS) using dielectrophoresis (DEP) alignment technique. After presenting the sensor material and deposition techniques in Chapter 2, the mechanical properties of the HNS sensor were addressed in Chapter 3. Mechanical ageing effects on the sensitivity and the hysteresis after 2 million bending cycles were discussed.

Previously, the effect of adding an encapsulation layer over sensitivity was evaluated. In this chapter, the effects of temperature and humidity are tested over non-encapsulated and encapsulated samples. As normally, HNS sensors are protected with an encapsulation layer, the influence of the temperature and humidity is eliminated. These pioneering works give clues for developing multimodal sensors, which can detect different types of stimuli with only one sensor device.

In particular, this chapter presents the preliminary tests on hand gesture recognition based on the data glove approach [1][2]. In order to verify the capabilities of our HNS sensors to be used in a sensing glove, gestures like bending and lifting positions of individual finger, wrist movements and pulse measurements were performed. Herein, the limits of developed HNS sensors are explored based on their capacity of real-time hand pose reconstruction and environment sensing with flexible multimodal sensors.

4.1 Temperature & Humidity Response

The stability of the strain sensors strongly depends on their environment and storage conditions. The output of strain sensors is potentially susceptible to variation in environmental conditions such as temperature and humidity. It is important that strain sensors are resilient to these changes in order to avoid undesired noise in long-term sensing response. To eliminate unwanted interferences, there is a strong need for new material approaches combined with advance-packaging methods. For example, super-hydrophobic coatings have been developed to block the penetration of water molecules into the strain sensing films [3] but usually protective adhesive thin films are used [4]. While other explored encapsulation methods include chemical; thermal; and mechanical encapsulation, such as liquid polymers, multi-layer sealing, resins and laser sealing [5][6][7].

On the contrary, the ability of a sensor to detect strain, temperature and humidity can be of great interest for human-machine interfaces or soft robotics [8][9][10][11][12]. Wang et al. developed a prosthetic hand which can hold a cup of water and reveal if the water is hot or cold, with the help of a sensor matrix that can detect temperature and pressure simultaneously [13]. However, the sensor matrix has to be integrated with five-pressure sensor and one temperature sensor as shown in Figure 4.1(a, b). In comparison to such complex matrix of sensors, a multimodal sensor might be better suited to simplify the equipment, reduce the required space and improve the working efficiency of the system. For instance, sensing of multiple external stimuli has been achieved through multifunctional epidermal electronics, Figure 4.1(d-f).

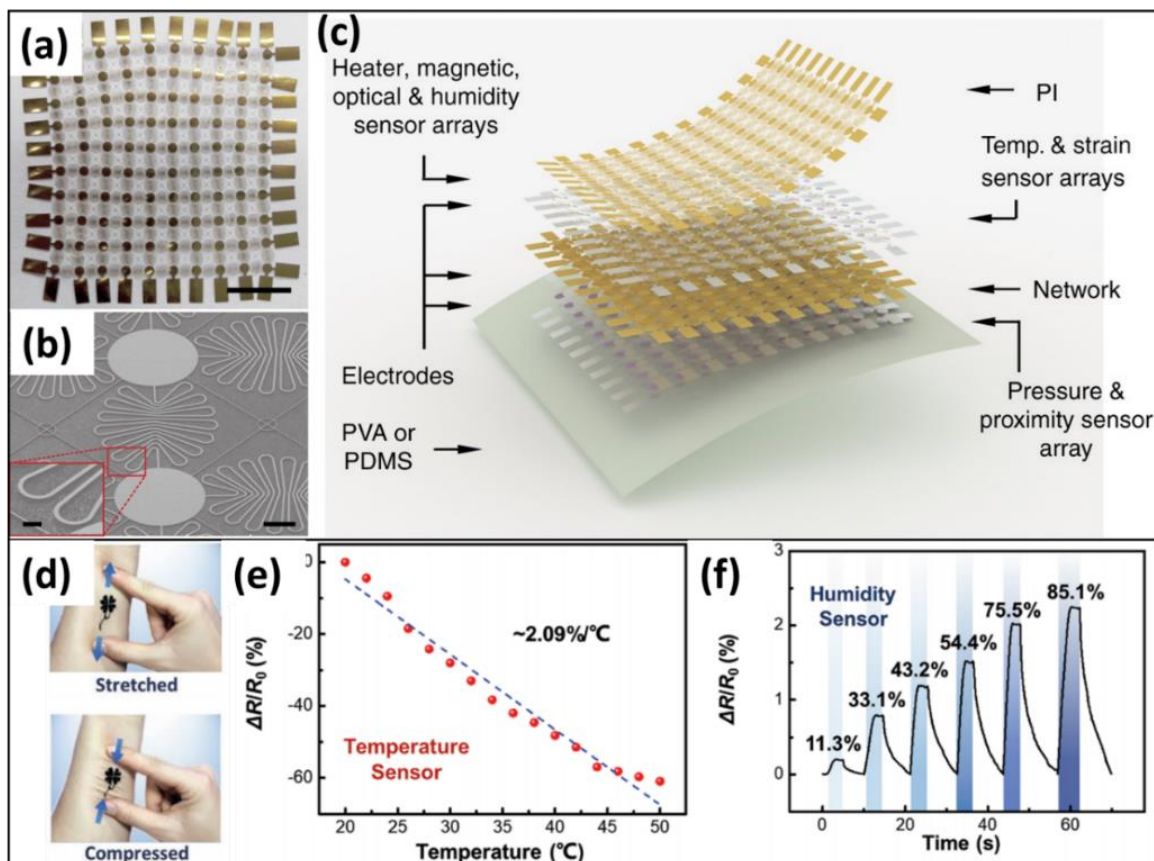


Figure 4.1: (a) Image of the fabricated polyimide network (10×10 array, scale bar: 5 mm). (b) SEM image of the polyimide network. (c) Schematic layout of an integrated sensor array with eight functions[13]. (d) Multifunctional Electronic Tattoos based on Silk and Graphene. (e) Temperature sensor performance of the corresponding tattoo-based sensor. (f) Real-time relative humidity sensing at several specific relative values [14].

In Chapter 3, to assess the strain performances of the HNS sensors, they were protected from temperature and humidity by a simple adhesive film to create a barrier with the outside atmosphere. Here, for the interest of exploring the ability and limits of our sensors, non-encapsulated HNS sensors were examined with regards to their sensitivity towards temperature and relative humidity, an information that might prove to be useful in fabrication of a multimodal sensor.

4.1.1 Temperature Tests

Temperature and humidity measurements were performed by Estelle Mazaleyrat and Fabrice Severac, engineers at Nanomade Concept in Toulouse.

The climatic measurements are achieved using a ZL-6004A programmable climatic chamber, Figure 4.2(a). This equipment has a capacity of 80L, allows a temperature control from -40°C to $+150^{\circ}\text{C}$ and a humidity control from 20 to 98% R_H. The HNS sensors after being glued on a glass slide are electrically connected via a dedicated PCB in order to achieve a robust connection, Figure 4.2(b).

The cyanoacrylate adhesive Loctite 401 is usually used to transfer the sensors onto glass slides. However, it does not perform well at high temperatures and high humidity, so it was replaced by an acrylic adhesive Loctite AA3921. It crosslinks under UV light and is stable under these same environmental conditions with equivalent mechanical performance. Sensitivity measurements are performed before and after subjecting to temperature variations, using the three-point bending equipment shown in Figure 4.2(c). The three-point bending setup used here is similar to what has been previously presented, in Chapter 3, for measurements of gauge factor as well as the calibration protocol. During temperature test, the humidity level is not controlled. In the test behavior recorded for two sensors, one is encapsulated and the other non-encapsulated.

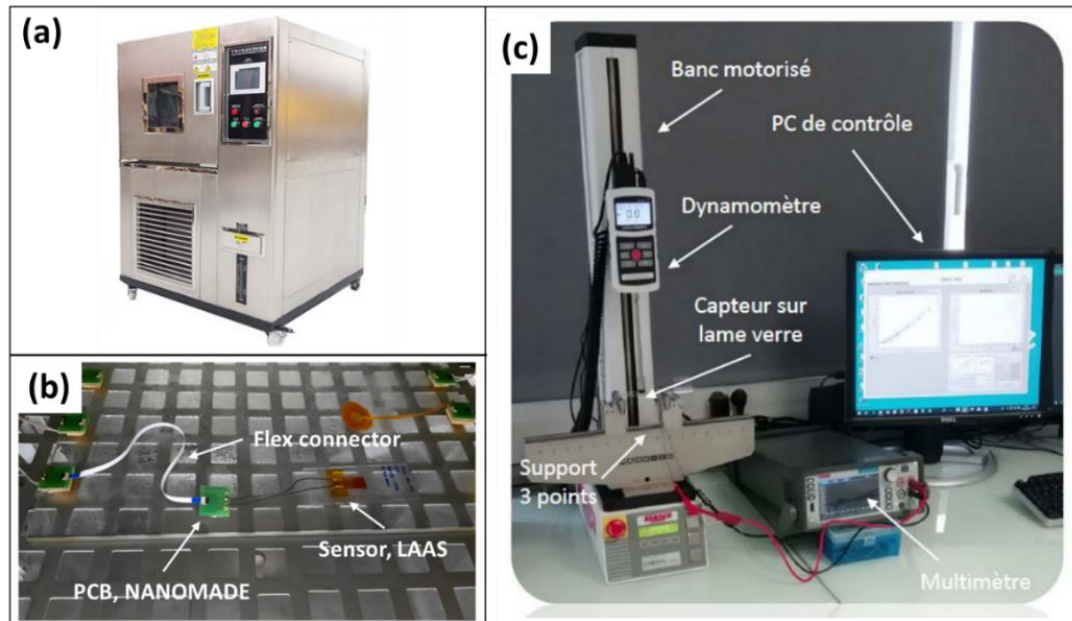


Figure 4.2: (a) Climatic chamber. (b) Sensor connection inside climatic chamber via PCB. (c) Three-point bending set-up.

Tests at elevated temperature (from room temperature to 85°C): Sensors are exposed for 1 hour at 85°C and kept at a constant temperature of 25°C for 30 minutes, before and after the elevated temperature exposure, as shown in Figure 4.3. The encapsulated sensor N8 shows a slight decrease until around 90 minutes, followed by a slight increase in resistance leading to an overall constant resistance until the end of the test, regardless of the temperature or humidity value. The final resistance value is less than 10% higher than the initial resistance. The variations in the uncontrolled humidity level measured are random. It can explain the variation in resistance between 75 and 150 min of cycle time as it seems to coincide more with the increase in humidity than with temperature. However, it is interesting to note for the non-encapsulated sensor, the variations in resistance show variations similar to those of the humidity, which is not the case for the encapsulated sensor.

For the non-encapsulated sensor N10, significant variations in resistance are noted throughout the cycle, the final resistance is more than 50% higher than the initial resistance, Figure 3 (blue). In particular, it is clearly observed that these variations in resistance follow perfectly the variations in humidity inside the enclosure throughout the cycle. The sensitivities of these sensors were measured after this climatic test at 85°C and compared with their initial sensitivity. The results obtained are shown in conclusion, Figure 4.3.

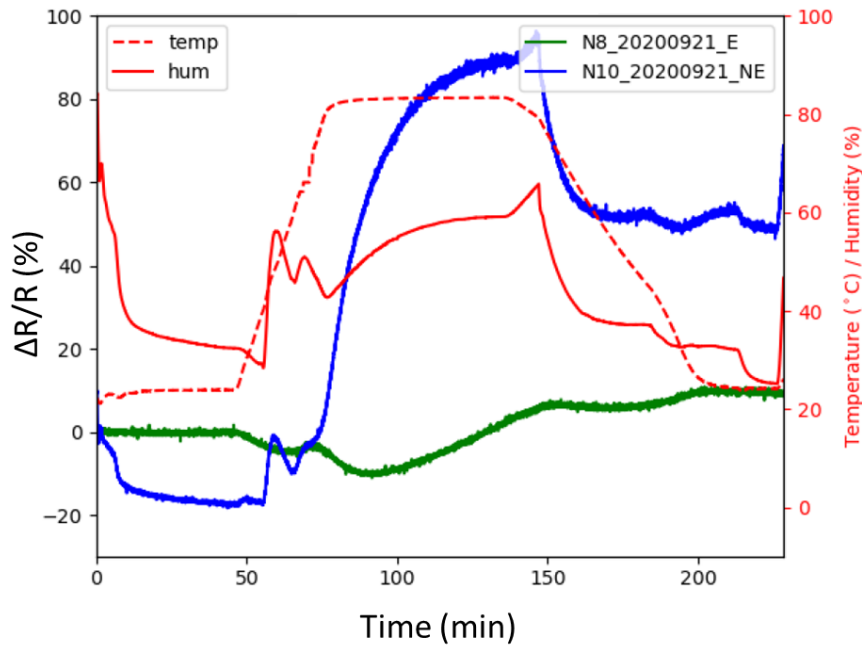


Figure 4.3: Resistance variations of encapsulated (green curve) and non-encapsulated sensors (blue curve) at elevated temperature from room temperature to 85°C (Figure from Nanomade).

Tests at low temperature (from -40°C to room temperature): The sensor response is then tested for low temperature condition. They are exposed for 1 hour at -40°C and kept at constant temperature of 20°C for 30 minutes before and after the variation, Figure 4.4. Observing the encapsulated sensor, the resistance variation from initial value and final value after the entire cycle is identical. Contrary to what has been observed for high temperature cycles, the resistance of the sensor increases as the temperature decreases. The resistance increases and remains constant over a time that corresponds to the plateau at -40°C and then gradually returns to its nominal value. For the non-encapsulated sensor, variations in electrical resistance followed the variations in humidity measured.

Concerning the influence of the humidity, similar variations are observed for almost the whole temperature cycle, where the resistance of the sensor increases with the humidity value.

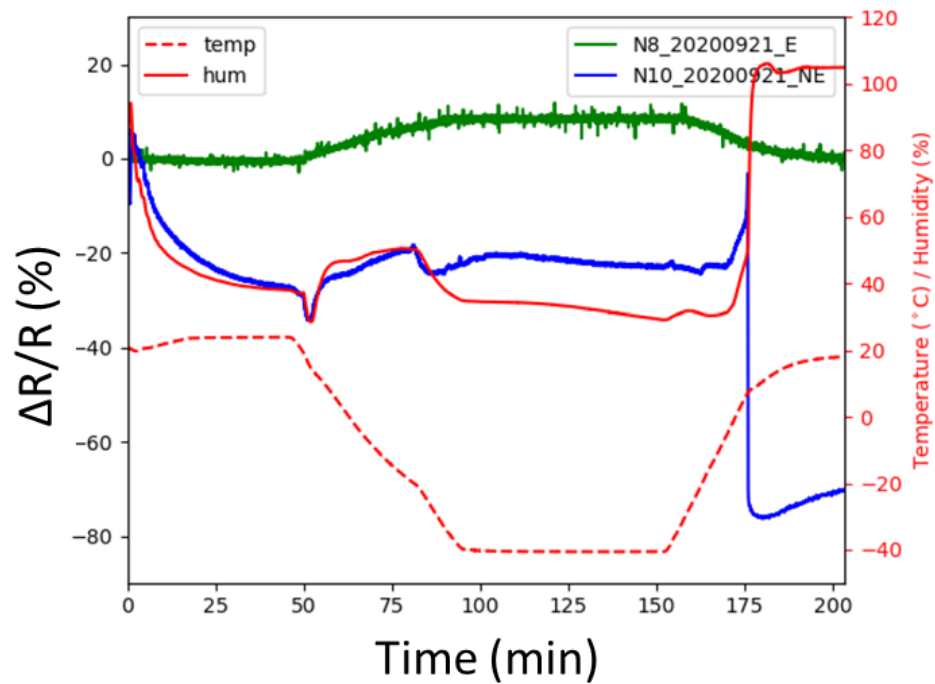


Figure 4.4: Resistance variations of encapsulated (green curve) and non-encapsulated sensors (blue curve) at low temperature (Figure from Nanomade).

Conclusion

During the temperature tests, there is a slight decrease in the sensitivity of the non-encapsulated sensor, though it retains a good linearity, as plotted in Figure 4.5. The low temperature measurements confirmed a strong dependence on humidity when the sensor is not kept in vacuum or is not encapsulated. The encapsulated sensor (en-HNS) remains relatively stable during the cycle and returns to the initial resistance value at the end of the temperature cycles. The encapsulated HNS does not show any drastic deterioration and maintains its sensitivity value, at high and low temperatures.

This series of experiments highlights the sensitivity of the HNS towards humidity, which is largely predominant, compared to temperature. When the active area is protected by a Kapton encapsulation, the resistance variations observed during the cycles are relatively small. On the contrary, when the HNS are in direct contact with the ambient air, the variations in resistance follow the variations in humidity. However, this effect on the electrical resistance does not affect the mechanical response of the sensor as the performance, GF value, is observed to remain unchanged after the climatic, Figure 4.5.

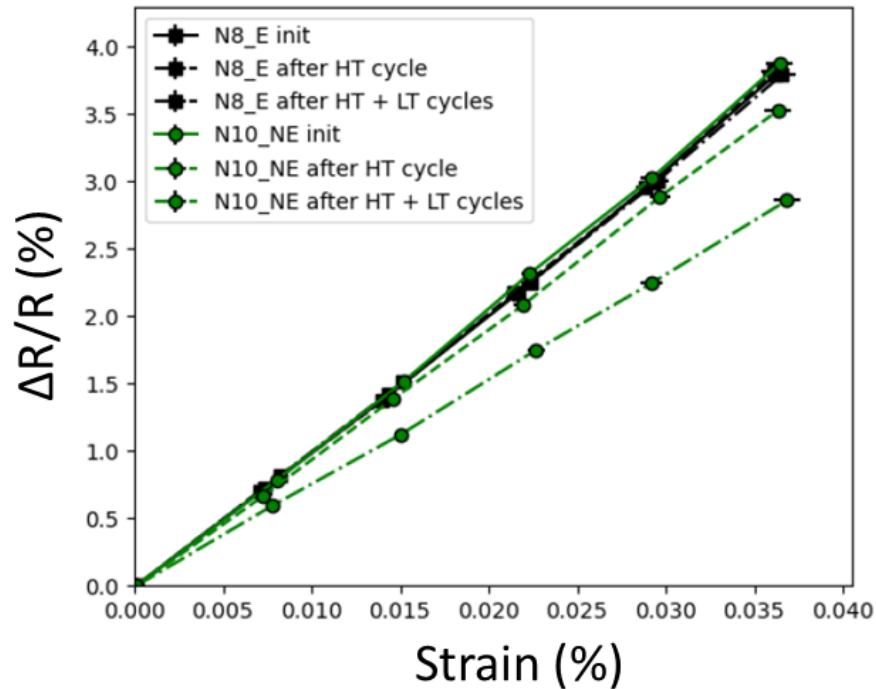


Figure 4.5: Stability over high temperature and low temperature cycles – Resistance variation as function of strain. Graph presents two HNS sensor samples encapsulated N8 (black) and non-encapsulated N10 (green). ‘inti’ refers to measurement before temperature cycle. HT refers to High Temperature, LT refers to Low Temperature (Figure from Nanomade).

4.1.2 Humidity Tests

Figure 4.6(a) shows a typical relative electrical resistance variation $\Delta R/R_0$ as a function of relative humidity (R_H), where R_0 is the electrical resistance measured at 0% R_H . The temperature is kept constant at 35°C during the whole humidity cycle. Measurements were performed with one encapsulated (en-HNS) and another non-encapsulated sensor.

The non-encapsulated sensor’s resistance value was first stabilized at 40% R_H for 1 hour, Figure 4.6(b). The R_H value is increased gradually by 10% and eventually decreased in steps of 10% after reaching an inversion point. This inversion point is observed when the sensor’s response behavior is inverted. Normally for HNS sensors, it is observed between 80 – 100%. Due to a possible hysteresis effect with respect to humidity, the inversion/de-inversion mechanisms are not symmetric. The inversion in resistance behavior of the non-encapsulated sensors occurs close to a humidity level of 98% R_H , while the de-inversion in resistance behavior occurs close to 81% R_H , Figure

4.6(a). Figure 4.6(b) is a zoom-in of Figure 4.6(a), at the beginning of the cycle from $t = 0$ to $t = 50$ min.

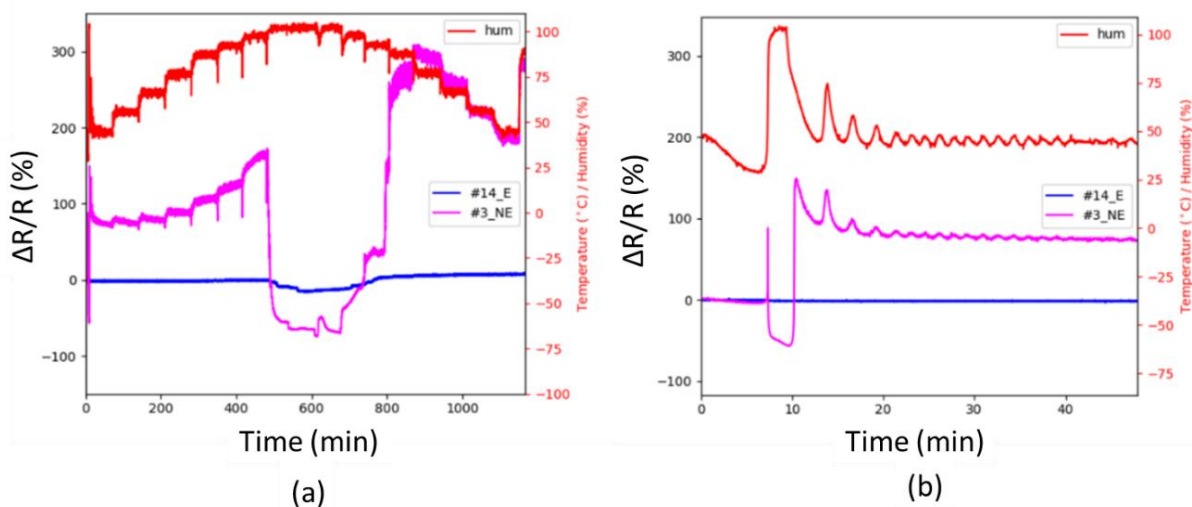


Figure 4.6: (a) Resistance variations of encapsulated (blue) and non-encapsulated sensors (pink) during the humidity cycle (red). The temperature is constant and equal to 35°C throughout the whole cycle. (b) Resistance variations with (blue) and w/o encapsulate (pink), zoomed on the beginning of the humidity cycle (Figures from Nanomade).

Discussion

It is observed that the electrical resistance increases when the humidity value increases, there is a sudden drop in resistance as humidity continues to increase. The physical phenomenon that comes into play could have the following possible origin:

1. Change in electrical conductance due to the water absorption by the nanoparticle network [15]. The swelling of the nanoparticle assembly induced by the absorption of water molecules causes an increase in the distance between the gold particles, which leads to an increase in electrical resistance.

Figure 4.7 presents the relative humidity response, from range 5% to 85%, for 4 (TEG) or 6 (HEG) ethylene glycol units combined with AuNPs based devices, [15]. Due to the non-linear hygroscopic characteristics of the ligands, there is a strong increase of the water up-take at humidity levels exceeding 70%, a reversible absorption/deabsorption of water molecules from the atmosphere. The AuNPs-OEG structure undergoes swelling upon absorption of water molecules yielding an increased interparticle distance which considerably affects the electrical resistance[16].

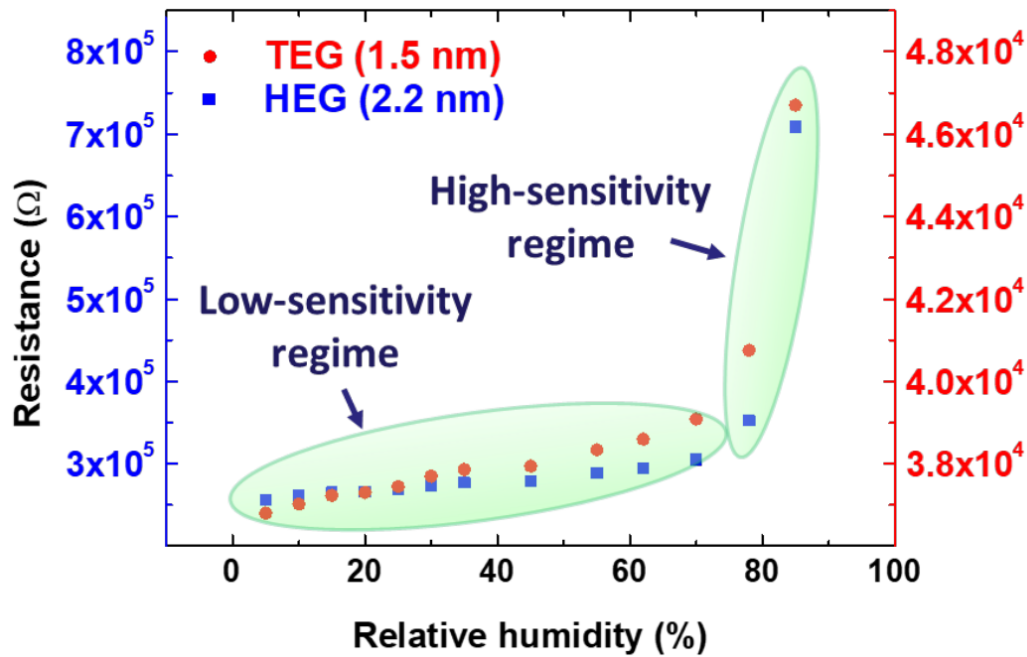


Figure 4.7: Resistance vs Relative humidity of AuNPs TEG and HEG based humidity sensors.

In case of HNS sensor devices the phenomenon is inverted i.e., a decrease in resistance after reaching a humidity level of 65%, which cannot be explained through the above description.

- Another explanation is when there is a significant change in the capacitance response of the nanoparticle assemblies, there is a change in the surrounding dielectric properties that results in resistance upturning. With increase in the humidity the effect on the dielectric properties of the film, tends to become significant. Depending on the relative value of the dielectric properties of water in comparison to the permittivity of the ligands, the variation of electrical resistance can be positive or negative.

Pang et al. observed a negative variation in electrical resistance on assemblies of gold nanoparticles protected by ligands. Figure 4.8 shows at low humidity (<40% relative humidity, RH) a film-coated sensor responds with a positive resistance and slight capacitance response at low humidity, while a negative resistance response and significant positive capacitance responses is seen at high humidity (>50% RH). This type of response can be explained by the more pronounced hydrophobic nature of these ligands surrounding the nanoparticles [17].

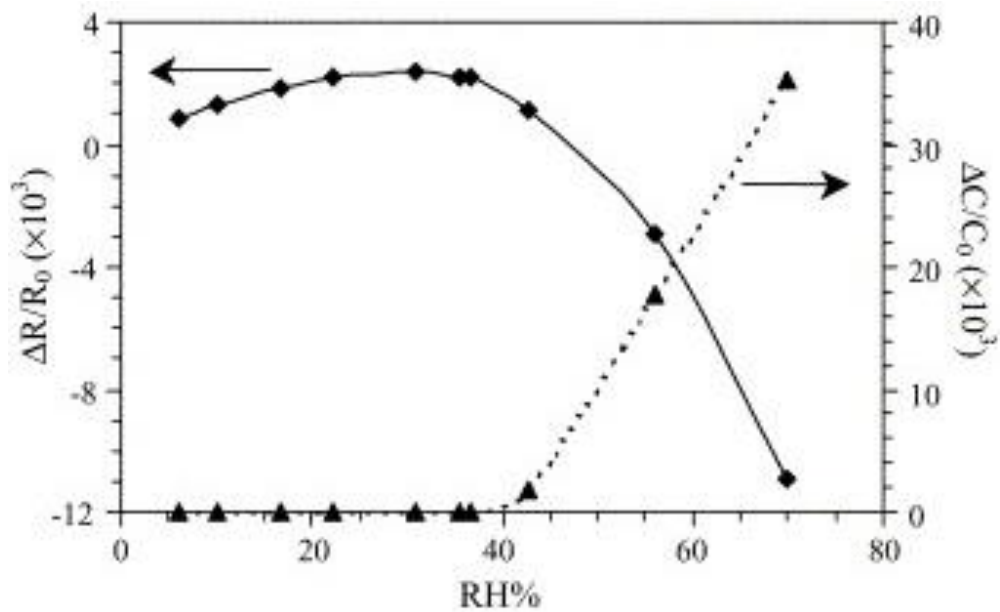


Figure 4.8: The relative resistance and capacitance changes with respect to relative humidity (RH%) [17].

- Another hypothesis to explain this phenomenon is that the ionic conduction (Grotthuss effect) is dominant between the inversion and de-inversion points, Figure 4.6(c), [18]. While before the inversion and after the de-inversion, the electronic conduction dominates. In presence of high humidity and in the absence of a barrier i.e., without encapsulation, H₂O molecules are physisorbed on the nanoparticles network. In this case ion conduction predominates via H₂O molecules (H⁺ ions jump conduction), Figure 4.9(a, b).

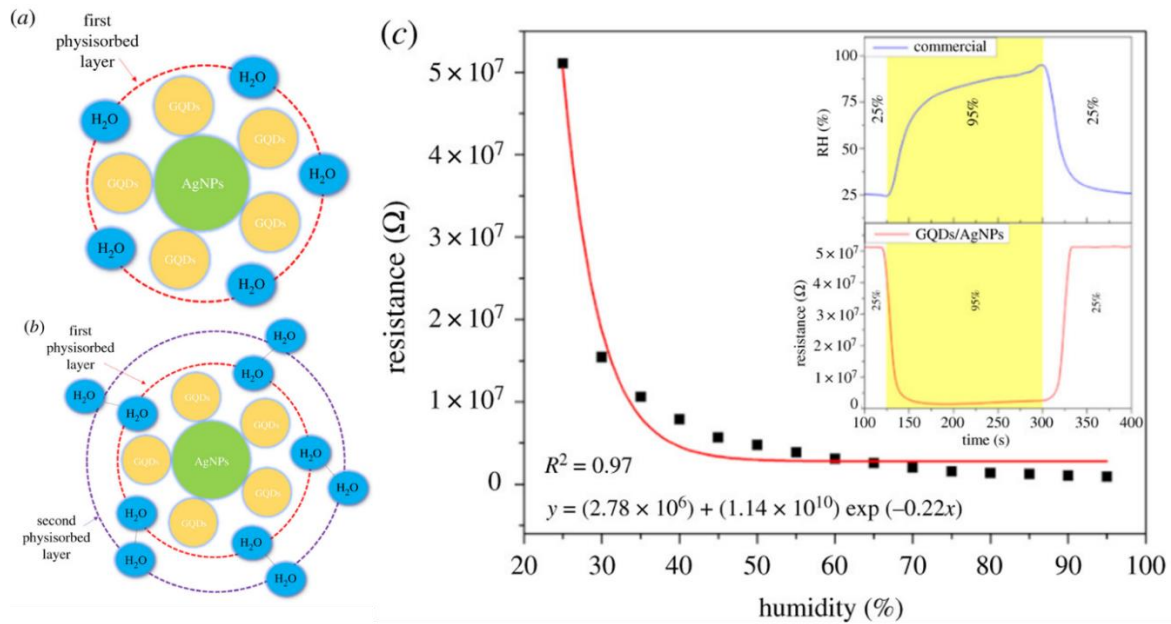


Figure 4.9: Illustration of sensing mechanism (a) the first and (b) the second physisorbed layer of the H₂O molecules. (c) Resistance of Graphene Quantum Dots(GQD) /AgNPs as a function of RH, the inset shows a humidity response of GQD/AgNPs sensor in comparison to a commercial humidity sensor [19].

Conclusion

HNS experimental results as seen in Figure 4.6, shows the influence of humidity on the electrical resistance value of sensors. The first regime between 0 and 65% humidity, characterized by a small increase in resistance to relative humidity, is governed by the changes induced through the swelling of the nanoparticle assembly and the increase in inter-particle distance.

In the second regime above 65%, the swelling effect is then predominated over by ionic conduction and the electrical resistance decreases. The presence of water molecules considerably changes the dielectric constant of the medium surrounding the nanoparticles, leading to a more pronounced effect on the electrical resistance.

The typical response of HNS strain gauges to relative humidity clearly emphasizes the importance of protecting the active area of nanoparticle-based strain gauges from water absorption. Encapsulation prevents the influence of the ambient environment on the strain transducer and its response, and thus lead to a more stable and reliable measurement from the applied strain.

4.2 Biological signal measurements

Commercially available strain sensors based on metal foils and semiconductors have extremely poor flexibility and low conformity to biological tissues. Our flexible HNS strain sensors exhibit high sensitivity, high durability, fast response, and excellent stability and hold the potential to be used as a biological signal input device for potential applications. We have performed some preliminary tests on some of them.

4.2.1 Cardiac Pulse Measurement

Currently, to acquire the pulse signal there are many categories of sensors such as infrared sensor, piezoelectricity sensor, liquid sensor, photoelectric sensor, acoustic sensor, and image sensor. Even with the commercially available sensors based on optics (photoplethysmography (PPG)), ultrasound, and tonometry, face challenges for robust continuous monitoring.

Photoplethysmography measures the intensity of light transmitted through or reflected by a tissue in order to monitor vascular pulsation. This method is widely used to monitor pulse wave, which are affected by the contact made between the PPG probe and the tissue. Therefore, there are deployed with straps and clamps that end up causing discomfort and irritation during the use. Moreover variation in the tightness of the strap the contact can change every time sensor is worn [20]. Ultrasound pulse wave sensor penetrates the skin to detect the fluctuations in the vessel. Their bulky and rigid imaging probes limit their use in daily life as wearable devices. While tonometry requires a precise placement at the center of the artery, the accuracy can vary with the position in millimeters. It is challenging to maintain a contact for long period among pulse wave sensors. It called for a sensor that is thin and uses a flexible substrate to improve contact and comfort of the user for unobtrusive monitoring in daily life.

Physicians habitually diagnose and pick up the human pulse information through superficial arteries by the means of fingertips palpating patient's pulses. Hence, the best option to imitate the physician's tactile sensation is in fact through pressure/strain sensor [21]. Flexible pulse wave sensors have potential to revolutionize the healthcare services. Strain sensor is attached to the radial artery. The sensor detects pulse waveform through percussion wave and descending limb wave. The pressure fluctuation of the artery generated the pulse signals and typically, it has a

waveform where three peaks are clearly distinguishable. It can successfully identify the pulse features like percussion wave, tidal and diastolic wave. As example of signal measurements, Figure 4.10(a) shows the pulse response detected by a Graphene/Silver Nanowire Nanocomposite having a gauge factor of 41.5. The use of a dry adhesive substrate for creating a contact between skin and sensor, Figure 4.10(b) shows that even a slight strain from pulse is clearly measured at a rate of ~ 1.5 beat per second.

Figure 4.10(c) show measurements from Thermoplastic Polyurethane (TPU)/graphene strain sensor with a novel intertwined coil configuration. In the waveform of a 7.8s range indicates presence of 10 peaks, it implies 77 beats per minute and has a sensitivity of 31.35 [22].

A sequence of six pulse waves presented Figure 4.10(d) measured using biocompatible GNP/PU sensors. They have a linear resistive response characterized by four-point bending test with a high gauge factor in the range of 10 and 100.

Figure 4.10(e, f) shows a strain sensor response based on polydimethylsiloxane (PDMS)/graphite sensing resistors for many wearable device applications such as arterial pulse measurement and for hepatic feedback, fingertip pressure monitoring. This flexible strain sensor makes use of a serpentine electrode design and has a total thickness of 200 μm [23].

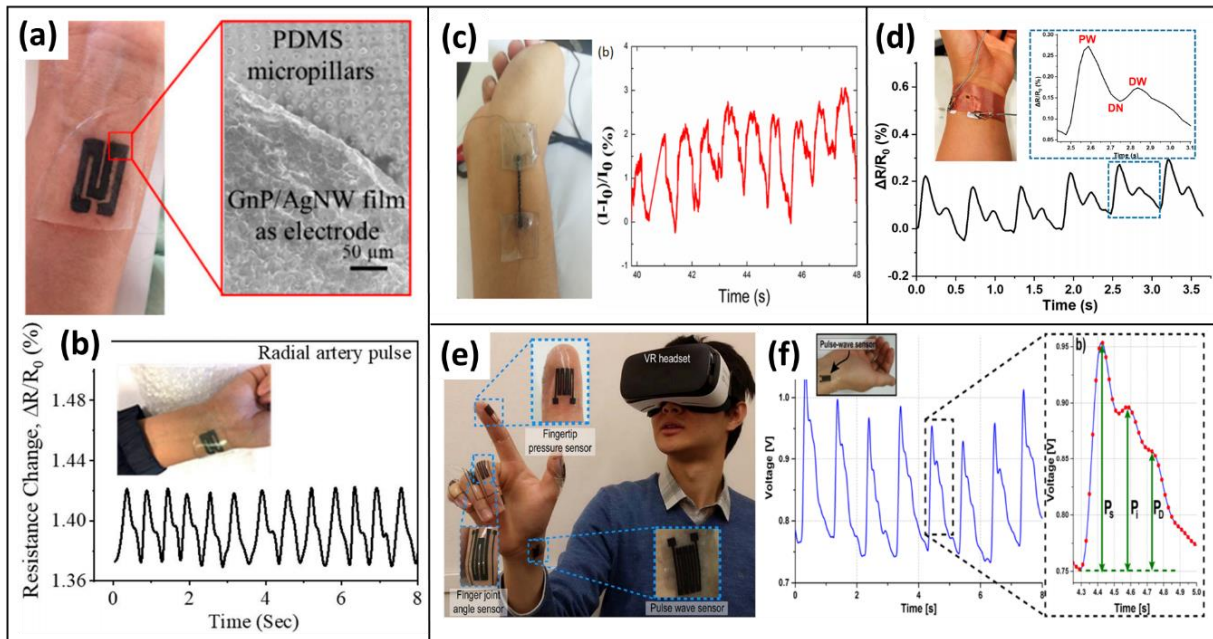


Figure 4.10: (a) Photographs of Graphene/Silver nanowire nanocomposite strain sensor attached onto the wrist, with an adhesive tape. (b) Real-time monitoring of radial artery pulse [24]. (c) Current variation of the Thermoplastic polyurethane/graphene strain sensor, with an intertwined-coil configuration, in response to the pulse [22]. (d) Resistance response of biocompatible gold nanoparticle/polyurethane (GNP/PU) strain sensor to the radial artery pulse [25]. (e) Wearable strain sensors together with a head mounted VR system. (f) The measured arterial pulse wave for 8 seconds. A close-up view of one cycle showing 3 peaks: systolic (P_s), inflection (P_i), diastolic (P_d) peaks [23].

Currently, most of the wearable devices use traditional rigid sensing material. The present-day pulse sensors are generally not sensitive enough and the detailed analysis of pulse waveform is lacking. Thickness of these sensors can go up to 2 – 3 mm. When placing pressure over the wrist with the help of a belt or cuff, it creates a problem as it generally involves rigid and bulky imaging probes. Further, many wearable devices are capable of detecting only one specific physiological signal (e.g., pulse or respiration rates) stimulus. There is a problem of mass production and uniformity of these sensors as they are limited by their complicated fabrication process.

This study moves toward testing the limits of previously (Chapter 2) fabricated and characterized (Chapter 3) HNS strain sensors. We propose a HNS pulse wave sensor, which offers high flexibility, ease of fabrication, and long-term operation under

daily life conditions. HNS sensors can measure the pulse signals with a high signal to noise ratio, owing to their high sensitivity to very low strain values, previously discussed in Chapter 3.

Results & Discussion For the pulse measurement, the strain sensor is attached on a wrist. In order to record the data, the center of the sensing area (interdigitated electrodes) should be placed on the radial artery, where there is a relatively strong beating pulse signal on the wrist. A layer of adhesive tape is wrapped around the wrist and over the HNS sensor. Because of the small size of the active sensing area and rigidity of the Kapton film, it is important to add extremely low pressure that will help to detect better the response, Figure 4.11(b). Another approach is to glue the sensor on the skin region where pulse movement is strongest, as done by Meng. et al [26]. For a complex motion association with the body, Tolvanen. et al made use of flexible Kapton tapes [27].

Further, the two ends of the sensor are connected to the VNA Instrument and a constant voltage of 0.5 V is applied to the strain sensor, Figure 4.11(a).

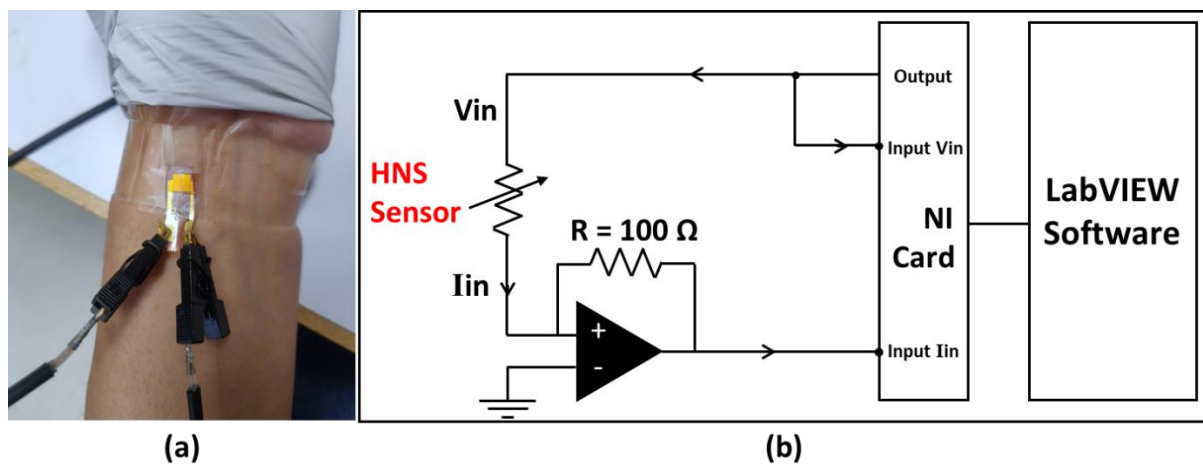


Figure 4.11: (a) Photograph images of a HNS strain sensor attached to wrist using adhesive tape to monitor pulse. (b) Electronic circuit diagram for measuring the resistance change of the HNS sensor due to geometrical deformation of the microchannel.

It is found that the three peaks of a pulse, systolic (P_s), inflection (P_i) and dicrotic peak (P_d) can be identified. The dicrotic peak (P_d) is known to be the result of the

reflected pulse waves from the lower extremities and aorta. Through Figure 4.12(a, b) real-time original signals measured with and without pulse wave, signal with the pulse wave clearly shows periodic peaks. For comparison, in Figure 4.12(b), only noise is recorded. The difference in nominal current value in the two graph is representative of slight pressure applied in case of pulse detection measurement to better adapt to the curve of the hand and detect the response. Because of the small size of the active sensing area and rigidity of the Kapton film (127 μm thickness) HNS sensor required additional pressure to place it closer on the surface of the wrist. This pressure can be applied manually, using an adhesive tape or by simply wearing it under a watch.

Figure 4.12(c) displays the measurement results of an arterial pulse waveform and a close-up view of one cycle from a 25-year-old female subject. The arterial waveform can be significant in monitoring physiological conditions of the human cardiovascular system for possible future applications in medical diagnostic systems.

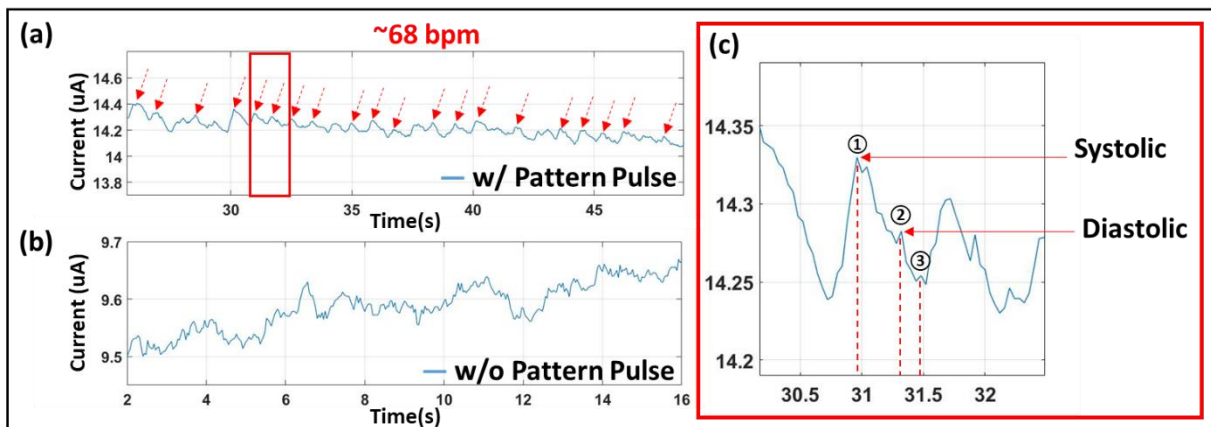


Figure 4.12: (a) Real-time pulse wave and small strain sensing performance, original signals measured (a) with and (b) without pulse detection. (c) A close-up view of one cycle showing three peaks: systolic (P_s), inflection (P_i), dicrotic (P_d) peaks.

According to the results shown in Figure 4.12(c):

- High-resolution measurement is essential for reliable pulse diagnosis. The fabricated HNS sensor can reveal tiny feature variation in the pulse wave, in which the majority of currently used sensors in arterial tonometry are inefficient.

- HNS sensor can more accurately and distinctly show the wrist pulse response [28]. In Figure 4.12 the data has been presented raw and without any data treatment [26][24].
- The small size of the HNS device is also a key feature to improve wearability for continuous, real-time, and elaborate pulse monitoring at home. It needs minimal amplification and additional circuitry. The active strain -sensing area is only 16mm².

However, one of the major drawbacks of the HNS sensors is there is a strong need to adjust the substrate thickness in order to accomplish an optimal balanced sensitivity, which will help to realize a complete wearable device. In the next section, the sensor's performance versus standard motion capturing capabilities is tested on finger and hand motion.

4.2.2 Hand movements

Hand therapists keep track of any changes prior to and following the treatment by measuring joint angles [29][30][31]. As an example, after a stroke, it is possible to improve the damaged parts of the brain through continuous and repetitive finger rehabilitation [32]. The current method during hand rehabilitation and assistance tasks is through implementation of manual goniometer and approximation through eye. Therefore, their efficiency is restricted by the fact of static measurement and large errors. Some studies have shown a great potential for detecting hand gesture by sensing muscle activity using electromyography and force-sensitive resistors. Figure 4.14(a, b) [33][34]. However, they are not easy to integrate into other wearable devices. These systems require additional hardware that further increases the cost and user discomfort.

Most of the current smart watches are equipped with accelerometers and gyroscope sensors. Figure 4.14(c); they offer a unique opportunity for gesture recognition [35][36]. Though it is anticipated that an arm's movements can be easily identified using a smart watch, it is not certain to what extent the user's hand and finger gestures are recognized.

Researchers have explored the integration of flexible devices into fabrics [37][38] with objective to realize improved sensing performance regarding body-part position reconstruction and posture classification. However, there are some downsides such as low sensitivity, and poor reliability of the sensor. In fabric-based sensors, the

strain sensing mechanism by the human movement has been related to only tensile behavior. The compressive strain properties have been hardly investigated using such sensors.

Therefore, a proper measurement of joint movement in daily physical activities, over long periods is of great interest. For application in fields such as computer gaming, virtual reality, rehabilitation, and robotics sensors, instrumented gloves based on piezoresistive sensors have been developed [39][2]. The proposed glove sensing system could translate some of the hand gestures of American Sign Language into an electrical signal, Figure 4.13. It is useful in designing the mobile device system to translate ASL alphabet using a human–machine interface [40].

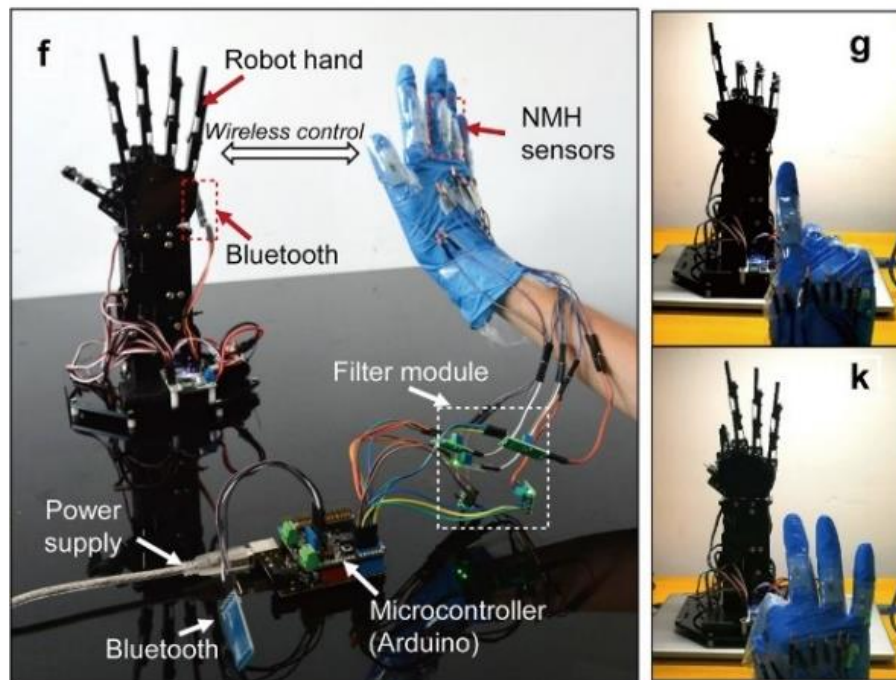


Figure 4.13: An interactive electronic system with five nanowire-microfluidic hybrid sensors using a multichannel data-glove to control a robotic hand through a wireless communication. (Right) Controlling different configurations of robotic fingers by a human hand wearing the data-glove [41].

Three-dimensional motion analysis systems are often used for dynamic recording of finger bending angles during the performance of daily activities. They are effective in capturing complex actions accurately but are bulky and expensive and have large space requirements. All this makes them less suitable for routine clinical use [42]. Studies on soft sensors have shown that owing to their superior flexibility and

conformability they are very promising sensing devices. These devices are lighter in comparison to glove-based system and are easier to fabricate, Figure 4.14(e). However, the design can have strict material requirements [43]. A new kind of sensors that uses a conductive liquid metal injected in a soft chamber has been proposed as well. This soft bending sensor works well for wearable devices, but the fluidity of liquid metal brings technical constraints and limits its practiced application [44][45][46][47].

Thus, considerable research efforts into the materials, structures, and processing have been conducted in recent years on resistance-type flexible strain sensors [1][48] due to their simple structure and superior sensing properties to various types of deformations.

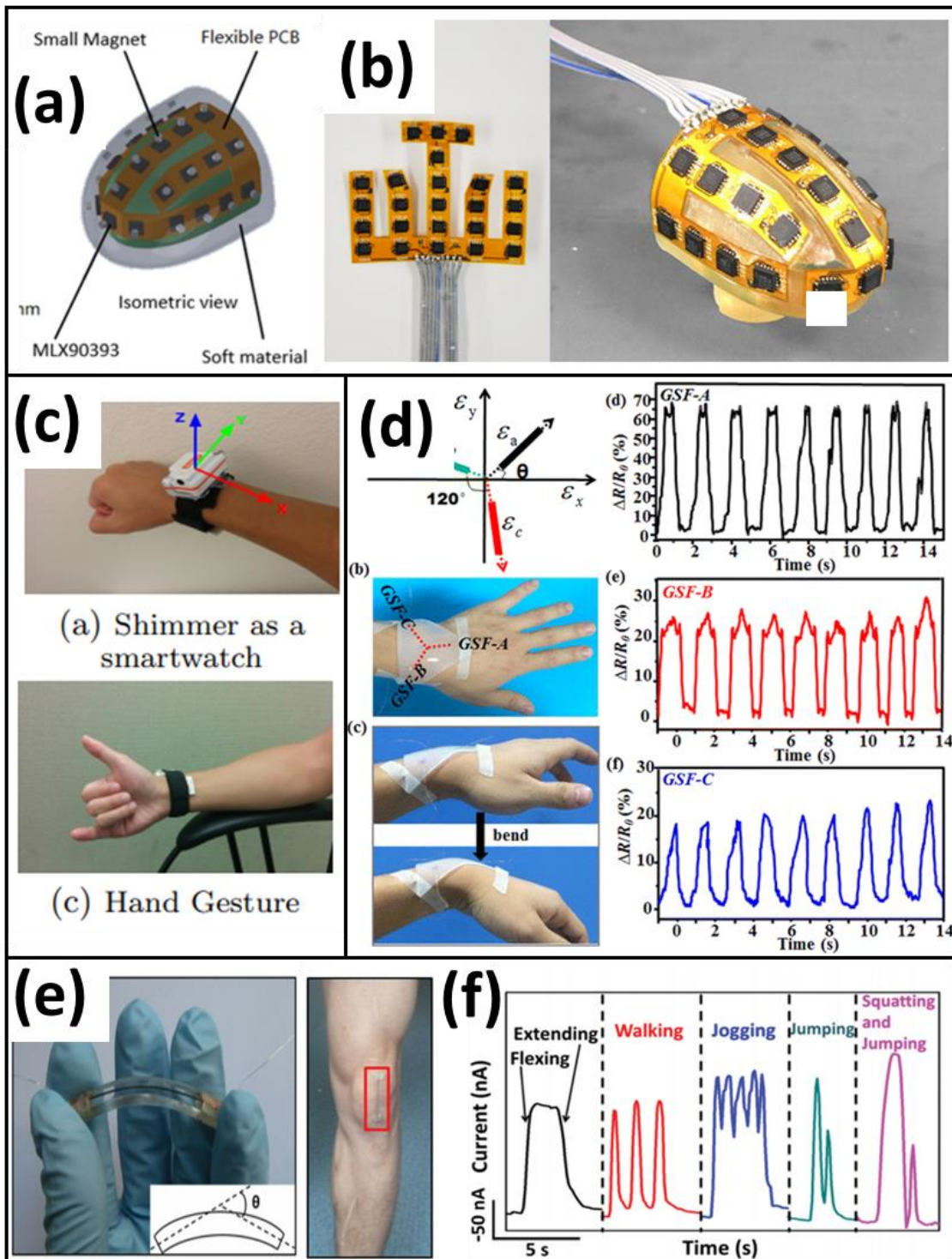


Figure 4.14 : (a) Design of uSkin for a fingertip (b) 3D printed fingertip with flexible PCB attached to it [33]. (c) Photographs showing experiment settings how Shimmers is used to measure wrist and forearm motion [36]. (d) Integrated rosette-shaped Graphite/Silk Fiber strain sensor for multidirectional motion detection and Responsive signals during cyclic bending-unbending motion of the wrist [49]. (e) Photographs of wearable sensor

attached to the knee marked in the red box. (f) Responsive curves of wearable sensor on the knee, shows various motions as labeled [50].

Results & Discussion

Prior to applying the sensor to the hand, the sensor is calibrated to obtain the relative variation of the resistance as a function of the applied force. The relative changes in electrical resistance are measured using a three-point bending machine, as shown in Figure 4.15(a). It is evaluated based on electrical resistance changes in small stepwise increment in force value.

Eventually, a measured variation of the resistance of the sensor corresponding to the force generated by the finger estimated using the graph generated with the same sensor showing the resistance variation with the applied force in Newton, Figure 4.15(b).

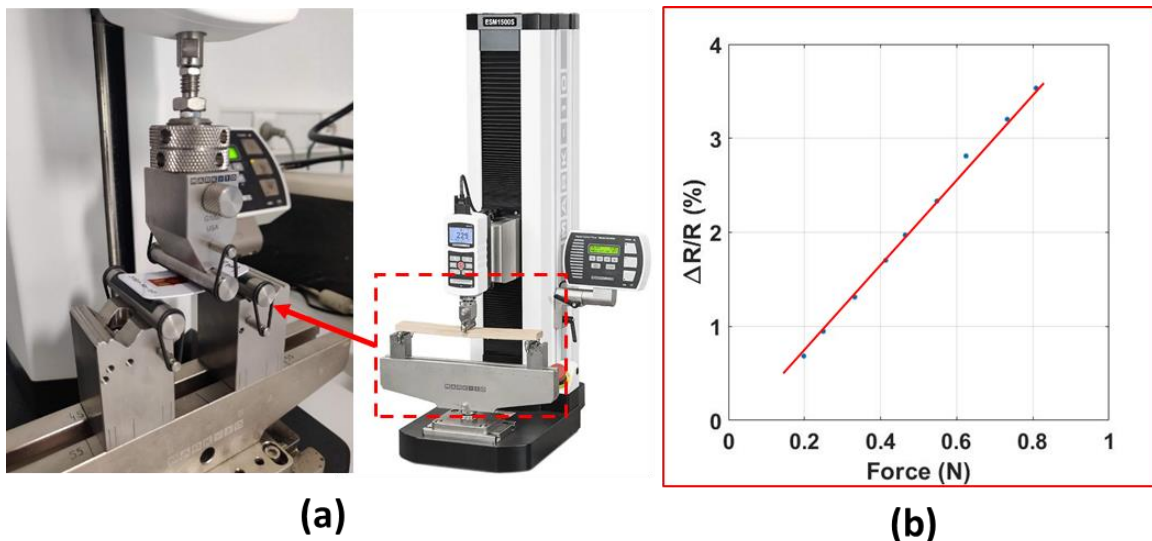


Figure 4.15: (a) Three-point bending set-up (b) Representative calibration curve. Sensor is calibrated before being installed on the subject. Force output in Newton was synchronized with resistance variation to produce a calibration equation, which was used subsequently to convert the resistance variation data from all trials on finger/hand into units of force. The fit for this sensor was linear with an R^2 value of 0.9.

- 1. Finger-joint bending** When measuring finger-joint bending, the HNS strain sensors are attached on the proximal phalanges over the joint of the index finger as show in Figure 4.16. The two ends of the sensor are connected to a VNA Instrument. A constant voltage of 0.5V is applied to the strain sensor. The

resistance of the strain sensor varies under a certain motion of hand. Figure 4.16 shows the resistance variation with time for the bending and relaxation state tests results.

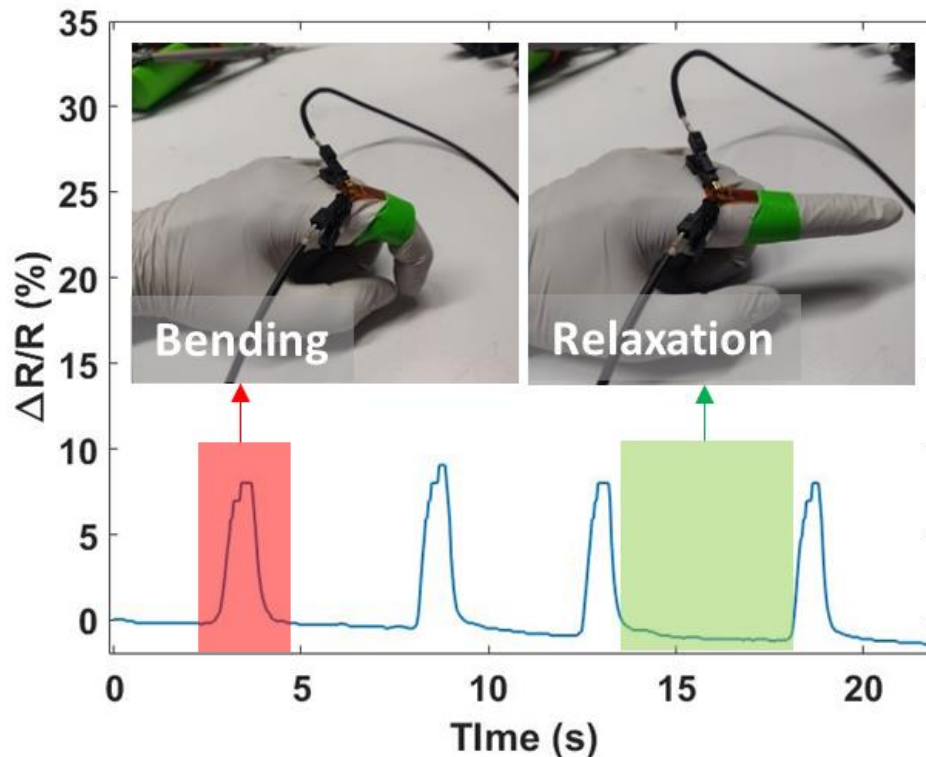


Figure 4.16: Relative resistance changes versus time of the finger motion on the tensile strain region.

By using the linear relation of increase in the sensor resistance variation with an increasing applied force, it quantifies that a 90-degree bending of finger generated 1.8 N. The finger joint bending sensor also shows good recovery capability after going through a 90-degree bending test, which is an indication of reliability of the sensor.

For monitoring the finger lifting effect, the thin Kapton sensor mounted on the palm as shown in Figure 4.17(a). Then one by one index finger (I) and little finger (L) lifted. The response of the resistance variation shows that the compressive strain experienced is stronger by lifting last finger (L) comparatively, Figure 4.17(b). It can be specified that resistance variation peaks strongly correlated with the motion of each finger successfully verifying the feasibility of the sensor in terms of small motion detection.

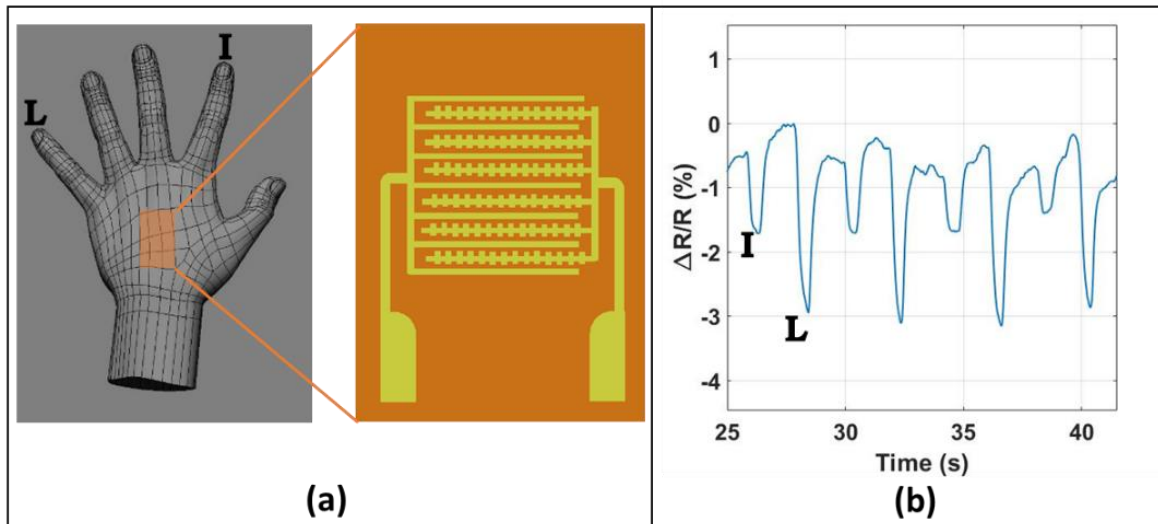


Figure 4.17: (a) Diagram showing the placement of the sensors as well as the letters 'I' and 'L' on each peak represents which finger is bent at each region. (b) Real-time output of the sensor glove showing individual finger response.

2. **Hand motion** Placing the sensor to the back of the hand is especially relevant, since hand plays an important role as a primary part of the body by which humans sustain tactile interaction with their environment. The sensor is mounted on the center of the opisthenar over a typical glove with associated electrical connections. The problem associated with direct attachment of sensor in the hand module can include hand tremors and temperature. To reduce the signal noises an adhesive tape (green) is added right over the active sensing area to firmly grip the sensor to the hand, Figure 4.18.

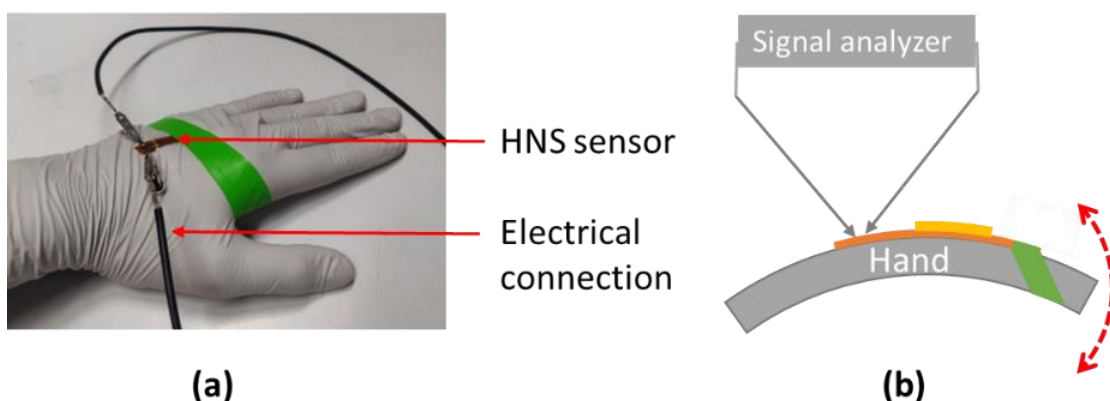


Figure 4.18: (a) Photograph and (b) the layout of the sensors on the glove.

In order to verify the performance of the developed sensing glove, three experiments are conducted regarding the HNS sensor. (1) First experiment is to test

two different configurations of placement of IDE, Figure 4.19(a). (2) Second is the electro-mechanical properties of the wrist flexion. Wrist extension are assessed using the relative changes in electrical resistance. Finally, a 10mins long flexion and extension is performed. The experiments performed are analyzed using MATLAB R2018a.

The sensor is placed on the back of the hand to be able to recognize the small movements through fingers. The two different configurations used, from first to second, are rotated by 90° from each other. When HNS network is deposited between the electrode gaps of IDE via DEP, they align almost parallel to each other. This implies in configuration 1 these 1D nanomaterials are parallel the motion of the hand while in configuration 2 their positioning is 90° to the direction of their stretching. The two configurations reveal the highly accurate sensing of HNS network. The sensor can capture the difference in the placement of the IDE movement, from Configuration 1 to Configuration 2. Closing of the wrist induces the bending of the sensor, therefore leading to an increase of the resistance value. While in Configuration 2, a sliding motion between the electrodes recorded, as seen in Figure 4.19(b). Leading to a decrease in resistance.

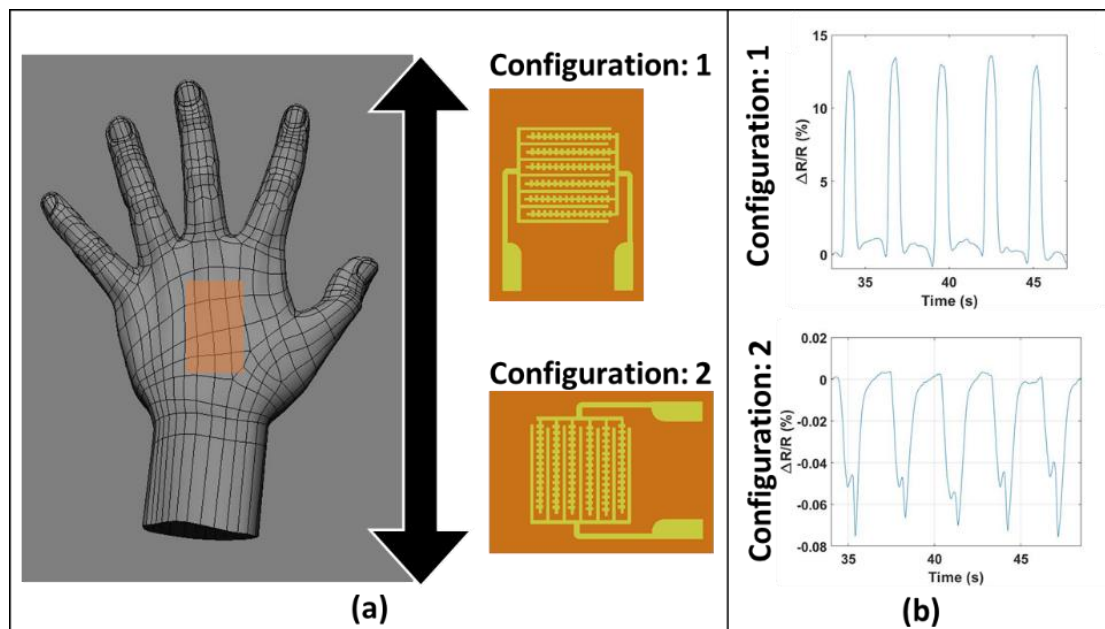


Figure 4.19: (a) Demonstration of real time tracking of the bending by the HNS stretch sensor glove at two different configurations. (b) Resistance response of Configuration 1 and Configuration 2. The particular case, Configuration 2, showing here tracks the ultralow sliding effect between the electrodes.

For the cyclic performance, repeated hand movements are captured over 10 minutes in real time, Figure 4.20. The consecutive cycles show a similar and stable pattern during the test, indicating that the sensors have good stability throughout long-term cycling of the deformations. Configuration of HNS sensor used here is in configuration 1.

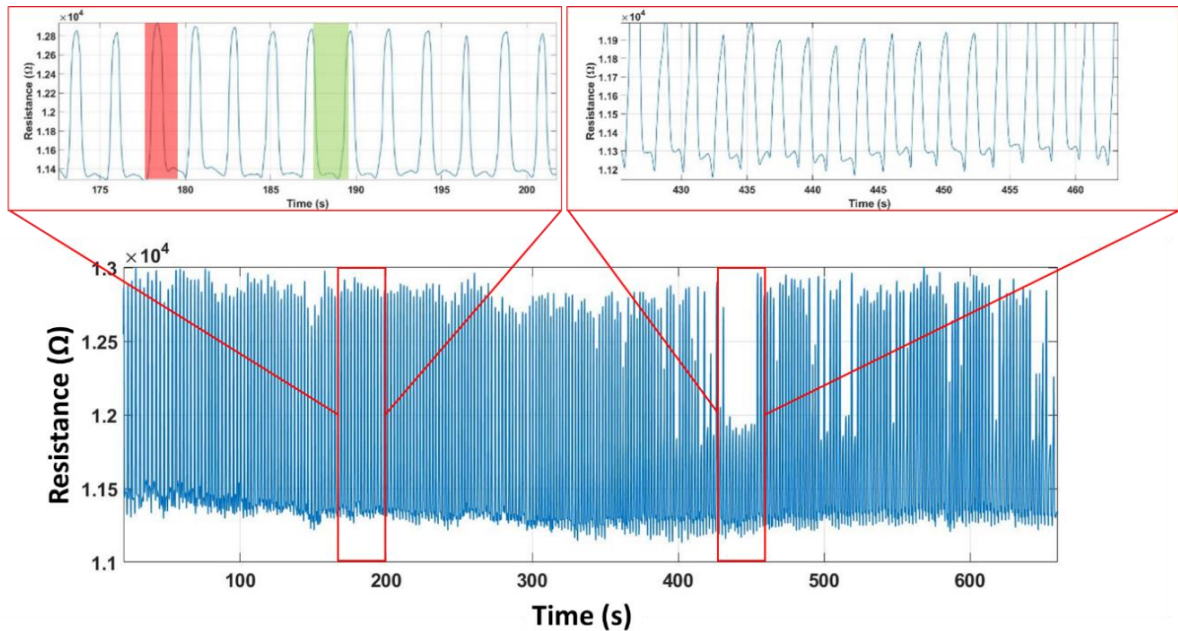


Figure 4.20: Real-time resistance responses of the strain sensor for monitoring hand motion for 10 minutes, the fatigue response after 6 minutes has been well recorded by the HNS sensor.

Here, we report the first tests of hand movements detection using HNS sensor system, under traction and compression strains. Traditional method of fixing the sensor position on the glove is used. It shows great sensitivity and linearity. IDE covers the very small area of skin i.e., 16 mm^2 that allows to increase wearability and user friendliness. The use of hand motion tracking glove modules based on HNS strain sensors has shown high accuracy. It also has advantages of easily integrating to the glove, that is subsequently worn by a volunteer and the sensing system that demands low-cost manufacturing.

4.3 Conclusion

In conclusion, HNS strain sensor response with temperature and humidity has been evaluated. The aim of using an encapsulation is to make HNS sensors insensitive to temperature and humidity; this has been experimentally verified and achieved. Another perspective of HNS ability in simultaneously detection of strain, temperature, and humidity with one device, makes it a potential candidate as a multimodal sensor [10]. However, there is a need for proper calibration and characterization, as without encapsulation there is a risk of hysteresis and less reproducible responses from HNS sensors. In addition to detection of temperature shifts and strain applied, the sensor has been used to monitor human motions.

The current work introduced HNS materials and IDE designs, to improve their sensitivity. The flexible piezoresistive strain sensors have a total thickness of 127 μm , which can be comfortably attached to hands. An overview of the mechanical and electrical behaviors of the HNS sensor to validate its usefulness and readiness in wearable systems was presented. A highly sensitive response for biological signal measurements, such as cardiac pulse monitoring, finger bending and lifting and wrist clutching using the HNS sensors has been demonstrated. The results exhibit several key sensing capabilities: (1) monitoring of human pulse waves with the identification of at least two distinct local peaks (2) finger-lifting pressure (3) angular motion detection. Additionally, even when they are not in direct contact with the skin, HNS sensors are able to detect the movements of the hand accurately.

Their extremely low power consumption makes HNS sensor very attractive for consumer applications and missions having constraints on power budget. One of the main limitations of this current prototype is the relatively inflexible Kapton substrate. Nevertheless, it holds immense possibility in improving the electrical connection points and attachment to the skin, which will be a step further to building a complete wearable device.

Bibliography

- [1] J. Lee *et al.*, “A stretchable strain sensor based on a metal nanoparticle thin film for human motion detection,” *Nanoscale*, vol. 6, no. 20, pp. 11932–11939, 2014.
- [2] M. Amjadi, K. U. Kyung, I. Park, and M. Sitti, “Stretchable, Skin-Mountable, and Wearable Strain Sensors and Their Potential Applications: A Review,” *Adv. Funct. Mater.*, vol. 26, no. 11, pp. 1678–1698, 2016.
- [3] L. Li, Y. Bai, L. Li, S. Wang, and T. Zhang, “A Superhydrophobic Smart Coating for Flexible and Wearable Sensing Electronics,” *Adv. Mater.*, vol. 29, no. 43, pp. 1–8, 2017.
- [4] E. Aslanidis, E. Skotadis, E. Moutoulas, and D. Tsoukalas, “Thin film protected flexible nanoparticle strain sensors: Experiments and modeling,” *Sensors (Switzerland)*, vol. 20, no. 9, pp. 25–27, 2020.
- [5] J. Chen *et al.*, “Polydimethylsiloxane (PDMS)-based flexible resistive strain sensors for wearable applications,” *Applied Sciences (Switzerland)*, vol. 8, no. 3, 2018.
- [6] R. Knechtel, “Glass frit bonding: An universal technology for wafer level encapsulation and packaging,” *Microsyst. Technol.*, vol. 12, no. 1-2 SPEC. ISS., pp. 63–68, 2005.
- [7] C. Park, H. Jung, H. Lee, S. Hong, H. Kim, and S. J. Cho, “One-step laser encapsulation of nano-cracking strain sensors,” *Sensors (Switzerland)*, vol. 18, no. 8, 2018.
- [8] C. Tan *et al.*, “A high performance wearable strain sensor with advanced thermal management for motion monitoring,” *Nat. Commun.*, vol. 11, no. 1, pp. 1–10, 2020.
- [9] D. Barmpakos and G. Kaltsas, “A review on humidity, temperature and strain printed sensors—current trends and future perspectives,” *Sensors (Switzerland)*, vol. 21, no. 3, pp. 1–24, 2021.
- [10] H. Liu *et al.*, “A Flexible Multimodal Sensor That Detects Strain, Humidity, Temperature, and Pressure with Carbon Black and Reduced Graphene Oxide Hierarchical Composite on Paper,” *ACS Appl. Mater. Interfaces*, vol. 11, no. 43, pp. 40613–40619, 2019.
- [11] Y. Huang, X. Fan, S. C. Chen, and N. Zhao, “Emerging Technologies of

- Flexible Pressure Sensors: Materials, Modeling, Devices, and Manufacturing,” *Adv. Funct. Mater.*, vol. 29, no. 12, pp. 1–24, 2019.
- [12] F. Zhang *et al.*, “Multi-modal strain and temperature sensor by hybridizing reduced graphene oxide and PEDOT:PSS,” *Compos. Sci. Technol.*, vol. 187, no. September 2019, p. 107959, 2020.
- [13] Q. Hua *et al.*, “Skin-inspired highly stretchable and conformable matrix networks for multifunctional sensing,” *Nat. Commun.*, vol. 9, no. 1, p. 244, 2018.
- [14] Q. Wang, S. Ling, X. Liang, H. Wang, H. Lu, and Y. Zhang, “Self-Healable Multifunctional Electronic Tattoos Based on Silk and Graphene,” *Adv. Funct. Mater.*, vol. 29, no. 16, pp. 1–8, 2019.
- [15] M. A. Squillaci, M. A. Stoeckel, and P. Samori, “3D hybrid networks of gold nanoparticles: Mechanoresponsive electrical humidity sensors with on-demand performances,” *Nanoscale*, vol. 11, no. 41, pp. 19319–19326, 2019.
- [16] M. Serhan *et al.*, “Total iron measurement in human serum with a smartphone,” *AIChE Annu. Meet. Conf. Proc.*, vol. 2019-Novem, 2019.
- [17] P. Pang, J. Guo, S. Wu, and Q. Cai, “Humidity effect on the dithiol-linked gold nanoparticles interfaced chemiresistor sensor for VOCs analysis,” *Sensors Actuators, B Chem.*, vol. 114, no. 2, pp. 799–803, 2006.
- [18] T. Addabbo *et al.*, “The effect of au nanoparticle addition on humidity sensing with ultra-small tio2 nanoparticles,” *Chemosensors*, vol. 9, no. 7, 2021.
- [19] G. Chaloeipote, J. Samarnwong, P. Traiwatcharanon, T. Kerdcharoen, and C. Wongchoosuk, “High-performance resistive humidity sensor based on Ag nanoparticles decorated with graphene quantum dots,” *Royal Society Open Science*, vol. 8, no. 7. p. 210407, 2021.
- [20] S. Kang, V. Pradana Rachim, J. H. Baek, S. Y. Lee, and S. M. Park, “A Flexible Patch-Type Strain Sensor Based on Polyaniline for Continuous Monitoring of Pulse Waves,” *IEEE Access*, vol. 8, pp. 152105–152115, 2020.
- [21] W. W. Jheng, Y. S. Su, Y. L. Hsieh, Y. J. Lin, and S. Der Tzeng, “Gold Nanoparticle Thin Film-Based Strain Sensors for Monitoring Human Pulse,” *ACS Appl. Nano Mater.*, vol. 4, no. 2, pp. 1712–1718, 2021.
- [22] W. Pan *et al.*, “Stretchable strain sensor for human motion monitoring based on an intertwined-coil configuration,” *Nanomaterials*, vol. 10, no. 10, pp. 1–15, 2020.

- [23] Y. Wu, L. Beker, I. Karakurt, W. Cai, J. Elwood, and X. Li, "High resolution flexible strain sensors for biological signal measurements," *19th Int. Conf. Solid-State Sensors, Actuators Microsystems*, pp. 1144–1147, 2017.
- [24] G. Shi *et al.*, "A Multifunctional Wearable Device with a Graphene/Silver Nanowire Nanocomposite for Highly Sensitive Strain Sensing and Drug Delivery," *C*, vol. 5, no. 2, p. 17, 2019.
- [25] S.-D. Wu, B. Ketelsen, S. Hsu, and T. Vossmeier, "Towards Nanomaterials-Based Biocompatible and Biodegradable Strain Sensors for Healthcare and Medical Applications," *Proceedings*, vol. 56, no. 1, p. 17, 2020.
- [26] Q. Meng *et al.*, "A facile approach to fabricate highly sensitive, flexible strain sensor based on elastomeric/graphene platelet composite film," *J. Mater. Sci.*, vol. 54, no. 15, pp. 10856–10870, 2019.
- [27] J. Tolvanen, J. Hannu, and H. Jantunen, "Stretchable and Washable Strain Sensor Based on Cracking Structure for Human Motion Monitoring," *Sci. Rep.*, vol. 8, no. 1, pp. 1–10, 2018.
- [28] S. W. Lee *et al.*, "Enhanced Sensitivity of Patterned Graphene Strain Sensors Used for Monitoring Subtle Human Body Motions," *ACS Appl. Mater. Interfaces*, vol. 9, no. 12, pp. 11176–11183, 2017.
- [29] J. Woo Park *et al.*, "Measurement of finger joint angle using stretchable carbon nanotube strain sensor," *PLoS One*, vol. 14, no. 11, pp. 1–11, 2019.
- [30] N. P. Oess, J. Wanek, and A. Curt, "Design and evaluation of a low-cost instrumented glove for hand function assessment," *J. Neuroeng. Rehabil.*, vol. 9, no. 1, pp. 1–11, 2012.
- [31] K. S. Lee and M. C. Jung, *Three-dimensional finger joint angles by hand posture and object properties*, vol. 59, no. 7. 2016.
- [32] B. S. Wesley, F. S. J. Paulo, E. C. S. Ewaldo, and C. S. F. Raimundo, "Wearable Electronic Glove for Supported to the Diagnosis of Repetitive Strain Injury," *Int. J. Adv. Eng. Res. Sci.*, vol. 7, no. 3, pp. 121–124, 2020.
- [33] T. P. Tomo *et al.*, "Covering a Robot Fingertip with uSkin: A Soft Electronic Skin with Distributed 3-Axis Force Sensitive Elements for Robot Hands," *IEEE Robot. Autom. Lett.*, vol. 3, no. 1, pp. 124–131, 2018.
- [34] S. Cho *et al.*, "Large-Area Cross-Aligned Silver Nanowire Electrodes for Flexible, Transparent, and Force-Sensitive Mechanochromic Touch Screens," *ACS Nano*, vol. 11, no. 4, pp. 4346–4357, 2017.

- [35] A. Wang, G. Chen, J. Yang, S. Zhao, and C. Y. Chang, "A Comparative Study on Human Activity Recognition Using Inertial Sensors in a Smartphone," *IEEE Sens. J.*, vol. 16, no. 11, pp. 4566–4578, 2016.
- [36] C. Xu, P. H. Pathak, and P. Mohapatra, "Finger-writing with smartwatch: A case for finger and hand gesture recognition using smartwatch," *HotMobile 2015 - 16th Int. Work. Mob. Comput. Syst. Appl.*, pp. 9–14, 2015.
- [37] S. J. Kim *et al.*, "High Durability and Waterproofing rGO/SWCNT-Fabric-Based Multifunctional Sensors for Human-Motion Detection," *ACS Appl. Mater. Interfaces*, vol. 10, no. 4, pp. 3921–3928, 2018.
- [38] S. Seyedin, P. Zhang, M. Naebe, and S. Qin, "Textile strain sensors: A review of the fabrication technologies, performance evaluation and applications," *Mater. Horizons*, vol. 6, no. 2, pp. 219–249, 2019.
- [39] A. Chortos, J. Liu, and Z. Bao, "Pursuing prosthetic electronic skin," *Nat. Mater.*, vol. 15, no. 9, pp. 937–950, 2016.
- [40] M. A. Ahmed, B. B. Zaidan, A. A. Zaidan, M. M. Salih, M. Modi Bin Lakulu, and M. M. Bin Lakulu, "A review on systems-based sensory gloves for sign language recognition state of the art between 2007 and 2017," *Sensors (Switzerland)*, vol. 18, no. 7, 2018.
- [41] S. Han *et al.*, "Multiscale nanowire-microfluidic hybrid strain sensors with high sensitivity and stretchability," *npj Flex. Electron.*, vol. 2, no. 1, 2018.
- [42] Y. Koga, "Three-dimensional motion analysis and its application in total knee arthroplasty: what we know, and what we should analyze," *J. Orthop. Sci.*, vol. 20, no. 2, pp. 239–249, 2015.
- [43] S. Lu, D. Chen, C. Liu, Y. Jiang, and M. Wang, "A 3-D finger motion measurement system via soft strain sensors for hand rehabilitation," *Sensors Actuators, A Phys.*, vol. 285, no. December, pp. 700–711, 2019.
- [44] Y. Mengüç *et al.*, "Wearable soft sensing suit for human gait measurement," *Int. J. Rob. Res.*, vol. 33, no. 14, pp. 1748–1764, 2014.
- [45] D. M. Vogt, Y. L. Park, and R. J. Wood, "Design and characterization of a soft multi-axis force sensor using embedded microfluidic channels," *IEEE Sens. J.*, vol. 13, no. 10, pp. 4056–4064, 2013.
- [46] Y. Menguc *et al.*, "Soft Wearable Motion Sensing Suit for Lower Limb," *Proc. - IEEE Int. Conf. Robot. Autom.*, no. May, pp. 5309–5316, 2013.
- [47] R. K. Kramer, C. Majidi, R. Sahai, and R. J. Wood, "Soft curvature sensors for

- joint angle proprioception,” *IEEE Int. Conf. Intell. Robot. Syst.*, pp. 1919–1926, 2011.
- [48] I. Kim *et al.*, “A photonic sintering derived Ag flake/nanoparticle-based highly sensitive stretchable strain sensor for human motion monitoring,” *Nanoscale*, vol. 10, no. 17, pp. 7890–7897, 2018.
- [49] M. Zhang, C. Wang, Q. Wang, M. Jian, and Y. Zhang, “Sheath-Core Graphite/Silk Fiber Made by Dry-Meyer-Rod-Coating for Wearable Strain Sensors,” *ACS Appl. Mater. Interfaces*, vol. 8, no. 32, pp. 20894–20899, 2016.
- [50] Y. Cheng, R. Wang, J. Sun, and L. Gao, “A Stretchable and Highly Sensitive Graphene-Based Fiber for Sensing Tensile Strain, Bending, and Torsion,” *Adv. Mater.*, vol. 27, no. 45, pp. 7365–7371, 2015.

General Conclusions & Future Directions

In this thesis, we have presented the fabrication of flexible strain sensors based on Helical Nanostructure (HNS) by using deposition and alignment technique called dielectrophoresis. The current work introduced HNS materials and IDE (Interdigitated electrode) designs to improve their sensitivity toward low strain values and achieve zero hysteresis response. Two aspects were more particularly developed. The first objective was to assemble helical nanostructure on an interdigitated electrode and to characterize the boundary conditions in order to optimize the deposition. The second objective was to calibrate and characterize the sensitivity response. Mechanical characterization included measuring the Gauge Factor and enhancing the performance. Finally, the potential application of HNS sensors as a wearable device was explored.

- **Elaboration and Characterization of HNS assemblies alignment**

Flexible strain sensors have been successfully fabricated with MPA@AuNP HNS as strain sensing media. A schematic of the easily manipulated protocol for fabricating the **1D helical nanomaterial**-based strain sensor is presented in this thesis. **Dielectrophoresis** has been compared with other techniques, one of which is Drop-Cast deposition. Altogether, dielectrophoresis proved to be an efficient, minimum-waste producing, and a quick alignment technique. Dielectrophoresis takes less than a minute to achieve a well-positioned deposition, feasible and prevents material wastage. HNS are deposited in the desired direction as well as in the appropriate localization in between IDE.

We saw that the electrical performances of the sensors are easily tunable by controlling the density of HNSs synthesized on the IDE. The experimental analysis of DEP provided more control on deposition density by carrying out **multiple DEP** over the same sample.

- **Shaping and Characterization of HNS based strain sensor**

We have addressed the mechanical analysis of the HNS based strain sensors. By making an estimation of HNS quantity present between the IDE through device resistance, an interesting strategy to tune and enhance the **Gauge Factor** of strain

sensors has been presented based on multiple DEP deposition. It is found that there is a zone of optimal resistance in case of HNS that allows achieving the best Gauge Factor, which lies in our case within the range of 500 to 20k Ω . It helps in building a more stable sensor that can retain its initial resistance i.e., no shift in resistance even after a series of bending tests.

Overall, the HNS based sensor showed excellent performance with good sensitivity, excellent durability against repeated loading cycles (**2M cycles** at 1% strain) and negligible hysteresis. The Helical Nanostructure morphology is the key contribution to negligible **hysteresis** response. The grafting gold nanomaterials over a helical spring-like base made it possible to achieve mechanical properties rivalling those of the metallic nanomaterial. The intrinsic mechanical properties of the HNS structure allow a faster recovery after deformation. A novel strain sensor is realized that can measure **ultralow strain up to 0.01%** and **fast response**. HNS strain sensor response to temperature and humidity variation is observed and presented. The aim of using an **encapsulation** is to make HNS sensors insensitive to temperature and humidity; this has been experimentally verified and achieved.

The flexible strain sensors built in this project have a total thickness of 127 μm , which can be comfortably attached to hands. A highly sensitive response for biological signal measurements, such as cardiac pulse monitoring, hand motion using the HNS sensors has been tested. The results exhibited several key sensing capabilities such as: (1) **monitoring of human pulse waves** with the identification of at least two distinct local peaks (2) **finger-lifting pressure** (3) **Wrist clutching detection** (4) **angular motion detection**. Additionally, even when they are not in direct contact with the skin i.e., using a glove, HNS sensors are able to detect the movements of the hand accurately. Their extremely low power consumption makes HNS sensor very attractive for consumer applications and missions having constraints on power budget.

- **Future work**

HNS Solution. The common drawbacks of current HNS sensors using functionalized gold nanoparticle are aggregation. From one dielectrophoresis deposition to another due to non-homogeneity of the HNS solution, the final resistance of devices may vary and eventually impact the performance. It is because dielectrophoresis force attracts bigger and bulkier particles first. For that reason, non-

homogeneity and aggregation of HNS solution need to be avoided to produce a device with uniform and unique deposition protocol.

Bulk Fabrication. In order to build IDE sensor for mass production at low cost the electrode gap must be increased, which is currently set to 3 μm . While trying to realize such small gap, interdigitated electrodes tend to have short circuits at the end of the microfabrication process. Increasing gap size would increase the yield of IDE production from a standard 4-inch wafer. This would also imply increasing the 1D helical nanostructure length to compensate the number of particles required to bridge the gap.

IDE Design. Further, to reduce possible strain coming from electrical connections (use of clips) during the biological measurements, the electrode design of IDE should be modified. One of the main limitations of this current prototype is the relatively inflexible Kapton substrate. To enhance the sensitivity and comfort of wearing them, thinner flexible substrate can be used. Nevertheless, HNS sensors holds immense possibility in improving the electrical connection points and attachment to the skin, which will be a step further to building a complete wearable device.

Altogether, a higher structural integrity and sensitivity is achieved through the HNS sensors. Small size of HNS devices makes them easily integrate in the sensory system. Although considerable progress has been made so far, as a wearable strain sensor, they are still in their prototype stage, and several challenges in the manufacturing, integration and automatization of HNS strain sensors are yet to be tackled.

Appendix

Beam theory. The bending moment for a beam supported at both ends and loaded in center, Figure 0.1, given by

$$M = \left| \frac{-Fx}{2} \right| \quad (1)$$

Where **F** is the applied load. Assuming that the deflection of the beam is sufficiently small, one can neglect the first derivative y . With this the differential equation becomes

$$\frac{d^2 \delta}{d^2 x} = \frac{M(x)}{EI} \quad (2)$$

Where I is the moment of inertia of the cross section with respect to the neutral z -axis $I = \frac{bh^3}{12}$, b is the width of the sample h its thickness; **E** is the bending modulus or young modulus of the mechanical substrate considering that the mechanical properties of the Kapton (Sensor sample) is negligible. It follows that

$$EI \frac{d^2 \delta}{d^2 x} = \left| \frac{-Fx}{2} \right| \quad (3)$$

And the integration procedures lead to

$$EI \frac{d\delta}{dx} = \frac{-Fx^2}{4} + C_1 \quad (4)$$

When $x = \frac{L}{2}$, $\frac{d\delta}{dx} = 0$ gives $C_1 = \frac{FL^2}{16}$

$$EI \delta = \frac{-Fx^3}{12} - \frac{FL^2x}{16} + C_2 \quad (5)$$

When $x = 0$, $\delta = 0$ gives $C_2 = 0$

The equation of deflection of supported rectangular sample which is centrally loaded becomes [1]:

$$\delta(x) = \frac{Fx}{48EI} (3L^2 - 4x^2), 0 < x < \frac{L}{2} \quad (6)$$

Where **F** is the applied load, x is the distance between the point of the applied load and the support, **L** is the suspension length. Thus, the deflection of the center of the beam is given by:

$$\delta\left(\frac{L}{2}\right) = \left| \frac{FL^3}{48EI} \right| \quad (7)$$

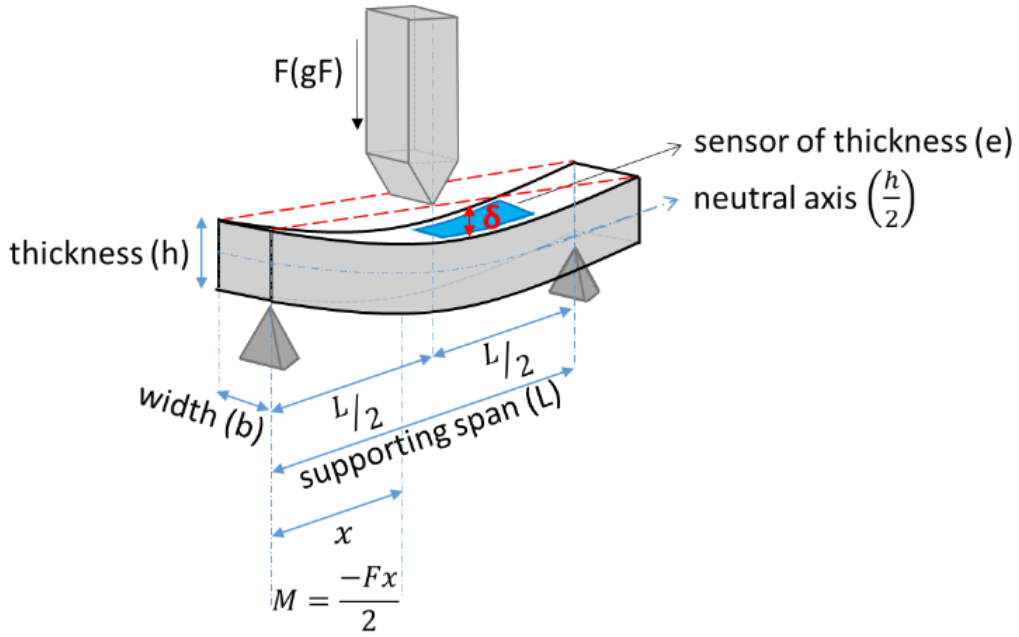


Figure 0.1: Symmetrical Three-point bend loading

The longitudinal strain, ϵ_{xx} at the surface of the sensor is given by

$$\epsilon_{xx} = -\left(\frac{h}{2} + e\right) \frac{d^2\delta(x)}{dx^2}, \quad 0 < x < L/2 \quad (8)$$

Where variable e is the thickness of the Kapton film. Strain varies linearly from zero at the supports to the maximum value at the center of the beam. Taking the integral along the length and using deflection as a function of applied load at the center (Eq.7), ϵ_{xx} is given by

$$\epsilon_{xx} = 3(h + 2e) \frac{Fx}{Eb^3h^3} \quad (9)$$

The strain can further be simplified as

$$\epsilon_{xx} = \frac{6(h + 2e)\delta}{L^2} \quad (10)$$

To estimate the gauge factor, strain is an important parameter. Using Eq.10, the strain is obtained through deflection in the substrate. In later section, a relation is established between applied load (F) and the generated strain (ϵ).

Bibliography

- [1] N. D. Madsen and J. Kjelstrup-Hansen, "Three-point bending setup for piezoresistive gauge factor measurement of thin-film samples at high temperatures," *Rev. Sci. Instrum.*, vol. 88, no. 1, 2017, doi: 10.1063/1.4973512.